Sorption enhanced steam methane reforming process for continuous production of hydrogen in pressure swing adsorptive reactors

A Dissertation Presented to the
UNIVERSIDADE DO PORTO
For the degree of Doctor in
Chemical and Biological Engineering
by
Eduardo L. G. Oliveira

Supervisor: Prof. Alirio E. Rodrigues
Co-supervisor: Doctor Carlos A. Grande
LSRE/LCM – Associated Laboratory
Department of Chemical Engineering
Faculty of Engineering
University of Porto
August 28, 2009.

Abstract

In this work, production of hydrogen by the steam methane reforming sorption enhanced reaction process (SMR-SERP) was studied. This process works by the combination of a SMR catalyst with a high temperature sorbent selective for CO_2. The removal of CO_2 enhances the methane conversion, producing high purity hydrogen at lower temperatures than traditional SMR. The periodic regeneration of the sorbent material requires multicolumn operation of the SMR-SERP.

An experimental unit was built to perform the experimental work of this PhD thesis. The unit was adapted to measure CO_2 breakthrough curves, SMR kinetics and diffusional limitations and for SMR-SERP experimental work.

Three commercial hydrotalcite materials from SASOL (Germany) were impregnated with potassium or cesium. The potassium impregnated extrudates showed the highest CO_2 equilibrium sorption capacity at 676 K. Carbon dioxide sorption equilibrium isotherms were measured at 579, 676 and 783 K in the MG30-K (K impregnated) and MG30-Cs (Cs impregnated) hydrotalcites. Both materials presented a maximum in the sorption capacity at 676 K. This maximum was modeled by the Bi-Langmuir isotherm considering endothermic adsorption and exothermic reaction as sorption mechanisms. The LDF model was employed to describe the sorption kinetics in the extrudates.

The true SMR kinetics of a commercial catalyst (Degussa) and a large-pore catalyst (Catalyst A) were measured employing catalyst powder. The reaction rate equations reported by Xu and Froment (1989) were used to describe the catalyst kinetics. Experiments with catalyst extrudates were used to determine the diffusional limitations of each catalyst. The presence of the large-pore network in Catalyst A increased the mass transfer of reagents and products inside the catalyst extrudates resulting in higher reaction effectiveness factors.

The influence of operating variables in SMR-SERP was measured with a reactor with layered distribution of catalyst (Catalyst A or Degussa) and sorbent (MG30-K). It was found that the operating conditions have opposed effects in the catalyst and sorbent. For example: increasing the temperature benefits the SMR reactions rates but decreases the sorption capacity of the sorbent; increasing the pressure reduces the SMR reaction rates but increases the CO_2 sorption capacity in the hydrotalcite.

The SMR-SERP reactive regeneration cycle proposed by Xiu et al (2002) was simulated using the Degussa catalyst or Catalyst A and the MG30-K hydrotalcite. At 680 K, a stream with 8 ppm CO and 88 % hydrogen was simulated with the Degussa catalyst. With Catalyst A, 29 ppm of CO and 82 % H_2 were obtained. The difference is due to the higher Ni content of the commercial Degussa catalyst.

Resumo

Nesta tese foi estudada a produção de hidrogénio por reformado de metano em reactores adsorptivos (SMR-SERP). O processo consiste na combinação no mesmo reactor, de um catalisador e de um adsorvente de alta temperatura selectivo para CO_2. A remoção de CO_2 pelo adsorvente permite obter conversões de metano superiores ao equilíbrio termodinâmico das reacções de reformado de metano. Este processo requer operação simultânea de múltiplos reactores uma vez que o adsorvente requer regeneração periódica.

Uma instalação experimental foi construída durante esta tese. A instalação foi utilizada para a medição de curvas de quebra de CO_2 a alta temperatura, cinética de reformado de metano (SMR) e limitações difusionais dos catalisadores e para experiencias de SMR-SERP.

Três amostras diferentes de hidrotalcites cedidas pela SASOL (Alemanha) foram impregnadas com potássio ou césio. A mais alta capacidade de adsorção de CO_2 a 676 K foi medida nos extrudados impregnados com potássio. Isotérmicas de equilíbrio de adsorção de CO_2 foram medidas a 579, 676 e 783 K numa amostra impregnada com potássio (MG30-K) e numa impregnada com césio. Foi medido um máximo na capacidade de adsorção a 676 K resultante da combinação de dois mecanismos de adsorção: adsorção física (endotérmica) e reacção química (exotérmica). A equação de Bi-Langmuir foi utilizada para descrever a adsorção. O modelo de LDF foi utilizado para descrever a cinética de adsorção nos extrudados.

Foram utilizados dois catalisadores para o reformado de metano: um catalisador comercial (Degussa) e um catalisador de poros largos (Catalyst A). A cinética verdadeira foi medida utilizando catalisador em pó e foi ajustada às equações propostas por Xu e Froment (1989). Foram também medidas as limitações difusionais dos extrudados de cada catalisador. Os poros largos do Catalyst A aumentam a transferência de massa, resultando em factores de eficiência de reacção mais elevados.

Foram feitas experiências de SMR-SERP num reactor com distribuição em camadas de catalisador (Catalyst A ou Degussa) e adsorvente (MG30-K). Os resultados indicam que as condições experimentais têm efeitos opostos no catalisador e no adsorvente. Por ex: aumentar a temperatura favorece a cinética de reacção mas diminui a capacidade do adsorvente; aumentar a pressão favorece a capacidade de adsorção mas diminui a cinética de reacção.

Foi também simulado o ciclo de regeneração reactiva reportado por Xiu et al (2002). A 680 K, utilizando o catalisador Degussa e MG30-K, foi obtida uma corrente com 8 ppm de CO e 88 % de H_2. Nas mesmas condições mas utilizado Catalyst A resultou em 29 ppm de CO e 82 % H_2. A diferença de resultados foi explicada pelo mais conteúdo de Ni do catalisador comercial (Degussa).

Resumé

Dans cette thèse la production d'hydrogène via la réaction de reformage vapeur du méthane améliorée par processus (SMR-SERP) a été étudiée. Ce processus est la combinaison d'un catalyseur SMR avec un absorbant spécifique du CO_2 à haute température. Le retrait du CO_2 améliore la conversion du méthane, produisant de l'hydrogène particulièrement pur à des températures inférieures à celles du SMR traditionnel. La régénération périodique de l'absorbant nécessite l'opération multi-colonnes du SMR-SERP

Une installation particulière a été mise en place afin d'effectuer les expériences relatives à cette thèse. Cette installation a été adaptée afin de réaliser les travaux expérimentaux de SMR-SERP, et de mesurer les courbe de perçage de CO_2, la cinétique et les limites de diffusion du SMR.

Trois matériaux hydrotalcites commerciaux de SASOL (Allemagne) ont été imprégnés de potassium ou de césium. Les extrudats imprégnés de potassium ont montré la plus haute capacité d'absorption de CO_2 à l'équilibre à 676 K. Les isothermes d'absorption du dioxyde de carbone ont été mesurées à 579, 676 et 783 K dans les hydrotalcites MG30-K (imprégnés de potassium) et MG30-Cs (imprégnés de césium). Les deux matériaux présentent un maximum de capacité d'absorption à 676 K. Ce maximum a été modélisé par l'isotherme Bi-Langmuir en considérant l'adsorption endothermique et la réaction exothermique comme des mécanismes d'absorption. Le modèle LDF a été utilisé pour décrire la cinétique d'absorption dans les extrudats.

Les cinétiques réelles d'un catalyseur commercial (Degussa) et d'un catalyseur à large pores (Catalyseur A) ont été mesurées à l'état de poudre. Les équations de vitesse de réaction décrites par Xu et Froment (1989) ont servi à décrire la cinétique des catalyses. Des expériences avec les extrudats de catalyse ont déterminé les limites de diffusion de chaque catalyseur. La présence d'un réseau à pores larges dans le Catalyseur A a augmenté le transfert de masse des réactifs et des produits au sein des extrudats de catalyse, contribuant ainsi à de facteurs de efficacité plus élevés.

L'influence des variables opérationnelles sur SMR-SERP a été mesurée grâce à un réacteur dans lequel les catalyseurs (Catalyseur A ou Degussa) et l'absorbant (MG30-K) ont été distribués en couches. Il a été observé que les conditions d'opération ont des effets opposés sur le catalyseur et l'absorbant. Par exemple, augmenter la température est bénéfique pour les vitesses de réaction SMR mais diminue la capacité d'absorption de l'absorbant, tandis que l'augmentation de la pression réduit la vitesse de réaction SMR tout en augmentant la capacité d'absorption du CO_2 de l'hydrotalcite.

Le cycle de régénération réactive SMR-SERP proposé par Xiu et al (2002) a été simulé en utilisant le catalyseur Degussa ou le Catalyseur A et l'hydrotalcite MG30-K. A 680 K, une vapeur à 8 ppm de CO et 88 % d'hydrogène a été obtenue avec le Degussa, contre une vapeur à 29 ppm de CO et 82 % de H_2 avec le Catalyseur A. Cette différence provient de la plus forte proportion de Ni dans le catalyseur commercial Degussa.

Acknowledgements

In this section I would like to acknowledge all of you who, in many different ways, gave me support throughout this work.

Primeiro que tudo gostaria de agradecer aos meus pais e irmãos a sua presença, amizade, carinho e apoio.

Quero agradecer ao Prof. Alírio Rodrigues pela sua orientação e pelo seu exemplo de trabalho incansável. Cada qual tem o seu papel e ele mostrou exigir tanto dos outros como de si mesmo.

Ao Carlos Grande, que me ajudou nos momentos difíceis e me orientou no caminho certo quando estava perdido.

Agradeço à FCT o apoio financeiro que tornou possível esta tese através da bolsa SFRH/BD/17132/2004.

Aos meus colegas a ajuda que num momento ou noutro me deram: Filipe Lopes, Rui Ribeiro, Marta Abrantes, Ganesh Kumar, Mónica Santos, Pedro Sá Gomes, Pedro Madeira, Viviana Silva, Vera Mata, Adriano Ribeiro e Avelino da Silva.

Deixo aqui uma palavra de agradecimento aos professores e funcionários do DEQ que me ajudaram quando necessitei e em especial ao professor Loureiro e ao Sr. Sousa Vale pela sua amizade.

Quero também agradecer ao Nelson Neves pela amizade e trabalho. Sem ele teria sido ainda mais difícil.

Quero também agradecer à minha família e amigos, em especial ao Fernando, Hugo, Aurora, Fátima, Carlos Silva e Daniel.

Thank you to my foreign friends that were also there for me: Anthony, Antti, Eeva, Tommi, Elena, Anne and Maria. 日本人の友達は友情に感謝します.

Finalmente a Deus por todos os dias e à Paula, a luz que me acompanha.

Contents

Chapter 3. Steam methane reforming 89

1. Introduction

1.1. Relevance and motivation

There is enough scientific evidence to say that there is a straight relation between the production of energy and fuels from fossil fuels and global warming. The consumption of these oil and gas reserves has enhanced the availability to commodities and in fact has improved our style of life. However, these changes were done in an unsustainable way. Emission of massive amounts of greenhouse gases has resulted in a phenomenon termed as global warming, threatening the future of mankind, at least as we know it now. Additionally to the environmental problem, the economics of energy production are also changing. The oil and gas reserves available until now will be depleted in some years and the new reserves that have been found in the last years are more difficult and expensive to extract.

Economic and environmental problems are boundary conditions that should be circumvented by developing new pathways to produce energy. It has been suggested that hydrogen may dominate the energy matrix in the near future solving sustainability issues. Hydrogen can be used for storage and production of energy [1] and as fuel, reason why is termed as energy carrier or energy vector. Hydrogen can be produced by fossil or renewable sources and one of the fundamental advantages is that it does not emit carbon dioxide when used. The main disadvantage in the actual use of energy is its low volumetric density when compared to fossil-derived chemicals.

Another important issue to be addressed in the production of energy is the cost of production. Hydrogen is now a feedstock in the chemical industry, representing only a very small amount of the market of energy and fuels. The worldwide hydrogen production capacity in refineries in January 2008 was 3.81×10^8 Nm^3/day [2]. Only 0.6 % of this hydrogen was produced in Portugal. The share of hydrogen markets [3] is shown in Figure 1.1. The bulk of the hydrogen is produced to supply the demand of existing industries. Even if all this hydrogen was used to replace fossil fuels, it only accounts for 2 % of the global energetic requirements [3].

To accomplish an increase in production capacity by 2 orders of magnitude in a sustainable way, new and more efficient technologies should be implemented. The main objective of this thesis is the study of an innovative route for production of hydrogen by combining reaction and in-situ separation of CO_2 to promote additional formation of products.

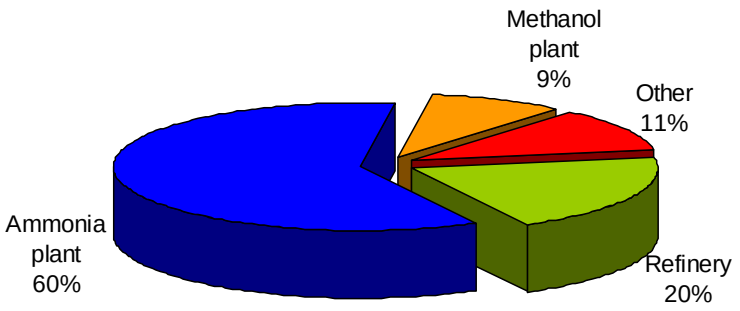

Figure 1.1. Hydrogen production capacities in different industries.

Current technologies for hydrogen production include steam and autothermal reforming, partial oxidation, water electrolysis, chloro-alkali processes, styrene manufacture, MTBE production, petroleum refining [1, 3].

Among the current technologies, steam methane reforming (SMR) is still, by far, the most economic and widely employed technology for hydrogen production [4], accounting for 48 % of the total H_2 produced in 2002 [1, 5] while the reforming of other petrochemicals accounts for 30 % and coal 18 % [1]. The SMR technology is a well established large-scale technology and produces the highest amount of H_2 per carbon input, reducing the carbon footprint per energy unit produced. To achieve long-term sustainability (usually translated to economical policies intending to Kyoto protocol targets [6]), the SMR can be modified to include carbon dioxide capture and storage, CCS. Capture of CO_2 can be implemented in different ways in a SMR process: modifying the current separation technology for H_2 cleaning or entirely modifying the plant flowsheet by integrating reaction and separation in a hybrid reactor.

Steam methane reforming, although based on non-renewable sources, is the best option available at the moment to produce H_2 in large quantities while other technologies do not achieve the required maturity. However, in the long term, the best option for energy and fuels production will always be the use of renewable sources like wind, solar, hydro, geothermal or tidal.

New processes include sorption enhanced reaction processes (SERP), membrane enhanced reaction processes, advanced coal gasification with carbon capture and storage (CCS), production from biomass, production using solar power by photoelectrochemical and photobiological technologies [1]. This thesis focuses on the SERP process, a technology that will be discussed in detail in the following chapters.

1.1.1. Steam reforming of carbon-based materials

Steam reforming refers to the combination of steam and carbon sources to produce hydrogen (H_2) and carbon oxides: carbon monoxide (CO) and/or carbon dioxide (CO_2). In the presence of CO and steam, the water-gas shift (WGS) reaction also takes place and accounts for the simultaneous production of CO_2. The carbon steam reforming and WGS reactions can be seen below [4]:

$$C + H_2O \leftrightarrow CO + H_2 \qquad \Delta H_{298K} = 131.3 kJ/mol \qquad (1.1)$$

$$CO + H_2O \leftrightarrow CO_2 + H_2 \qquad \Delta H_{298K} = -41 kJ/mol \qquad (1.2)$$

The steam reforming process dates back to the beginning of the 20th century. At that time, the demand for cheap H_2 for the synthesis of ammonia and methanol was the driving force for the development of this process. Ammonia was a major source of fixed nitrogen and was

used in the production of fertilizers, explosives, nitric acid, refrigeration fluid, disinfectants [4, 7]. The production of cheap ammonia was important to increase the output of farms and consequently lower the price of food. The Second World War also raised the demand for explosives and consequently for more ammonia. Parallel to the demand of ammonia was the demand for methanol for the production of formaldehyde. Formaldehyde is used to produce polymers, paints and explosives [8]. Methanol is obtained by the combination of synthesis gas (CO and H_2) at high pressure.

The first steam reforming process was developed in 1917 by Haber and Bosh [4]. This process relied on coke to provide the carbon necessary for reaction 1. BASF developed the technology for the steam methane reforming. In this process, methane (CH_4) – from natural gas – was combined with steam over a catalyst at high temperatures to produce H_2. In 1931 the BASF process was applied industrially in New Jersey to reform refinery off-gases. An example of an industrial steam methane reformer can be seen in Figure 1.2 [9]. Later, ICI developed better catalysts and introduced a desulphurization step to clean the feed gas. In places where natural gas was not so readily available, steam reforming processes were developed for other hydrocarbons [4], namely naphtha, ethane, methanol, ethanol among others.

More recently steam reforming of methane and oxygenated carbon sources (methanol, ethanol) have been studied for the production of H_2 for fuel cells [10-13]. In fact, with the maturity that reforming technology has attained, it has been presented as an alternative to boost overall process economic of production of bio-fuels [14].

The main source of methane is natural gas. Natural gas composition is different depending on the extraction site [4, 15]. Other components that can be found are ethane, propane as well as small amounts of other hydrocarbons, nitrogen, carbon dioxide, sulfur and chlorine [4, 15].

Figure 1.2. Methane steam reformer for the production of hydrogen (~112x10³ Nm³/h) [9].

The C_{2+} hydrocarbons (hydrocarbons with two or more carbons) are not problematic in small amounts as they also undergo steam reforming resulting in H_2. However, chlorine and sulfur are poisons to the catalyst and have to be removed before the reforming reactor. Sulfur can be removed by a desulphurization step using a bed of zinc oxide (ZnO). As chlorine destroys the ZnO, usually a chlorine guard is installed before desulphurization step [4]. Nitrogen and CO_2 are not hazardous to the catalyst but act as diluents, decreasing the H_2 yield as well as the energy efficiency of the process and therefore, if economically feasible, should also be removed.

The production of hydrogen by SMR is associated to several technological difficulties that were overcome over time, but sometimes

in an expensive way. Reaction is carried out at high pressure (25-40 bar) and very high temperature (up to 1100 K). The presence of large amount of steam and the strongly endothermic nature of SMR result in severe heat transfer limitations, normally solved by direct firing of the reactor tubes. Such conditions result in a very short life of reactor tubes (3-4 years depending on the operating conditions and tube wall thickness) that are made of expensive materials (chromium and nickel). Reducing the reaction temperature will be a very interesting approach since less energy will be spent in heating and cheaper materials can be used.

1.1.2. Improvements to current SMR technology: hybrid reactors

Among the list of the suggested improvements to SMR process are hybrid reactors. The concept of hybrid reactor refers to the use of the same vessel to perform reaction and separation. There are several processes where hybrid reactors were proposed, such as synthesis of diethylacetal [16] or dimethylacetal [17], production of TAME and n-Propyl propionate [18] and SMR [19-24] among others. The hybrid reactor concept is specially suited for equilibrium-limited reactions: when one of the products is removed, the equilibrium is shifted towards the formation of more products according to Le Chatelier's principle. Therefore, in a hybrid reactor it is possible to obtain higher conversions than in a conventional reactor operating in the same conditions. In the case of SMR, a hybrid reactor allows the use of lower temperatures of operation (~500 ºC) while maintaining high methane conversion and hydrogen yield. The temperature decrease reduces both operational

costs (heating) and investment costs (materials) improving the overall life cycle analysis and thus carbon footprint. The number of separation processes necessary to purify the H_2 after the reactor will also be smaller as, inside the reactor, one of the products – CO_2 or H_2 – is removed as soon as it is produced. In the effluent stream, the carbon monoxide content will be close to zero as CO will react with the excess steam to produce more CO_2 and H_2 (reaction 1.2).

Literature dealing with hybrid reactor suitable for steam methane reforming report the use of membranes [25] or sorbents [26] to achieve the equilibrium shift towards the products. Membranes permeable to hydrogen can be used to obtain a stream composed of high purity hydrogen. In the other stream leaving the reactor, the unconverted methane has to be separated from the CO and CO_2. The methane can then be recycled to the reactor and the carbon dioxide captured. An important problem of this technology is that H_2 is obtained at low pressure and therefore there is an extra cost of compression that must be considered in the economic balance. Additionally, the life of membranes and sealing under SMR conditions still represent important technological problems to be solved.

High temperature carbon dioxide sorbents are also suitable to achieve the equilibrium shift. Removing the CO_2 from the reactor shifts the equilibrium, increasing the methane and carbon monoxide conversion to more hydrogen. This is known as sorption-enhanced reaction process. The effluent stream of the SERP is composed of methane, hydrogen and steam at high pressure. The SERP reactor has to be periodically regenerated to desorb carbon dioxide from the sorbent material. This means that, unlike the membrane reactor, more than one column has to be operated simultaneously to achieve a continuous H_2

production. The carbon dioxide recovered during the regeneration stage can be purified for chemical uses or for permanent sequestration in secure geological formations. Simulation of SERP has been already performed at the LSRE to determine new operating conditions [20-24] employing published data of carbon dioxide sorption equilibrium and kinetics and catalyst reaction kinetics.

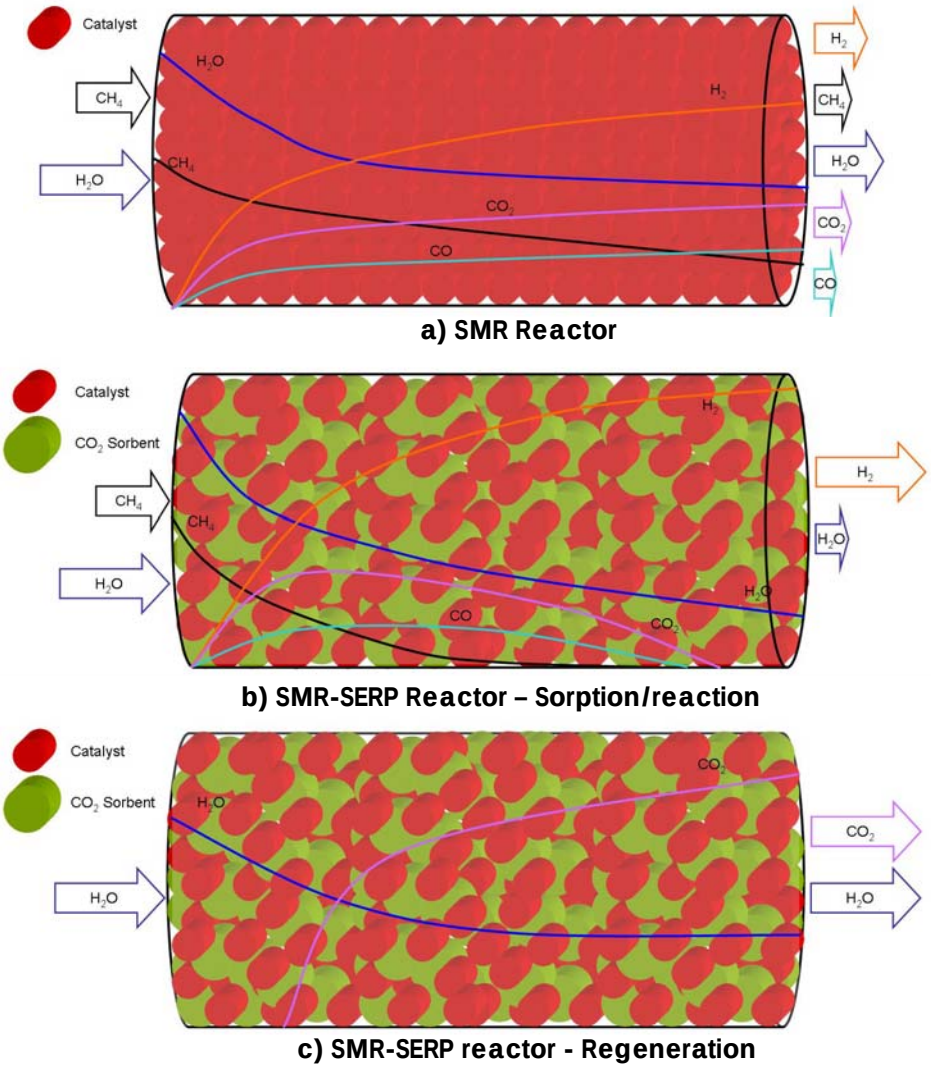

Figure 1.3. a) Steam methane reforming reactor; b) SERP reactor during sorption step; c) SERP reactor during regeneration of the CO_2 sorbent step.

A comparison example of evolution of gas concentration in the SMR reactor and in SERP can be seen in Figure 1.3. Note that the original SMR reactor may operate in steady state conditions while SMR by SERP require periodical switching of columns.

The process design and optimization as well as technology transfer of SERP process for H_2 production is strongly linked to the development of materials able to remove CO_2 from a "difficult" reaction media. For this reason, an important topic within this thesis was devoted to research of CO_2 removal at high temperatures under presence of large amounts of steam.

1.1.3. Sorption of CO_2 at high temperature (> 573 K)

Physical adsorption is an endothermic process and therefore the equilibrium sorption capacity decreases with temperature. This is a problem for steam reforming reaction running at temperatures higher than 400 °C. There are many materials that can be used to sorb CO_2 at low temperatures such as activated carbons, silica gel, zeolite 13X and others [27] but at high temperatures and in the presence of steam most of them are destroyed or show very low capacities and therefore cannot be used.

One of the first reported sorbents was calcium oxide (CaO) [28, 29]. Since then, several sorbent materials have been employed in basic research to study the sorption of CO_2 at high temperature in presence of steam: lithium oxides [30-32], calcium oxides [33], hydrotalcites [19, 34-42], double salts [43] and basic alumina [26]. Hydrotalcites, at low temperatures, have low sorption capacity when compared to other

sorbents but as this material can withstand steam and high temperatures it was selected for this work.

When the sorbent is saturated with CO_2, the sorbent has to be regenerated. The most common regeneration techniques are pressure and temperature swing.

Temperature swing regeneration is carried out by increasing the temperature of the solid, decreasing its loading and releasing CO_2. The main drawback of this technology is the time needed to heat and cool the sorbent. Temperature swing is used when CaO is selected as sorbent [33, 44].

In pressure swing, desorption is achieved by decreasing the partial pressure of CO_2. An energy penalty exists if the goal is to store the CO_2, since energy has to be used to compress the carbon dioxide from the low pressure of the effluent stream to the pressure of storage. The regeneration of the hydrotalcite sorbent selected can be achieved by either pressure [45] or temperature swing [46]. This work will focus on pressure swing.

1.2. Objective and outline of the thesis

The objective of the present work is the production of high purity hydrogen using a sorption-enhanced reaction process (SERP) applied to the steam methane reforming reaction. The use of a high temperature carbon dioxide sorbent and a steam reforming catalyst in the reactor was studied to produce high purity hydrogen at temperatures bellow 550 °C. Fundamental preparation and characterization of alkali-modified hydrotalcites was performed as well as SMR tests in two different Ni-Al_2O_3 catalysts. Finally, SERP experiments were conducted to

validate a mathematical model used for simulation of a process for continuous production of H_2.

This thesis is outlined as follows.

In chapter 2 the sorption of CO_2 in a suitable sorbent is addressed. Commercial hydrotalcite samples were used as the base material and several alkali-modified sorbents were prepared in the scale of 100 g /batch. The nine sorbents (3 commercial and 6 prepared samples) were screened and 2 were selected for the measurement of their sorption properties at high temperature. A fixed bed model was developed to describe the high temperature carbon dioxide breakthrough curves.

In chapter 3 two Ni/Al_2O_3 catalysts were studied for steam methane reforming. The main difference between them is the presence of large pores in one of them. The intrinsic kinetics were measured for both catalysts in the powder form. Conventional steam methane reforming was performed to measure the effect of diffusional resistances within the catalysts.

Chapter 4 deals with SERP. Two different configurations – random mixture and alternating layers of catalyst and sorbent – were studied to illustrate the improvements achieved by the SERP when compared with regular steam methane reforming. A mathematical model of the SERP reactor was developed and was validated by experiments made to produce high purity hydrogen. With this mathematical model, a SERP process with reactive purge was designed.

The final chapter presents the conclusions of this work and some suggestions for future work.

1.3. References

1. Padró, C. E. G.; Keller, J. O. Kirk-Othmer Encyclopedia of Chemical Technology: Hydrogen Energy. Online ed, John Wiley & Sons, Inc, 2005.
2. Hydrogen Analysis Resource Center, http://hydrogen.pnl.gov/cocoon/morf/hydrogen/article/706 (Accessed June 2009).
3. Baade, W. F.; Parekh, U. N.; Raman, V. S. Kirk-Othmer Encyclopedia of Chemical Technology: Hydrogen. Online ed, John Wiley & Sons, Inc, 2001.
4. Twigg, M. V. Catalyst Handbook. Second Edition ed, Wolfe Publishing Ltd, England, 1989.
5. Vehicle Technologies Program, http://www1.eere.energy.gov/vehiclesandfuels/facts/favorites/fcvt_fotw205.html (Accessed June 2009).
6. Kyoto Protocol, United Nations Framework Convention On Climate Change, 1999.
7. Ammonia, http://en.wikipedia.org/wiki/Ammonia (Accessed June 2009).
8. Methanol, http://en.wikipedia.org/wiki/Methanol (Accessed June 2009).
9. Steam Hydrocarbon Reforming, http://www.selasfluid.com/international/web/le/us/likelesfus.nsf/docbyalias/Reformers (Accessed June 2009).
10. Agrell, J.; Birgersson, H.; Boutonnet, M. Steam reforming of methanol over a $Cu/ZnO/Al_2O_3$ catalyst: A kinetic analysis and strategies for suppression of CO formation. *J. Power Sources* (2002), 106, 249-257.

11. Liu, Z.-W.; Jun, K.-W.; Roh, H.-S.; Park, S.-E. Hydrogen production for fuel cells through methane reforming at low temperatures. *J. Power Sources* (2002), 111, 283-287.
12. Peppley, B. A.; Amphlett, J. C.; Kearns, L. M.; Mann, R. F. Methanol-steam reforming on Cu/Zno/Al_2O_3. Part 1: The reaction network. *Appl. Catal., A* (1999), 179, 21-29.
13. Shen, J.-P.; Song, C. Influence of preparation method on performance of Cu/Zn-based catalysts for low-temperature steam reforming and oxidative steam reforming of methanol for H_2 production for fuel cells. *Catal. Today* (2002), 77, 89-98.
14. Slinn, M.; Kendall, K.; Mallon, C.; Andrews, J. Steam reforming of biodiesel by-product to make renewable hydrogen. *Bioresour. Technol.* (2008), 99, 5851-5858.
15. Cavenati, S. Separação de Misturas $CH_4/CO_2/N_2$ por Processos Adsorptivos. PhD thesis, University of Porto, Porto, 2005.
16. Silva , V. M. T. M. Diethylacetal synthesis in simulated moving bed reactor. PhD thesis, University of Porto, Porto, 2003.
17. Gandi, G. K. Process development for fine chemicals (Acetaldehyde Dimethylacetal) synthesis. PhD thesis, University of Porto, Porto, 2006.
18. Duarte, C. F. M. Production of TAME and n-Propyl propionate by reactive distillation. PhD thesis, University of Porto, Porto, 2006.
19. Hufton, J. R.; Mayorga, S.; Sircar, S. Sorption-enhanced reaction process for hydrogen production. *AIChE J.* (1999), 45, 248-256.
20. Xiu, G.-h.; Li, P.; Rodrigues, A. E. Sorption-enhanced reaction process with reactive regeneration. *Chem. Eng. Sci.* (2002), 57.
21. Xiu, G.-h.; Li, P.; Rodrigues, A. E. Adsorption-enhanced steam-methane reforming with intraparticle-diffusion limitations. *Chem. Eng. J.* (2003).

22. Xiu, G.-h.; Li, P.; Rodrigues, A. E. New generalized strategy for improving sorption-enhanced reaction process. *Chem. Eng. Sci.* (2003), 58, 3425-3437.
23. Xiu, G.-h.; Li, P.; Rodrigues, A. E. Subsection-controlling strategy for improving sorption-enhanced reaction process. *Chem. Eng. Res. Des.* (2004), 82, 192-202.
24. Xiu, G.-h.; Soares, J. L.; Li, P.; Rodrigues, A. E. Simulation of five-step one-bed sorption-enhanced reaction process. *AIChE J.* (2002), 48, 2817.
25. Mahecha-Botero, A.; Boyd, T.; Gulamhusein, A.; Comyn, N.; Lim, C. J.; Grace, J. R.; Shirasaki, Y.; Yasuda, I. Pure hydrogen generation in a fluidized-bed membrane reactor: Experimental findings. *Chem. Eng. Sci.* (2008), 63, 2752-2762.
26. Yong, Z.; Mata, V.; Rodrigues, A. E. Adsorption of carbon dioxide at high temperature - a review. *Sep. Purif. Technol.* (2002), 26, 195-205.
27. Kikkinides, E. S.; Yang, R. T.; Cho, S. H. Concentration and recovery of CO_2 from flue gas by pressure swing adsorption. *Ind. Eng. Chem. Res.* (1993), 32, 2714-2720.
28. Gulker, F. Method of producing hydrogen. GB275273, 1928.
29. Gulker, F. Improvements in and relating to the preparation of hydrogen and to the absorption of carbon dioxide from gas mixtures. GB301499, 1930.
30. Ida, J.-I.; Lin, Y. S. Mechanism of high-temperature CO_2 sorption on lithium zirconate. *Environ. Sci. Technol.* (2003), 37, 1999-2004.
31. Kato, M.; Yoshikawa, S.; Nakagawa, K. Carbon dioxide absorption by lithium orthosilicate in a wide range of temperature and carbon dioxide concentrations. *Journal of Materials Science Letters* (2002), 21, 485-487.
32. Ochoa-Fernandez, E.; Rusten, H. K.; Jakobsen, H. A.; Ronning, M.; Holmen, A.; Chen, D. Sorption enhanced hydrogen production by

steam methane reforming using Li_2ZrO_3 as sorbent: Sorption kinetics and reactor simulation. In International Conference on Gas-Fuel 05, Brugge, November, *Catalysis Today* (2005), 41-46.
33. Gupta, H.; Fan, L.-S. Carbonation-calcination cycle using high reactivity calcium oxide for carbon dioxide separation from flue gas. *Ind. Eng. Chem. Res.* (2002), 41, 4035-4042.
34. Ding, Y.; Alpay, E. Equilibria and kinetics of CO_2 adsorption on hydrotalcite adsorbent. *Chem. Eng. Sci.* (2000), 55, 3461-3474.
35. Ding, Y.; Alpay, E. High temperature recovery of CO_2 from flue gases using hydrotalcite adsorbent. *Trans IChemE, Part B* (2001), 79, 45-51.
36. Ebner, A. D.; Reynolds, S. P.; Ritter, J. A. Understanding the Adsorption and Desorption Behavior of CO_2 on a K-Promoted Hydrotalcite-like Compound (HTlc) through Nonequilibrium Dynamic Isotherms. *Ind. Eng. Chem. Res.* (2006), 45, 6387-6392.
37. Ebner, A. D.; Reynolds, S. P.; Ritter, J. A. Nonequilibrium kinetic model that describes the reversible adsorption and desorption behavior of CO_2 in a K-promoted hydrotalcite-like compound. *Ind. Eng. Chem. Res.* (2007), 46, 1737-1744.
38. Lee, K. B.; Verdooren, A.; Caram, H. S.; Sircar, S. Chemisorption of carbon dioxide on potassium-carbonate-promoted hydrotalcite. *J. Colloid Interface Sci.* (2007), 308, 30-39.
39. Ram Reddy, M. K.; Xu, Z. P.; Lu, G. Q.; Diniz da Costa, J. C. Layered Double Hydroxides for CO_2 Capture: Structure Evolution and Regeneration. *Ind. Eng. Chem. Res.* (2006), 45, 7504-7509.
40. Reijers, H. T. J.; Valster-Schiermeier, S. E. A.; Cobden, P. D.; van den Brink, R. W. Hydrotalcite as CO_2 Sorbent for Sorption-Enhanced Steam Reforming of Methane. *Ind. Eng. Chem. Res.* (2006), 45, 2522-2530.

41. Sircar, S.; Golden, C. M. A. PSA process for removal of bulk carbon dioxide from a wet high-temperature gas. US Patent 6,322,612 B1, 2001.
42. Yong, Z.; Mata, V.; Rodrigues, A. E. Adsorption of carbon dioxide onto hydrotalcite-like compounds (HTlcs) at high temperatures. *Ind. Eng. Chem. Res.* (2001), 40, 204-209.
43. Mayorga, S. G.; Gaffney, T. R.; Brzozowski, J. R.; Weigel, S. J. Carbon dioxide adsorbents containing magnesium oxide suitable for use at high temperatures. European Patent 1074297, 2001.
44. Hildenbrand, N.; Readman, J.; Dahl, I. M.; Blom, R. Sorbent enhanced steam reforming (SESR) of methane using dolomite as internal carbon dioxide absorbent: Limitations due to $Ca(OH)_2$ formation. *Appl. Catal., A* (2006), 303, 131-137.
45. Ding, Y.; Alpay, E. Adsorption-enhanced steam-methane reforming. *Chem. Eng. Sci.* (2000), 55, 3929-3940.
46. Lee, K. B.; Beaver, M. G.; Caram, H. S.; Sircar, S. Production of fuel-cell grade hydrogen by thermal swing sorption enhanced reaction concept. *Int. J. Hydrogen Energy* (2008), 33, 781-790.

2. CO_2 sorption at high temperature in hydrotalcites

2.1. Introduction

In a sorption-enhanced reaction process (SERP), the thermodynamic equilibrium of a reversible reaction is displaced by selectively removing one of the products from the reaction media. This chapter focuses on the selection, preparation and characterization of a proper sorbent material able to remove CO_2 for the production of H_2 in a SERP process. Based on previous experience at LSRE, the work was oriented to use hydrotalcites. This chapter shows details on the preparation of large amounts of alkali-modified hydrotalcites as well as their characterization. Measurements of sorption at high temperature and with large amounts of steam were conducted to determine equilibrium and kinetics of sorption of CO_2 within the prepared materials.

2.2. Carbon dioxide sorption

2.2.1. Why is carbon dioxide capture important?

Water vapor, carbon dioxide, methane and some other gases present in the atmosphere absorb a part of the thermal radiation reflected from the surface of Earth [1], maintaining the atmospheric temperature. These gases are known as greenhouse gases (GHG) because they act as a partial blanket for thermal radiation producing a natural greenhouse effect that maintains the average temperature on earth at 15 °C, instead of the average -18 °C without the greenhouse effect [1]. However, since the industrial revolution, the amount of GHG in the atmosphere has been increasing as can be seen in Figure 2.1. The global CO_2 concentration increased from about 280 ppm to 380 ppm in 150 years.

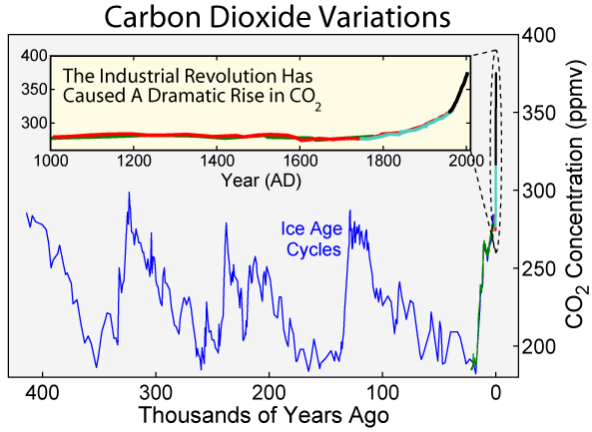

Figure 2.1. Atmospheric carbon dioxide concentration over the last 400 thousand years [2].

The higher concentration of greenhouse gases in the atmosphere due to anthropogenic emissions results in an enhanced greenhouse

effect with unknown consequences in global and regional climate. However, to avoid irreversible changes in global climate, the United Nations have agreed to establish goals to reduce the emissions of CO_2 to limit its concentration in atmosphere to less than 550 ppm. It is expected that keeping CO_2 below this concentration, the global increment of temperature is contained within 2 ºC. The starting point of these international agreements is the Kyoto protocol [3]. By signing this commitment, the industrialized countries have agreed to reduce its emissions to 8% of their emission levels in 1990. However it must be stated that the Kyoto protocol is the kick-off point in a series of measures to decarbonise the energy and fuels markets.

Power plants are the most important stationary sources of CO_2 emissions. In these plants, coal, fuel oil, natural gas or other fossil fuels are burned to produce electricity. Other sources include industrial processes such as reforming of hydrocarbons, paper and cement production, co-generation plants and industrial utilities such as boilers and heaters fuelled by hydrocarbons. In Portugal, 83.5 % of all the energy is produced using fossil fuels [4].

In all these industrial streams, CO_2 is vented to the atmosphere. Therefore, innovative processes are required to capture and purify the CO_2 produced to be sequestered or to be employed as reactant in a new CO_2-based chemistry. The main problem is that no general solution to CO_2 capture can be obtained due to the wide range of operating conditions of the processes that produce carbon dioxide.

One of the most challenging conditions for CO_2 removal is when the stream is at high temperature, possibly also in the presence of large quantities of steam, SO_x and NO_x. This is the case of CO_2 capture from flue gases where temperatures range between 473 and 773 K. The CO_2

removal at high temperatures also appears in the context of hydrocarbon reforming to produce hydrogen in sorption enhanced reaction process. This application will be specifically considered within the scope of this thesis.

2.2.2. Current technologies for carbon dioxide capture

Carbon dioxide and other "acid gases" are commonly present in natural gas streams. The most common way for natural gas sweetening is the removal of carbon dioxide using amine scrubbing [5, 6], where the reversible reaction of an amine with CO_2 is employed. The stream containing carbon dioxide should be at a temperature between 313-333 K to enter into the absorber where it contacts with the liquid stream containing the amine. When the amine is saturated with CO_2, it goes through a blower to a thermal regeneration in a stripper – normally at temperatures around 373-413 K and low pressure – where the carbon dioxide is released. The most commercialized amine is monoethanolamine (MEA), although other amines with lower reactivity but higher resistance to contaminants can be employed. The cost of this process is estimated to be between 40-70 $/ton CO_2 [6].

The extension of amine scrubbing to capture of CO_2 from flue gases arises some operating problems: stream available at high temperature, low partial pressure of CO_2 and contaminants leading to high make-up requirements. The stream to be treated by amines has to be cooled to, at least, 333 K. Also, when the CO_2 concentration is low, the energetic penalty of the process is high. Other gases present in the stream, such as SO_x, NO_x, O_2, etc. create irreversible interactions with the amines requiring a make-up stream, again increasing the costs of

operation [5]. Research in this technology is currently focused in developing new amines to prevent the problems mentioned previously [5-7].

Apart from amines, several substances act as physical solvents when they come in contact with CO_2. Rectisol is a physical sorbent (methanol plus additives) commercialized by Linde Engineering (Germany) [8]. Other solvents like Purisol, Selexol are also commercialized [5-7]. Alstom Power (Germany) [9] is demonstrating a carbon dioxide capture technology using chilled ammonium carbonate solution to absorb the CO_2, in the form of ammonium bicarbonate. The CO_2 is desorbed by heating the resulting bicarbonate to 393 K.

Membranes are an interesting technology for separation of carbon dioxide. High temperature membranes for hybrid reaction-separation processes are in the development stage for the production of hydrogen, in a project funded by Tokyo Gas (Japan) [10]. Other works are focused in flue gas treatment by composed systems like membrane-solvents [11] and membranes with potassium carbonate and glycerol [12].

Pressure swing adsorption (PSA) is another, more recent, technology that is already in use for the separation of CO_2 from industrial streams. The CO_2 containing stream is passed through a bed of adsorbent at high pressure and the CO_2 is more adsorbed than the other components in the mixture. Continuous operation requires a multicolumn system that switches the production to a clean column as soon as the one in use is saturated with CO_2. The carbon dioxide is recovered at low pressure during the regeneration of the sorbent. Pressure swing is currently used for low temperature separations as the adsorption capacity decreases with increasing temperature [13-15].

This technology can use a variety of adsorbents such as activated carbons, zeolites or other materials [13-15]. Commercial units for removal of carbon dioxide from industrial streams exist for natural gas [16] and for steel industry [17].

Extension of the PSA technology to CO_2 capture in energy production presents some challenges: in physical sorbents, when temperature increases the capacity of sorption decreases, increasing the size of the plant and its energetic penalties. The presence of SO_x in feed stream is also detrimental as it poisons the adsorbents. Finally, the presence of water is critical for some sorbents such as zeolites, as water is more adsorbed than CO_2 or can even destroy the structure of the sorbent. The solution to problems such as processes for carbon dioxide capture [18], competitive adsorption of CO_2/H_2O mixtures [19] and the presence of impurities [20] are part of the current focus of the Cooperative Research Centre for Greenhouse Gas Technologies (CO2CRC) in Australia .

In energy and fuel production applications, the use of high temperature sorbents is an interesting option since it is not necessary to spend energy to cool down the gas stream. In SERP applied for H_2 production by hydrocarbon reforming, a high temperature sorbent is essential since CO_2 should be removed from the reaction media (at high temperature and in presence of large amounts of steam). According to some studies of SERP units for H_2 production, high temperature sorbents should present suitable CO_2 sorption capacity (> 0.3 mol/kg [21]) and fast diffusion kinetics as well as good resistance to steam. The following section illustrates the ongoing research in the area of high temperature carbon dioxide sorbents.

2.2.3. High temperature carbon dioxide sorption

The first reference to the use of a high temperature sorbent dates back to 1868 [22]. In the 20th century various patents were issued for the integration of a high temperature sorbent with a steam reforming catalyst [23-26], particularly dolomite but the research was not continued due to the low cost of energy at the time [22].

In recent years, the concerns about GHG emissions combined with the increase in oil prices renewed the interest of researchers in high temperature sorbents for CO_2. The works published in this field covers different materials such as: calcium oxide [22, 27-37]; lithium oxides (zirconate and orthosilicate) [38-48]; hydrotalcites [21, 49-79]; carbon-based adsorbents [80]; basic aluminas [81]; double salts [82] and sodium oxides [83-85]. A "rule of thumb" comparison of the general properties of four of these adsorbents can be seen in Table 2.1 [69].

Table 2.1. Characteristics of CO_2 sorbent materials [69]

Sorbent	Capacity	Stability	Kinetics
Calcium oxide	Good	Poor	Good
Hydrotalcites	Poor	Good	Poor
Double salts	Fair	Unknown	Fair
Lithium oxides	Fair	Fair	Good

The high temperature carbon dioxide sorbents listed in Table 2.1 can be divided in two groups according to the regeneration protocol required to operate a cyclic process:

1. Thermal swing regeneration – Calcium, lithium and sodium oxides;
2. Pressure swing regeneration – Hydrotalcites, double salts, basic aluminas and carbon-based adsorbents.

Recently, a few works were published considering the regeneration of hydrotalcites by thermal swing [75, 77]. A detailed description of each of these materials and new trends in research are discussed below.

2.2.3.1. Calcium-based sorbents

Calcium-based materials are available in several combinations on Earth. The most important ones are: limestone – a naturally occurring mineral consisting mainly of $CaCO_3$ – and dolomite – a combination of calcium and magnesium carbonates, $CaMg(CO_3)_2$. The materials obtained from dolomites decompose into separate oxides and it was verified that only CaO is involved in CO_2 sorption while MgO stabilizes the pore network and acts as a carrier for the calcium phase [36].

Due to its abundance in nature, calcium oxide is the cheapest of the sorbents presented in Table 2.1 [7]. Calcium oxide sorbs CO_2 at high temperature by the carbonation reaction [33]:

$$CaO(s) + CO_2(g) \leftrightarrow CaCO_3(s) \qquad \Delta H_{298K} = -182.1 kJ/mol \qquad (1.1)$$

Acceptable carbonation (sorption) rates in the range of 0.08-0.4 mmol/s can be achieved at temperatures higher than 773 K, while the decarbonation reaction (desorption) temperature should be above 1173 K [22, 31, 33-35]. Carbonation of CaO is characterized by a rapid initial reaction rate followed by an abrupt transition to a quite slow rate. This change in reaction rate was attributed to the formation of a layer of carbonate around the sorbent that increases the mass transfer resistance to the diffusion of CO_2 to the center of the CaO particle. Cyclic studies suggested that the thickness of $CaCO_3$ layer formed in

the carbonation cycle has 22 nm [27]. The $CaCO_3$ layer also influences the activation energy which is initially low but increases with conversion.

Ca-based sorbents are also significantly deactivated by the high-temperature calcination treatment. This cyclical disadvantage was attributed mainly to pore blockage [32] and sintering [30] and was accompanied by textural and surface area changes [29]. A decrease of CO_2 capacity to lower than 20% of the initial value was reported for large carbonation times using pure CO_2 due to the formation of a bottleneck in the limestone pore network [32]. A direct consequence of these deactivation problems is that both capacity and kinetics of CO_2 are smaller and slower as the number of calcination/carbonation cycles increases, which is not desirable for cyclic operation. When dolomite was used, the rate of sintering was less pronounced due to the excess pore volume created by decomposition of $MgCO_3$ [30]. The true density of calcium oxide is 3.3 g/cm^3 while for CaO synthesized from natural dolomite this value was around 1.4 g/cm^3 (porosities up to 55%). The work from Barker [27] showed that if 10 nm CaO particles were used, the conversion was maintained at 93 % over 30 cycles at 902 K.

A strategy followed to achieve large conversions, keeping sorbent durability, was its synthesis in laboratory. In one study, CaO was prepared from a mesoporous (5-20 nm) high-surface area calcium carbonate precipitated from $Ca(OH)_2$ using CO_2. This sorbent did not show sintering and kept its high sorption capacity (16.1 mol/kg) in the first three carbonation-calcination cycles [28]. The influence of different precursors in the BET area and pore volume was also investigated. Calcium acetate and calcium propionate were the precursors that gave the best results for the sorption of CO_2, with capacities of 16.1 and 17 mol/kg, respectively, in the carbonation reaction – 10.7 and 14.6

mol/kg in the first 15 min [37]. The high sorption and kinetics were credited to the higher macroporosity of the materials that was not blocked by the calcium carbonate.

Finally, the carbon dioxide sorption capacity of CaO can also be increased by doping with alkali-metals. As CO_2 is a weak acid, increasing the basicity of the surface increases the sorption capacity. The CO_2 sorption capacity using alkali-metal dopants increases with atomic number and electropositivity of the metals: Cs > Rb > K > Na > Li [31]. A sample prepared with 20 % Cs/CaO showed a capacity of 11.4 mol/kg at 873 K when tested in a flow of pure CO_2. Almost the same capacity was obtained when a flow of 40 % CO_2, 50 % air and 10 % water were used [31].

2.2.3.2. Lithium salts

Lithium zirconate sorbs CO_2 at temperatures above 723 K [38]. The desorption can be performed at temperatures above 923 K. Lithium zirconate sorbs CO_2 by the following carbonation reaction:

$$Li_2ZrO_3(s) + CO_2(g) \leftrightarrow Li_2CO_3(s) + ZrO_2 \qquad \Delta H_{298K} = -160 kJ/mol \qquad (1.2)$$

A sorption capacity of 4.54 mol/kg was initially reported [40], but the sorption kinetics were slow. Doping lithium zirconate with potassium and lithium carbonate improved the sorption kinetics by 40 times when compared to the pure sample, as the CO_2 diffuses faster to reach the lithium zirconate [40]. Sodium carbonates and oxides were also reported to show promoting effects on Li_2ZrO_3 and Li_4SiO_4 if added in a maximum amount of 30 % mol [41]. More recent works reported lithium zirconates with improved capacities for CO_2 sorption – 5.0 mol/kg at 673 K [45]. The sorption kinetics were very good, with saturation in less

than 10 min. The improvement in the characteristics of the material was credited to a new preparation method that was able to produce high purity lithium zirconate crystals [47]. Regeneration of the new material was achieved at 923 K.

Lithium orthosilicate also shows promising results in the sorption of CO_2. The sorption is also achieved by a carbonation reaction:

$$Li_4SiO_4(s) + CO_2(g) \leftrightarrow Li_2SiO_3(s) + Li_2CO_3(g) \quad (1.3)$$

Lithium orthosilicate is cheaper than lithium zirconate and has an sorption rate 30 times faster than pure lithium zirconate at 773 K and CO_2 concentrations of 20 % – sorption capacity of 6.13 mol/kg [44]. The carbon dioxide can be desorbed at temperatures above 973 K, which is much lower than the 1173 K required using CaO. Another feature of lithium orthosilicates is the capacity to remove CO_2 even from diluted streams (with 2 % of CO_2). It was reported that Li_4SiO_4 can adsorb up 5.91 mol/kg of CO_2 in 50 min, from the diluted stream. Bretado and coworkers [42] proposed the impregnated suspension method to prepare lithium orthosilicate, claiming that with this method higher purity of the material is achieved. The new material achieved showed a CO_2 sorption capacity of 8.2 mol/kg – which they compared with the value of 6.9 mo/kg reported by Kato *et al* [44].

When Li_4SiO_4 crystals were inserted into a pellet, mass transfer limitations and sintering were observed. Essaki *et al* [46] reported a decrease of 25 % in the capacity at 873 K between the powder and pellet samples. Kato *et al* [44] reported a 27 % decrease in the capacity of the pellets during cyclic tests. The decrease in the capacity could be reduced by doping the orthosilicate with 5 % lithium zirconate.

Other lithium-metal combinations such as lithium ferrite ($LiFeO_2$), lithium nickel ($LiNiO_2$), lithium titanate (Li_2TiO_3) and lithium methasilicate (Li_2SiO_3) were already tested at various temperatures [41]. Despite of the large number of lithium salts investigated, Li_4SiO_4 was found to have the highest capacity and reactivity to CO_2.

The interest in lithium salts as CO_2 high temperature sorbents can be seen by the two international patents registered by Toshiba corporation [38, 39] and the patent by the group of NTNU in Norway [48].

2.2.3.3. Hydrotalcites

Hydrotalcites are naturally occurring, bi-dimensional layered double hydroxides from the family of anionic clays having the general formula:

$$M^{2+}_{1-x}M^{3+}_{x}(OH)_2\left(A^{n-}\right)_{x/n}\cdot mH_2O \qquad (1.4)$$

where M^{2+} and M^{3+} are divalent (Mg, Mn, Fe, Co, Ni, Cu, Zn, Ga) and trivalent (Al, Cr, Mn, Fe, Co, Ni, and La) metal ions and A is an anion ($CO_3^{2-}, OH^-, NO_3^-, SO_4^{2-}, ClO_4^-$). The divalent and trivalent ions form a crystalline structure that is positively charged due to the presence of the trivalent ion: $0.2 \leq x \leq 0.33$. The excess of positive charge will be balanced by the anions present in the interstitial position between the two positive layers [86, 87]. In the case of the hydrotalcites used for carbon dioxide sorption at high temperature, M^{2+} is magnesium (Mg) and M^{3+} is aluminum (Al). The CO_2 can be sorbed in the form of the carbonate ion (CO_3^{2-}) in the interstitial layer. A representation of the structure of a hydrotalcite can be seen in Figure 2.2 [68].

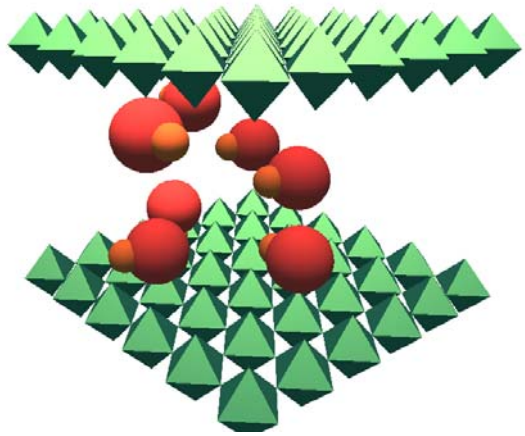

Figure 2.2. Structure diagram of a hydrotalcite sorbent. Top and bottom are the metal layers. Between the metal layers is the interlayer space where water and/or CO_2 are sorbed [68].

Hydrotalcites are relatively new materials that have been studied for CO_2 sorption at high temperatures [51, 56, 58, 63, 65-68, 72, 74, 79], for CO_2 capture from flue gas [55, 70, 71] and for SERP [49, 50, 52, 53, 57, 59-62, 64, 69, 73, 75-78]. Their main advantage is the high stability and resistance to steam in cyclic operation [51, 57].

The first reported use of hydrotalcites to sorb carbon dioxide at high temperature came from the research developed at Air Products and Chemicals (USA), funded by the American Department of Energy (DOE) [49]. The purpose of the work was to develop a SERP process for steam methane reforming. The hydrotalcite was modified using potassium carbonate and the carbon dioxide equilibrium capacity was determined at three different temperatures – 573, 673, 773 K. It was found that the capacity decreased with increasing temperature from around 1 mol/kg at 573 K to 0.6 mol/kg at 773 K (at P_{CO2} = 1.52 bar and P_{H2O} = 10.1 bar). A working capacity of 0.45 mol/kg was determined after 15 sorption/desorption cycles in the presence of steam (T = 673 K,

P_{CO2} = 0.3 bar, P_{H2O} = 10.1 bar). This work resulted in several patents and papers in international journals [50, 53, 56, 57, 82] describing the preparation of promoted hydrotalcites and PSA processes for production of hydrogen by sorption-enhanced reaction.

Ding and Alpay developed a similar work in the United Kingdom [51]. A CO_2 sorption capacity of 0.62 mol/kg at 44 kPa and 673 K in the presence of steam was reported using K-promoted hydrotalcites. The sorption capacity of the samples was restored after treatment with steam, which indicated that hydrotalcites are suitable for cyclic operation in PSA. The Langmuir model was used to describe the sorption equilibrium data at 673 and 753 K and the linear driving force model (LDF) was used to describe the sorption kinetics. However, the desorption kinetics could not be described by the simple LDF model. The LDF model was modified calculating the effective diffusivity from the mass balance to the extrudate, assuming that pore diffusion is dominant. The modified LDF gave a good fit of the experimental results.

The sorption capacity of several hydrotalcite samples in powder form was investigated at LSRE at temperatures up to 573 K and CO_2 partial pressures up to 1 bar [58]. Two different types of hydrotalcites were tested, one with CO_3^{2-} and other with OH^- as the anions in the hydrotalcite layer. At 573 K and 1 bar, a CO_2 sorption capacity of 0.52 mol/kg was reported for the EXM696 sample (CO_3^{2-} anion). It was reported that the CO_3^{2-} anion is larger and has a higher charge than OH^- thus providing more void spaces to accommodate CO_2.

In 2005, the group from the University of South Carolina (USA) used the carbon dioxide sorption equilibrium and kinetics published by Ding and Alpay [51] to model the carbon dioxide removal from flue gas at high temperature by PSA [65]. They selected a 4-step Skarstrom cycle –

high pressure feed, countercurrent blowdown to vaccum pressure, countercurrent low pressure purge and pressurization – and simulated different purge-to-feed ratios, cycle times (equal step times) and pressure ratios (between high and low pressure). A feed of 1.0 L STP/min at 575 K containing 15 % CO_2, 75 % N_2 and 10 % H_2O was used. A 100 % CO_2 recovery at a purity of 39 % were obtained at a purge-to-feed ratio of 1.5 and a pressure ratio of 12. However, the highest CO_2 purity (58.5%) was obtained at a recovery of 87 % by changing the purge-to-feed ratio to 0.5. The same feed temperature and composition was used in a following paper but different cycle types were tested [70]. A CO_2 recovery of 17.4 % and a purity of 82.7 % were obtained using a 4-bed, 4-step cycle with high pressure rinse and countercurrent depressurization. The last report by Reynolds and coworkers focused on the influence of the mass transfer coefficients in the process parameters [71]. Increasing the mass transfer parameters 5 fold yielded a recovery of 72 % and a purity of 89.2 %. If the sorption mass transfer coefficient was used both for sorption and desorption, a purity of 88.9 % and a recovery of 72.3 % are obtained.

The simulation results obtained by the group from the University of South Carolina indicated that it is important to understand the mass transfer kinetics as well as the mechanism of sorption of the hydrotalcite sorbents. The simulation work was based on the data determined by Ding and Alpay [51]. Therefore, experiments were necessary to generate new data. As a result, Ebner and coworkers [66] conducted a series of non-equilibrium experiments in potassium promoted hydrotalcites and proposed a new mechanism combining three coupled, temperature-dependent, reactions with different kinetics and CO_2 sorption capacities. In a more recent work, Ebner *et al* [72]

proposed a model to describe the sorption mechanism [66] based on the reaction of sorbed CO_2 with gaseous CO_2.

A group at ECN (Energy research Centre of the Netherlands) published their work in sorption-enhanced steam methane reforming [69] in 2006. They reported results for CO_2 sorption capacity using several pure commercial hydrotalcites. It was found that the hydrotalcite with 30 % Mg impregnated with 22 % K_2CO_3 had a sorption capacity of 0.44 mol/kg at 573 K (using a feed of 5 % CO_2 and 29 % H_2O). Impregnation of the hydrotalcite using K_2CO_3 increased 3 times the CO_2 sorption capacity of the hydrotalcite samples when compared to the pure samples. No model was proposed to describe the carbon dioxide sorption in the hydrotalcites.

Lee and coworkers [74] performed a series of breakthrough experiments at 673 and 793 K using a CO_2 + N_2 stream. They used K-promoted hydrotalcites supplied by Air Products and Chemicals (USA). At 673 K and 3 bar CO_2 partial pressure, the equilibrium sorption capacity was 0.87 mol/kg while at 793 K was 0.6 mol/kg. The sorption at low carbon dioxide partial pressures (< 0.2 bar) was fitted by a Langmuir isotherm but the extension to higher pressures was poor. Therefore, Lee *et al* [74] proposed that at low CO_2 partial pressures the sorption was Langmuir type. As the partial pressure increased, a complexation reaction took place between the sorbed and gaseous CO_2 that increased the sorption capacity. This model gave a good fit at 673 K but presented an overshoot of the experimental data at 793 K. The LDF model was used to describe the sorption kinetics and the LDF parameters were only temperature dependent.

The carbon dioxide sorption on hydrotalcites was intensively studied in several groups in Europe and in the United states since 1996.

Different models were proposed to describe the sorption mechanism in the material, from physical sorption to chemical reaction. The LDF model was always employed to describe the mass transfer kinetics but different parameters were reported by different groups. The different sorption mechanisms proposed by the various groups – as well as the parameters involved – are reported in Table 2.2 and Table 2.3.

Table 2.2. Experimental conditions and LDF parameters for CO_2 sorption on potassium modified hydrotalcites

T [K]	P [bar]	y_{CO2} [%]	y_{H2O} [%]	$k_{LDF,\ sorption}$ [s^{-1}]	Ref.
673	4.48	2.61	0	0.008	[51]
	4.48	2.60	24	0.01	
	17.26	1.62	0	0.006	
	18.70	1.51	21	0.006	
	1.14	19.93	0	0.02	
	1.14	19.93	0	2.0[a]	
793	~1.103	40, 50, 60	0	0.050	[74]
	~1.103	40, 50, 60	0	0.083	

a – LDF model with pore diffusion. Sorption and desorption

Table 2.3. Mechanisms and parameters proposed for carbon dioxide sorption on potassium promoted hydrotalcites

<table>
<tr><td>Reference</td><td>[51]</td><td>[74]</td><td colspan="2">[72]</td></tr>
<tr><td rowspan="3">Mechanism</td><td rowspan="3">Langmuir</td><td rowspan="3">Langmuir and complexation</td><td>$CO_2(g) \rightarrow A$ (fast)</td><td>LDF model</td></tr>
<tr><td>$A + E \rightarrow B$ (i) (intermediate)</td><td rowspan="2">Langmuir-Hinshelwood</td></tr>
<tr><td>$A + B \rightarrow C$ (ii) (slow)</td></tr>
<tr><td>Equation</td><td>$q_{CO2} = m\frac{K(T)P_{CO2}}{1+K(T)P_{CO2}}$</td><td>$q_{CO2} = m\frac{K_C P\left[1+(1+a)K_R P^a\right]}{1+K_C P+K_C K_R P^{a+1}}$</td><td colspan="2">–</td></tr>
<tr><td rowspan="2">Parameters</td><td>T = 673 K (humid)
K = 23.6 bar^{-1}
m = 0.65 mol/kg</td><td>T = 673 K (dry)
K_C = 36.9 bar^{-1}
K_R = 2.47 bar^{-1}
m = 0.25 mol/kg
a = 2.5</td><td colspan="2" rowspan="2">$k_{LDF,\ sorption}$ = 2.030 x 10^{-2} s^{-1}
$k_{LDF,\ desorption}$ = 2.328 x 10^{-3} s^{-1}
$k_{i,\ forward}$ = 3.653 x 10^{-4} s^{-1}
$k_{i,\ reverse}$ = 9.655 x 10^{-4} kg/(mol.s)
$k_{ii,\ forward}$ = 2.667 x 10^{-6} s^{-1}
$k_{ii,\ reverse}$ = 2.037 x 10^{-5} kg/(mol.s)</td></tr>
<tr><td>T = 753 K (humid)
K = 19.3 bar^{-1}
m = 0.58 mol/kg</td><td>T = 793 K (dry)
K_C = 20.9 bar^{-1}
K_R = 0.79 bar^{-1}
m = 0.25 mol/kg
a = 2.5</td></tr>
</table>

2.2.3.4. Double salts, carbon-based materials, basic aluminas and sodium oxides

Double salts are solid adsorbents containing magnesium oxide and alkali metal salts. Double salts were tested in the temperature range 573-773 K. At 673 K and P_{CO2} of 0.7 bar these sorbents showed a CO_2 sorption capacity above 1 mol/kg [82].

Carbon based sorbents were modified by addition of calcium oxide, magnesium oxide or both and tested for carbon dioxide sorption at high temperatures. A sorption capacity for CO_2 of 0.28 mol/kg was reported at 573 K and 1 bar of CO_2 using the MgO modified sample [80].

Basic aluminas were tested for sorption of CO_2 at temperatures up to 573 K. The best alumina sample showed a CO_2 sorption capacity for of 0.62 mol/kg at a CO_2 partial pressure of 1 bar [81].

The excellent results achieved with lithium oxides led Lopez-Ortiz and coworkers [83] to investigate sodium oxides as they are potentially cheaper than lithium sorbents. They tested Na_2TiO_3, Na_3SbO_4 and Na_2ZrO_3 and compared these sorbents with lithium zirconate and orthosilicate. The sodium zirconate showed the best capacity and kinetics of the sodium sorbents. When compared to the lithium sorbents, the sodium zirconate showed the highest sorption kinetics but the lithium orthosilicate presented higher capacity (6.82 mol/kg for the lithium orthosilicate and 5.85 mol/kg for the sodium zirconate).

Sodium oxide promoted alumina has also been investigated for carbon dioxide sorption [84, 85]. Carbon dioxide sorption isotherms were determined at 523, 623 and 723 K and different CO_2 partial pressures. A

model combining Langmuir type sorption at low CO_2 partial pressures (< 0.02 bar) and a combination of Langmuir sorption and a complexation reaction at high partial pressures was proposed [74] (the same model was used for the hydrotalcites). The heat of sorption was 64.9 kJ/mol while the heat of the complexation reaction was 37.5 kJ/mol. The LDF mass transfer coefficients The LDF mass transfer coefficients were independent of the CO_2 concentration but were temperature dependent – 4 min^{-1} at 523 K and 5 min^{-1} at 623 K.

2.2.4. Finding the most suitable adsorbent

The four groups of adsorbents mentioned in the previous sections show good capacities for the sorption of CO_2 at high temperatures. In the beginning of this work (2004) it was necessary to select a sorbent to be used in SERP. The selection of the sorbent was based on several parameters such as [21, 50]:

1. High selectivity and capacity for CO_2;
2. Good sorption kinetics;
3. Stable capacity for cyclic operation;
4. Good mechanical strength for operation at high pressure in the presence of steam.

A summary of the data collected on several high-temperature sorbents is reported in Table 2.4.

Table 2.4. Sorption capacity of CO_2 for different sorbents at high temperature.

Material	T [K]	y_{CO2}	P [bar]	q [mol/kg]	Ref.
Limestone	923	0.05	1.01	2.3	[33]
Limestone (La Blanca)	923	1	1.01	2.14[a]	[32]
	923	0.1	1.01	3.57	[29]
Dolomite	1023	0.15	1.01	9.1	[36]
CaO	573	0.2	1.01	2.68	[30]
	773	0.2	1.01	8.4	
CaO (PCC)	923	1	1.01	16.1	[28]
CaO (LH)	923	1	1.01	14.5	
CaO from $CaAc_2$	873	0.30	1.01	17.3	[35]
	973	0.30	1.01	17.3	
CaO from $Ca(C_2H_5COO)_2$	973	0.30	1.01	17.05	[37]
Cs-CaO (20 % Cs)	873	0.40	1.01	11.4	[31]
Hydrotalcite	673	0.153	1.01 (dry)	1.18	[67]
	773	0.161	1.01 (dry)	0.97	
	800	0.155	1.01 (dry)	0.80	
	673	0.153	1.01 (humid)	1.07	
	773	0.161	1.01 (humid)	0.87	
	800	0.155	1.01 (humid)	0.66	
	573	~1.0 bar CO_2 (dry)		0.25	[68]
Hydrotalcite	673	~1.0 bar CO_2 (dry)		0.17	[68]
EXM696 Hydrotalcite	573	1.0 bar CO_2 (humid)		0.52	[58]
K-Promoted Hydrotalcite	673	0.45 bar CO_2 (dry)		0.58	[51]
	753	0.57 bar CO_2 (dry)		0.47	
	673	0.45 bar CO_2 (dry)		0.62	
	753	0.55 bar CO_2 (dry)		0.58	
	575	1 bar CO_2 (humid)		0.80	[55]
	673	0.505 bar CO_2 (dry)		0.35	[74]
	673	3.03 bar CO_2 (dry)		0.88	
	793	0.505 bar CO_2 (dry)		0.30	
	793	3.03 bar CO_2 (dry)		0.59	
	723	1.31 bar CO_2 (dry)		0.55	[66]
	723	0.9 bar CO_2 (dry)		0.53	[49]
	723	0.71 bar CO_2		0.45[b]	

a — Capacity determined after 100 cycles

b — Cyclic steady state capacity after 6000 cycles of sorption/desorption

Table 4. (cont) Sorption capacity of CO_2 for different sorbents at high temperature.

Material	T [K]	y_{CO2}	P [bar]	q [mol/kg]	Ref.
Sorbplus K-Hydrotalcite	673	0.7 bar CO_2 (humid)		0.78	[49]
LR K-Hydrotalcite	673	0.7 bar CO_2 (humid)		0.67	
K-Promoted Hydrotalcite (MG70; 22 % K_2CO_3)	673	0.05	1.0	0.33	[69]
	723	0.05	1.0	0.32	
	773	0.05	1.0	0.27	
K-Promoted Hydrotalcite (MG30; 22 % K_2CO_3)	673	0.05	1.0	0.44	
K- Hydrotalcite (pellet)	673	0.7 bar CO_2 (humid)		0.39	[49]
	773	0.7 bar CO_2 (humid)		0.56	
Double Salts (sample 3c)	623	0.70 bar CO_2 (dry)		1.21	[82]
	648	0.70 bar CO_2 (dry)		2.45	
	673	0.70 bar CO_2 (dry)		2.02	
Double Salts (example 12)	673	0.70 bar CO_2 (dry)		11.6	[82]
	673	0.70 bar CO_2 (humid)		7.2	
Basic Aluminas (98AA)	573	1	0.992	0.619	[81]
Basic Aluminas (98AX)	573	1	0.998	0.385	
Carbon based adsorbents (with MgO)	573	1	1.01	0.28	[80]
Na_2O-Alumina	623	3.03 bar CO_2 (humid)		0.760	[84]
	723	3.03 bar CO_2 (humid)		0.696	
$NaZr_2O_3$	873	1	1.01	5.85	[83]
Na_3SbO_4	873	1	1.01	3.29	
Li_2ZrO_3	873	1	1.01	5.00	[45]
	848	1	1.01	6.14	[47]
	773	1	1.01	4.54	[40]
	873	1	1.01	2.97	[83]
	773	0.2	1.01	3.64	[44]
K-Li_2ZrO_3	673	1	1.01	3.86	[40]
Li_4SiO_4	873	1	1.01	6.82	[83]
	973	0.8	1.01	8.22	[42]
	773	0.2	1.01	5.91	[44]
	973	1	1.01	7.95	
K-Li_4SiO_4 (extrudates)	873	0.2	1.01	5.00	[46]
	873	0.05	1.01	0.45	[43]
	873	0.10	1.01	5.23	
	873	0.15	1.01	6.36	

Calcium oxide based sorbents show very good sorption capacities but the reported high sorption/desorption temperatures (> 873 K) as well as the reduced cyclic stability make these sorbents less suitable for SERP, despite that it is a cheap and naturally available material. Lithium oxides show promising sorption capacities and kinetics – especially orthosilicates – but, as in the case of CaO, require high temperatures for desorption. As for double salts, carbon-based materials, basic aluminas and sodium oxides there is still very little data published – properties and simulations – to determine if they are interesting for sorption of CO_2.

Hydrotalcites fulfill the required criteria of minimum sorption capacity (> 0.3 mol/kg), selectivity towards CO_2 and cyclic stability in the presence of steam and are commercially available materials. Also, despite having slow sorption kinetics when compared to calcium or lithium oxides, hydrotalcites can be regenerated at temperatures lower than 823 K by pressure swing. Based on this assessment, hydrotalcites were selected for this work.

The present chapter details the preparation of six hydrotalcite samples by impregnation of K_2CO_3 or Cs_2CO_3 in three different pure hydrotalcite samples. A total of nine samples (pure and modified) were screened by measuring their carbon dioxide equilibrium sorption capacity in the presence of steam at 673 K. Two samples were selected for measurement of sorption equilibrium isotherms at 579, 676 and 783 K. The stability of the hydrotalcite material was investigated by performing 77 sorption/desorption cycles at 676 K (0.40 bar of CO_2 in the presence of steam). A mathematical model was developed to simulate the sorption column. The model and the experimental data were used to fit the CO_2 sorption kinetics.

2.3. Experimental

2.3.1. Sorbent preparation

Three commercial hydrotalcite extrudates (MG30, MG50, MG70) from Sasol (Germany) were impregnated with K_2CO_3 and Cs_2CO_3 from Sigma-Aldrich (ACS reagents). The impregnation protocol [54] started by calcination of 100 g of the pure hydrotalcite in the presence of air at 673 K for 4h. Following the calcination, the samples were put in contact with 112.5 ml of a solution containing 35.35 g of potassium carbonate or 24.52 g of cesium carbonate, to achieve a K or Cs loading of 20 %. After 1 h of contact, the remaining liquid (< 2 ml) was decanted and the samples were dried at 393 K for 16 h. Finally, the samples were calcinated in air at 673 K during 4 h. To establish the same thermal treatment for all the samples, the pure hydrotalcites (without modification) were also calcinated in air at 673 K for 4 hours prior to testing.

2.3.2. Characterization of the hydrotalcite samples

Scanning Electron Microscopy (SEM) was performed on a JEOL JSM-6301F (JEOL, Japan) coupled with an Energy dispersive X-ray spectroscope (EDX) Oxford INCA Energy 350 (Oxford Instruments, UK) was used to determine the composition of the sorbent. The surface area of the fresh sorbents was determined by N_2 adsorption at 77 K with a Coulter Omnisorp 100 CX apparatus. The specific surface areas were calculated by applying the BET method.

2.3.3. Equipment built to measure CO_2 sorption capacity at high temperature in the presence of steam

The carbon dioxide sorption equilibrium points were measured by breakthrough experiments. The equipment shown in Figure 2.3 was build during the course of this thesis and was used to measure the carbon dioxide breakthrough curves at high temperature in the presence of steam.

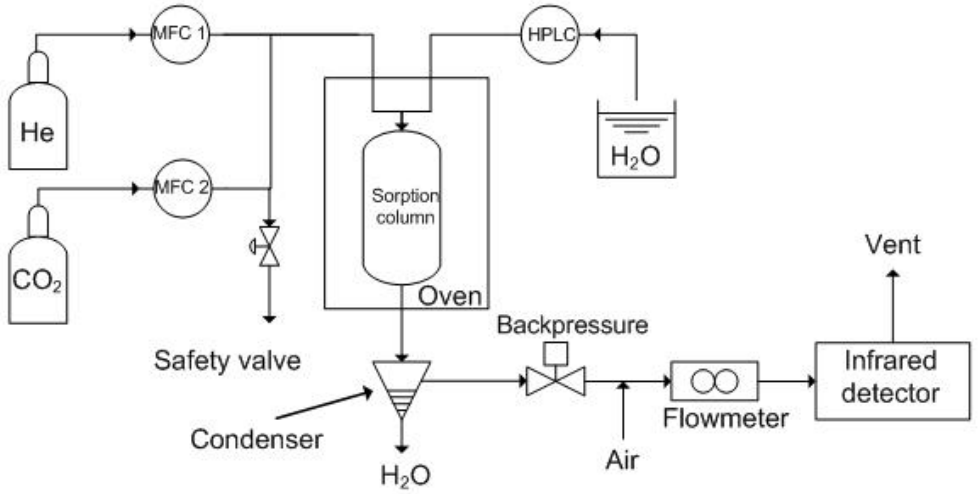

Figure 2.3. Experimental set-up employed to measure sorption equilibrium of CO_2.

The liquid water flowrate is controlled using a HPLC pump (Merck-Hitachi, Japan). The water is pumped into the oven and then vaporized in a tube coil of 1/16 in. Both CO_2 and He flowrates are controlled by independent mass flow controllers. The gases are mixed with the vaporized water in a T-shape fitting before entering the sorption column. The gas mixture was fed to the top of the sorption column.

The sorption column has a diameter of 0.027 m and a total length of 0.166 m. Temperature histories were followed in two different points using thermocouples inserted at 51.5 and 92.0 mm from feed inlet.

The effluent stream leaving the sorption column passes through an ice trap to condense the water. A backpressure regulator (Parker, USA) was placed after the ice trap to maintain the pressure inside the sorption column.

The CO_2 concentration was measured each 10 seconds using an infrared detector (Madur, Austria). Prior to the CO_2 detector, a known flowrate of Air type K was added to the dry effluent stream as make-up. The total flowrate was measured using an air flow sensor from Omega (USA).

The temperature and flowrate signal signals were acquired at a rate of 1 point per second, using a program developed in the Labview software (National Instruments Corporation, USA).

In every breakthrough experiment, a known amount of extrudates (particle diameter ranging from 0.44-0.48 cm) was loaded into the sorption column and heated in helium flow to 676 K at 1 K/min, with 30 min stops every 100 K. Usually the heating was made overnight. After the set-point temperature was reached, the steam flow was initiated. When steam is added to the inlet stream, the hydrotalcites start to release CO_2. This carbon dioxide comes from the interlayer structure of the hydrotalcite [86, 87]. The steam flow was kept until no CO_2 is detected in the effluent, which can take a few hours. At t = 0 s, the carbon dioxide flow was added to the inlet stream. Sorption was continued until the effluent concentration was equal to the feed concentration. After the sorption was finished, CO_2 feed was cut and the He and H_2O streams were adjusted to start the desorption step.

To test the stability of the MG30-K sorbent (the one with higher CO_2 equilibrium sorption capacity), 75 sorption/desorption cycles were carried out. A complete CO_2 breakthrough experiment was performed followed by 1 hour regeneration of the sorbent and a cyclic sequence of 74 sorption/desorption steps. Each sorption step (stream with CO_2 + H_2O + He) took 150 seconds – with the exception of the first 2 cycles that lasted 200 s – while the desorption step (with H_2O + He) took 1200 seconds. Desorption in cycle 74 was performed until no CO_2 was detected in the outlet stream. Then the initial CO_2 breakthrough experiment was repeated.

Table 2.5. Operating conditions used in the carbon dioxide breakthrough experiments

Experiment	Screening[a]	Isotherms				Cyclic	
P_T [bar]	2	1.3[b]; 2				2	
T [K]	676	579, 676, 783				676	
y_{CO2} [%]	19.9	3.8	4.5	9.4	19.9	19.9	0
y_{H2O} [%]	26.5	27.3	27.1	27.0	26.5	26.5	26.5
y_{He} [%]	53.6	68.9	68.4	63.6	53.6	53.6	73.5
P_{CO2} [bar]	0.40	0.05	0.09	0.19	0.40	0.40	0
F_T [mmol/min]	23.0	22.40	22.54	22.65	23.05	23.05	23.02

a – for MG50: F_T = 32.7 x 10^{-3} mol/min; y_{CO2} = 18.9 %; y_{H2O} = 16.9 %; y_{He} = 64.2 %;

b – P_T = 1.3 bar for y_{CO2} = 3.8 %.

The operating conditions of the experiments are reported in Table 2.5. In Table 2.6 the mass of sorbent used in each experiment is shown along with the measured particle density and the column porosity. The reproducibility of all the equilibrium points was checked by repeating the measurements at least 2 times.

Table 2.6. Mass of sorbent, particle density and column porosity for each sorption experiment

Sample	mass [kg] x 10^3 (wet basis)	Particle Density [kg/m^3]	Column Porosity[a]
Screening			
MG30	49.6655	1139	0.54
MG30-K	91.1944	1845	0.48
MG30-Cs	64.2833	1439	0.53
MG50	68.3420	1336	0.46
MG50-K	89.5949	1688	0.44
MG50-Cs	84.6851	1572	0.43
MG70	60.4428	1186	0.46
MG70-K	88.1809	1530	0.39
MG70-Cs	81.9792	1497	0.42
Isotherms			
MG30-K	92.1944	1845	0.47
MG30-Cs	80.8914	1439	0.41
Cyclic			
MG30-K cyclic	96.2023	1845	0.45

a – The porosity was calculated by $\varepsilon_{column} = \left(V_{column} - m_{sorbent}/\rho_{sorbent}\right)/V_{column}$.

2.4. Theoretical: modeling sorption in hydrotalcites

2.4.1. Sorption equilibrium

The CO_2 sorption capacity of the hydrotalcite samples was calculated by a mass balance over the sorption column [88]. The notation used in this work is detailed at the end of the thesys. The stoichiometric time ($\overline{t_{st}}$) was employed for this purpose and was defined by:

$$\overline{t_{st}} = \int_0^t \left(1 - \frac{QC_{CO2}}{Q_{feed}C_{CO2feed}}\right)dt = \int_0^t \left(1 - \frac{F_{CO2}}{F_{CO2feed}}\right)dt = \frac{L_c}{u_i}\left(1 + \left(\frac{1-\varepsilon_c}{\varepsilon_c}\right)\rho_{sorb}\frac{q_{eq,CO2}}{C_{feed,CO2}}\right) \quad (1.5)$$

where $q_{eq,CO2}$ is the CO_2 equilibrium sorption capacity in mol/kg. Note that the stoichiometric time equation can also be expressed in terms of the feed and effluent molar flowrates ($F_{CO2,feed}$ and F_{CO2}).

The experimental CO_2 sorption isotherms on the MG30-K and MG30-Cs samples were fitted with a bi-Langmuir model [88]. This mathematical model was used to describe the observed maximum in the CO_2 sorption capacity. This maximum can be described by the combination of two types of sorption, one endothermic and one exothermic. It was thus assumed that the overall sorption of CO_2 is taking place by a combination of physical sorption and chemical reaction. The bi-Langmuir model is a simple model that allows the consideration of 2 different and independent types of sites. The bi-Langmuir model is:

$$q_{eq,CO2} = q_{max1}\frac{K_{eq1,CO2}P_{CO2,sorb}}{1+K_{eq1,CO2}P_{CO2,sorb}} + q_{max2}\frac{K_{eq2,CO2}P_{CO2,sorb}}{1+K_{eq2,CO2}P_{CO2,sorb}} \qquad (1.6)$$

where $P_{CO2,sorb}$ is the carbon dioxide partial pressure inside the sorbent extrudates in bar, q_{max} is the maximum capacity in mol/kg for sites 1 (exothermic physical adsorption) and 2 (endothermic chemical reaction) and $K_{eq,CO2}$ and $K_{eq2,CO2}$ are given by the Arrhenius equation:

$$K_{eq1,\,CO2} = k_{0eq1,\,CO2} \times e^{\frac{-\Delta H_{sorb}}{R_g T_{sorb}}}\;;\; K_{eq2,\,CO2} = k_{0eq2,\,CO2} \times e^{\frac{-E_{sorb}}{R_g T_{sorb}}} \qquad (1.7)$$

where $k_{0eq1,CO2}$ and $k_{0eq2,CO2}$ are the pre-exponential factors in bar^{-1}, ($-\Delta H_{sorb}$) is the heat of physical sorption and ($-E_{sorb}$) is the heat of reaction, both in J/mol. The model was fitted to the experimental data using the *fmins* function in Matlab 6.0 software (Mathworks, USA).

2.4.2. Sorption kinetics

The CO_2 sorption kinetics were determined by fitting the carbon dioxide breakthrough experiments. The mathematical model used to fit the experiments was developed with the following assumptions:

1. Axially dispersed plug flow;
2. Ideal gas behavior;
3. No mass or heat variations in the radial direction of the column;
4. Sorption in the hydrotalcite pellets was only considered for CO_2;
5. The carbon dioxide sorption equilibrium was described by the bi-Langmuir model [88] proposed in the previous section;
6. The porosity was considered constant throughout the column;
7. Helium (used as balance gas) and steam are not adsorbed in the hydrotalcite.

The hydrotalcite sorbent particles were modeled as spheres since the radius and the height of the particle are identical.

The mass balance for each component in the gas mixture (CO_2, H_2O and He) can be seen in equation 1.8.

$$\varepsilon_c \frac{\partial C_i}{\partial t} = \varepsilon_c \frac{\partial}{\partial z}\left(D_{ax} C_T \frac{\partial y_i}{\partial z}\right) - \frac{\partial (u C_i)}{\partial z} - (1-\varepsilon_c)\frac{a_{p,sorb} k_{f,sorb}}{Bi+1}\left(C_i - \overline{C}_{sorb,i}\right) \qquad (1.8)$$

where *Bi* is the Biot adimensional number and $\overline{C}_{sorb,i}$ is the average concentration of component "*i*" in the pore network of the sorbent.

A heterogeneous model was used to describe energy transfer. Three energy balances were made to the gas and solid phases and to the wall of the sorption column. The energy balance of the gas phase is:

$$\varepsilon_c C_T \hat{C}_{vg} \frac{\partial T}{\partial t} = \frac{\partial}{\partial z}\left(\lambda_{ax} \frac{\partial T}{\partial z}\right) - uC_T \hat{C}_{pg} \frac{\partial T}{\partial z} + \varepsilon_c R_g T \frac{\partial C_T}{\partial t} - (1-\varepsilon_c) a_{p,sorb} h_{f,sorb} (T - T_{sorb}) - 2\frac{h_w}{R_c}(T - T_w) \quad (1.9)$$

where λ_{ax} is the gas phase thermal conductivity in J/(m.s.K) and R_g is the ideal gas constant in J/(mol.K).

The mass transfer from the gas phase to the pore network of the sorbent was approximated using the linear driving force [89].

$$\frac{\partial \overline{C}_{sorb,i}}{\partial t} = \frac{15 D_{p,sorb}}{R_{sorb}^2} \frac{Bi}{Bi+1}\left(C_i - \overline{C}_{sorb,i}\right) - \frac{\rho_{sorb}}{\varepsilon_{p,sorb}} \frac{\partial \overline{q}_i}{\partial t} \quad (1.10)$$

where $\varepsilon_{p,sorb}$ is the particle porosity, $D_{p,sorb}$ is the sorbent pore diffusivity in m^2/s. The sorbed concentration of He and H_2O was assumed to be zero as these gases are considered non-sorbing.

The sorption of CO_2 was also approximated using the linear driving force [89].

$$\frac{\partial \overline{q}_{CO2}}{\partial t} = k_{CO2,sorb}\left(q_{eq,CO2} - \overline{q}_{CO2}\right) \quad (1.11)$$

The parameter k_{CO2} will be used as the only fitting parameter to model the experimental breakthrough curves. The equilibrium carbon dioxide sorption capacity in the hydrotalcite was calculated using the bi-Langmuir model [88] expressed in equation 1.6.

The energy balance to the sorbent particle is:

$$\left[\varepsilon_{p,sorb}\hat{C}_{vg}\overline{C}_{T,sorb} + (1-\varepsilon_{p,sorb})\rho_{solid,sorb}\hat{C}_{ps,sorb} + (1-\varepsilon_{p,sorb})\frac{\rho_{sorb}}{(1-\varepsilon_{p,sorb})}\left(\sum_{i=1}^{3}\overline{q}_i\right)\hat{C}_{vg}\right]$$
$$(1-\varepsilon_c)\frac{\partial T_{sorb}}{\partial t} = (1-\varepsilon_c)a_{p,sorb}h_{f,sorb}(T - T_{sorb}) + (1-\varepsilon_c)\varepsilon_{p,sorb}R_g T_{sorb}\frac{\partial \overline{C}_{T,sorb}}{\partial t} + \quad (1.12)$$
$$(1-\varepsilon_c)\rho_{sorb}\sum_{i=1}^{3}\frac{\partial \overline{q}_i}{\partial t}(\beta(-\Delta H_{sorb}) + (1-\beta)(-E_{sorb}))$$

where β is the fraction of physical sorption in the total sorption.

Finally, the energy exchange with the surroundings is described by the following equation:

$$\rho_w \hat{C}_{pw} \frac{\partial T_w}{\partial t} = \frac{2R_c}{\left(w_{thick}\left(2R_c + w_{thick}\right)\right)} h_w \left(T - T_w\right) - \\ - \frac{1}{\left(\left(2R_c + w_{thick}\right) \ln\left(\frac{2r_c + w_{thick}}{2R_c}\right)\right)} U\left(T_w - T_\infty\right) \tag{1.13}$$

where U is the global heat transfer coefficient in $W/(m^2_{col}.K)$ and T_∞ is the temperature in the oven in K.

The Ergun equation was used to describe the pressure drop inside the column [90].

$$-\frac{\partial P_T}{\partial z} = 150 \frac{\mu_{gas}\left(1-\varepsilon_c\right)^2}{4R^2_{sorb}\,\varepsilon_c^3} u + 1.75 \frac{\rho_{gas}\left(1-\varepsilon_c\right)}{2R_{sorb}\,\varepsilon_c^3} |u| u \tag{1.14}$$

where P_T is the total pressure in bar.

The equations of the transport parameters required solve the mathematical model are detailed in Appendix A. The mass, energy and momentum balances to the reactor and sorbent extrudates require boundary conditions to be solved. The boundary conditions used in the breakthrough curves are:

$$\varepsilon_c D_{ax} \left.\frac{\partial C_i}{\partial z}\right|_{z=0} = -u_{feed}\left(\frac{y_{i,feed} P_T\big|_{z=0}}{R_g T\big|_{z=0}} - C_i\big|_{z=0}\right) \tag{1.15}$$

$$\left.\frac{\partial C_i}{\partial z}\right|_{z=L_C} = 0.0 \tag{1.16}$$

$$\lambda_{ax} \left.\frac{\partial T}{\partial z}\right|_{z=0} = -u_{feed} C_T \hat{C}_{pg}\left(T_{feed} - T\big|_{z=0}\right) \tag{1.17}$$

$$\left.\frac{\partial T}{\partial z}\right|_{z=L_C} = 0.0 \tag{1.18}$$

$$u_{feed} = \frac{Q_{total}}{A_{col}} \tag{1.19}$$

$$P_T\big|_{z=L_c} = P_{out} \tag{1.20}$$

2.5. Results and discussion

In this section the commercial and prepared hydrotalcite materials will be screened. Sorption equilibrium and kinetics will be measured in the most promising material for SERP. The sorbent extrudates are shown in Figure 2.4.

Figure 2.4. Hydrotalcite extrudates used in this work.

2.5.1. Characterization of the prepared samples

The SEM and EDX images of the pure commercial hydrotalcite extrudates (MG30, MG50 and MG70) are shown in Figure 2.5.

The hydrotalcites show a highly porous lamellar structure, as has been reported in the literature [63]. The EDX shows that the MG30

hydrotalcite has 28.5% magnesium oxide, while the quantity of this oxide in MG50 is 53.3% and in MG70 is 63.5%. These Mg contents are in agreement with the expected values of the Mg and Al content for these hydrotalcites (30, 50 and 70% respectively).

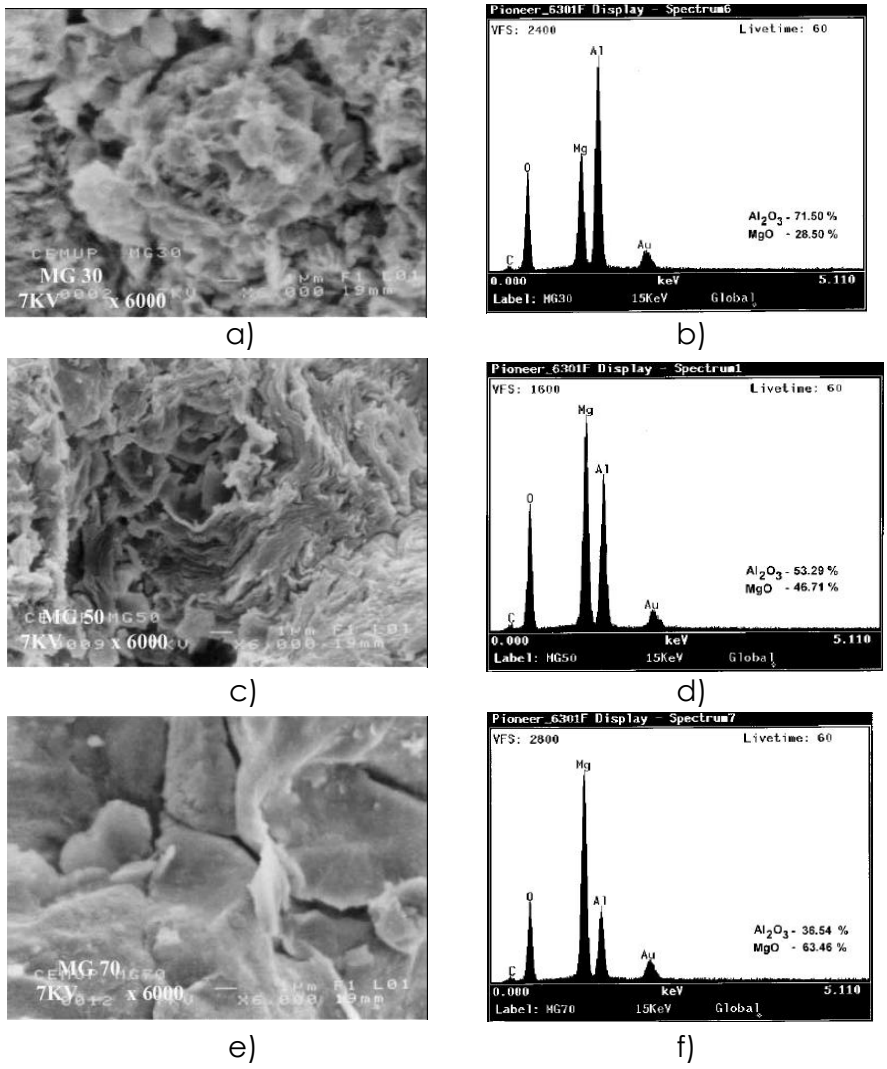

Figure 2.5. SEM (x6000) and EDX images of pure hydrotalcites: (a,b) MG30; (c-d) MG50; (e-f) MG70.

The potassium modified samples showed two kinds of morphologies that were more evident at the surface of the extrudates.

The external surface of the MG30-K modified hydrotalcite is shown in Figure 2.6. Some "agglomerates" in coalescence with some "needle-like" structures can be observed. The EDX spectra taken to these structures (marked with boxes in Figure 2.6) showed that the amount of potassium in both structures is similar. The "needle-like" morphology is also present in the inner part of the extrudates, although their amount and size are much smaller as can be observed in Figure 2.7.

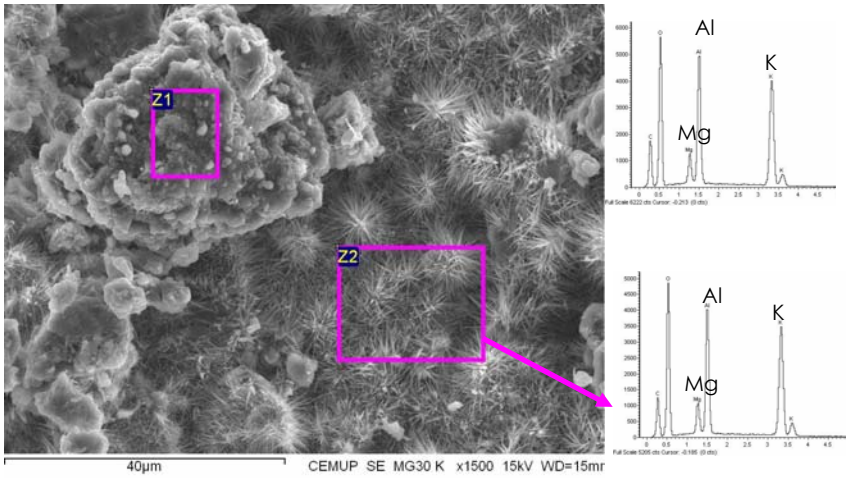

Figure 2.6.SEM of the MG30-K sample at 1500x magnification and the EDX analysis to the selected areas.

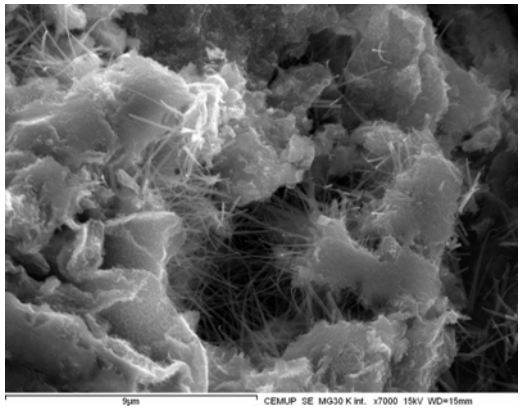

Figure 2.7. SEM of the inner part of the extrudate of MG30-K sample (x7000).

One extrudate employed for CO_2 sorption tests was also analyzed by SEM/EDX, as can be seen in Figure 2.8. The "needle-like" morphology is neither present in the porous structure nor at the extrudate surface. It is possible that these structures were mainly formed by potassium carbonates (the Al shown in the EDX analysis of Figure 2.6 is from the background) that were dissolved by the presence of steam during the sorption tests. According to the analysis of the water recovered from a CO_2 experiment performed for cyclic stability (in continuous operation during 48 hours), only 2 ppm of potassium were present. From these results it is possible to conclude that only minor amounts of potassium were removed by the water employed in the experiments, indicating that the potassium in the "needle-like" structures may be rearranged in the structure.

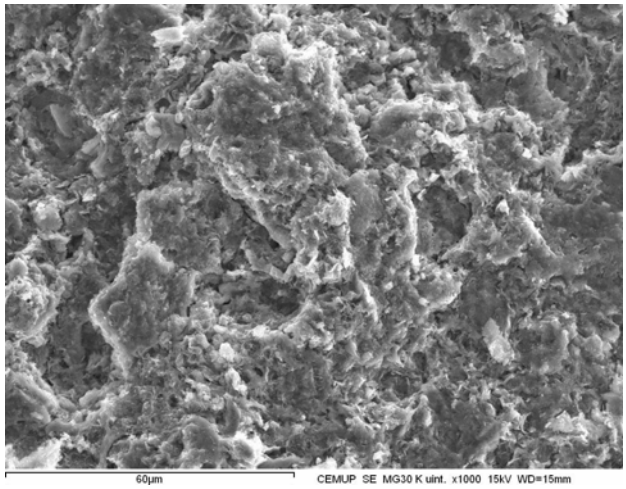

Figure 2.8. SEM of the interior of the MG30-K used sample at 1000x magnification.

To determine if there were limitations to the diffusion of potassium during the preparation of the modified samples, a series of EDX spectra were measured along the diameter of one extrudate (MG30-K). The SEM image showing the location of the analysis together with the results

obtained, are shown in Figure 2.9. Although the dispersion of the values is high, it can be observed that there were no diffusional limitations for potassium cations during the preparation of the sample. Similar results were obtained with a Cs-modified extrudate.

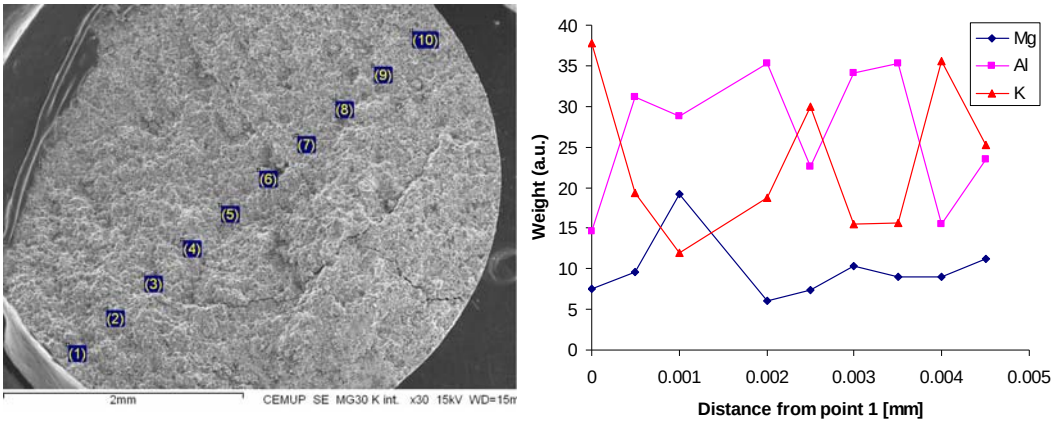

a) b)

Figure 2.9. SEM image (a) showing the locations where EDX spectra were taken to determine the potassium concentration inside MG30-K; (b) EDX results.

As an example of the characterization of the Cs-modified samples, a back-scattered electron (BE) image with different EDX results taken in three different areas of the extrudate is shown in Figure 2.10. The BE image shows "brighter" zones where heavy elements (Cs cations in this case) are located. In all the Cs-modified samples "agglomerates" were observed although no "needle-like" morphology was present, even in the fresh samples.

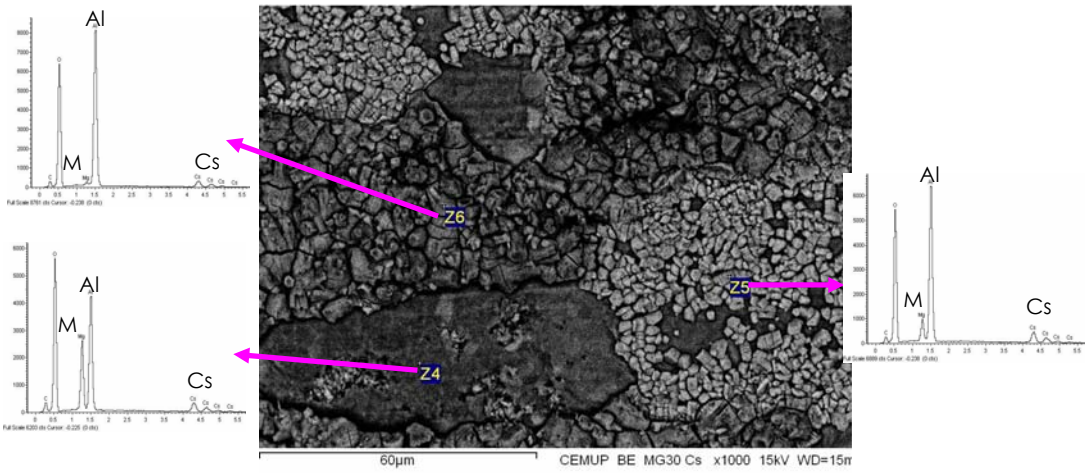

Figure 2.10. BE image of the MG30-Cs sample at 1000x magnification and the EDX analysis to the selected points.

2.5.2. Determination of the BET areas of the prepared samples

The N_2 sorption isotherms at 77 K were measured in the alkali-modified hydrotalcites (with Cs and K) to determine the BET area of these samples. The sorption isotherms are reported in Figure 2.11.

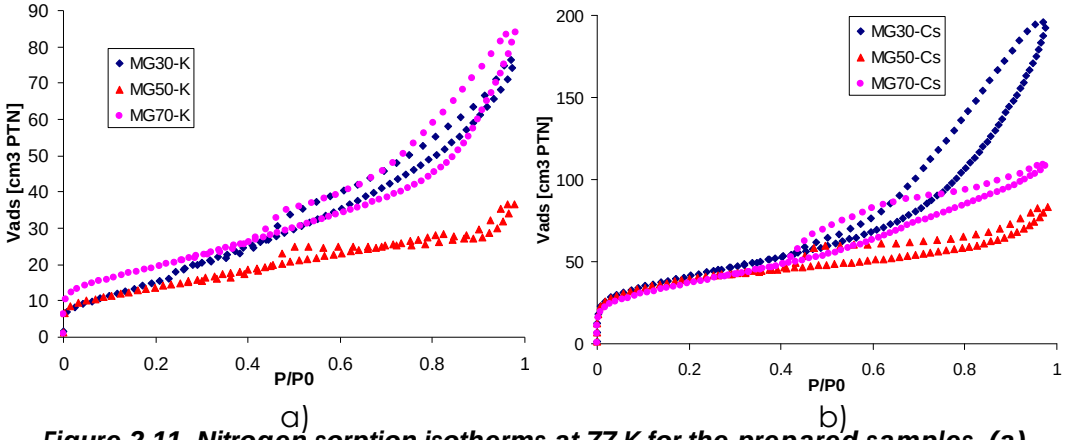

Figure 2.11. Nitrogen sorption isotherms at 77 K for the prepared samples. (a) Potassium-modified MG30, MG50 and MG70; (b) Cs-modified MG30, MG50 and MG70.

All the cesium samples show a similar trend in the N_2 isotherm until $P/P_0 < 0.35$ indicating that that the BET area is similar. The isotherm of the MG70-K shows higher N_2 sorption capacity than the isotherms of the other potassium modified samples and as a consequence the BET area will be higher (29 % higher than the MG50-K and 13% higher than the MG30-K samples respectively).

Using the information from the N_2 sorption isotherms at 77 K, the BET surface area was calculated for all the samples and is shown in Figure 2.12. Comparing the pure hydrotalcite samples, the surface area decays in the order MG30 > MG50 > MG70 [91]. When the hydrotalcites were impregnated with cesium, surface area reduction was between 7 and 25 %, following the same trend of the surface area of the commercial hydrotalcite extrudates. When the impregnation was performed with potassium, the reduction of the surface area was much more important and the BET areas presented the following order MG70 > MG30 > MG50. The surface area reduction of the potassium samples might be due to pore blocking, particularly in the mesopore region as can be observed by comparison of Figure 2.11 with the isotherms of pure MG30 [63]. A reduction of 30% in the BET area of MG30-K sample was also observed after CO_2 breakthrough experiments: from an initial value of 61.9 m^2/g to a final value of 40.0 m^2/g after CO_2 breakthrough.

From the SEM, EDX and N_2 sorption characterizations of all the samples it can be concluded that there was an important loss of surface area in the K-modified samples and that the area reduction was less pronounced for the Cs-modified ones. The reduction in surface area was also observed when CaO is promoted with alkali metals [31]. The K-modified samples also showed the existence of two different morphologies: "agglomerates" and "needle-like" structures with high

content of K. The "agglomerates" and "needle-like" structures become smaller as the Mg amount becomes higher in the base hydrotalcite (MG30 > MG50 > MG70). The "needle-like" structures disappeared after the samples were employed in tests of CO_2 sorption at 676 K in the presence of water vapor, but only a very small amount of potassium was lost. From the SEM images it was also observed that MG30-Cs presented a layered structure that became less apparent in the MG50-Cs and MG70-Cs samples.

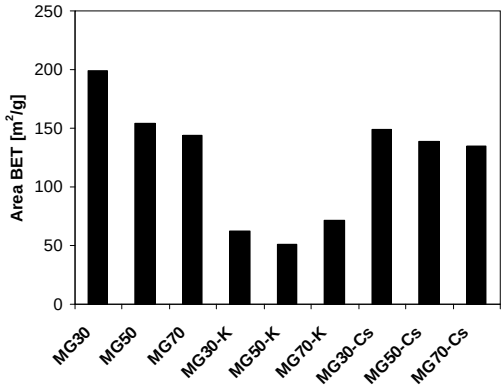

Figure 2.12. BET areas for all the hydrotalcite samples.

2.5.3. Sorbent Screening

The three pure hydrotalcite samples – MG30, MG50 and MG70 – as well as the alkali-modified materials – with K and Cs – were tested to determine the material with higher capacity for carbon dioxide sorption in the presence of water vapor. The screening was based in a single point of CO_2 sorption equilibrium at 676 K obtained by breakthrough curves employing a stream with carbon dioxide, water vapor and helium (considered as inert gas). In all the experiments, the partial pressure of CO_2 was close to 0.40 bar and the total pressure of the

system was 2 bar. The operating conditions of all the screening experiments are detailed in Table 2.5. The purpose of this screening is to select the best two samples to measure sorption equilibrium isotherms at three different temperatures. The molar flowrate of CO_2 of each sample can be observed in Figure 2.13. The temperature history, inside the sorption column, of the MG50 pure and modified samples is also shown in Figure 2.13 as illustration of the temperature behavior of the other hydrotalcite samples.

The first experiments were carried out with the pure hydrotalcite samples. The CO_2 breakthrough was very fast and equilibrium was reached after 400 seconds, indicating a very low capacity for CO_2 sorption, as previously reported [69].

The next set of samples tested was the K-modified hydrotalcites. Note that the mass of solid employed in these experiments was much higher than in the pure hydrotalcite samples due to the difference in the density of the extrudates (see Table 2.6). In all the samples it was observed that the surface area available for sorption was much smaller than in the pure hydrotalcite. On the other hand, it can be seen in Figure 2.13 that the CO_2 in these samples takes more than five times to breakthrough, which indicates that the sorption capacity of the K-modified hydrotalcites was greatly improved. It can also be observed that the K-modified hydrotalcites show non-isothermal behavior (temperature increases around 8 K during sorption).

Finally, the Cs-modified samples were tested (see operating conditions in Table 2.5). In these samples, the CO_2 takes around three times more than the pure hydrotalcites to breakthrough. The temperature within the column during the experiments was also not constant with variations of 6 K.

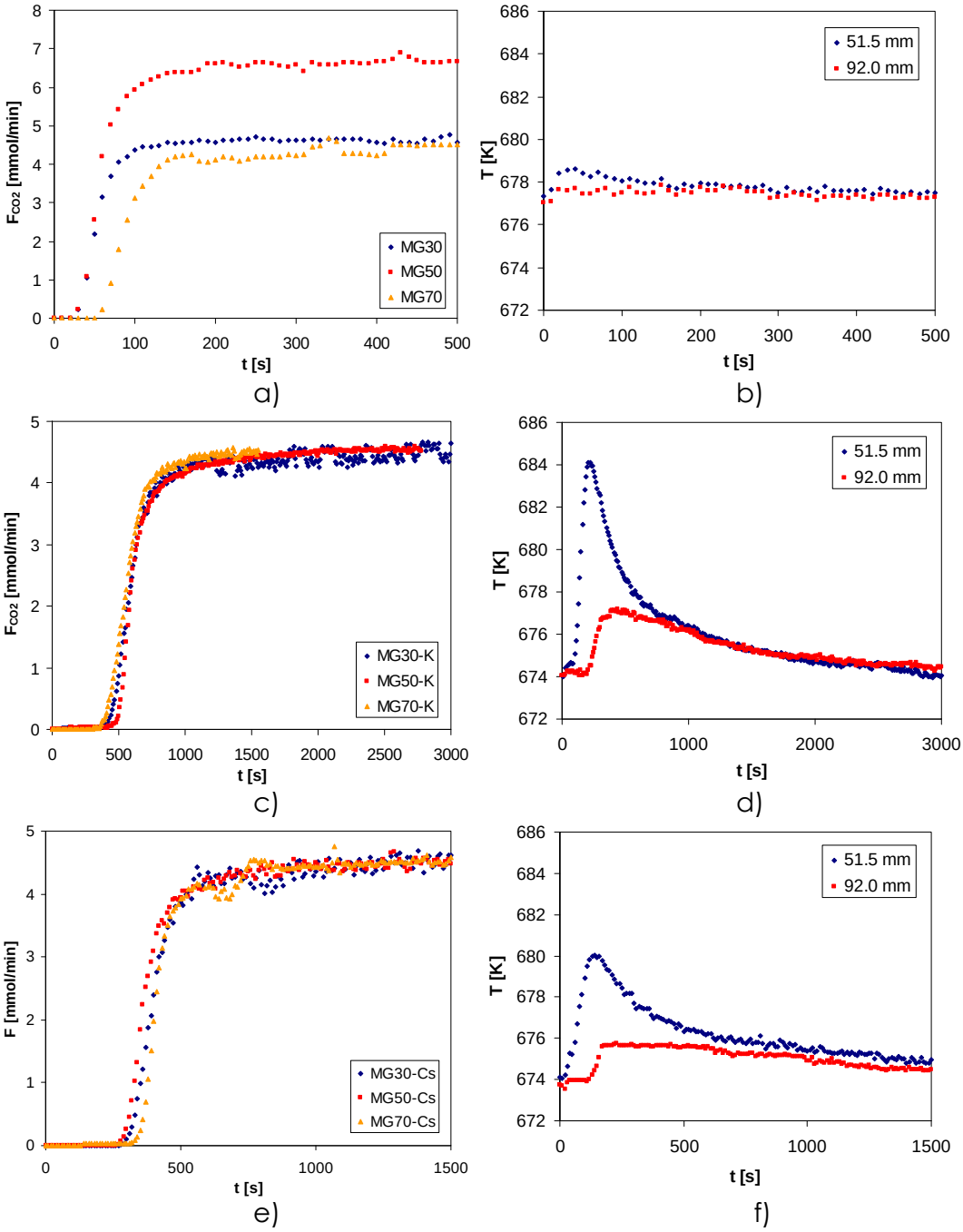

Figure 2.13. Molar flowrate at the exit of the column for breakthrough experiments of CO_2 (0.40 bar partial pressure) at 676 K at 2 bar total pressure with steam: a) Pure hydrotalcites; c) K-modified hydrotalcites; e) Cs-modified hydrotalcites. Temperature profiles inside the column for b) MG50; d) MG50-K; f) MG50-Cs.

The breakthrough curves shown in Figure 2.13 were employed to calculate the stoichiometric time of CO_2 and the carbon dioxide sorption capacity according to equation 1.5. The CO_2 equilibrium sorption capacity is shown in Figure 2.14.

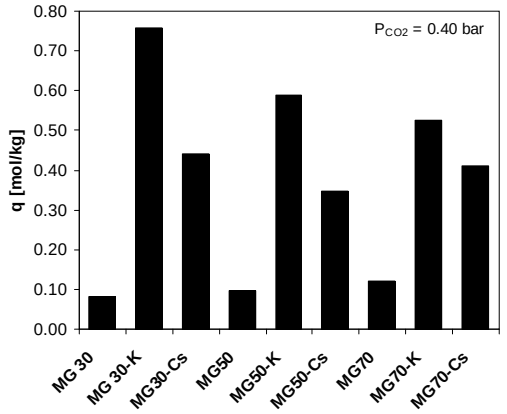

Figure 2.14. Comparison of the sorption capacity of CO_2 for pure and alkali-modified (Cs and K) hydrotalcites at 676 K, 2 bar total pressure, P_{CO2} = 0.40 bar in the presence of water.

All the pure hydrotalcites showed almost the same capacity, around 0.10 mol/kg. This capacity is very small to be employed in SERP processes. When the pure hydrotalcite was modified with cesium, the surface area decreased (25% for MG30, 10% in MG50 and 7% in MG70) but the sorption capacity is higher, going up to 0.35-0.44 mol/kg. The material with higher capacity is MG30-Cs. In the samples modified with potassium, the area reduction was higher: 69% for MG30, 67% for MG50 and 50% for MG70. In this case, the sample with higher capacity was the MG30-K (0.76 mol/kg) which was not the sample with the higher surface area. This indicates that the surface area is not a key factor in the CO_2 sorption in the K-modified samples (existence of specific interaction with or aided by the potassium cation). The sorption capacity obtained for

the MG30-K hydrotalcite is higher than the one obtained by Lee *et al*. [74] – 0.29 mol/kg – and Ding and Alpay [51] – 0.62 mol/kg.

Ebner *et al*. [66, 72] reported that the sorption in this type of materials could be due to different reactions in parallel with different kinetics. According to their work, only after long CO_2 contact time the hydrotalcite can be considered to be in equilibrium. In the present work, equilibrium was considered in the breakthrough experiments when there was no variation in the concentration of the exit stream for at least 300 s in the case of the screening experiments and 600 s in the case of the determination of the sorption isotherms.

From the results obtained from this screening, the sample MG30-K was selected as it was the one presenting higher sorption capacity of CO_2. For comparison purposes and to study the effects of other alkali metal in the hydrotalcite, the MG30-Cs material was also selected for a more detailed study of the CO_2 sorption properties.

2.5.4. CO_2 Sorption Isotherms on MG30-K and MG30-Cs

The determination of CO_2 sorption at high temperatures is required to use alkali-modified hydrotalcites in SERP. It is necessary to determine the temperature conditions at which the material possesses the highest CO_2 capacity in the presence of steam. For this reason, sorption equilibrium isotherms were measured in the MG30-K and MG30-Cs hydrotalcites at three different temperatures: 579, 676 and 783 K. The experimental conditions were reported in Tables 2.5 and 2.6. As an example of the experimental data measured in each run, Figure 2.15 shows the CO_2 concentration, volumetric flowrate and temperature data.

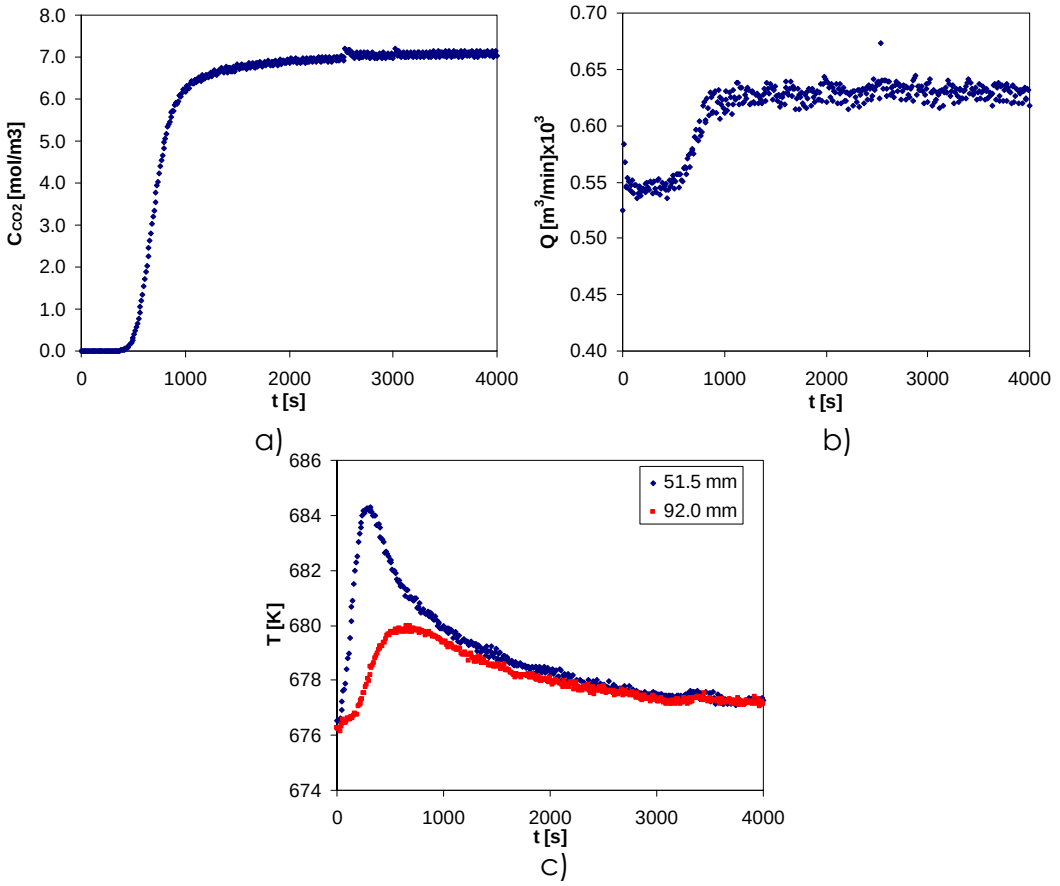

Figure 2.15. Breakthrough experiment of CO_2 (0.40 bar partial pressure) at 676 K with MG30-K. a) CO_2 concentration at the exit stream; b) volumetric flowrate; c) temperature profiles in the column at 51.5 and 92.0 mm from feed inlet.

The CO_2 isotherms of MG30-K modified sample are shown in Figure 2.16. The solid lines in this figure correspond to the fitting of the data with the bi-Langmuir model. The dashed and dotted lines correspond to the contribution of the physical and chemical sorption terms of the model, respectively. The equilibrium point measured at 0.09 bar CO_2 partial pressure at 676 K using the MG30-K material – 0.58 mol/kg – is higher than the one obtained by Reijers *et al* [69] – 0.44 mol/kg. In the MG30-K hydrotalcite, the sorption capacity at 676 K is higher than at 579 or 783 K. This result is consistent with results obtained in previous works, where it

was shown that capacity at about 673 K is higher than at temperatures higher than 750 K [51, 74]. A maximum in the CO_2 sorption equilibrium capacity was also reported by Hufton *et al* [49] for the potassium promoted Sorbplus sample.

The existence of a maximum in the CO_2 capacity cannot be due only due to physical sorption. This fact is supported by the enhanced capacity of CO_2 when the samples were modified with both Cs and K: the surface area available for CO_2 sorption is much smaller in the modified samples, but the capacity is higher indicating that there are some specific interactions between the CO_2 molecules and the alkali metals when they are present in the hydrotalcite structure.

Physical adsorption is an exothermic spontaneous process (where $(-\Delta H) > 0$) attributed to Van der Walls [88, 92, 93] and electrostatic forces [88], and hence the capacity must decrease with temperature. Chemical adsorption is also spontaneous, (usually) exothermic at high temperatures and frequently irreversible [88, 92, 93]. Physical adsorption is considered when the heat of sorption is in the region of 25 kJ/mol whereas for chemical adsorption the heats are in the region of 200 kJ/mol [93]. The value of the heat of physical adsorption can be higher when electrostatic forces are significant (zeolites) [88]. In the case of hydrotalcites, the metal layer is positively charged and the electrostatic contribution to the sorption might not be negligible. The physical adsorption term is thus considered to be more accurately described by the first part of the bi-Langmuir model with a heat of sorption of 40.0 and 35.9 kJ/mol for MG-30-K and MG30-Cs, respectively.

In the isotherms presented in Figure 2.16, the capacity at 676 K is higher than at 579 K and the sorption is reversible. This "crossing" in

isotherms and the reversibility cannot be explained only by adsorption (physical or chemical). One possible explanation is that together with adsorption, an endothermic reaction also occurs and its conversion increases with temperature. At 676 K, a maximum was observed as a result of two different and opposite effects: at low temperature the physical adsorption dominates while at higher temperatures, the chemical reaction has a more important role. The bi-Langmuir model describes these phenomena as can be seen in Figure 2.16 for the contribution of each part of the model. In a recent work using a similar sorbent [74], a combination of chemisorption and complexation to account for the CO_2 sorption was proposed. The model by Lee *et al* [74] does not account for a maximum of the sorption capacity of CO_2 with increasing temperature and thus it is not adequate to describe the results in Figure 2.16.

In the MG30-Cs hydrotalcite, the CO_2 sorption capacity is higher than the pure hydrotalcite but is lower than in the MG30-K sample. A maximum in the CO_2 sorption capacity was also obtained at 676 K.

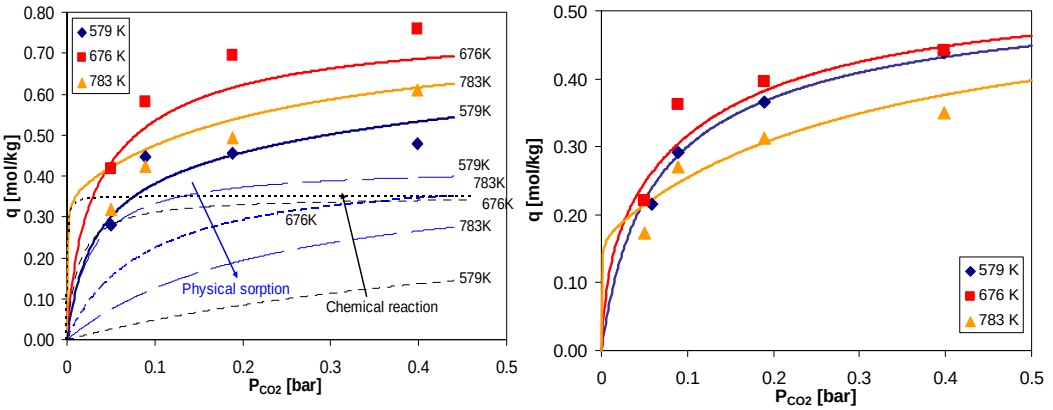

Figure 2.16. Sorption equilibrium isotherms of CO_2 (in the presence of water) at 579, 676 and 783 K on: a) MG30-K hydrotalcite; b) MG30-Cs hydrotalcite.

The fitting parameters of the bi-Langmuir model for both MG30-K and MG30-Cs are reported in Table 2.7. The model follows the general trend shown by the experimental data of both hydrotalcite samples. Ebner *et al*. [66, 72], Lee *et al*. [74] and Ding and Alpay [51] proposed different models to account for the sorption mechanism of CO_2 in the K-promoted hydrotalcites. All the models are aimed at different effects but none considers the observed maximum of sorbent capacity as a function of temperature observed in this work. Table 2.8 compares the monolayer capacity of the referred works to the total capacity of CO_2 fitted by the bi-Langmuir model ($q_{max1}+q_{max2}$). In the case of the work by Ebner *et al*. [72], the fast sorption of CO_2 on site A was considered as it should correspond to the fast kinetics that are represented by the Langmuir model used by other authors. Although the models used are different, the monolayer capacity gives some insight of the maximum sorption capacity that each author predicts for the fast kinetics stage.

Table 2.7. Fitting parameters of the bi-Langmuir model for the MG30-K and MG30-Cs hydrotalcite samples

Parameters	MG30-K	MG30-Cs
q_{max1} [mol/kg]	0.423	0.383
k_{01} [bar^{-1}]	9.07 x10^{-3}	1.26x10^{-2}
-ΔH [kJ/mol]	40.000	35.924
q_{max2} [mol/kg]	0.351	0.164
k_{02} [bar^{-1}]	1.01 x10^{12}	9.13x10^{11}
E [kJ/mol]	-130.831	-127.406

In Table 2.8, we can see that there is a large spread of values. The present work shows values intermediate to the ones reported by Ding and Alpay [51] and Ebner *et al*. [72]. The differences in the values can be due to different preparations of the materials and/or different K_2CO_3 loadings.

Table 2.8. Monolayer capacity of K-promoted hydrotalcite in literature

Work	Monolayer capacity [mol/kg]	Hydrotalcite type	Conditions	
			Mixture	T [K]
Ding and Alpay [51]	0.63	K promoted	CO_2+N_2+H_2O	673-753
Ebner et al. [72]	0.932	Mg/Al = 0.75 K/Al = 1	CO_2	673
Lee et al. [74] (q_A)	0.25	K promoted	CO_2+N_2	673, 793
bi-Langmuir (this work) (q_{max1}+q_{max2})	0.806	Mg/Al = 0.3 K_2CO_3 = 20%	CO_2+He+H_2O	579-783

2.5.5. Determination of the cyclic stability of the MG30-K hydrotalcite

To be effective for reversible carbon dioxide sorption, the hydrotalcite material has to be able to keep its properties over hundreds of sorption/desorption cycles. In this work, the MG30-K hydrotalcite was cycled during 48 h (75 sorption/desorption cycles) in the presence of 26.5 % H_2O to investigate the stability of the material.

The cyclic test was performed by swinging the partial pressure of CO_2 between one specified value and zero for pre-defined intervals of time. The results of the cyclic test are reported in Figures 2.17 to 2.19. In the cyclic test, a first breakthrough was carried out until equilibrium. The next cycles were only performed partially, with 150 s for sorption and 1200 s for desorption. Figure 2.17 and Figure 2.18 show the temperature history and the CO_2 molar flowrate of the first and last full breakthrough, respectively. In Figure 2.19 we can see the molar flowrate at the exit of the column in the whole experiment and the

temperature history for the whole cyclic experiment (in the thermocouple located at 51.5 mm from the feed inlet).

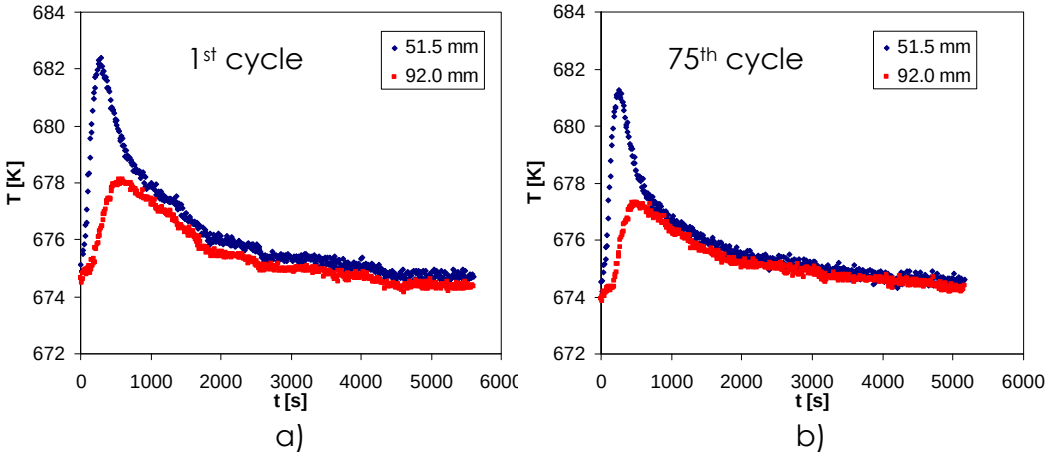

Figure 2.17. Temperature variation for the: a) first CO_2 sorption; b) last CO_2 sorption. Results for the MG30-K sample at 676 K, P_{CO2} = 0.40 bar and y_{H2O} = 0.265.

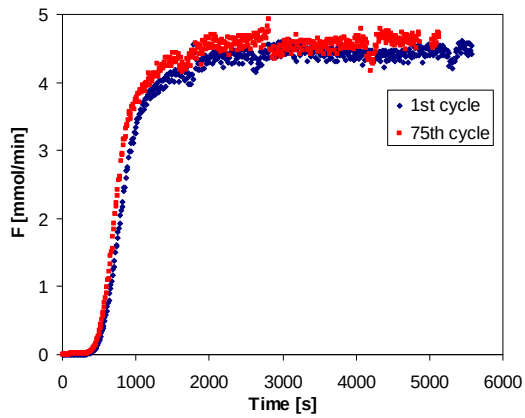

Figure 2.18. CO_2 molar flowrate variation with time for the first and last sorption. Results for the MG30-K sample at 676 K, P_{CO2} = 0.40 bar and y_{H2O} = 0.265.

The sorption capacity was 0.84 mol $CO_2/kg_{sorbent}$ in the first experiment and 0.77 mol CO_2/kg after 75 cycles. From the measurement of the sorption capacity in the first and last CO_2 breakthrough curves and the fact that during the cyclic operation the temperature and concentration curves are similar for all the cycles, it

can be concluded that there is a small loss (7%) in sorption capacity during cyclic operation. In previous works it was shown that activity loss occurs in the initial cycles until it stabilizes in a long term value [50, 51, 69]. However, the work by Ebner *et al*. [72] showed that K-modified hydrotalcites have long term stability without loss of CO_2 capacity.

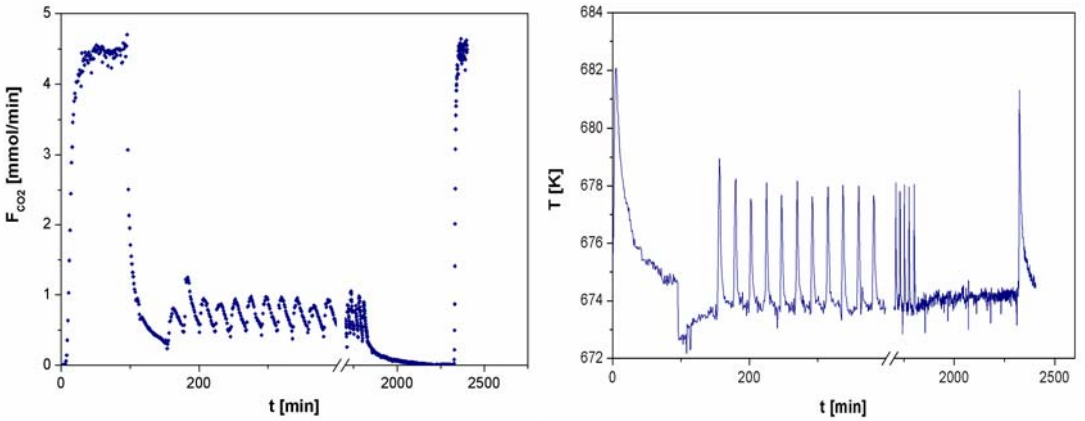

Figure 2.19. Cyclic carbon dioxide sorption experiments in the MG30-K sample at 676 K, 2 bar total pressure, P_{CO2} = 0.40 bar and y_{H2O} = 0.265. a) CO_2 effluent molar flowrate; b) Temperature at 51.5 mm from feed inlet.

2.5.6. Sorption kinetics

The carbon dioxide sorption breakthrough curves measured on the MG30-K and MG30-Cs hydrotalcite samples were used to determine the sorption kinetics in the temperature range 676-783 K. This is the range of interest for sorption-enhanced reaction process.

The mathematical model described in Section 2.4.2 was used to fit the breakthrough curves, using k_{CO2} as fitting parameter. The k_{CO2} constant is important in the design of a cyclic sorption unit as it influences the shape of the carbon dioxide front inside the sorption column. The constants used in the mathematical model are shown in Table 2.9 and the experimental conditions were previously reported in

Table 2.5. The equations used to calculate the different parameters are detailed in Appendix A.

Table 2.9. Parameters of the mathematical model used to fit the CO_2 sorption breakthrough experiments in the MG30-K and MG30-Cs hydrotalcite samples.

Parameter		Parameter of sample MG30-K	
L_c [m]	0.166	m_{sorb} [kg] x 10^3	92.1944
R_c [m]	0.0133	r_{sorb} [mm]	2.215
w_{thick} [m]	0.0091	$a_{p,sorb}$ [m^{-1}]	1354
ε_c (MG30-K)	0.47	ρ_{sorb} [kg/m^3]	1845
ε_c (MG30-Cs)	0.41	$\rho_{solid,sorb}$ [kg/m^3]	2440
h_w [W/(m^2.K)][a]	25	r_{pore} [nm]	4.55
U [W/(m^2.K)][a]	15	$\varepsilon_{p,sorb}$	0.27
$\hat{C}p_w$ [J/(kg.K)]	500	β	0.95
ρ_w [kg/m^3]	7750	Parameter of sample MG30-Cs	
$\hat{C}_{p,sorb}$ [J/(kg.K)]	850		
h_f [W/(m^2.K)][a]	80.7	m_{sorb} [kg]	80.8914
k_f [m/s][a]	0.08	r_{sorb} [mm]	2.215
λ_{gas} [W/m.K][a]	0.84	$a_{p,sorb}$ [m^{-1}]	1354
D_{ax} [m^2/s][a]	8.67x10^{-5}	ρ_{sorb} [kg/m^3]	1439
D_k [m^2/s][a]	4.13x10^{-6}	$\rho_{solid,sorb}$ [kg/m^3]	2760
D_p [m^2/s][a]	1.90x10^{-6}	r_{pore} [nm]	4.00
ρ_{gas} [kg/m^3][a]	0.56	$\varepsilon_{p,sorb}$	0.46
μ_{gas} [Pa.s][a]	3.08x10^{-5}	β	0.98

a– Calculated for the feed conditions at 676 K and 2 bar.

2.5.6.1. MG30-K hydrotalcite sample

Simulations were performed for MG30-K hydrotalcite at the four different CO_2 feed partial pressures – 0.05; 0.09; 0.19 and 0.40 bar – used in the sorption breakthrough experiments. The experimental and simulated breakthrough curves are shown in Figure 2.20 for the experiments at 676 K and in Figure 2.21 for the experiments at 783 K. The temperature peaks when the CO_2 feed partial pressure is 0.40 bar are

also shown as an example of the simulated results. The fitting of the experimental breakthrough curves is quite reasonable considering that the sorption equilibrium model does not match some of the CO_2 sorption equilibrium points. The fitted value of the k_{CO2} constant in the temperature range 676-783 K is:

$$k_{CO2}\left(s^{-1}\right) = 24.9e^{\frac{-50911}{RT}} \qquad (2.21)$$

The desorption of carbon dioxide in the presence of steam was also simulated. As an example, Figure 2.22 shows the desorption curves at 676 and 783 K corresponding to the sorption at 0.40 bar feed carbon dioxide partial pressure. The simulation results were obtained using equation 2.21 to determine the value of k_{CO2}. As the carbon dioxide sorption isotherm is unfavorable for desorption, the time required for desorption was more than one order of magnitude higher than the time required for complete sorption. The mathematical model is able to describe this behavior, although at 783 K the model predicts a slower desorption than observed experimentally. This means that, in the design of a cyclic process, a part of the sorbent will not be used but the purity of the non-sorbed components will be higher.

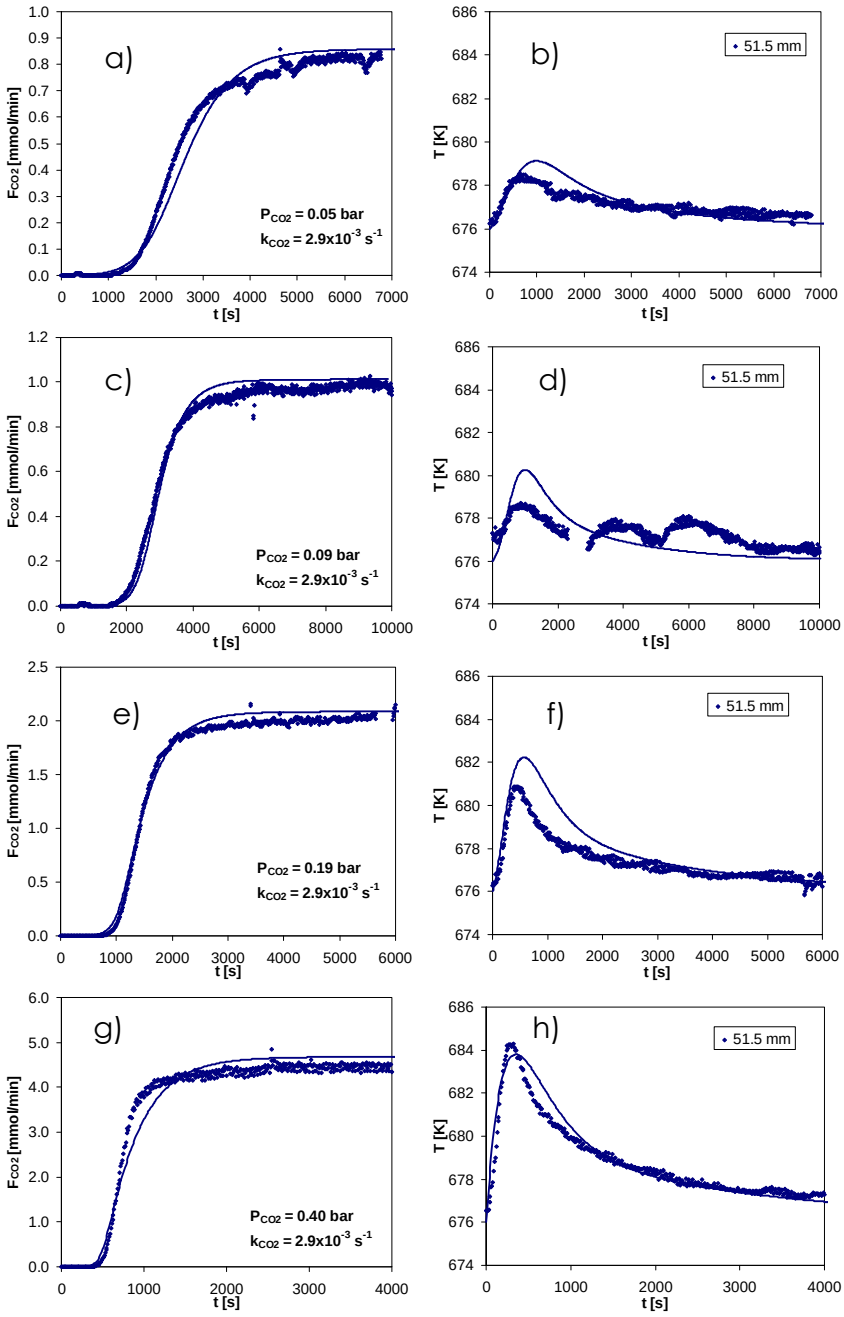

Figure 2.20. Experimental and simulated CO_2 effluent molar flowrates measured at 676 K in the MG30-K hydrotalcite at 4 different CO_2 partial pressures: a-b) 0.05; c-d) 0.09; e-f) 0.19 and g-h) 0.40 bar in the presence of steam (see operating conditions in Table 2.5).

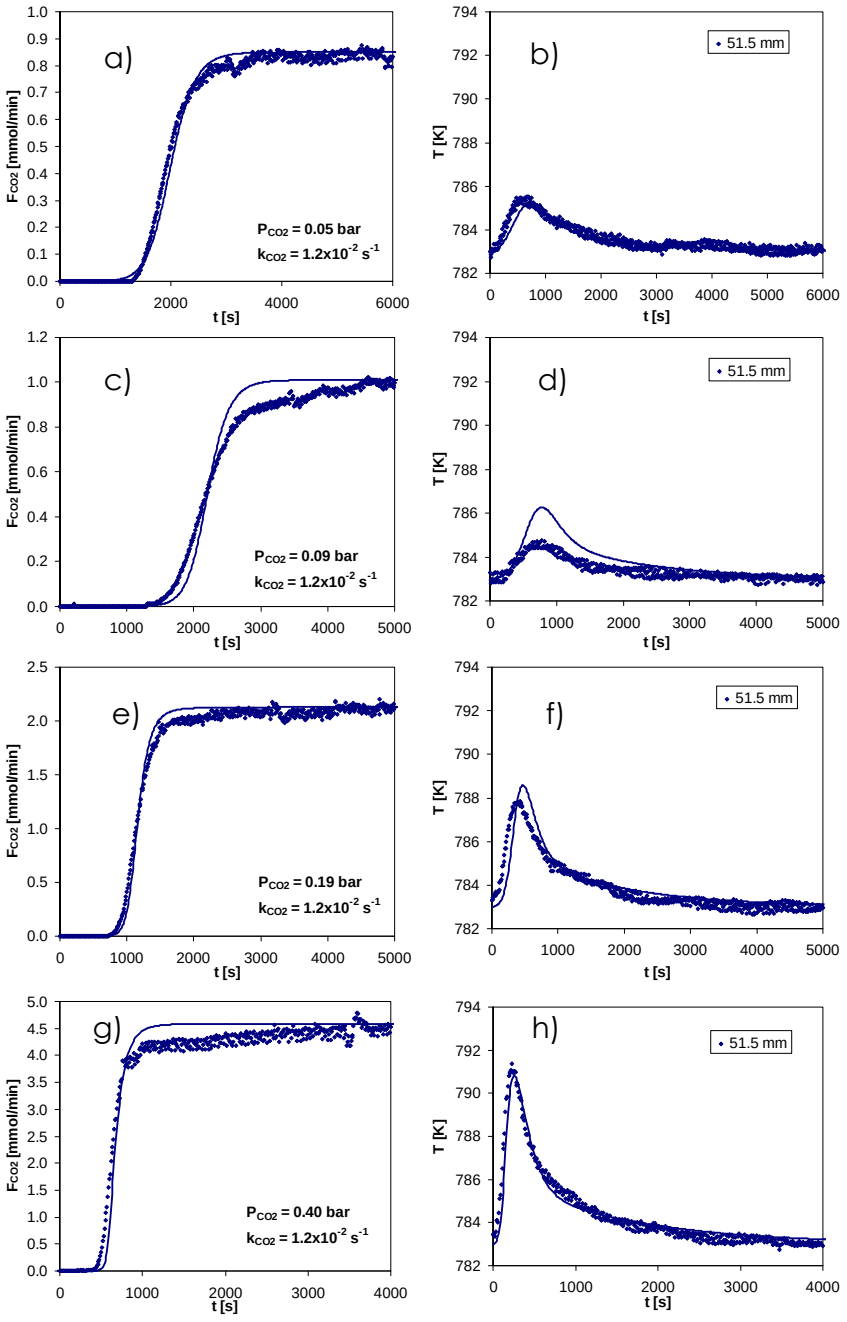

Figure 2.21. Experimental and simulated CO_2 effluent molar flowrates measured at 783 K in the MG30-K hydrotalcite at 4 different CO_2 partial pressures: a-b) 0.05; c-d) 0.09; e-f) 0.19 and g-h) 0.40 bar in the presence of steam (see operating conditions in Table 2.5).

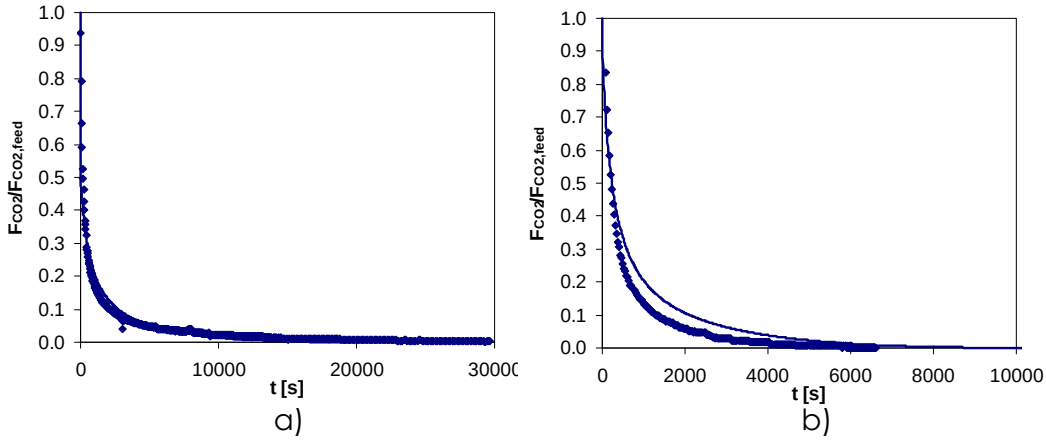

Figure 2.22. Carbon dioxide desorption experiments at 22.57 mmol/min feed molar flowrate, 2 bar total pressure and a) 676 K and P_{CO2} = 0.40 bar (sorption); b) 783 K and P_{CO2} = 0.40 (sorption). Lines are simulated values.

2.5.6.2. MG30-Cs hydrotalcite sample

The carbon dioxide sorption breakthrough curves measured using the MG30-Cs hydrotalcite sample were also simulated, employing the mathematical model reported previously, in order to determine the CO_2 sorption kinetics. The experimental and simulated normalized breakthrough curves are shown in Figure 2.23 along with the temperature peaks obtained at 676 and 783 K and 0.40 bar CO_2 feed partial pressure. The simulated curves closely follow the experimental results when the equilibrium point and the equilibrium isotherm correspond.

The value of the k_{CO2} constant was determined using the simulations at different temperatures and partial pressures and its temperature function in the temperature range 676-783 K is:

$$k_{CO2}\left(s^{-1}\right) = 4.47e^{\frac{-33765}{RT}} \qquad (2.22)$$

The carbon dioxide sorption kinetics of the MG30-Cs hydrotalcite at 676 K is almost four times higher than the MG30-K hydrotalcite. At 783 K, the value decreases to little over two times. Impregnating the hydrotalcite with potassium gives the hydrotalcite the highest equilibrium sorption capacity but impregnating with cesium produces a material with fastest CO_2 sorption kinetics.

At this point a choice has to be made concerning the material to be used in SERP. The alternative is between a material with a high sorption capacity and a material with fast sorption kinetics. In cyclic sorption enhanced operation it would be good to have a sorbent that was capable of removing CO_2 at the same rate that it is produced. However, if the CO_2 sorption capacity is low the sorption enhancement of the hydrogen production is also low. In the temperature range of interest for SERP using the hydrotalcite materials 673-823 K, the MG30-Cs sample has a maximum sorption capacity of 0.44 mol/kg at 676 K. At 783 K the CO_2 equilibrium sorption capacity is very close to the threshold of 0.3 mol/kg [21, 49]. Therefore the MG30-K hydrotalcite is the more viable candidate for SERP.

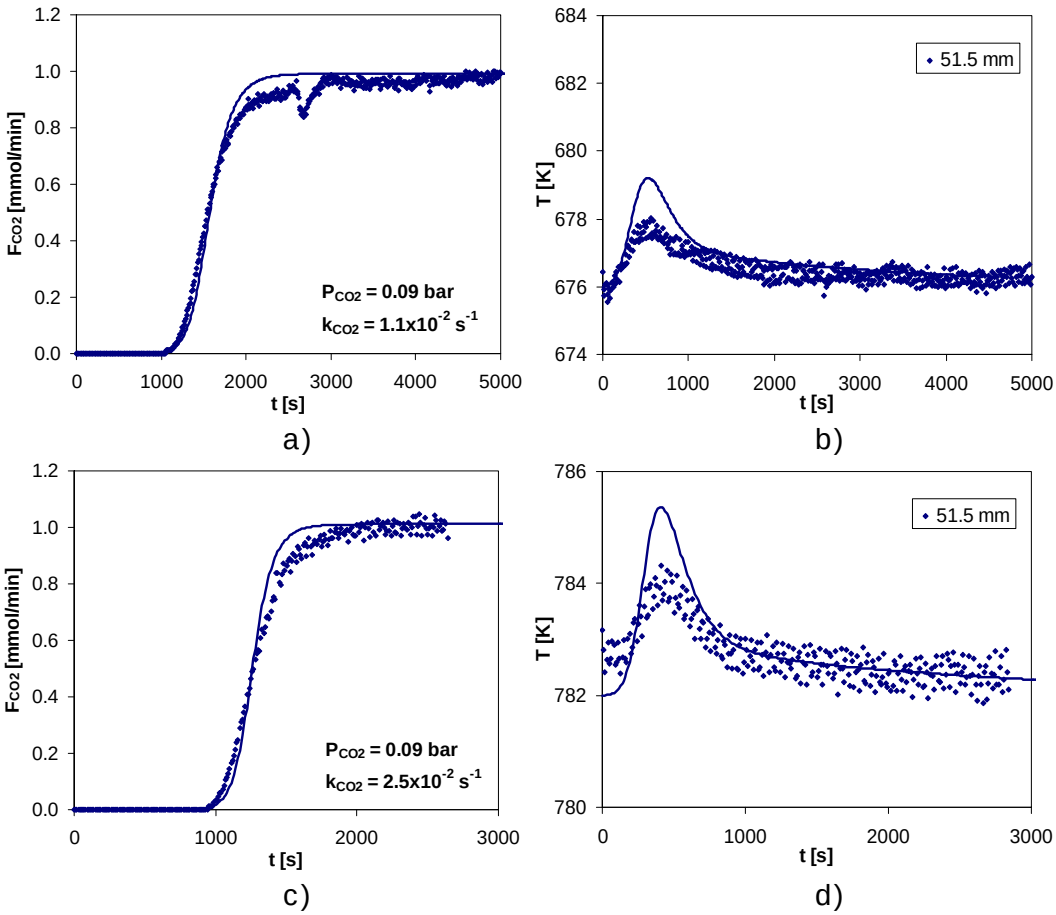

Figure 2.23. Experimental and simulated CO_2 breakthrough curves and sorbent temperatures determined at P_{CO2} = 0.09 bar, (a-b) 676 K feed temperature and (c-d) 783 K feed temperature employing the MG30-Cs hydrotalcite in the presence of steam (see operating conditions in Table 2.5).

2.6. Conclusions

Alkali-modified hydrotalcites were prepared and tested for CO_2 sorption at high temperatures in presence of large amounts of steam. Batches of 100 grams were prepared by impregnating alkali carbonates (potassium and cesium) into commercial hydrotalcites with different Mg/Al ratios. A one-point screening analysis (676 K, 2 bar total pressure, 0.40 bar CO_2 and 26% of steam) and determine that the samples with

potassium presented higher loadings than the ones impregnated with cesium. The hydrotalcite with the highest sorption capacity was the MG30-K (0.76 mol/kg). Among the Cs impregnated samples, the MG30-Cs presented a capacity of 0.44 mol/kg, while the commercial samples presented CO_2 sorption capacities around 0.10 mol/kg

The CO_2 sorption isotherms for the hydrotalcites MG30-K and MG30-Cs were determined at the temperatures of 579, 676 and 783 K and CO_2 partial pressures up to 0.40 bar in the presence of steam. The CO_2 sorption capacity at 676 K in both alkali-modified hydrotalcites was higher than at 579 and 783 K. Therefore a bi-Langmuir sorption mechanism combining physical adsorption and an endothermic chemical reaction was proposed. This model fits the experimental data of the MG30-K and MG30-Cs samples.

A study of the cyclic stability on the MG30-K sample was performed, showing that there was a small loss of capacity (7 %) after 75 cycles.

A mathematical model was developed to simulate the carbon dioxide sorption/desorption breakthrough experiments and determine the sorption kinetics. The value of the kinetic parameter (k_{CO2}) determined using the MG30-Cs sample was approximately the double of the value determined for the MG30-K sample at 783 K.

When comparing the MG30-K and MG30-Cs samples, the MG30-K shows higher CO_2 sorption capacity in the temperature range studied. However, the MG30-Cs hydrotalcite shows faster CO_2 sorption kinetics. According to the higher capacity showed by the MG30-K hydrotalcite, it was decided that this material will be employed in SERP experiments.

2.7. References

1. Causes of climate change, http://www.physicalgeography.net/fundamentals/7y.html (Accessed June 2009).
2. Carbon dioxide in the Earth's atmosphere, http://en.wikipedia.org/wiki/Carbon_dioxide_in_the_Earth's_atmosphere (Accessed June 2009).
3. Kyoto Protocol, United Nations Framework Convention On Climate Change, 1999.
4. Relatório do estado do ambiente, Agencia Portuguesa do Ambiente, 2004.
5. Rao, A. B.; Rubin, E. S. A technical, economic, and environmental assessment of amine-based CO_2 capture technology for power plant greenhouse gas control. *Environ. Sci. Technol.* (2002), 36, 4467-4475.
6. Aaron, D.; Tsouris, C. Separation of CO_2 from flue gas: A review. *Sep. Sci. Technol.* (2005), 40, 321-348.
7. Abanades, J. C.; Rubin, E. S.; Anthony, E. J. Sorbent cost and performance in CO_2 capture systems. *Ind. Eng. Chem. Res.* (2004), 43, 3462-3466.
8. Linde Engineering, http://www.linde-process-engineering.com/process_plants/gas_processing/rectisol_wash.php (Accessed June 2009).
9. Alstom Power, http://www.alstompower.com/ (Accessed June 2009).
10. Mahecha-Botero, A.; Boyd, T.; Gulamhusein, A.; Comyn, N.; Lim, C. J.; Grace, J. R.; Shirasaki, Y.; Yasuda, I. Pure hydrogen generation in a

fluidized-bed membrane reactor: Experimental findings. *Chem. Eng. Sci.* (2008), 63, 2752-2762.
11. Teramoto, M.; Nakai, K.; Ohnishi, N.; Huang, Q.; Watari, T.; Matsuyama, H. Facilitated transport of carbon dioxide through supported liquid membranes of aqueous amine solutions. *Ind. Eng. Chem. Res.* (1996), 35, 538-545.
12. Chen, H.; Kovvali, A. S.; Majumdar, S.; Sirkar, K. K. Selective CO_2 separation from CO_2-N_2 mixtures by immobilized carbonate-glycerol membranes. *Ind. Eng. Chem. Res.* (1999), 38, 3489-3498.
13. Kapoor, A.; Yang, R. T. Kinetic separation of methane-carbon dioxide mixture by adsorption on molecular sieve carbon. *Chem. Eng. Sci.* (1989), 44, 1723-1733.
14. Chue, K. T.; Kim, J. N.; Yoo, Y. J.; Cho, S. H.; Yang, R. T. Comparison of activated carbon and zeolite 13X for CO_2 recovery from flue gas by pressure swing adsorption. *Ind. Eng. Chem. Res.* (1995), 34, 591-598.
15. Siriwardane, R. V.; Shen, M. S.; Fisher, E. P.; Poston, J. A. Adsorption of CO_2 on molecular sieves and activated carbon. *Energy Fuels* (2001), 15, 279-284.
16. Dolan, W. B.; Mitariten, M. J. Heavy hydrocarbon recovery from pressure swing adsorption unit tail gas. US6610124, 2003.
17. Schroter, H. J.; Juntgen, H., Gas Separation by Pressure Swing Adsorption Using Carbon Molecular Sieves. In *Adsorption Science and Technology - NATO ASI series. Series E, no. 158*, Rodrigues, A. E.; LeVan, M. D.; Tondeur, D. (Eds.), First ed, Kluwer Academic Publishers, 1988.
18. Xiao, P.; Wilson, S.; Xiao, G.; Singh, R.; Webley, P. Novel adsorption processes for carbon dioxide capture within a IGCC process. *Energy Procedia* (2009), 1, 631-638.

19. Li, G.; Xiao, P.; Webley, P. A.; Zhang, J.; Singh, R. Competition of CO_2/H_2O in adsorption based CO_2 capture. *Energy Procedia* (2009), 1, 1123-1130.
20. Zhang, J.; Xiao, P.; Li, G.; Webley, P. A. Effect of flue gas impurities on CO_2 capture performance from flue gas at coal-fired power stations by vacuum swing adsorption. *Energy Procedia* (2009), 1, 1115-1122.
21. Yong, Z.; Mata, V.; Rodrigues, A. E. Adsorption of carbon dioxide at high temperature - a review. *Sep. Purif. Technol.* (2002), 26, 195-205.
22. Kwang, B. Y.; Harrison, D. P. Low-pressure sorption-enhanced hydrogen production. *Ind. Eng. Chem. Res.* (2005), 44, 1665-1669.
23. Gulker, F. Method of producing hydrogen. GB275273, 1928.
24. Gulker, F. Improvements in and relating to the preparation of hydrogen and to the absorption of carbon dioxide from gas mixtures. GB301499, 1930.
25. Williams, R. Hydrogen production. US1938202 1933.
26. Gorin, E.; Retallick, W. B. Method for the production of Hydrogen. US3108857, 1963.
27. Barker, R. Reversibility of the reaction $CaCO_3$ reversible reaction CaO plus CO_2. *J. Appl. Chem. Biotech.* (1973), 23, 733-742.
28. Gupta, H.; Fan, L.-S. Carbonation-calcination cycle using high reactivity calcium oxide for carbon dioxide separation from flue gas. *Ind. Eng. Chem. Res.* (2002), 41, 4035-4042.
29. Abanades, J. C.; Alvarez, D. Conversion limits in the reaction of CO_2 with lime. *Energy Fuels* (2003), 17, 308-315.
30. Kuramoto, K.; Fujimoto, S.; Morita, A.; Shibano, S.; Suzuki, Y.; Hatano, H.; Shi-Ying, L.; Harada, M.; Takarada, T. Repetitive carbonation-calcination reactions of Ca-based sorbents for efficient CO_2 sorption at

elevated temperatures and pressures. *Ind. Eng. Chem. Res.* (2003), 42, 975-981.

31. Reddy, E. P.; Smirniotis, P. G. High-temperature sorbents for CO_2 made of alkali metals doped on CaO supports. *J. Phys. Chem. B* (2004), 108, 7794-7800.

32. Alvarez, D.; Abanades, J. C. Pore-size and shape effects on the recarbonation performance of calcium oxide submitted to repeated calcination/recarbonation cycles. *Energy Fuels* (2005), 19, 270-278.

33. Satrio, J. A.; Shanks, B. H.; Wheelock, T. D. Development of a novel combined catalyst and sorbent for hydrocarbon reforming. *Ind. Eng. Chem. Res.* (2005), 44, 3901-3911.

34. Hildenbrand, N.; Readman, J.; Dahl, I. M.; Blom, R. Sorbent enhanced steam reforming (SESR) of methane using dolomite as internal carbon dioxide absorbent: Limitations due to $Ca(OH)_2$ formation. *Appl. Catal., A* (2006), 303, 131-137.

35. Lu, H.; Reddy, E. P.; Smirniotis, P. G. Calcium oxide based sorbents for capture of carbon dioxide at high temperatures. *Ind. Eng. Chem. Res.* (2006), 45, 3944-3949.

36. Harrison, D. P. Sorption-Enhanced Hydrogen Production: A Review. *Ind. Eng. Chem. Res.* (2008), 47, 6486-6501.

37. Lu, H.; Khan, A.; Smirniotis, P. G. Relationship between Structural Properties and CO_2 Capture Performance of CaO-Based Sorbents Obtained from Different Organometallic Precursors. *Ind. Eng. Chem. Res.* (2008), 47, 6216-6220.

38. Nakagawa, K.; Kato, M.; Oohashi, T.; Yoshikawa, S.; Essaki, K. Carbon dioxide gas absorbent. EP10038576, 2000.

39. Kato, M.; Yoshikawa, S.; Essaki, K.; Nakagawa, K. Carbon dioxide gas absorbent and carbon dioxide gas separating apparatus US6712879, 2002.
40. Ida, J.-I.; Lin, Y. S. Mechanism of high-temperature CO_2 sorption on lithium zirconate. *Environ. Sci. Technol.* (2003), 37, 1999-2004.
41. Nakagawa, K.; Kato, M.; Yoshikawa, S.; Essaki, K.; Uemoto, H. A novel CO_2 Absorbents using lithium-containing oxides. In Second annual conference on Carbon Sequestration, Alexandria, VA, (2003).
42. Bretado, M. E.; Guzman Velderrain, V.; Lardizabal Gutierrez, D.; Collins-Martinez, V.; Ortiz, A. L. A new synthesis route to Li_4SiO_4 as CO_2 catalytic/sorbent. *Catal. Today* (2005), 107-108, 863-867.
43. Essaki, K.; Kato, M.; Uemoto, H. Influence of temperature and CO_2 concentration on the CO_2 absorption properties of lithium silicate pellets. *J. Mater. Sci.* (2005), 40, 5017-5019.
44. Kato, M.; Nakagawa, K.; Essaki, K.; Maezawa, Y.; Takeda, S.; Kogo, R.; Hagiwara, Y. Novel CO_2 absorbents using lithium-containing oxide. *Int. J. Appl. Ceram. Technol.* (2005), 2, 467-475.
45. Ochoa-Fernandez, E.; Rusten, H. K.; Jakobsen, H. A.; Ronning, M.; Holmen, A.; Chen, D. Sorption enhanced hydrogen production by steam methane reforming using Li_2ZrO_3 as sorbent: Sorption kinetics and reactor simulation. In International Conference on Gas-Fuel 05, Brugge, November, *Catalysis Today* (2005), 41-46.
46. Essaki, K.; Kato, M.; Nakagawa, K. CO_2 removal at high temperature using packed bed of lithium silicate pellets. *J. Ceram. Soc. Jpn.* (2006), 114, 739-742.
47. Ochoa-Fernandez, E.; Ronning, M.; Grande, T.; Chen, D. Nanocrystalline lithium zirconate with improved kinetics for high-temperature CO_2 capture. *Chem. Mater.* (2006), 18, 1383-1385.

48. Ronning, M.; Ochoa-Fernandez, E.; Grande, T.; Chen, D. Carbon dioxide gas acceptors. WO2006111343 (A2), 2006.
49. Mayorga, S. G.; Hufton, J. R.; Sircar, S.; Gaffney, T. R. Sorption Enhanced Reaction Process for the production of hydrogen. Phase I Final Report, Proceedings of U.S. DOE Hydrogen program Review, Washington DC, 1997.
50. Hufton, J. R.; Mayorga, S.; Sircar, S. Sorption-enhanced reaction process for hydrogen production. *AIChE J.* (1999), 45, 248-256.
51. Ding, Y.; Alpay, E. Equilibria and kinetics of CO_2 adsorption on hydrotalcite adsorbent. *Chem. Eng. Sci.* (2000), 55, 3461-3474.
52. Ding, Y.; Alpay, E. Adsorption-enhanced steam-methane reforming. *Chem. Eng. Sci.* (2000), 55, 3929-3940.
53. Hufton, J. R.; Waldron, W. E.; Weigel, S. J.; Rao, M.; Sircar, S. Sorption Enhanced Reaction (SERP) for the production of hydrogen, Proceedings of U.S. DOE Hydrogen program Review, Washington DC, 2000, 70-81.
54. Nataraj, S.; Carvill, B. T.; Hufton, J. R.; Mayorga, S. G.; Gaffney, T. R.; Brzozowski, J. R. Materials selectively adsorbing CO_2 from CO_2 containing streams. European Patent 1006079 A1, 2000.
55. Ding, Y.; Alpay, E. High temperature recovery of CO_2 from flue gases using hydrotalcite adsorbent. *Trans IChemE, Part B* (2001), 79, 45-51.
56. Sircar, S.; Golden, C. M. A. PSA process for removal of bulk carbon dioxide from a wet high-temperature gas. US6322612 B1, 2001.
57. Waldron, W. E.; Hufton, J. R.; Sircar, S. Production of hydrogen by cyclic sorption enhanced reaction process. *AIChE J.* (2001), 47, 1477-1479.
58. Yong, Z.; Mata, V.; Rodrigues, A. E. Adsorption of carbon dioxide onto hydrotalcite-like compounds (HTlcs) at high temperatures. *Ind. Eng. Chem. Res.* (2001), 40, 204-209.

59. Xiu, G.-h.; Li, P.; Rodrigues, A. E. Sorption-enhanced reaction process with reactive regeneration. *Chem. Eng. Sci.* (2002), 57, 3893-3908.
60. Xiu, G.-h.; Soares, J. L.; Li, P.; Rodrigues, A. E. Simulation of five-step one-bed sorption-enhanced reaction process. *AIChE J.* (2002), 48, 2817-2832.
61. Xiu, G.-h.; Li, P.; Rodrigues, A. E. Adsorption-enhanced steam-methane reforming with intraparticle-diffusion limitations. *Chem. Eng. J.* (2003), 95, 83-93.
62. Xiu, G.-h.; Li, P.; Rodrigues, A. E. New generalized strategy for improving sorption-enhanced reaction process. *Chem. Eng. Sci.* (2003), 58, 3425-3437.
63. Soares, J. L.; Moreira, R. F. P. M.; Jose, H. J.; Grande, C. A.; Rodrigues, A. E. Hydrotalcite materials for carbon dioxide adsorption at high temperatures: Characterization and diffusivity measurements. *Sep. Sci. Technol.* (2004), 39, 1989-2010.
64. Xiu, G.-h.; Li, P.; Rodrigues, A. E. Subsection-controlling strategy for improving sorption-enhanced reaction process. *Chem. Eng. Res. Des.* (2004), 82, 192-202.
65. Reynolds, S. P.; Ebner, A. D.; Ritter, J. A. New Pressure Swing Adsorption Cycles for Carbon Dioxide Sequestration. *Adsorption* (2005), 11, 531-536.
66. Ebner, A. D.; Reynolds, S. P.; Ritter, J. A. Understanding the Adsorption and Desorption Behavior of CO_2 on a K-Promoted Hydrotalcite-like Compound (HTlc) through Nonequilibrium Dynamic Isotherms. *Ind. Eng. Chem. Res.* (2006), 45, 6387-6392.
67. Ficicilar, B.; Dogu, T. Breakthrough analysis for CO_2 removal by activated hydrotalcite and soda ash. *Catal. Today* (2006), 115, 274-278.

68. Ram Reddy, M. K.; Xu, Z. P.; Lu, G. Q.; Diniz da Costa, J. C. Layered Double Hydroxides for CO_2 Capture: Structure Evolution and Regeneration. *Ind. Eng. Chem. Res.* (2006), 45, 7504-7509.
69. Reijers, H. T. J.; Valster-Schiermeier, S. E. A.; Cobden, P. D.; van den Brink, R. W. Hydrotalcite as CO_2 Sorbent for Sorption-Enhanced Steam Reforming of Methane. *Ind. Eng. Chem. Res.* (2006), 45, 2522-2530.
70. Reynolds, S. P.; Ebner, A. D.; Ritter, J. A. Stripping PSA cycles for CO_2 recovery from flue gas at high temperature using a hydrotalcite-like adsorbent. *Ind. Eng. Chem. Res.* (2006), 45, 4278-4294.
71. Reynolds, S. P.; Ebner, A. D.; Ritter, J. A. Carbon dioxide capture from flue gas by pressure swing adsorption at high temperature using a K-promoted HTlc: Effects of mass transfer on the process performance. *Environ. Prog.* (2006), 25, 334-342.
72. Ebner, A. D.; Reynolds, S. P.; Ritter, J. A. Nonequilibrium kinetic model that describes the reversible adsorption and desorption behavior of CO_2 in a K-promoted hydrotalcite-like compound. *Ind. Eng. Chem. Res.* (2007), 46, 1737-1744.
73. Koumpouras, G. C.; Alpay, E.; Stepanek, F. Mathematical modelling of low-temperature hydrogen production with in situ CO_2 capture. *Chem. Eng. Sci.* (2007), 62, 2833-2841.
74. Lee, K. B.; Verdooren, A.; Caram, H. S.; Sircar, S. Chemisorption of carbon dioxide on potassium-carbonate-promoted hydrotalcite. *J. Colloid Interface Sci.* (2007), 308, 30-39.
75. Lee, K. B.; Beaver, M. G.; Caram, H. S.; Sircar, S. Reversible chemisorption of carbon dioxide: Simultaneous production of fuel-cell grade H_2 and compressed CO_2 from synthesis gas. *Adsorption* (2007), 13, 385-397.

76. Lee, K. B.; Beaver, M. G.; Caram, H. S.; Sircar, S. Novel thermal-swing sorption-enhanced reaction process concept for hydrogen production by low-atemperature steam-methane reforming. *Ind. Eng. Chem. Res.* (2007), 46, 5003-5014.
77. Lee, K. B.; Beaver, M. G.; Caram, H. S.; Sircar, S. Production of fuel-cell grade hydrogen by thermal swing sorption enhanced reaction concept. *Int. J. Hydrogen Energy* (2008), 33, 781-790.
78. Koumpouras, G. C.; Alpay, E.; Lapkin, A.; Ding, Y.; Stepanek, F. The effect of adsorbent characteristics on the performance of a continuous sorption-enhanced steam methane reforming process. *Chem. Eng. Sci.* (2007), 62, 5632-5637.
79. Singh, R.; Ram Reddy, M. K.; Wilson, S.; Joshi, K.; Diniz da Costa, J. C.; Webley, P. High temperature materials for CO_2 capture. *Energy Procedia* (2009), 1, 623-630.
80. Yong, Z.; Mata, V. G.; Rodrigues, A. E. Adsorption of carbon dioxide on chemically modified high surface area carbon-based adsorbents at high temperature. *Adsorption* (2001), 7, 41-50.
81. Yong, Z.; Mata, V.; Rodrigues, A. E. Adsorption of carbon dioxide on basic alumina at high temperatures. *J. Chem. Eng. Data* (2000), 45, 1093-1095.
82. Mayorga, S. G.; Gaffney, T. R.; Brzozowski, J. R.; Weigel, S. J. Carbon dioxide adsorbents containing magnesium oxide suitable for use at high temperatures. EP1074297, 2001.
83. Lopez-Ortiz, A.; Rivera, N. G. P.; Rojas, A. R.; Gutierrez, D. L. Novel carbon dioxide solid acceptors using sodium containing oxides. *Sep. Sci. Technol.* (2004), 39, 3559-3572.

84. Lee, K. B.; Beaver, M. G.; Caram, H. S.; Sircar, S. Chemisorption of carbon dioxide on sodium oxide promoted alumina. *AIChE J.* (2007), 53, 2824-2831.
85. Lee, K. B.; Beaver, M. G.; Caram, H. S.; Sircar, S. Performance of Na_2O promoted alumina as CO_2 chemisorbent in sorption-enhanced reaction process for simultaneous production of fuel-cell grade H_2 and compressed CO_2 from synthesis gas. *J. Power Sources* (2008), 176, 312-319.
86. Hutson, N. D.; Speakman, S. A.; Payzant, E. A. Structural effects on the high temperature adsorption of CO_2 on a synthetic hydrotalcite. *Chem. Mater.* (2004), 16, 4135-4143.
87. Das, J.; Das, D.; Parida, K. M. Preparation and characterization of Mg-Al hydrotalcite-like compounds containing cerium. *J. Colloid Interface Sci.* (2006), 301, 569-574.
88. Ruthven, D. M. Principles of Adsorption and Adsorption Processes. first ed, John Wiley and Sons, Inc, USA, 1984.
89. Glueckauf, E. Theory of chromatography. Part 10. - Formulae for diffusion into spheres and their application to chromatography. *Trans. Faraday Soc.* (1955), 51, 1540-1551.
90. Bird, R. B.; Stewart, W. E.; Lightfoot, E. N. Transport Phenomena. Second ed, John Wiley & Sons, Inc, New York, 2002.
91. Soares, J. L. Desenvolvimento de novos adsorventes e processos híbridos em reforma catalítica por vapor de água. PhD thesis, Universidade Federal de Santa Catarina, Florianópolis, 2003.
92. Voyutsky, S. Colloid Chemistry. first ed, MIR Publishers, Moscow, 1978.
93. Atkins, P. W. Physical Chemistry. fourth ed, Oxford University Press, Oxford, 1990.

3. Steam methane reforming

3.1. Introduction

In the production of hydrogen by sorption enhanced reaction processes (SERP) a sorbent as well as a catalyst are required. In the previous chapter, two adequate sorbents (MG30-K, MG30-Cs) were prepared and the sorption equilibrium and kinetics of carbon dioxide were determined.

The present chapter focuses on the catalytic component of SERP. A brief introduction dealing with steam methane reforming (SMR) process and catalysts is provided, since many of the operating principles can provide a rationale for SERP operation. This chapter also includes experimental work on the SMR reaction in two different Ni/Al_2O_3 catalysts: a commercial one and a sample presenting large pores. By performing proper experiments, the kinetic rate constants as well as

diffusional limitations were determined using a well-known reaction rate mechanism.

3.2. Steam methane reforming

Steam reforming is a well known reaction between a carbon source and steam to produce hydrogen, carbon monoxide and carbon dioxide [1, 2]. The most employed feed for steam reforming is methane. There is a large number of possible reactions that can take place in this system, but under the operating conditions studied, the most important ones are [3]:

$CH_4 + H_2O \leftrightarrow CO + 3H_2$	ΔH = 205.8 kJ/mol	SMR	(3.1)
$CO + H_2O \leftrightarrow CO_2 + H_2$	ΔH = -41.2 kJ/mol	Water gas shift	(3.2)
$CH_4 + 2H_2O \leftrightarrow CO_2 + 4H_2$	ΔH = 164.6 kJ/mol	Global SMR	(3.3)

The first reaction, called the steam reforming reaction describes the conversion of methane to carbon monoxide. The second reaction, called the water gas shift reaction, regulates the composition of carbon monoxide and carbon dioxide. This reaction is exothermic and is more active than the SMR reaction at temperatures lower than 723 K. Finally, there is the global SMR reaction. This equation is necessary because (according to the reaction mechanism), CO_2 can also be produced directly from methane. The SMR and Global SMR reactions are highly endothermic as indicated by the heat of reaction.

Steam methane reforming has been applied industrially since 1931, when BASF commissioned a plant in the United States [2]. Over the years, the steam methane reforming process was improved as a result of the high demand of hydrogen for the ammonia and methanol

industries. Figure 3.1 shows a schematic diagram of the steam methane reforming process [1, 2, 4, 5].

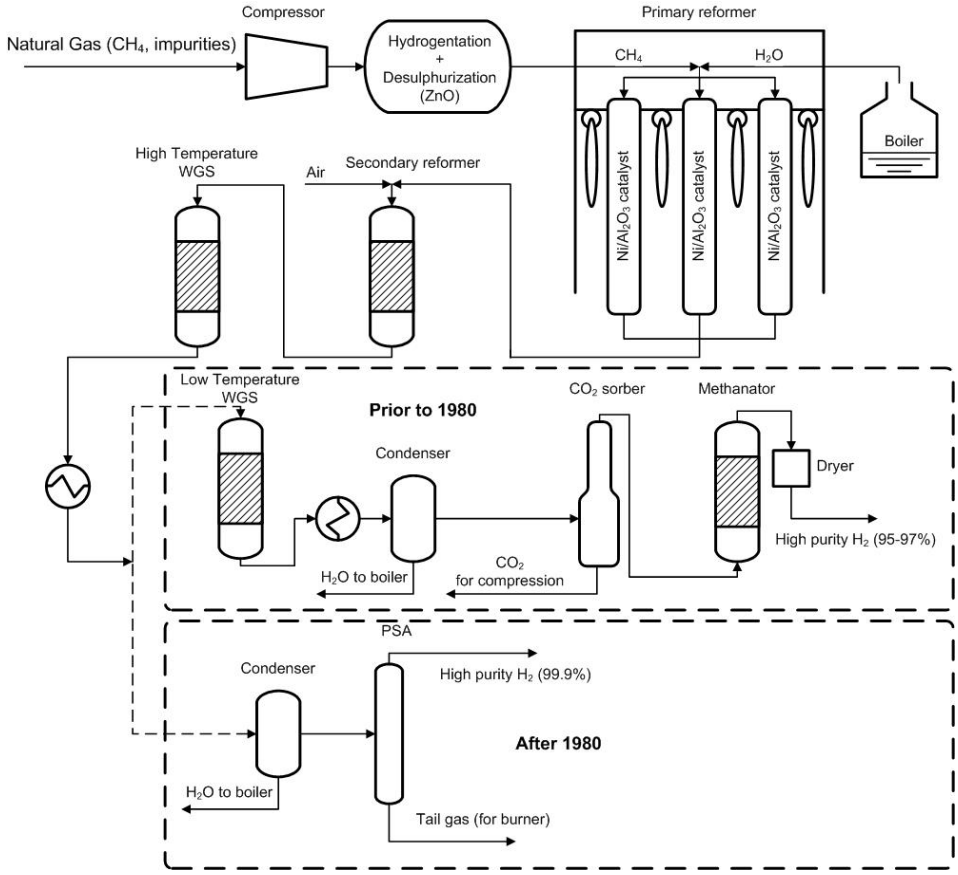

Figure 3.1. Steam methane reforming process for the production of hydrogen [1, 2, 4, 5].

The natural gas from arrives at the plant and undergoes pressurization to the reformer feed pressure. Reformers were initially operated in the pressure range of 10-20 bar [5]. Nowadays, due to the improvement of the materials of the reformer tubes, the primary reformer is operated in the pressure range of 30-40 bar [1, 4]. The compression step is carried out prior to the reactor in order to increase the plant productivity that should be compensated by increase of temperature since there is an increase in the number of moles during

the reforming process. The pressurized gas then undergoes a purification step to remove sulfur compounds to less than 0.1 ppm [4].

The high pressure natural gas is mixed with steam in a steam to carbon ratio (S/C) in the range 2.5-4 [1, 2, 4, 5] to prevent the deposition of carbon in the catalyst. The gas is then pre-heated to 670-770 K and fed to the primary reformer [1].

The primary reformer is where the bulk of the natural gas is converted to hydrogen. The burners inside the furnace can be arranged in different configurations that influence the heat flow in the reformer: at the top, at the bottom or on the sides of the furnace. Figure 3.1 shows a top fired furnace that is usually used to obtain a compact design. Inside the reformer the temperature increases from about 770 K to an exit temperature of about 1060 K [1]. The feed is distributed to several reformer tubes – between 40 and 400 – placed inside the furnace. A high number of tubes is employed to allow a fast heat transfer to the catalyst because the steam reforming reaction is highly endothermic. Each reformer tube has a diameter in the range 70-160 mm, up to 12 m in length and is filled with Ni/Al_2O_3 catalyst. Due to the high temperature, the tubes expand and are subjected to mechanical stress that reduces their lifetime [1]. Increasing the feed pressure also increases the stress and it is the reason why the reforming pressure is limited at 40 bar. The high costs of materials to produce the reformer tubes represents the bulk of the investment costs in the primary reformer [1]. During the operation of the primary reformer it is also necessary to detect the formation of hot-spots as they indicate a decrease in catalyst activity and increase in internal pressure. The effluent gas from the primary reformer usually contains up to 10 % of methane [1, 4].

The effluent from the primary reformer is mixed with air or oxygen before entering the secondary reformer. In this unit, the heat is supplied by the reaction of oxygen with methane. The amount of oxygen is regulated to achieve a temperature of about 1270 K while using up only a minimum amount of methane. After the secondary reformer the amount of methane is reduced to about 0.3 % [1, 4].

The process stream then undergoes a high temperature water gas shift to convert the carbon monoxide to carbon dioxide. The high temperature shift reactor is filled with iron oxide catalyst and operates in the range 650-800 K [1, 4]. As the WGS reaction is exothermic the reactor is sometimes divided into two columns separated by a heat exchanger to maintain the temperature inside the catalyst [4]. The excess heat is used to produce steam, decreasing operating costs.

In older hydrogen production plants the process stream goes through a low temperature water gas shift reactor to further convert the remaining carbon monoxide to carbon dioxide [1, 4]. This reactor is usually operated in the temperature range of 470-540 K using a copper based catalyst. The carbon monoxide content is reduced to about 0.3 % while the carbon dioxide content increases to about 19 % [4]. After the low temperature shift reactor, the temperature of the stream is decreased and the bulk of the water is removed. The condensed water is sent to the boiler to be reused. The gas phase stream undergoes CO_2 absorption using amines or other absorbent such as Selexol [6], Rectisol [7], etc. The remaining CO is converted to methane in the methanator and finally the hydrogen stream goes through a dryer to remove trace amounts of water. This process results in a stream with a hydrogen purity in the range of 95-97 % [4, 5] with methane as the main contaminant.

Since the 1980's, a new carbon dioxide removal process was proposed. In the new process, the low temperature water gas shift was not used. Instead, after the high temperature water gas shift reactor, the temperature of the process stream is reduced and the water is removed in a condenser. The gas stream then goes to a pressure swing adsorption (PSA) unit where high purity (>99.99 %) hydrogen is produced at a pressure slightly lower than the feed pressure of the primary reformer (~ 40 bar) [4]. However, the H_2 recovery of the process ranges between 70-90 % [8]. A second stream, termed as tail gas, is also produced. This stream is composed of CO, CO_2, CH_4 and hydrogen. This stream is used as feed to the primary reformer furnace and comprises about 90 % of the energy requirements of the furnace. The PSA based process allows higher water and energy recovery when compared to the older process. However, when the carbon dioxide can be exported to nearby plants, the low temperature shift/carbon dioxide absorption route is preferred [4], since the purity of CO_2 can be higher than 99 %.

Since the first industrial application, the steam methane reforming process has been improved to produce higher purity hydrogen; the heat integration and reactor operating temperature were also increased. However, the high temperature employed in the primary reformer still represent an important challenge to the operation of the SMR process due to the stress of the materials employed and the high energy costs [1, 2, 4, 5, 9, 10].

3.2.1. Steam reforming catalysts

A variety of carbon sources can be used for steam reforming. Methane is the most employed [1, 2], but naphta-reformers are usually found in refineries to produce H_2 for internal uses. Recently ethanol and methanol have been proposed as feeds for hydrogen production by steam reforming as they can be produced using renewable sources. Important developments in this area are also taking place in the reforming of coal within the CTL (Coal to Liquid) projects. Reforming of glycerol and other undesired by-products of bio-fuels is also proposed as an alternative to reduce wastes and improve economic feasibility of bio-projects.

Depending on the feed used, different catalysts and supports were proposed for steam reforming, as shown in Table 3.1 [3, 11-45].

Table 3.1. Metals and supports used in steam reforming catalysts for different feeds [3, 11-45].

	Metal	**Support**
Methane	Ni, Rh, Mo, Pt, Ce, Zr, Co, Nb	Al_2O_3, ZrO_2, Ce-ZrO_2, Ce- ZrO_2/Al_2O_3, SiO_2
Methanol	Cu, Pd, Cu/Zn/Al, CuO-ZnO, Cu-Cr_2O_3	ZnO/Al_2O_3, Al_2O_3, ZrO_2
Ethanol	Ni, Rh, Rh-Ce, Co, CuO, Cu-Ni-K	MgO, Al_2O_3, SiO_2, ZnO/Al_2O_3

Many different metals are active for steam methane reforming, but the most commonly used industrially is nickel due to its lower cost [1, 2]. The addition of small amounts of MoO_3 to the Ni/Al_2O_3 catalyst was proposed to increase the activity as well as the resistance to steam [18, 43]. Recently, many studies have focused on other supports such as ZrO_2 and Ce-ZrO_2 [28, 31, 35] to increase thermal stability, activity and

resistance to steam [43]. It was proposed that the steam adsorbs faster in the Ce or Ce-ZrO_2 sites than in the Ni crystallites. The adsorbed H_2O molecule then transfers to the Ni site to react with methane. In the work from Roh *et al* [31] it is possible to compare the performance of a few Ni catalysts with different supports. The combination of Ce and ZrO_2 in the support showed the highest methane conversion and CO_2 selectivity ($S_{CO2} = F_{CO2}/F_{CO}$) while maintaining high thermal stability. The catalyst with $MgAl_2O_4$ support presented higher methane conversion than the one with Al_2O_3 support but its methane conversion dropped significantly when the gas hourly space velocity was increased to 288 $dm^3/(g_{cat}.h)$ showing that the $MgAl_2O_4$ is less stable. Table 3.2 shows a brief summary of different catalysts and supports studied for steam methane reforming.

The use of high temperatures was always the biggest challenge to operate a SMR reactor due to the heating costs and investment costs in materials that withstand the high temperatures and pressures of operation [1, 2, 4, 5, 9, 10]. Another problem are hotspots in the reactor (areas where the temperature is higher than normal) caused by carbon deposition in the catalyst (coke). Carbon can build up in the catalyst in two ways: between the support and the Ni site - whisker-like carbon – and covering the surface of the Ni crystallite – encapsulating carbon and pyrolytic carbon.

The whisker carbon raises the Ni crystallite from the surface and can either promote the loss of the Ni crystallite or break-down the extrudate [1]. The encapsulating carbon and pyrolytic carbon cover the Ni site, making it inaccessible to the reagents.The formation of coke leads to lower activity of the catalyst, increasing the local temperature (less endothermic reaction). Increasing the steam to carbon ratio (S/C) solves this issue by promoting the gasification of any deposited carbon

[23] but cannot be used in catalysts that have poor resistance to steam. Alkali-metals can also be used s promoters to reduce coking [1].

Table 3.2. Metals and supports used in steam-reforming catalysts

Catalyst	m [g]	T [K]	P [bar]	S/C	X_{CH4} [%]	S_{CO2}	Ref.
$Ni/MgAl_2O_4$ (15% Ni)	0.4	823	5	5[a]	17	-	[3]
Ni/α-Al_2O (15-17% Ni)	0.3	823	1.2	4[b]	12.5	0.87	[25]
Ni/Ce-ZrO_2 (15% Ni)	0.05	1023	1.01	3	97.0	0.5	[28]
Ni/Ce-ZrO_2 (30 % Ni)	0.05	1023	1.01	3	60.9	3.5	
$Ni/Ce–ZrO_2/\theta$-Al_2O_3 (12 % Ni)	2	823	1.01	2.98	60	3.17	[29]
$Ni/Ce–ZrO_2$ (15 % Ni)	0.05	1023	1.01	3	97	48.7	[31]
Ni/ZrO_2 (15 % Ni)					75	6.3	
Ni/CeO_2 (15 % Ni)					54	4.9	
$Ni/MgAl_2O_4$ (15 % Ni)					79	7.7	
Ni/Al_2O_3 (15 % Ni)					57	4.7	
Pd/Ce (1 % Pd)	0.05	773	1.01	2		13.1	[33]
$Ni/Ce–ZrO_2/\theta$-Al_2O_3 (12 % Ni)	-	973	1.01	3	97	0.78	[35]
Ni/ZrO_2 (20 % Ni)	0.3	773	1.01	2	25.5	6.6	[41]
Ni/SiO_2 (9 % Ni)	0.2	873	1.01	2	75	-	[43]

a – $H_2/CH_4 = 1.25$;

b – $H_2/CH_4 = 1$; $S/C = F_{H2O,,feed} / F_{CH4,feed}$; $S_{CO2} = F_{CO2}/F_{CO}$

One alternative to the development of new catalysts is to use lower operation temperatures. The conversion is lower but the methane

can be separated and recycled. Works in this area [29, 41] show that there is an almost linear increase of the H_2 yield and CH_4 conversion with temperature from 673 to 873 K. At temperatures higher than 873 K the increase in H_2 yield was slower as the water gas shift reaction (see reaction 3.2) is less significant.

Industrial catalysts have many different shapes, but the most employed ones are perforated cylinders with six or more holes or ring shaped particles that are used in order to reduce pressure drop [1]. The large size of the catalyst particles also promotes heat transfer as the effective heat transfer is proportional to the particle diameter. However, the increasing particle size increases mass transfer limitations. Rostrup-Nielsen [1] indicates that the effectiveness factor – ratio between observed and true reaction kinetics – decreases as particle size increases. Therefore an optimal particle size has to be selected.

In a regular catalyst, the reaction takes place in the active metal sites, dispersed in the porous structure. Reagents and products are transported inside the pore network by diffusion but this is a slow mechanism. The diffusional limitations can be overcome by intraparticle convection [46-51] inside the catalyst. In other works, to have significant intraparticle convection the catalyst needs to have large pores (> 500 Å) [51], where pressure gradients can take place. The large-pore catalysts have been extensively studied for catalytic applications such as: depolymerization of paraldehyde [47], plant cultures in biocatalysts [52], methane steam reforming [53], selective oxidation of o-xylene [54] and protein chromatography [55-58].

The Ni/Al_2O_3 catalyst will be used in this work since it is the most commonly used in industrial reformers. The performance of a large-pore catalyst will be compared against a porous commercial catalyst

without large pores to test the influence of the intraparticle convection in the performance of the reforming catalysts.

3.2.2. Steam methane reforming kinetics

The first known study of the kinetics of steam methane reforming was published in the first volume of the AICHE Journal [12]. This paper was focused in the study of the kinetics of natural gas on a reduced nickel catalyst supported on Kieselguhr – chalk-like stone with high porosity composed mainly of silica (86 %) with small amounts (< 5 %) of sodium, magnesium and iron –in the temperature range of 609-911 K. The reaction rate was considered first order to methane and the rate-controlling step was the surface decomposition of methane. The thermodynamic calculations indicated that the WGS reaction was very slow. This result was in contradiction with a previous paper [11] dealing with calculation of steam reforming thermodynamic equilibrium that stated that the WGS was very fast.

In 1964, Bodrov *et al* [45, 59] determined the steam methane reforming kinetics in a nickel foil using a flow reactor with recycle in the temperature range 1073-1173 K. The following expression was proposed to describe the steam methane reforming reaction rate (R_{SMR}):

$$R_{SMR} = \frac{k_{SMR} P_{CH_4}}{1 + a\frac{P_{H_2O}}{P_{H_2}} + bP_{CO}} \qquad (3.4)$$

where "a" and "b" are temperature dependent constants. Allen *et al* [13] also carried out SMR experiments at 911 K, S/C = 3 and different pressures in the range of 1-18.2 bar using a commercial nickel catalyst

and concluded that the rate controlling step was the desorption of the products.

De Denken *et al* [59, 60] determined the kinetics of a Ni/Al_2O_3 catalyst (12 % Ni) in the temperature range of 823-953 K, S/C in the range of 3-5 and pressure range of 5-15 bar. Hydrogen was added to the feed stream between 1 and 3.25 times the methane content. The kinetic model was composed of two expressions that accounted for the formation of CO and CO_2.

In 1989, Xu and Froment [3, 61] proposed a kinetic model, using a nickel catalyst supported on $MgAl_2O_4$. This kinetic reaction model is the most widely employed in literature for the simulation of steam methane reforming. Reactions 3.1-3.3 were proposed to describe the steam methane reforming kinetics. The following expressions were developed using the Langmuir-Hinshelwood methodology:

$$R_{SMR} = \frac{k_{SMR}}{P_{H_2}^{2.5}} \frac{\left(P_{CH_4} P_{H_2O} - \frac{P_{H_2}^3 P_{CO}}{K_{SMR}} \right)}{DEN^2} \tag{3.5}$$

$$R_{WGS} = \frac{k_{WGS}}{P_{H_2}} \frac{\left(P_{CO} P_{H_2O} - \frac{P_{H_2} P_{CO_2}}{K_{WGS}} \right)}{DEN^2} \tag{3.6}$$

$$R_{Global\ SMR} = \frac{k_{Global\ SMR}}{P_{H_2}^{3.5}} \frac{\left(P_{CH_4} P_{H_2O}^2 - \frac{P_{H_2}^4 P_{CO_2}}{K_{Global\ SMR}} \right)}{DEN^2} \tag{3.7}$$

$$DEN = 1 + K_{CO} P_{CO} + K_{H_2} P_{H_2} + K_{CH_4} P_{CH_4} + \frac{K_{H_2O} P_{H_2O}}{P_{H_2}} \tag{3.8}$$

where carbon dioxide was considered non-adsorbing in the catalyst. Hou and Hughes [25] later developed a similar model to fit the kinetics

of a Ni/α-Al_2O catalyst but required six more parameters as the exponents of the partial pressures were also fitted.

The kinetic constants reported by Xu and Froment [3] can be calculated using the following equations:

$$k_{SMR}\left[\frac{mol.bar^{0.5}}{kg_{cat}.s}\right]=1.16x10^{15}e^{\left(-\frac{240100}{RT}\right)} \quad (3.9)$$

$$k_{WGS}\left[\frac{mol}{kg_{cat}.bar.s}\right]=5.41x10^{5}e^{\left(-\frac{67130}{RT}\right)} \quad (3.10)$$

$$k_{Global\ SMR}\left[\frac{mol}{kg_{cat}.bar.s}\right]=2.79x10^{14}e^{\left(-\frac{243900}{RT}\right)} \quad (3.11)$$

The steam methane reforming kinetics of Bodrov *et al* [45, 59], De Denken *et al* [59, 60] and Xu and Froment [3] were compared by Elnashaie and coworkers [59]. One of the most important conclusions was that the dependence of the different kinetic reaction models on steam partial pressure was different: negative in the work of Bodrov *et al* [45, 59], positive in the work of de Denken *et al* [59, 60] and positive and negative in the work of Xu and Froment [3]. Elnashaie *et al* [59] showed that the steam methane reforming reaction rate goes through a maximum when the steam partial pressure increases. The maximum in the reaction rate shifts to lower steam partial pressures when the temperature increases and to higher steam partial pressures when the total pressure or H_2/CH_4 increase. Finally, it was found that the range of steam partial pressures used by the different works was not the same and that the work of Xu and Froment [3] covered both the range studied by Bodrov *et al* [45, 59] and by de Denken *et al* [59, 60].

Recently in 2007, El-Bousiffi and Gunn [62] performed 600 h of steam methane reforming experiments to determine a reaction rate

kinetic model. The experiments were made in the temperature range of 873-1113 K and pressure range of 3.5-10 bar using a catalyst containing 15 % NiO, 15 % CaO and 70 % Al_2O_3. It was reported that there was an improvement in the reaction rate at lower temperatures (973 K) after the catalyst was used at higher temperatures (1073 K) due to the higher catalyst reduction at higher temperature. Results show the catalyst reduction is incomplete below 1073 K.

Elnashaie *et al* [59] have also shown that the kinetic model proposed by Xu and Froment [3] this kinetic model is more general than the SMR kinetics proposed by other authors. Therefore, in this chapter, the rate equations proposed by Xu and Froment [3] will be used to describe reaction rates of steam reforming of the two Ni/Al_2O_3 catalysts. However, the kinetic parameters will be determined for each catalyst.

3.3. Experimental

3.3.1. Characterization of the catalyst samples

The catalyst extrudates were analyzed by Scanning Electron Microscopy (SEM) in a JEOL JSM-6301F (JEOL, Japan). The particle and solid densities and pore size distribution of the sample were measured using a Quantachrome PoreMaster 60 (Quantachrome, UK) and in a He picnometer, respectively. X-Ray diffraction was performed to determine the qualitative composition of catalyst. The quantitative composition of both catalyst samples was determined by inductively coupled plasma atomic emission spectroscopy (ICP-AES) in an ICP-AES model 70 Plus (Jobin Yvon, Germany).

3.3.2. Experimental unit for SMR

The equipment used to determine the carbon dioxide sorption equilibrium and kinetics in the hydrotalcite sorbents was modified to perform the steam methane reforming experiments. The modified equipment is reported in Figure 3.2. The main modifications were the use of a gas chromatograph (GC) to measure the composition of the gas stream leaving the reactor and the use of two different stainless steel reactor columns (both with R_{col} = 0.0133 m): one with a maximum length of 0.05 m employed to measure the true SMR kinetics using catalyst in powder form and one with a maximum length of 0.160 m employed to measure the observed SMR kinetics using catalyst extrudates. The smaller column has a thermocouple inserted in the center of the radial axis, in contact with the catalyst powder. The longer reactor column has two thermocouples inserted in two different axial positions.

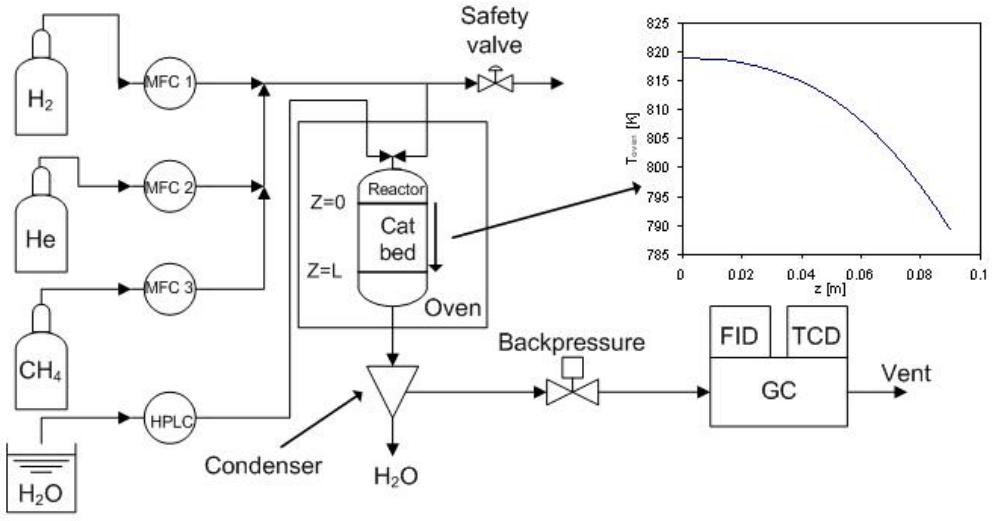

Figure 3.2. Experimental set-up employed for the experiments with SMR catalysts.

The feed flowrates of the different gases (H_2, CH_4 and He) were controlled by mass flow controllers. Helium was used during heating/cooling and when no experiments were taking place. A high performance liquid chromatography (HPLC) pump was used to control the flow of water that was vaporized and heated inside the oven where the reactor was placed. The different feed streams were mixed just before entering the reactor. After the reactor, an ice-cooled condenser was used to remove the water from the effluent stream. A backpressure was employed to regulate the pressure inside the reactor.

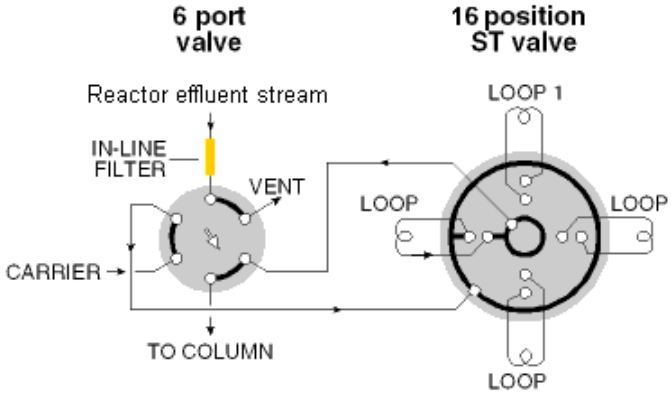

Figure 3.3. Diagram of the 2 valve system used for sample storage

The gas chromatograph (Dani, Italy) employed was equipped with a Carboxen-1010 PLOT (Supelco, USA) capillary column. The separation column has and external diameter of $5.3x10^{-4}$ m and a length of 30 m. Helium was used as carrier gas. The composition of the dry basis effluent was analyzed in a thermal conductivity detector (H_2, CO, CO_2) and in a flame ionization detector (CH_4) connected in series (TCD before FID). Two valves (Vici, Switzerland) were placed inside the GC oven to allow gas storage for analysis or gas venting to exhaust. The scheme of the valves can be seen in Figure 3.3. The first valve is a 6 port valve that receives the stream from the reactor and can send it either to the 16

positions valve or to the vent. The 16 position valve is used to store samples of the effluent stream at different times.

3.3.3. Steam methane reforming experiments

Two catalysts where Ni is the active metal were tested in this work: the "Octolyst 1001" from Degussa (Germany) – named here Degussa – and a large pore catalyst – named here catalyst A. The experimental conditions of the experiments with powder catalyst are reported in Table 3.3.

Table 3.3. Operating conditions used in the steam methane reforming experiments using catalyst powder.

Sample	Degussa			Catalyst A		
m_{cat} [kg] x 10^3	6.212×10^{-2}			8.043×10^{-2}		
T_{cat} [K]	720, 743, 765, 839			757, 780, 804		
P_T [bar]	2					
L_c [m]	0.5×10^{-3}					
R_c [m]	0.0133					
$y_{feed, CH4}$	0.157					
$y_{feed, H2O}$	0.646					
$y_{feed, H2}$	0.197					
S/C (H_2O/CH_4)	4.1					
$F_{H2,feed}$	$1.25 \times F_{CH4,feed}$					
F_{feed} [mol/min] x 10^3	12.9	17.9	25.4	30.4	35.4	40.4
Q_{feed} [SLPM][a]	0.293	0.406	0.577	0.690	0.803	0.917

a – Standard conditions are: 273 K and 1 bar.

The typical procedure to evaluate kinetic rate constants of a given mechanism is to measure the true reaction rate. This means that no diffusion effects are expected. Using catalyst particles will result in unavoidable diffusion-limited process and for this reason is common practice to reduce the catalyst particle diameter, for example by

grinding the catalyst [63]. In this work the catalyst was grinded to particle sizes smaller than 150 μm. The SMR experiments were done by inserting the catalyst powder, between two thick layers of quartz wool. The catalyst was distributed in all the diameter of the column (0.0266 m) having a total bed length of $5x10^{-4}$ m. A thermocouple was inserted within the catalyst bed to register the variations of temperature.

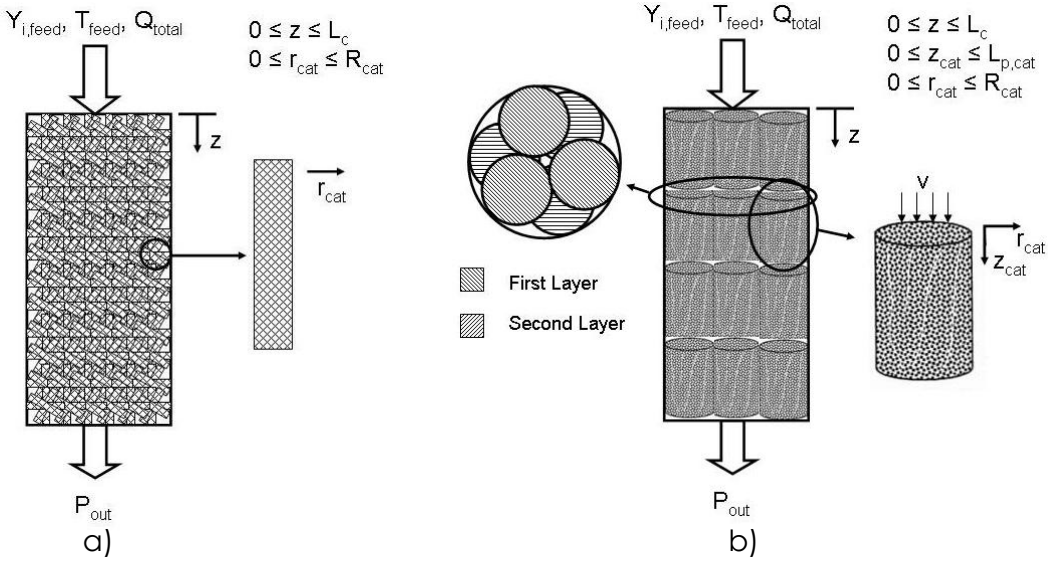

Figure 3.4. Reactor configurations used in the steam methane reforming experiments with extrudates: a) Reactor using the Degussa extrudates; b) Reactor using the large pore extrudates (Catalyst A).

After determination of true kinetic rate constants, experiments were made using the catalyst particles to correlate the true reaction rate with diffusional/thermal limitations (observed rate). Prior to the catalyst bed, an initial layer of quartz particles (~ 0.04 m) was used to accommodate flow variations of a small feed tube diameter into a much larger column. In the case of catalyst A, the extrudates (diameter ~ 11.2 mm) were placed in four different layers as shown in Figure 3.4b. Each layer of catalyst was composed by three extrudates rotated relatively to the previous layer to reduce gas by-passing. The

experimental conditions used in the experiments with catalyst extrudates are reported in Table 3.4. A schematic drawing of the different catalyst beds is presented in Figure 3.4.

A detailed and reproducible protocol for conditioning the catalyst should be performed to avoid irreversible deactivation of the catalyst. Nickel has to be reduced to be active for the SMR reaction [1, 2]. This reduction was performed all days during the experimental campaign, both for the powder and for the extrudate samples. The reduction or activation protocol was performed for one hour using a stream with 5 % hydrogen balanced with helium. After the activation, the reducing stream was switched to a mixture of hydrogen and steam balanced with helium to complete the total flowrate used. This step took 150 seconds, being long enough to accommodate temperature variations due to water adsorption but fast to reduce nickel sintering risks. After that period, the helium stream was switched to methane and the SMR reaction started. Hydrogen was added to the inlet stream prevent reoxidation of the catalyst by steam [3, 44].

Table 3.4. Operating conditions used in the steam methane reforming experiments using catalyst extrudates.

Sample	**Degussa**			**Catalyst A**		
m_{cat} [kg] x 10^3	33.233			30.4854		
T_{oven} [K]	747, 762, 806, 813 (± 3)			704 ± 4	753 ± 3	800 ± 3
P_{out} [bar]	2			2		
L_c [m]	0.0818			0.0620		
R_c [m]	0.0133			0.0133		
S/C	4.25			4.25		
Q_{feed} [SLPM][a]	0.562	0.666	1.194	0.284	0.658	1.090
F_{feed} [mol/min]x10^3	24.8	29.3	52.6	12.5	29.0	48.1
$y_{feed, CH4}$	0.154		0.160	0.154		
$y_{feed, H2O}$	0.654		0.681	0.654		
$y_{feed, H2}$	0.192		0.160	0.192		

a – Standard conditions are: 273 K and 1 bar.

An initial SMR experiment was always performed using the activation conditions, either using the powder or the extrudates and the results were taken as "reference conditions" (experiments with powder catalysts: 765 K (Degussa) or 804 K (catalyst A) catalyst bed temperature, 2 bar total pressure and 25.4 mmol/min total feed molar flowrate; Experiments with extrudates: 803 K feed temperature, 2 bar total pressure, 29.0 mmol/min total feed molar flowrate) to determine that no deactivation took place. These initial experiments with a new catalyst sample were performed during more than 7 hours. When no catalyst deactivation was detected, the different experiments reported here were performed at different temperatures and/or feed flows. The heating / cooling rate to switch from one temperature to other was always 1 K/min. Experiments using the "reference conditions" were repeated each day before each experimental run to ensure that there was no decrease in the catalyst activity. Within all days of the experimental campaign for a given catalyst, the system was kept overnight under He flow.

All the experiments were performed in a vertical oven with a single-point controller. The oven has a semi-parabolic temperature profile, with higher temperatures in the top of the oven. This profile was measured as a function of the axial position of the catalyst bed to describe $T_{\infty}(z)$ in the simulations performed (see Figure 3.2).

3.4. Theoretical

In this thesis, the steam methane reforming was described by a set of three reactions (SMR, WGS and Global SMR, equations 3.1-3.3),

proposed by Xu and Froment [3] with the corresponding kinetic expressions presented in equations 3.5-3.8.

The reaction rate coefficients (k_j) and the adsorption constants of the gases (K_i) have an Arrhenius type dependence with temperature:

$$k_j = k_{0j} \times e^{\frac{-E_j}{R_g T}} \quad j = SMR, WGS, Global\ SMR \tag{3.12}$$

$$K_i = K_{0i} \times e^{\frac{-\Delta H_i}{R_g T}} \quad i = CO, H_2, CH_4, H_2O \tag{3.13}$$

The values of the adsorption constants (K_{0i} and ΔH_i) were taken from the work of Xu and Froment [3]. The equilibrium constants of the reactions (K_{SMR}, K_{WGS}, $K_{GlobalSMR}$) were calculated using the standard Gibbs free energy of each reaction at the corresponding temperature. Figure 3.5 shows the temperature profile of all equilibrium constants.

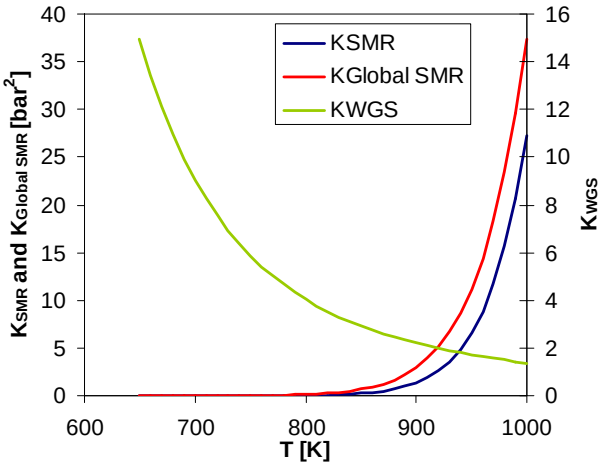

Figure 3.5. Equilibrium constants of the SMR, WGS and Global SMR reactions as a function of the temperature, calculated using the Gibbs free energy of reaction.

3.4.1. Mathematical model of experiments using catalyst powder

The mathematical model employed to fit the steam methane reforming kinetic rate constants assumed that the reactor was a fixed bed with negligible axial dispersion. The steam reforming reactions are highly endothermic as can be observed by the values of heats of reaction shown in equations 3.1 and 3.3 and thus, the catalyst bed temperature decreases after the reaction starts. However, after certain time when steady state is reached, the temperature remains constant. As the kinetic parameters were determined using the steady state concentrations, it was assumed constant temperature. Ideal gas behavior was also assumed. The mass balance for each component is expressed by:

$$\frac{\partial F_i}{\partial m_{cat}} = r_i \quad i = CO, H_2, CH_4, H_2O \tag{3.14}$$

The plug flow reactor model was chosen instead of the differential reactor model since the simulations of the steam reforming of methane using the parameters proposed by Xu and Froment [3] showed that, for the experimental flowrates and temperatures used, the mass of the catalyst had to be at least 500 times smaller to behave as a continuous stirred-tank reactor.

The reaction rates of each component (r_i) were calculated using the expressions:

$$r_{CH_4} = -R_{SMR} - R_{Global\ SMR} \tag{3.15}$$

$$r_{H_2O} = -R_{SMR} - 2R_{Global\ SMR} - R_{WGS} \tag{3.16}$$

$$r_{H_2} = R_{WGS} + 3R_{SMR} + 4R_{Global\ SMR} \tag{3.17}$$

$$r_{CO} = R_{SMR} - R_{WGS} \quad (3.18)$$

$$r_{CO_2} = R_{WGS} + R_{Global\ SMR} \quad (3.19)$$

The following boundary condition was considered in the integration of the differential equations:

$$F_i(0) = F_{i,feed} \quad i = CO, H_2, CH_4, H_2O \quad (3.20)$$

The centered finite difference method with second order approximation using 100 elements was used for the discretisation of the differential equations. The energies of activation and pre-exponential factors of the rate coefficients of the reactions were predicted by a sequential quadratic programming algorithm (Newton method for unconstrained optimization that uses the first order derivative to determine its search direction) using gPROMS (Process System Enterprise, UK) software.

3.4.2. Mathematical model of experiments using catalyst extrudates

To model the steam methane reforming experiments with catalyst extrudates, the following assumptions were made:

1. Axially dispersed plug flow;
2. Ideal gas behavior;
3. There are no mass or heat variations within the radial direction of the column;
4. There are film mass and heat transfer resistances in the external layer of the extrudates;

5. The mass transfer in the radial direction of the catalyst particles is described by pore diffusion;
6. The reaction takes place in the Ni crystallites present in the catalyst solid phase, where the reagents should be adsorbed;
7. Constant porosity within the reactor.

In the case of the extrudates of catalyst A, there is a large pore network that increases the mass transfer. Therefore, in the case of catalyst A the additional assumption is:

8. The mass transfer in the axial direction of the catalyst particles is described by pore diffusion and also by convection within the catalyst.

The extrudates of Degussa catalyst were assumed as semi-infinite cylinders as the length (5 mm) was much larger than the diameter (1.6 mm).

This model was solved using different coordinate domains for the reactor and particle extrudates (see Figure 3.4).

The general mass balance for component "*i*" in the fixed bed reactor is:

$$\varepsilon_c \frac{\partial C_i}{\partial t} = -\frac{\partial (u C_i)}{\partial z} + \varepsilon_c \frac{\partial}{\partial z}\left(D_{ax} C_T \frac{\partial y_i}{\partial z} \right) - (1-\varepsilon_c) a_{p,cat} k_{f,cat} \left(C_i - C_{cat,i}\big|_{r_{cat}=R_{cat}} \right) \quad (3.21)$$

The energy transfer was simulated with a heterogeneous model with independent equations for the gas and solid phases and reactor wall where energy is exchanged with the surroundings. The energy balance of the gas phase is given by:

$$\varepsilon_c C_T \hat{C}_{vg} \frac{\partial T}{\partial t} = \varepsilon_c \frac{\partial}{\partial z}\left(\lambda_{ax} \frac{\partial T}{\partial z} \right) - u C_T \hat{C}_{pg} \frac{\partial T}{\partial z} + \varepsilon_c R_g T \frac{\partial C_T}{\partial t} - (1-\varepsilon_c) a_{p,cat} h_{f,cat} \left(T - T_{cat}\big|_{r_{cat}=R_{cat}} \right) - 2\frac{h_w}{R_c}(T - T_w) \quad (3.22)$$

The mass balance for component "*i*" within the catalyst extrudate, considering diffusion, convection and reaction is represented by [48]:

$$\varepsilon_{p,cat}\frac{\partial C_{cat,i}}{\partial t}=\varepsilon_{p,cat}D_{p,cat}\left(\frac{\partial^2 C_{cat,i}}{\partial r_{cat}^2}+\frac{1}{R_{cat}}\frac{\partial C_{cat,i}}{\partial r_{cat}}+\frac{\partial^2 C_{cat,i}}{\partial z_{cat}^2}\right)- v_{cat}\frac{\partial C_{cat,i}}{\partial z_{cat}}+\rho_{cat}\sum_{j=1}^{3}\upsilon_{j,i}R_j \quad (3.23)$$

where the sub-index "*j*" represents the reforming reaction rate given by equations 3.5-3.7. The transport by convection and by diffusion in the axial direction was considered zero for the Degussa catalyst.

An energy balance to the catalyst extrudate is:

$$\left(\varepsilon_{p,cat}\hat{C}_{vg}\sum C_{cat,i}+\left(1-\varepsilon_{p,cat}\right)\rho_{cat}\hat{C}_{ps,cat}\right)\frac{\partial T_{cat}}{\partial t}=-v_{cat}\hat{C}_{pg}\sum C_{cat,i}\frac{\partial T_{cat}}{\partial z_{cat}}+ \lambda_{cat}\left(\frac{\partial^2 T_{cat}}{\partial r_{cat}^2}+\frac{1}{R_{cat}}\frac{\partial T_{cat}}{\partial r_{cat}}+\frac{\partial^2 T_{cat}}{\partial z_{cat}^2}\right)+\rho_{cat}\sum_{j=1}^{3}\upsilon_{j,i}R_j\left(-\Delta H_j\right) \quad (3.24)$$

Note that in this equation, the first term on the right-hand side was also included to account for energy transfer by convection in the large pores of the catalyst A extrudates.

The energy exchange with the surroundings is described by:

$$\rho_w\hat{C}_{pw}\frac{\partial T_w}{\partial t}=\frac{2R_c}{\left(w_{thick}\left(2R_c+w_{thick}\right)\right)}h_w\left(T-T_w\right)- -\frac{1}{\left(\left(2R_c+w_{thick}\right)\ln\left(\frac{2R_c+w_{thick}}{2R_c}\right)\right)}U\left(T_w-T_\infty\right) \quad (3.25)$$

The Ergun equation [64] was used to describe the pressure drop inside the reactor.

$$-\frac{\partial P_T}{\partial z}=150\frac{\mu_{gas}\left(1-\varepsilon_c\right)^2}{4R_{cat}^2\varepsilon_c^3}u+1.75\frac{\rho_{gas}\left(1-\varepsilon_c\right)}{2R_{cat}\varepsilon_c^3}|u|u \quad (3.26)$$

In the large pores inside the catalyst particles the gas flow was considered laminar and therefore the Darcy equation was used to describe the pressure drop [65].

$$-\frac{\partial p_{T,cat}}{\partial z_{cat}} = \frac{\mu_{gas}}{B_{p,cat}} v_{cat} \tag{3.27}$$

where the particle permeability ($B_{p,cat}$) is defined by:

$$B_{p,cat} = \frac{d^2_{microsphere,cat}\,\varepsilon^3_{p,cat}}{150\left(1-\varepsilon_{p,cat}\right)^2} \tag{3.28}$$

The following equation was used to simplify the calculation of the intraparticle velocity [53, 66, 67]:

$$\frac{\Delta P_T}{L_c} = \frac{\Delta p_{T,cat}}{L_{p,cat}} \tag{3.29}$$

This equation means that the pressure drop inside each catalyst particle should be the same as the pressure drop in the reactor. This simplification saves computational time as the intraparticle velocity is obtained as a function of the superficial velocity.

$$v_{cat} = \frac{\left(1-\varepsilon_c\right)^2 \varepsilon^3_{p,cat} d^2_{microsphere,cat}}{\left(1-\varepsilon_{p,cat}\right)^2 \varepsilon^3_c \left(2R_{cat}\right)^2} u + \frac{1.75\left(1-\varepsilon_c\right)\rho_{gas}\varepsilon^3_{p,cat} d^2_{microsphere,cat}}{150\left(1-\varepsilon_{p,cat}\right)^2 \mu_{gas}\varepsilon^3_c \left(2R_{cat}\right)} |u| u \tag{3.30}$$

3.4.2.1. Boundary conditions

The problem presented here is composed by a set of partial differential equations that require boundary conditions to be solved. The boundary conditions used for the fixed bed balances are:

$$\varepsilon_c D_{ax} \left.\frac{\partial C_i}{\partial z}\right|_{z=0} = -u_{feed}\left(\frac{y_{i,feed}P_T}{R_g T}\bigg|_{z=0} - C_i\big|_{z=0}\right) \tag{3.31}$$

$$\left.\frac{\partial C_i}{\partial z}\right|_{z=L_C} = 0.0 \tag{3.32}$$

$$\lambda_{ax}\left.\frac{\partial T}{\partial z}\right|_{z=0} = -u_{feed}C_T\hat{C}_{pg}\left(T_{feed} - T|_{z=0}\right) \tag{3.33}$$

$$\left.\frac{\partial T}{\partial z}\right|_{z=L_C} = 0.0 \tag{3.34}$$

$$u_{feed} = \frac{Q_{total}}{A_{col}} \tag{3.35}$$

$$P_T|_{z=L_c} = P_{out} \tag{3.36}$$

To solve the mass and energy balances in the radial coordinate of the catalyst extrudates, the boundary conditions are:

$$\left.\frac{\partial C_{cat,i}}{\partial r_{cat}}\right|_{r_{cat}=0} = 0.0 \tag{3.37}$$

$$\varepsilon_{P,cat}D_{p,cat}\left.\frac{\partial C_{cat,i}}{\partial r_{cat}}\right|_{r=R_{cat}} = k_{f,cat}\left(C_i - C_{cat,i}|_{r_{cat}=R_{cat}}\right) \tag{3.38}$$

$$\left.\frac{\partial T_{cat}}{\partial r_{cat}}\right|_{r_{cat}=0} = 0.0 \tag{3.39}$$

$$\lambda_{cat}\left.\frac{\partial T_{cat}}{\partial r_{cat}}\right|_{r_{cat}=R_{cat}} = h_{f,cat}\left(T - T_{cat}|_{r_{cat}=R_{cat}}\right) \tag{3.40}$$

In the case of the large pore extrudates, four more boundary conditions are required for the top and bottom of the extrudates.

$$-\varepsilon_{P,cat}D_{p,cat}\left.\frac{\partial C_{cat,i}}{\partial z_{cat}}\right|_{z_{cat}=0} + v_{cat}C_{cat,i}|_{z_{cat}=0} = k_{f,cat}\left(C_i - C_{cat,i}|_{z_{cat}=0}\right) \tag{3.41}$$

$$-\varepsilon_{P,cat}D_{p,cat}\left.\frac{\partial C_{cat,i}}{\partial z_{cat}}\right|_{z_{,cat}=L_{cat}} + v_{cat}C_{cat,i}|_{z_{cat}=L_{cat}} = k_{f,cat}\left(C_i - C_{cat,i}|_{z_{cat}=L_{cat}}\right) \tag{3.42}$$

$$-\lambda_{cat}\left.\frac{\partial T_{cat}}{\partial z_{cat}}\right|_{z_p=0}+v_{cat}\hat{C}_{pg}\sum C_{cat,i}\,T_{cat}\big|_{z_{cat}=0}=h_{f,cat}\left(T-T_{cat}\big|_{z_{cat}=0}\right) \tag{3.43}$$

$$-\lambda_{cat}\left.\frac{\partial T_{cat}}{\partial z_{cat}}\right|_{z_{cat}=L_{cat}}+v_{cat}\hat{C}_{pg}\sum C_{cat,i}\,T_{cat}\big|_{z_{cat}=L_{cat}}=h_{f,cat}\left(T-T_{cat}\big|_{z_{cat}=L_{cat}}\right) \tag{3.44}$$

The performance of the catalyst was calculated using the methane conversion (X_{CH4}), hydrogen yield (Y_{H2}), carbon dioxide selectivity (S_{CO2}). These variables were calculated by:

$$X_{CH4}=\frac{F_{CH4,feed}-F_{CH4}}{F_{CH4,feed}}\times 100 \tag{3.45}$$

$$Y_{H2}=\frac{F_{H2}-F_{H2,feed}}{m_{cat}\left(F_{CH4,feed}-F_{CH4}\right)} \tag{3.46}$$

$$S_{CO2}=\frac{F_{CO2}}{F_{CO}} \tag{3.47}$$

The particle effectiveness factor of each reaction (η_j) correlates the observed reaction rate to the reaction rate that would be obtained if the concentration inside the catalyst particle was the same as the one observed at the surface of the extrudate. Therefore, the effectiveness factor is a measure of the mass transfer limitations inside the catalyst particle.

$$\eta_j=\frac{2\int_0^{L_{cat}}\int_0^{R_{cat}} r_{cat}R_j(r)\,dr_{cat}\,dz_{cat}}{R_{cat}^2\int_0^{L_{cat}}R_{j,r_{cat}=R_{cat}}\,dz_{cat}} \tag{3.48}$$

The centered finite difference method with second order approximation was used for the discretisation of the differential equations using 100 elements for the axial coordinate of the reactor

and 20 elements for the radial coordinate of the extrudates. In the case of catalyst A, 25 elements were used for the axial coordinate of the extrudate. The software package gPROMS was used to solve this model.

3.5. Results and discussion

In this section, the kinetic rate constants and diffusional limitations of two different catalysts are presented. The two different catalyst extrudates employed have very different size. Additionally, Octolyst 1001 catalyst is a porous particle while catalyst A has large pores in its structure that can be seen in naked eye, as shown in Figure 3.6b.

a) b)

Figure 3.6. Nickel-based catalyst extrudates used in this work: a) commercial Octolyst 1001 from Degussa; b) Catalyst A with large-pore structure.

3.5.1. Commercial catalyst Octolyst 1001 (Degussa)

3.5.1.1. Characterization of the catalyst

The catalyst extrudates, purchased from Degussa, have a diameter of 1.6 mm and a length of approximately 5 mm. Scanning

electron microscopy was performed on the catalyst pellets and can be seen in Figure 3.7.

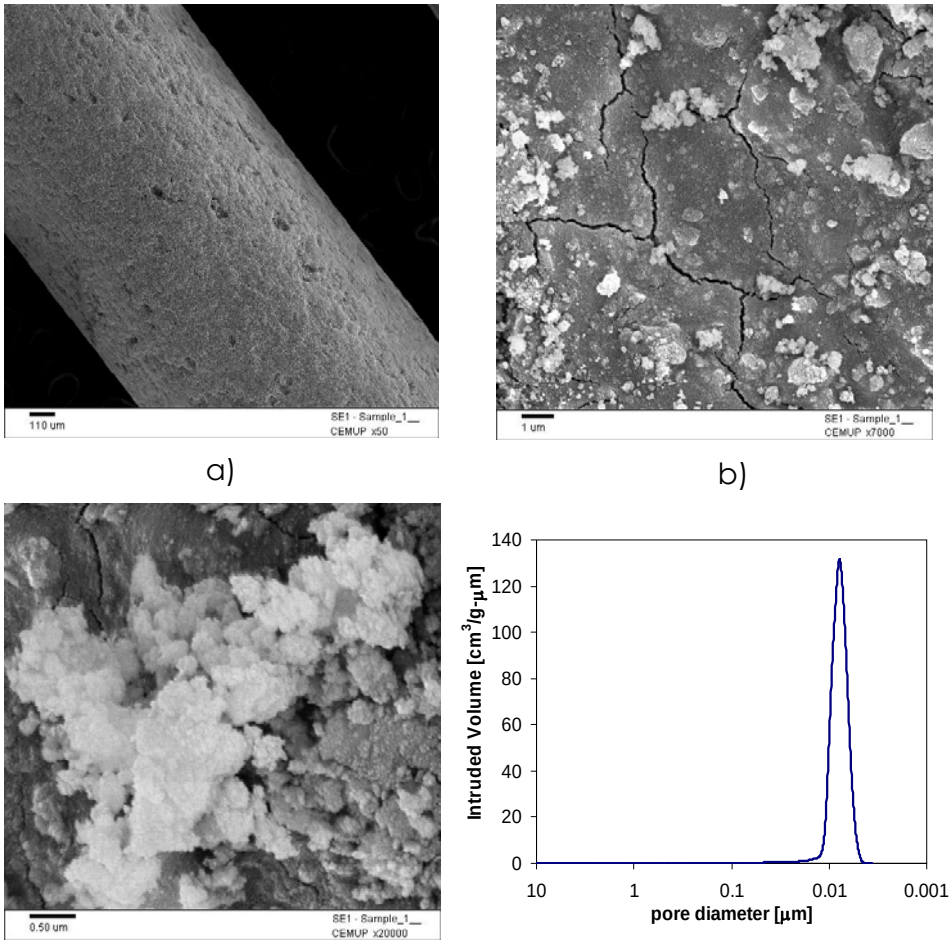

Figure 3.7. Characterization of the Degussa catalyst extrudate. SEM at different magnifications: a) x50; b) x7000; c) x20000. d) Mercury porosimetry.

The catalyst composition was determined by inductively coupled plasma atomic emission spectroscopy. The catalyst is composed of Ni (15.4 %) and Al_2O_3 (84.6 %). Scanning electron microscopy showed that the catalyst support (Al_2O_3) is covered with Ni clusters with sizes ranging from 170 to 3720 nm. The catalyst also shows a narrow pore distribution with average diameter of 8.5 nm (see Figure 3.7d). The particle density

of the catalyst is 1274 kg/m^3 and the solid density is 3630 kg/m^3. A porosity of 64.9 % was calculated based on the values of the particle and solid densities.

It should be pointed out that this catalyst is quite different from the commercial large holes catalysts used in SMR processes actually. The commercial catalyst is much larger (diameter of 16 mm), normally ring-shaped with holes of 3.5 mm diameter [1]. The extrudates of this catalyst are much smaller and comparable with the size of sorbent extrudates resulting in a better particle distribution in small units of SMR-SERP for hydrogen production. The main disadvantage is that smaller particles result in a higher pressure drop across the reactor.

3.5.1.2. Steam methane reforming kinetics in catalyst powder

To determine the reaction rate constants for the true steam methane reforming model, the Degussa catalyst was grinded to a fine powder. It was previously reported that there is an initial deactivation of the catalyst probably due to some sintering of the Ni crystallites [3, 25]. To detect this deactivation and to avoid its interference in further experiments, an initial experiment was performed. This experiment lasted 31 h at 743 K, 2 bar and 0.577 SLPM total flowrate. An initial decrease in conversion (2 %) was detected after the first 10 h, as shown in Figure 3.8, but no other reductions were observed after 15 h. The other experiments reported in this work were performed after this long run using the same sample (see Table 3.3 for experimental conditions).

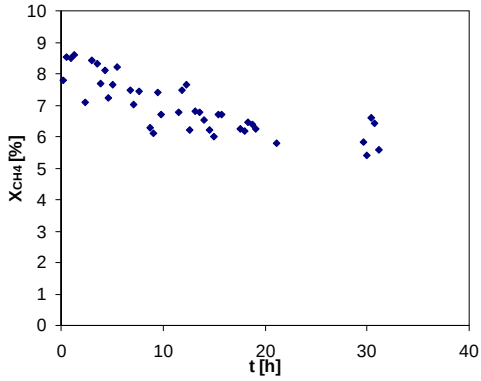

Figure 3.8. Conversion of methane vs time for a 31 h SMR experiment using Degussa catalyst powder at 763 K, 2 bar and 0.577 SLPM feed flowrate (see Table 3.3 for other experimental conditions).

An example of the temperature variation inside the catalyst bed and outside the reactor column during an experiment can be seen in Figure 3.9. In all experiments, the H_2O flowrate was started first to allow a steady flow when the reaction starts. After 150 s of introducing water and hydrogen, the methane flowrate was also initiated. This is t = 0 s in the reaction experiments. The initial temperature peak that can be observed in Figure 3.9 at about 50 s is due to water adsorption on the catalyst. A decrease of 17 K was observed in the first 100 s of reaction and then the temperature reached steady state.

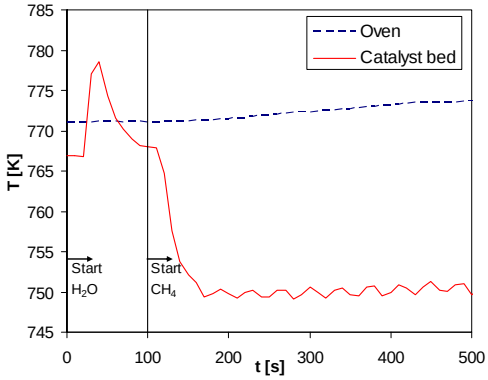

Figure 3.9. Evolution of catalyst and oven temperature in the SMR experiments using catalyst powder. This reaction was performed at the bed temperature of 749 K, total flowrate of 0.577 SLPM, 2 bar total pressure and S/C of 4.2.

The conversion of methane and the selectivity towards carbon dioxide obtained in all the experiments are shown in Figure 3.10. The conversion of methane increases with temperature due to the endothermic nature of the steam reforming reaction.

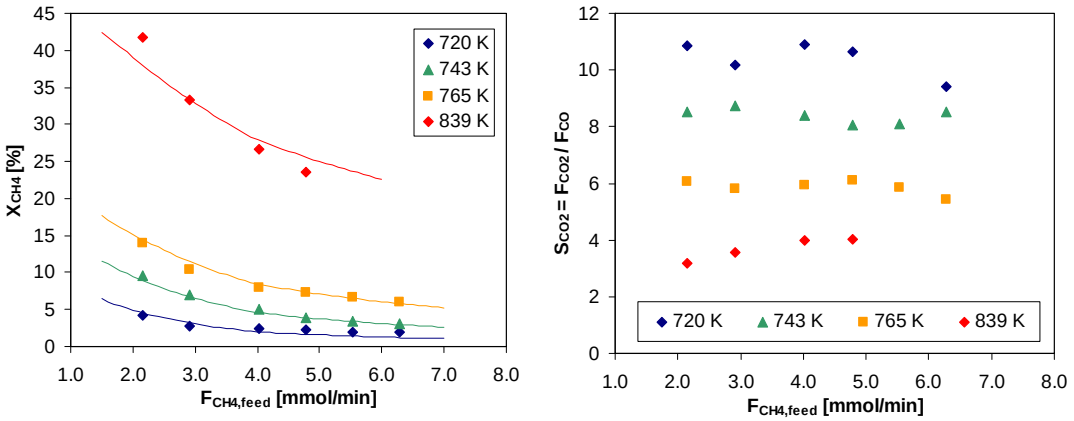

Figure 3.10. a) Methane conversion and b) carbon dioxide selectivity vs methane feed molar flowrate for the Degussa catalyst powder experiments in bed temperature range 720-839 K (see Table 3.3 for other experimental conditions). Lines are simulation results using the kinetic rate constants reported in Table 3.5.

It was also observed that conversion decreases with increasing inlet flowrate due to a reduction of the contact time between the catalyst and reactants. Another important feature observed is that the increase of the amount of CO with temperature is higher than the increase in the amount of CO_2 formed, resulting in a decrease of the selectivity towards CO_2 as can be observed in Figure 3.10. This decrease in selectivity is due to the exothermic nature of the water gas shift reaction (equation 3.2) that converts less CO to CO_2 when temperature increases. In applications such as SMR-SERP, this catalyst shows two advantages in terms of CO_2 selectivity: One is that the selectivity is always higher than one, which is important since CO is a poison for some (PEM for example) fuel cells and a catalyst selected to produce

fuel cell grade H_2 should be as selective toward CO_2 as possible [68]; Another is that, at the same temperature, the selectivity is nearly constant with the feed flowrate showing that it is possible to reduce the feed flowrate to maximize methane conversion without significantly affecting CO_2 selectivity.

Comparing the catalyst tested in this work with the one tested by Xu and Froment [3], the Degussa catalyst presents a lower methane conversion at 839 K while higher values are observed in the lower temperature range studied. The selectivity towards CO_2 is always higher in the catalyst tested in this work.

The molar flowrates of the effluent gases in the powder experiments is provided in Figure 3.11. For hydrogen, the figure shows the value of the molar flowrate after subtraction of the inlet H_2 flowrate in order to show the H_2 that was effectively formed.

The experimental effluent molar flowrates at each temperature were used to fit the kinetic rate constants using the mathematical model developed in Section 4.1. The parameters obtained from the fitting are shown in Table 3.5 and the results are represented as solid lines in Figure 3.11. The parameters give a good fit over the range of experimental conditions, particularly for CH_4, H_2 and CO_2 flowrates. The simulations of the carbon monoxide flowrate follow the same trend as the experimental points but its flowrate is always underestimated. This underestimation may be due to a smaller influence in the error function used by the numerical method employed to find the appropriate fitting values; note that the absolute value of CO flowrate is much smaller than the flowrates of other gases.

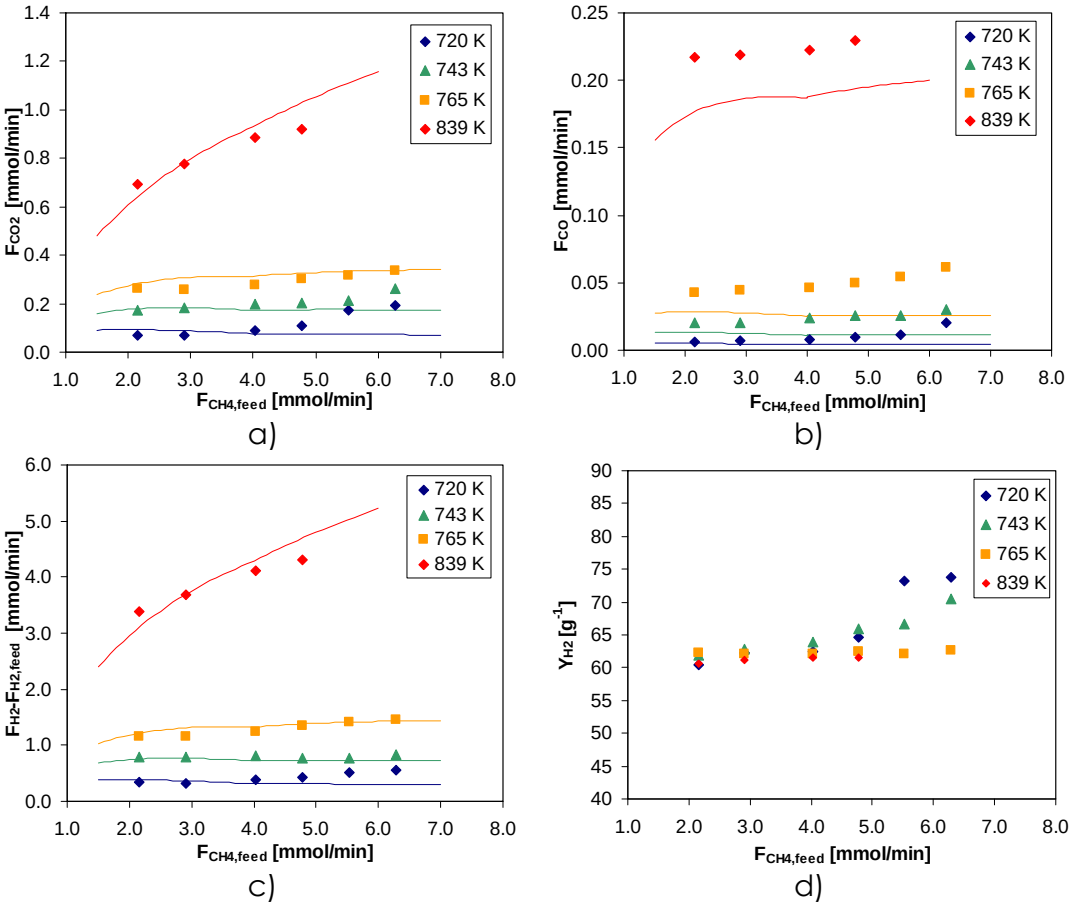

Figure 3.11. Dry effluent molar flowrates of: a) CO_2; b) CO; c) H_2 produced and d) hydrogen yield vs methane feed molar flowrate for the Degussa catalyst powder in the bed temperature range of 720-839 K (see Table 3.3 for other experimental conditions). Lines are simulation results using the kinetic rate constants reported in Table 3.5.

The energies of activation obtained for the Degussa catalyst can be compared with the previously reported values [3] (240.1 kJ/mol, 67.1 kJ/mol and 243.9 kJ/mol for reactions 3.1-3.3, respectively). It can be observed that the energies of activation of the Degussa catalyst are lower, indicating that higher conversion can be obtained operating at lower temperatures. This is very important for SMR-SERP process where

hydrotalcites will be used as sorbent and thus the operating temperature is limited to 823 K.

Table 3.5. Kinetic rate constants obtained from fitting of the true kinetic rate experiments of SMR reactions in a Ni/Al_2O_3 catalyst: comparison of values obtained for the Degussa catalyst and the values reported by Xu and Froment [3]. Adsorption parameters used in this work are the same as the ones reported by Xu and Froment [3].

	This work: Degussa	Xu and Froment [3]
Reaction parameters		
$k_{0,SMR}$ [mol.bar$^{0.5}$/(kg$_{cat}$.s)]	5.79x10^{12}	1.16x10^{15}
E_{SMR} [kJ/mol]	217.01	240.1
$k_{0,WGS}$ [mol/(kg$_{cat}$.s.bar)]	9.33x10^{5}	5.41 x10^{5}
E_{WGS} [kJ/mol]	68.20	67.13
$k_{0,Global\ SMR}$ [mol.bar$^{0.5}$/(kg$_{cat}$.s)]	1.29x10^{13}	2.79x10^{14}
$E_{Global\ SMR}$ [kJ/mol]	215.84	243.9

Adsorption parameters			
K_{CO} [bar^{-1}]	8.25 x10^{-5}	ΔH_{CO} [kJ/mol]	-70.65
K_{H2} [bar^{-1}]	6.15 x10^{-9}	ΔH_{H2} [kJ/mol]	-82.90
K_{CH4} [bar^{-1}]	6.66 x10^{-4}	ΔH_{CH4} [kJ/mol]	-38.28
K_{H2O} [bar^{-1}]	1.77 x10^{5}	ΔH_{H2O} [kJ/mol]	88.68

3.5.1.3. Steam methane reforming in Degussa extrudates

After the determination of the true SMR kinetics in the catalyst powder, it is important to measure the influence that the diffusion of the species will have in the real behavior of SMR using catalyst extrudates. To evaluate the effect of diffusion, five different experiments were performed using a reactor column filled with catalyst extrudates. The experimental conditions are reported in Table 3.4.

Since a large amount of catalyst was introduced in the column, a strong temperature variation was expected. The temperature was measured in two different axial positions: 45 mm and 87.5 mm from feed inlet (just after the end of the catalyst bed). In these experiments

hydrogen was also added to the feed stream to prevent formation of coke in the catalyst.

A long experiment was also performed before the experimental runs reported here in order to avoid the effect of initial deactivation. This experiment was performed for 7 h at 806 K and 2 bar total pressure and with a total flowrate of 24.8 mmol/min, S/C ratio of 4.24 and H_2/CH_4 ratio of 1.26.

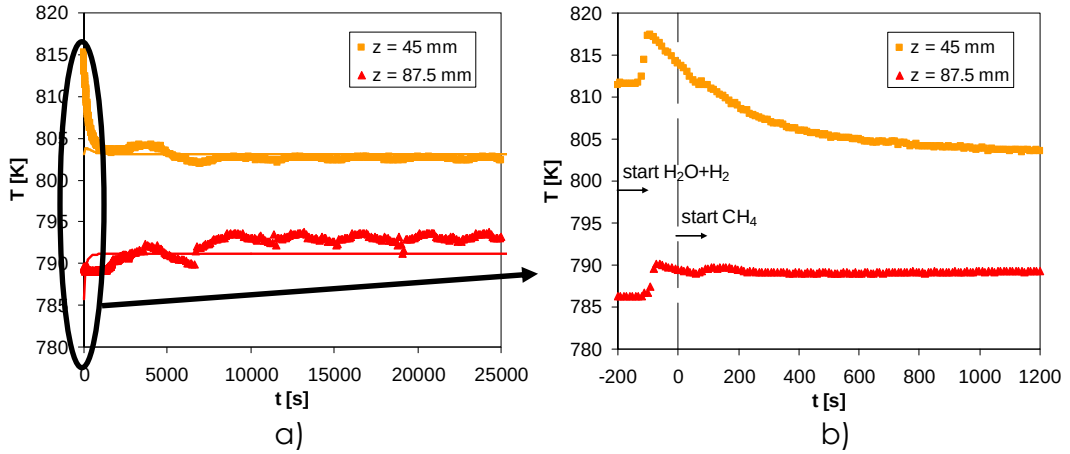

Figure 3.12. Evolution of the temperature for the initial experiment of steam methane reforming using Degussa catalyst extrudates. The steam methane reforming was performed at 806 K, 2 bar and total flowrate of 24.8 mmol/min (see Table 3.4 for other experimental conditions)

The steam flowrate was always started prior to the methane flowrate. It can be noticed in Figure 3.12b that when steam adsorbs in the catalyst extrudate there is an increment in temperature. It can be noted in Figure 3.12 that the steady state is achieved after about 20 min of reaction.

A total of five different experimental conditions (feed temperature and flowrates and different H_2/CH_4) were used. The temperature profiles of runs 2-5 are reported in Figure 3.13 and the effluent dry molar flowrates in steady state are compiled in Table 3.6.

Table 3.6. Operating conditions and steady state effluent molar flowrates of the steam methane reforming experiments performed using Degussa catalyst extrudates. Corresponding simulated values obtained at t = 10 000 s are in parenthesis.

	Run				
	1	**2**	**3**	**4**	**5**
Inlet operating conditions					
$F_{H2,feed}$ **[mmol/min]**	4.79	5.64	5.64	8.40	8.40
$F_{CH4,feed}$ **[mmol/min]**	3.81	4.51	4.51	8.40	8.40
$F_{H2O,feed}$ **[mmol/min]**	16.16	19.14	19.14	35.82	35.82
T_{oven} **[K]**	806	806	747	762	813
P_{out} **[bar]**	2	2	2	2	2
Outlet flowrates and performance variables					
F_{CH4} **[mmol/min]**	2.63 (2.65)	3.06 (3.11)	3.88 (3.88)	6.48 (6.67)	4.93 (5.30)
F_{H2}-$F_{H2,feed}$ **[mmol/min]**	4.76 (5.04)	6.05 (6.24)	3.57 (2.95)	7.95 (8.38)	12.54 (14.26)
F_{CO2} **[mmol/min]**	1.04 (1.12)	1.29 (1.37)	0.58 (0.69)	1.78 (1.90)	3.03 (3.04)
F_{CO} **[mmol/min]**	0.14 (0.18)	0.18 (0.23)	0.06 (0.05)	0.16 (0.17)	0.45 (0.56)
X_{CH4} **[%]**	30.9 (30.5)	32.3 (31.2)	14.0 (14.1)	23.0 (20.7)	41.4 (37.0)
S_{CO2}	7.43 (6.21)	7.17 (6.00)	9.67 (13.96)	11.12 (11.36)	6.73 (5.40)
Y_{H2} **[g^{-1}]**	0.12 (0.13)	0.12 (0.13)	0.17 (0.14)	0.12 (0.14)	0.11 (0.14)

Figure 3.13 shows that after an initial unsteady state, the temperature remains stable throughout the steam reforming experiments, indicating that the activity of the catalyst remains stable. Comparing the performance of runs 1 and 2 (different total flowrate), it can be observed that the methane conversion, carbon dioxide selectivity and H_2 yield are very close. This fact, together with the very small decrease in the temperature in the last portion of the column indicates that the equilibrium concentration is reached within the

reactor. In all the experiments performed it can be concluded that temperature is the most important operating variable. However, the reduction of hydrogen in the feed step is also important in increasing the conversion and the hydrogen yield, with the consequence of having a smaller selectivity to CO_2: more CO is formed from the reforming reactions than what is consumed by the water gas shift.

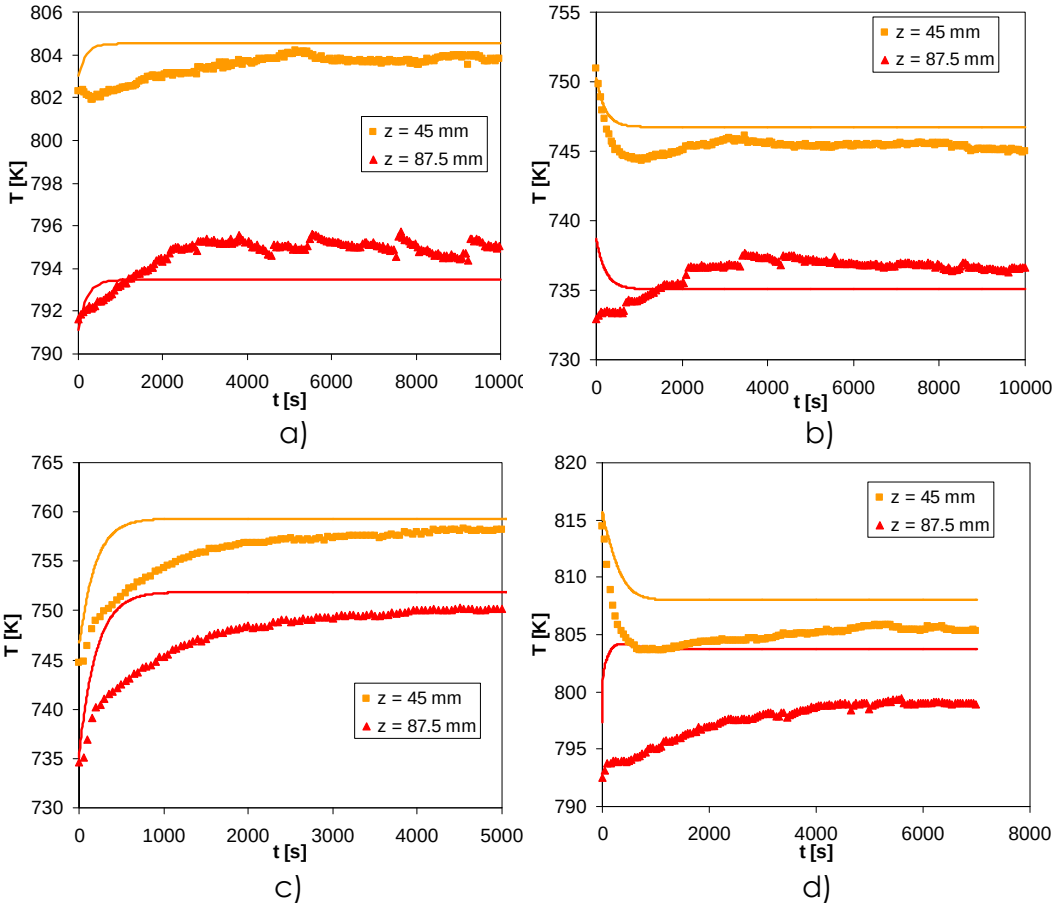

Figure 3.13. Temperature profiles vs reaction time for: a) Run 2; b) Run 3; c) Run 4; d) Run 5. Lines are simulation results (see Table 3.4 for experimental conditions).

The objective of these experiments using extrudates was to evaluate the effect of diffusion on the "observed" rate of reaction. In

this case, since three different reactions were considered to take place (equations 3.1-3.3), three effectiveness factors are necessary. In order to calculate them, it is important to know the reaction rates in the different axial positions. The reaction rates as well as the concentration and molar flowrates of the gases within the column were obtained by simulating the behavior of the column for each experiment using the mathematical model developed in section 3.2. In the model, the only parameter to be fitted was the pellet tortuosity. Using a value of τ_p = 1.56 a good correlation was obtained between all the experimental runs (exit concentration of gases and temperatures within the column) and the model predictions. All other parameters employed in the simulations are detailed in Table 3.7. The reaction rates, internal temperature profiles and molar flowrates of all gases were obtained using the mathematical model. The simulated effluent molar flowrates of all runs are compiled in Table 3.6 (values in parenthesis). The method of calculation of the transport parameters is detailed in Appendix A.

Table 3.7. Parameters used in the simulations of the non-isothermal steam methane reforming reactor with the Degussa catalyst extrudates.

Parameter		Parameter	
L_c [m]	0.0818	m_{cat} [kg]	0.0332
R_c [m]	0.0133	ρ_{cat} [kg/m³]	1274
w_{thick} [m]	0.0091	R_{cat} [mm]	0.8
ε_c	0.43	$L_{p,cat}$ [mm]	5.0
h_w [W/(m².K)]	400	r_{pore} [nm]	4.25
U [W/(m².K)]	200	$\varepsilon_{p,cat}$	0.64
$\hat{C}p_w$ [J/(kg.K)]	500	τ_p	1.56
ρ_w [kg/m³]	7750	$a_{p,cat}$ [m⁻¹]	2500
$\hat{C}_{ps,cat}$ [J/(kg.K)]ª	1072	D_{ax} [m²/s]ª	9.59×10^{-5}
ρ_{gas} [kg/m³]ª	0.44	$D_{k,cat}$ [m²/s]ª	3.83×10^{-6}
μ_{gas} [Pa.s]ª	2.75×10^{-5}	D_m [m²/s]ª	1.30×10^{-4}
$h_{f,cat}$ [W/(m².K)]ª	116.9	$D_{p,cat}$ [m²/s]*ª	2.38×10^{-6}
$k_{f,cat}$ [m/s]ª	0.216	λ_{ax} [W/m.K]ª	0.56

a – Calculated for the feed conditions at 800 K and 2 bar.

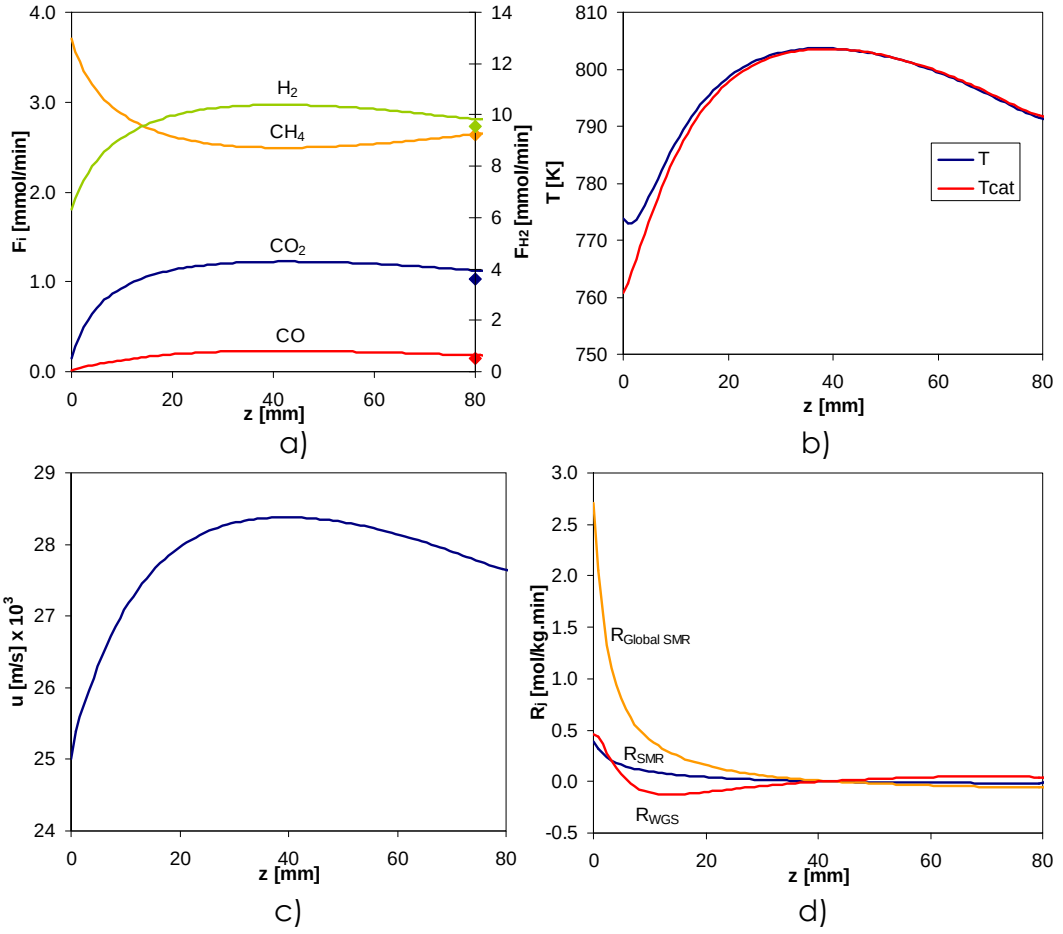

Figure 3.14. Simulated results of SMR using Octolyst 1001 (Degussa) extrudates at steady state (t = 10 000 s): molar flowrates (a), gas and solid temperatures (b), gas velocity (c) and reaction rate at r_{cat} = 0.8 mm (surface of the catalyst) (d).

Comparing the simulation results with the experimental data (both in Table 3.6), it is shown that the mathematical model is able to describe well the experiments made with the catalyst pellets. Based on the agreement between experimental data and mathematical model, the simulation results obtained for Run 1 will be described in more detail, since a similar behavior was observed for all other runs. In Figure 3.14 we can see the simulated molar flowrate (lines) of each gas across the

column after steady state was reached; the experimental results are also shown at the outlet of the reactor (points). The simulated temperature, superficial velocity and reaction rate profiles are also displayed in Figure 3.14.

It can be observed that, the molar flowrate of hydrogen and carbon oxides is relatively stable after the initial portion of the reactor, decreasing slightly towards the end of the catalyst bed. Another important observation is the reaction rate of the water gas shift reaction (R_{WGS}). It can be observed that this reaction rate passes through zero two times: the first one in the initial portion of the reactor and the second one in the middle of the catalyst bed. These variations are related to temperature changes within the reactor and are very important in controlling the formation of hydrogen and carbon oxides. In the initial portion of the reactor there is a large heat consumption to convert methane (SMR is strongly endothermic). The temperature decay is so intense at the initial part of the reactor that after some point, the amount of CO_2 produced is in excess and it starts to form CO (reverse water gas shift and thus negative reaction rate). After the initial section, less heat is necessary because the driving force to equilibrium is smaller and thus the gas starts to increase its temperature and the WGS starts to operate as desired (converting CO into CO_2). As can be observed in Figure 3.14, the methane conversion in the second half of the reactor is very small. At that point, a reduction of the temperature of the oven (according to the semi-parabolic profile in the heating oven) forces a reduction of the temperature of the reactor column that is reflected in the gas composition. When the temperature decreases, the thermodynamic equilibrium dictates that the amount of formed

hydrogen should be smaller and the reactions proceed towards the consumption of hydrogen, instead of its formation.

The model can also be used to determine what is occurring inside the catalyst particles. The concentration and reaction rate profiles inside the catalyst extrudates in two different positions of the reactor (z = 0.0 and 10.0 mm) are shown in Figure 3.15. Simulations also show that there was no temperature variation in the radial coordinate of the extrudates (see Figure 3.15b and d).

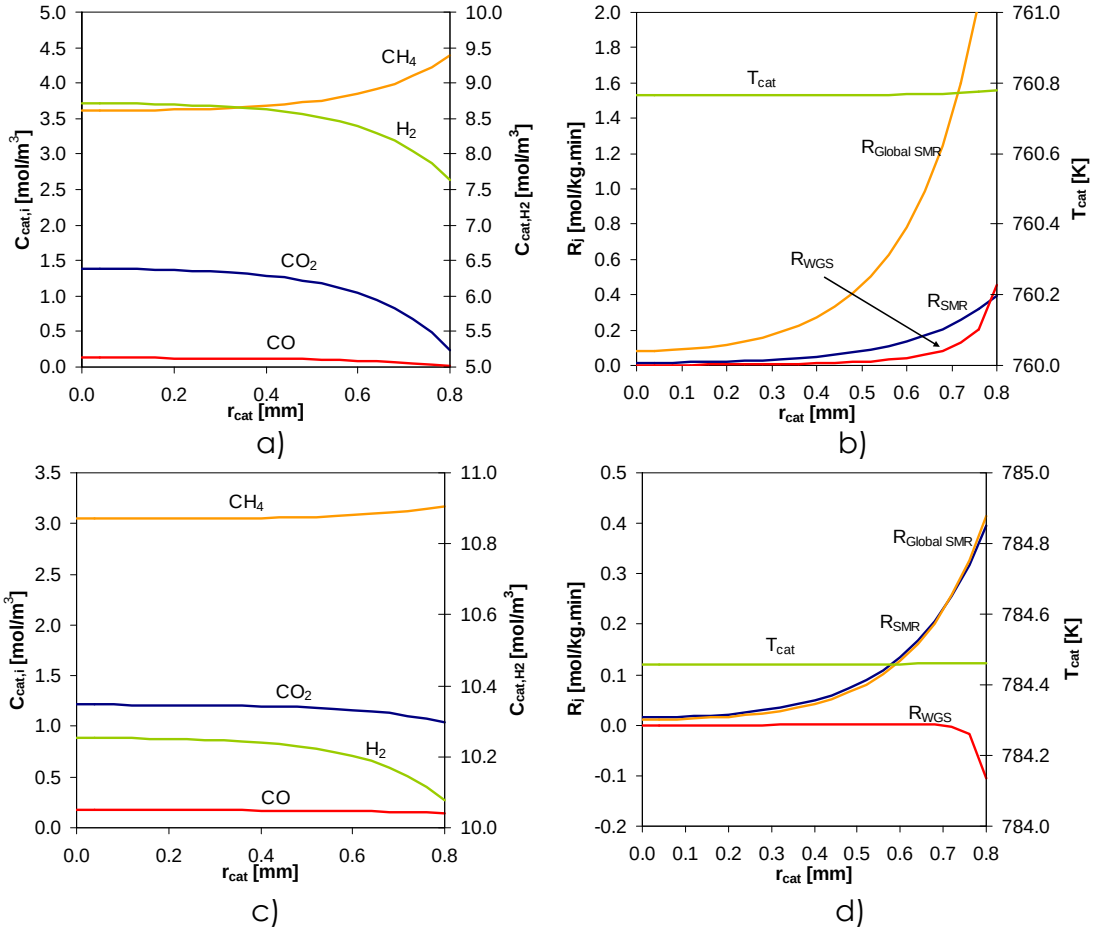

Figure 3.15. Catalyst (Degussa) extrudate profiles obtained for the SMR simulations of run 1 (see Table 3.4 for operating conditions) at t = 10 000 s. a) Concentration profiles at z = 0.0 mm; b) Reaction rate profiles at z = 0.0 mm; c) Concentration profiles at z = 10 mm; d) Reaction rate profiles at z = 10 mm.

The reaction rates are a function of the concentration and temperature inside the particle. Figure 3.15 shows that, at the top of the catalyst bed (z = 0), the highest variations of concentration (and therefore reaction rate) occur in the 0.4 mm (radius) closest to the surface of the catalyst particle. This means that the diffusional limitations reduce the "effective" catalyst radius to about half the size of the catalyst particles. The diffusional limitations are caused by the pore network of the catalyst that consists of mesopores with an average pore radius of 8.5 nm. Another interesting result from Figure 3.15b is that the Global SMR reaction rate was much higher than the SMR reaction rate within the particle. This result is consistent with a CO_2 selectivity higher than 1.

The calculated reaction rates can be employed to calculate the effectiveness factors of each reaction, using equation 3.48. The determination of the effectiveness factors is important to consider simplifications to the reactor model, i.e., eliminating the mass and energy balances to catalyst extrudate and therefore reducing the computational time. The results of the integration of the reaction rates can be observed in Figure 3.16.

It is important to notice that, according to equation 3.48, when the reaction rate changes direction, it passes through zero creating a discontinuity in the effectiveness factor as observed for the WGS at about 5 mm from the feed end. Two different asymptotes are observed in Figure 3.16. In the case of the second asymptote, it happens after the maximum in the temperature shown in Figure 3.14c. The change in the direction of the reaction rates happens as the global composition of the system is above the equilibrium values due to the subsequent decrease in the temperature (see Figure 3.14c-d). Asymptotes in the effectiveness

factor were already reported by other authors [59, 61, 69] for a steam methane reforming reactor.

The experiments performed using the extrudates have shown that it is possible to describe the results with the mathematical model proposed. Average values of the effectiveness factor of each reaction were calculated for each experimental run and are reported in Table 3.8. The data obtained in this section provided the necessary information to model the behavior of the Degussa catalyst in the temperature range of a SMR-SERP process operated using hydrotalcites as CO_2 sorbent.

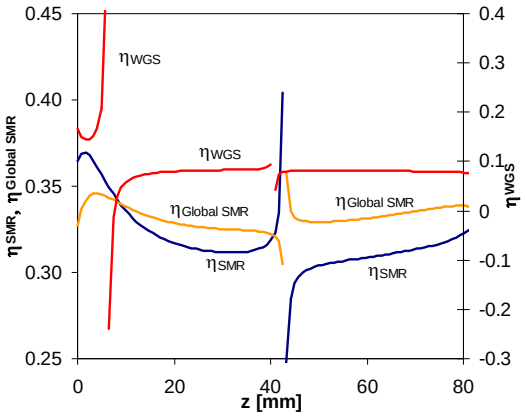

Figure 3.16. Simulated reaction effectiveness factors of SMR in Ni-based catalyst as a function of the catalyst bed length. Results for run 1 (P = 2.0 bar, S/C = 4.24, T_{feed} = 806 K) at t = 10 000 s after start of reaction.

Table 3.8. Average values of the SMR reaction effectiveness factors for the Degussa catalyst extrudates, in the feed temperature range of 747-813 K.

Effectiveness factor (η_j)					
Reaction	**Run 1**	**Run 2**	**Run 3**	**Run 4**	**Run 5**
SMR (1)	0.32	0.32	0.40	0.38	0.32
Water gas shift (2)	0.08	0.08	0.03	0.05	0.08
Global SMR (3)	0.33	0.33	0.41	0.39	0.32

3.5.2. Large pore catalyst (Catalyst A)

3.5.2.1. Characterization of the catalyst

In this work, a second nickel-based catalyst was employed to study the SMR reaction. This catalyst, termed as Catalyst A characterized by a large-pore network that promoted enhanced mass transfer by convection inside the pores. The SEM images of the catalyst are shown in Figure 3.17.

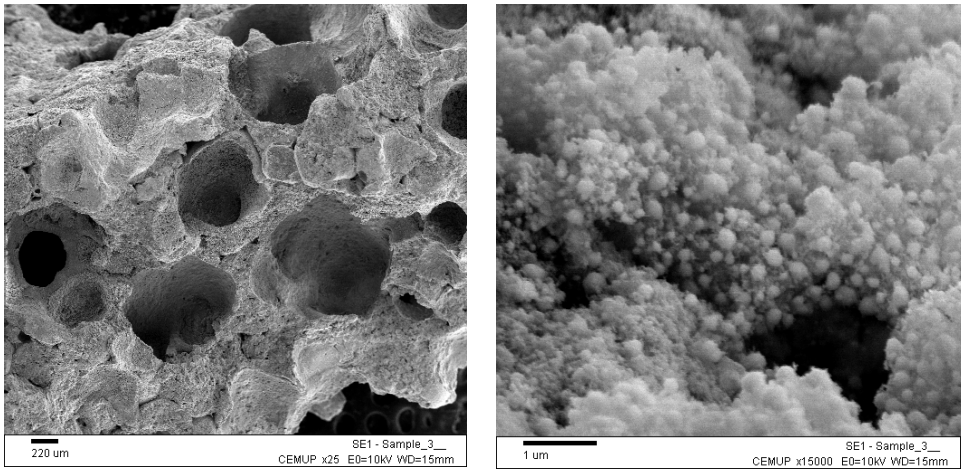

a) b)

Figure 3.17. SEM of Catalyst A extrudates at different magnifications: a) 25X; b) 15000X.

The extrudates of catalyst A are composed by small Ni crystallites that are linked by a macroporous structure containing a mixture of meso-macropores and large pores that can be observed even macroscopically (see Figure 3.6b). The presence of these large pores intends to reduce diffusional limitations of reagents and products into the extrudate.

X-Ray diffraction was also performed on the catalyst sample and is reported in Figure 3.18. Results show that the catalyst is composed of nickel, alumina and potassium. ICP measurements show that the catalyst has 10.0 % of Ni, 4.7 % of K and 35.6 % Al_2O_3. Nickel is the active metal for steam methane reforming while aluminum oxide is the structural binder. In this catalyst, potassium oxide was used as catalyst promoter with the objective of increasing resistance to coking.

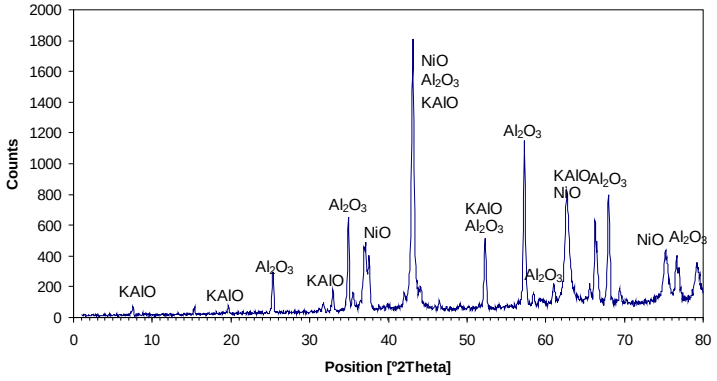

Figure 3.18. XRD of Catalyst A.

Mercury porosimetry was used to determine the pore size distribution and the particle density. Figure 3.19 shows that the catalyst has a wide distribution of pores starting with the smaller ones with an average pore diameter of 3.7×10^{-8} m and the larger pores with an average diameter of 8×10^{-4} m, as determined by SEM images (see Figure 3.17).

The pores larger than 3.6×10^{-4} m are not taken into account in the mercury porosimetry: mercury can penetrate into the large-pores at atmospheric pressure and they are assumed to be intraparticular spaces. To avoid errors in the density calculation due to the presence of large pores, the particle density was calculated based on the volume of the extrudate. The average particle density is 1687 kg/m^3. The solid

density measured by helium picnometry is 3900 kg/m^3, resulting in a porosity of 57 %.

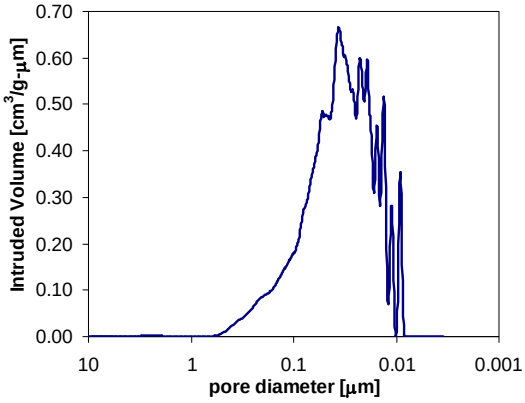

Figure 3.19. Pore size distribution of Catalyst A measured by mercury porosimetry.

3.5.2.2. Steam methane reforming kinetics in catalyst powder

The determination of the true kinetics of a catalyst is the first step in explaining how fast a catalyst approaches thermodynamic equilibrium at a given temperature, pressure and composition. The kinetic rate expressions proposed by Xu and Froment [3] and the model developed in section 3.1 were used to determine the steam methane reforming kinetic constants of catalyst A.

To detect if the catalyst presented deactivation with time, an experiment of SMR that lasted 5 h was made at 757 K (catalyst bed temperature), 2 bar total pressure, S/C = 4.1 and H_2/CH_4 = 1.25 (see Table 3.3 for other operating conditions). The experimental methane conversion is shown in Figure 3.20. The decrease in the first hours observed in the Degussa catalyst was not observed with catalyst A.

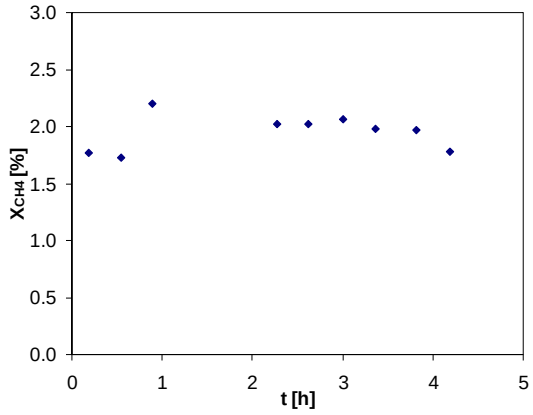

Figure 3.20. Conversion of methane vs time for a 5 h steam methane reforming experiment at 757 K, 2 bar, S/C = 4.1 and H_2/CH_4 = 1.25 (see Table 3.3 for operating conditions).

The complete set of experiments (operating conditions are detailed in Table 3.3) performed to determine the reaction kinetic constants, together with the fitting of the mathematical model proposed are shown in Figure 3.21. It can be observed that the total conversion increases with temperature as expected for endothermic reactions.

The H_2 yield is displayed in Figure 3.22, being rather constant with the inlet feed of methane at each temperature and always lower than the results obtained with the Degussa catalyst. The carbon dioxide selectivity (CO_2/CO ratio) is higher than 10 and always higher than the selectivity measured with the Degussa catalyst in the whole temperature range studied, as shown in Figure 3.22. This high selectivity is due to the low temperature of operation and is higher than reported values for other Ni catalysts [70-72] and comparable to the selectivity reported by Hou and Houghes [25]. Since CO_2 is removed by the sorbent in SERP operation, a catalyst that produces a low CO content is

preferred for SERP operation as CO is a poison for some types of fuel cells.

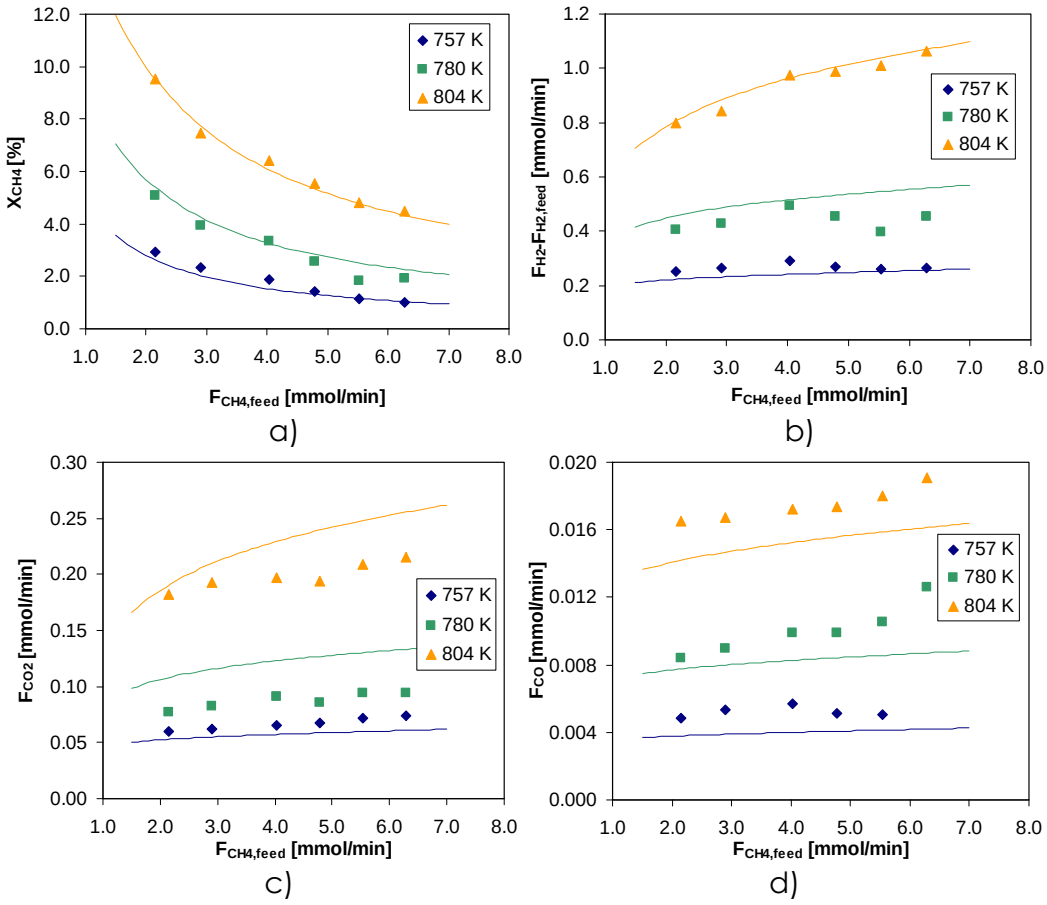

Figure 3.21. Steam methane reforming experiments using the powder of catalyst A at 2 bar total pressure (see Table 3.3 for experimental conditions): a) methane conversion; b) hydrogen produced; c) carbon dioxide produced; d) carbon monoxide produced. Lines are simulation results.

The experimental data allowed us to fit the reaction rate constants of the kinetic expressions that are showed in Table 3.9. The adsorption parameters employed by Xu and Froment [3] were used in equations 3.5-3.8. The values of the reaction rate constants were obtained by a fitting protocol that included the methane conversion and the concentration of the gases in a dry-basis. Therefore, as the experimental

concentrations of CO and CO_2 are lower than the concentrations of H_2 or CH_4, their relative weight in the fitting is lower.

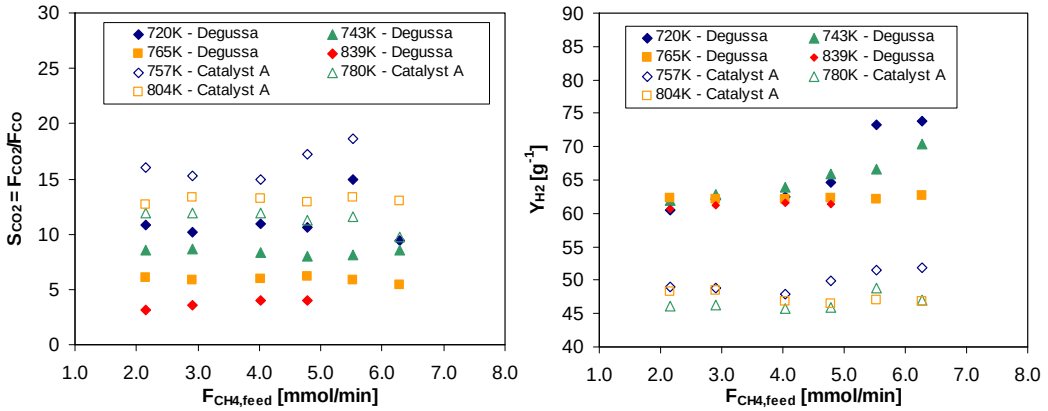

Figure 3.22. Comparison between the carbon dioxide selectivity (S_{CO2}) and hydrogen yield (Y_{H2}) using catalyst A and the commercial catalyst from Degussa. Results obtained with the catalysts in powder form.

Table 3.9. Methane steam reforming kinetic rate constants determined with powder of catalyst A (true kinetics) compared with the kinetic rate constant reported by Xu and Froment [3]. Adsorption parameters used in this work are the same as the ones reported by Xu and Froment [3].

	This work: Catalyst A		Xu and Froment [3]
Reaction parameters			
$k_{0,SMR}$ [mol.bar$^{0.5}$/(kg$_{cat}$.s)]	5.83x10^{11}		1.16x10^{15}
E_{SMR} [kJ/mol]	218.55		240.1
$k_{0,WGS}$ [mol/(kg$_{cat}$.s.bar)]	2.51x10^{4}		5.41 x10^{5}
E_{WGS} [kJ/mol]	73.523		67.13
$k_{0,Global\ SMR}$ [mol.bar$^{0.5}$/(kg$_{cat}$.s)]	4.67x10^{13}		2.79x10^{14}
$E_{Global\ SMR}$ [kJ/mol]	236.85		243.9
Adsorption parameters			
K_{CO} [bar^{-1}]	8.25 x10^{-5}	ΔH_{CO} [kJ/mol]	-70.65
K_{H2} [bar^{-1}]	6.15 x10^{-9}	ΔH_{H2} [kJ/mol]	-82.90
K_{CH4} [bar^{-1}]	6.66 x10^{-4}	ΔH_{CH4} [kJ/mol]	-38.28
K_{H2O} [bar^{-1}]	1.77 x10^{5}	ΔH_{H2O} [kJ/mol]	88.68

In the temperature range of interest for SERP (673-823 K), the catalyst proposed by Xu and Froment [3] is the most active for the

steam methane reforming reaction, followed by the commercial catalyst from Degussa and the large pore catalyst A. For the water-gas shift and global SMR reactions, the order is Degussa > Xu and Froment [3] > catalyst A. These results show that the commercial catalyst is the most active for CO_2 production. Catalyst A shows the lowest activity of all, probably due to a lower nickel content (10 %). The advantage of this catalyst is the presence of the large pores that enable higher effectiveness for the steam reforming reactions.

3.5.2.3. Steam methane reforming in large pore extrudates

There are two characteristics that influence the performance of a catalyst particle: reaction rate and diffusion; a very active catalyst surface will have a poor performance if the extrudates have very high diffusional limitations. The degree of diffusional limitations is given by the catalyst effectiveness factor for each reaction. For the proposed reaction mechanism with three simultaneous reactions, it is necessary to calculate three different effectiveness factors.

A total of nine different operating conditions (three different temperatures with three flowrates) were screened to determine the diffusional limitations using the extrudates of catalyst A. The experimental conditions are detailed in Table 3.4. Seventeen experiments were performed to check the reproducibility of the data. All the results obtained are detailed in Table 3.10.

After loading the reactor with the catalysts extrudates and reducing the catalyst for 1 h, a steam methane reforming experiment was carried out during 7 hours in the reference conditions (2 bar, 800 K and 29 mmol/min) to detect if the catalyst looses its activity. The

reference experiment was also repeated everyday within the experimental campaign during 1 h. After that, the feed flowrate or temperature were changed to test the effect of different operating conditions. The dry-basis molar fractions of the effluent were measured by GC.

Table 3.10. Effluent molar flowrates (mmol/min) for the steam methane reforming experiments made at 2 bar total pressure, S/C = 4.25 and H_2/CH_4 = 1.25 and feed temperatures in the range of 701-800 K and total molar flowrate in the range 12.5-48.1 mmol/min.

Feed		Effluent [mmol/min]				X_{CH4}	Y_{H2}	S_{CO2}
T [K]	F_{feed}	F_{CH4}	$F_{H2} - F_{H2,feed}$	F_{CO}	F_{CO2}	[%]	[g^{-1}]	
701	12.5	1.78	0.36	0.01	0.16	7.51	0.08	10.82
701	29.0	4.12	1.21	0.04	0.36	7.85	0.11	10.01
708	48.1	6.77	2.01	0.05	0.59	8.61	0.10	10.83
749	12.5	1.56	1.11	0.04	0.34	18.93	0.10	9.24
749	29.0	3.64	2.57	0.08	0.80	18.59	0.10	9.55
749	29.0	3.63	2.51	0.09	0.79	18.75	0.10	9.01
749	48.1	6.06	4.18	0.15	1.29	18.11	0.10	8.50
800	12.5	1.26	2.45	0.11	0.57	34.53	0.12	5.25
800	29.0	2.94	4.89	0.24	1.29	34.25	0.10	5.30
800	29.0	2.97	4.94	0.24	1.26	33.40	0.11	5.33
800	29.0	2.93	5.21	0.25	1.31	34.40	0.11	5.27
800	29.0	2.92	5.19	0.25	1.30	34.68	0.11	5.29
800	29.0	2.90	4.92	0.24	1.31	35.03	0.10	5.41
800	29.0	2.89	5.89	0.26	1.34	35.27	0.12	5.20
800	29.0	2.93	5.59	0.24	1.31	34.38	0.12	5.43
800	48.1	5.00	9.32	0.39	2.06	32.54	0.13	5.30
800	48.1	5.00	8.72	0.40	2.09	32.43	0.12	5.27

The temperature of the catalyst bed was also measured at z = 17 mm and z = 58 mm. As an example of a complete daily run (where one operating condition was changed three times), Figure 3.23 shows the thermal history and the dry basis molar fractions measured at different feed molar flowrates (29.0 mmol/min; 12.5 mmol/min and 48.1 mmol/min).

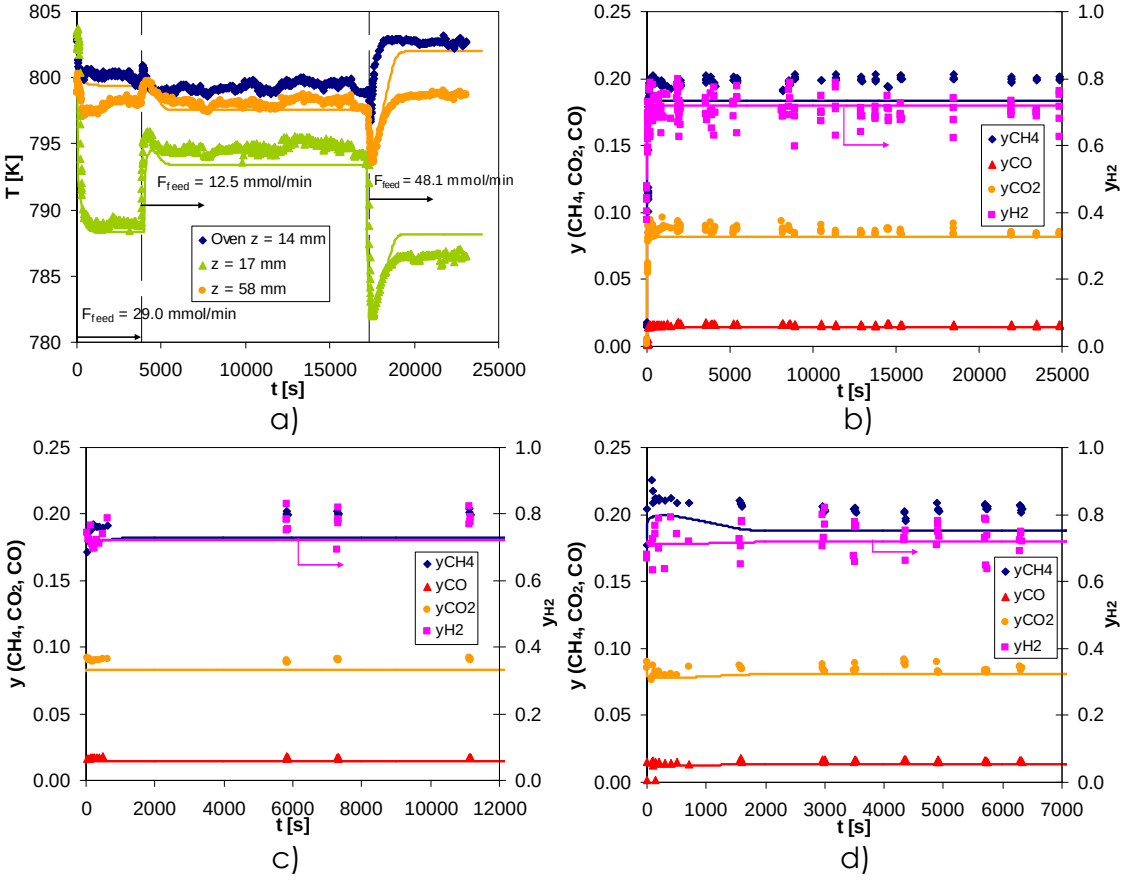

Figure 3.23. Steam methane reforming 1 day experimental run using the large pore catalyst in a fixed bed reactor operated at 800 K and 2 bar. a) Temperature profile; b) dry effluent molar fractions obtained at F_{feed} = 29.0 mmol/min; c) dry effluent molar fractions obtained at F_{feed} = 12.5 mmol/min; d) dry effluent molar fractions obtained at F_{feed} = 48.1 mmol/min. Lines are simulation results.

In all the experiments, the effluent concentration and temperature took about 400 s to achieve steady state. The duration of the unsteady state is related with diffusional effects inside the catalyst extrudates and also with heat transfer limitations. The temperature decrease is more pronounced in the initial section of the catalyst bed where the methane conversion is higher. In all the experiments, the effluent hydrogen concentration obtained is very close to equilibrium due to the large

amount of catalyst used for all feed flowrates. The formation of CO increases with temperature due to a faster increase of the reaction rate of SMR reaction against WGS and global SMR. The carbon dioxide selectivity decays with temperature according to: 10.1 (701 K) > 9.2 (749 K) > 5 (800 K). The variations of methane conversion and CO_2 molar flowrate against total feed flowrate are shown in Figure 3.24. It can be observed that the model can predict very well the amount of CO_2 formed, which is very important to size a SERP unit.

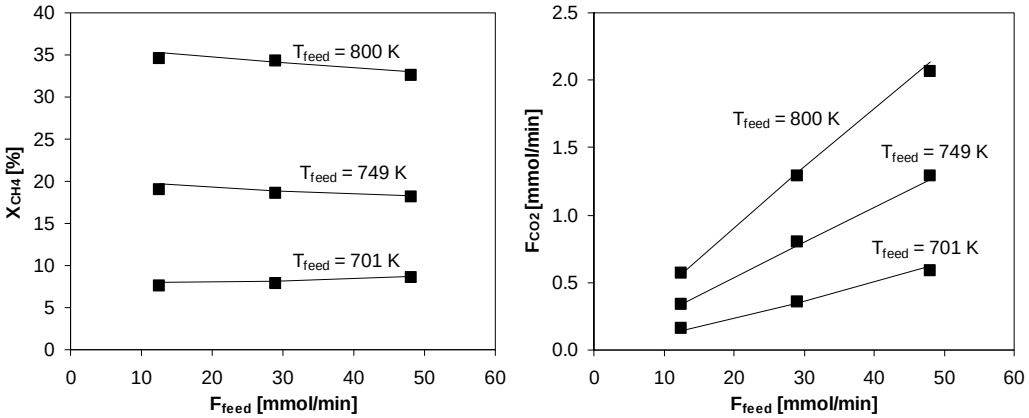

Figure 3.24. a) Methane conversion and b) carbon dioxide effluent molar flowrate as a function of the feed molar flowrate for the steam methane reforming experiments made at different temperatures and feed flowrates using the catalyst extrudates (See Table 3.4 for experimental conditions).

The performance of catalyst A can be compared with previously obtained data using the same experimental system and the Degussa catalyst with extrudates of 1.6 mm diameter (nearly seven times thinner). The overall conversion was similar because the temperature decrease within the bed is comparable. However, in a larger column, the pressure drop caused by catalyst A extrudates should be much smaller, increasing the overall efficiency of the SMR reactor.

The parameters in Table 3.11 were used with the mathematical model proposed in Section 3.2. to simulate the experimental runs of

Table 3.4. The heat transfer parameters shown in Table 3.11 were fitted from the initial experiment. The tortuosity of the particle was estimated to be $1/\varepsilon_p$ [63]. The model was able to predict the behavior of the reactor in the conditions studied.

Table 3.11. Parameters used in the simulations of the non-isothermal steam methane reforming reactor with Catalyst A extrudates.

Parameter		Parameter	
L_c [m]	0.0620	m_{cat} [kg]	0.0305
R_c [m]	0.0133	ρ_{cat} [kg/m³]	1687
w_{thick} [m]	0.0091	R_{cat} [mm]	5.6
ε_c	0.48	$L_{p,cat}$ [mm]	15.5
h_w [W/(m².K)]	400	$r_{pore,cat}$ [mm]	0.4
U [W/(m².K)]	200	$\varepsilon_{p,cat}$	0.57
$\hat{C}p_w$ [J/(kg.K)]	500	τ_p	1.76
ρ_w [kg/m³]	7750	$a_{p,cat}$ [m⁻¹]	354.3
$\hat{C}_{ps,cat}$ [J/(kg.K)]ª	1107	D_{ax} [m²/s]ª	1.31×10^{-4}
ρ_{gas} [kg/m³]ª	0.44	$D_{k,cat}$ [m²/s]ª	3610×10^{-4}
μ_{gas} [Pa.s]ª	2.75×10^{-5}	D_m [m²/s]ª	1.29×10^{-4}
$h_{f,cat}$ [W/(m².K)]ª	187.8	$D_{p,cat}$ [m²/s]ª	0.73×10^{-4}
$k_{f,cat}$ [m/s]ª	0.049	λ_{ax} [W/m.K]ª	0.56

a – Calculated for the feed conditions at 800 K and 2 bar.

An example of how the reaction is proceeding along the axial coordinate of the catalyst bed is shown in Figure 3.25a. The mathematical model could predict the effluent concentration of the gases as well as temperature variations.

In Figure 3.25, the internal behavior of the reactor (simulated) is provided for the reference conditions (2 bar, 800 K and 29 mmol/min) after steady state is achieved. On the other side, the variations of the gas concentration can be observed in Figure 3.25b. It is shown that the highest variation in the concentrations was in the 2-3 mm closest to the surface of the catalyst particle. The temperature of the solid decreases rapidly from 800 to 775 K when the feed comes in contact with the catalyst due to the highly endothermic SMR reaction (ΔH_{SMR} = 205.8

kJ/mol). In the initial portion of the reactor, the difference between gas and solid temperature is considerable indicating strong film heat transfer limitations (see Figure 3.25c).

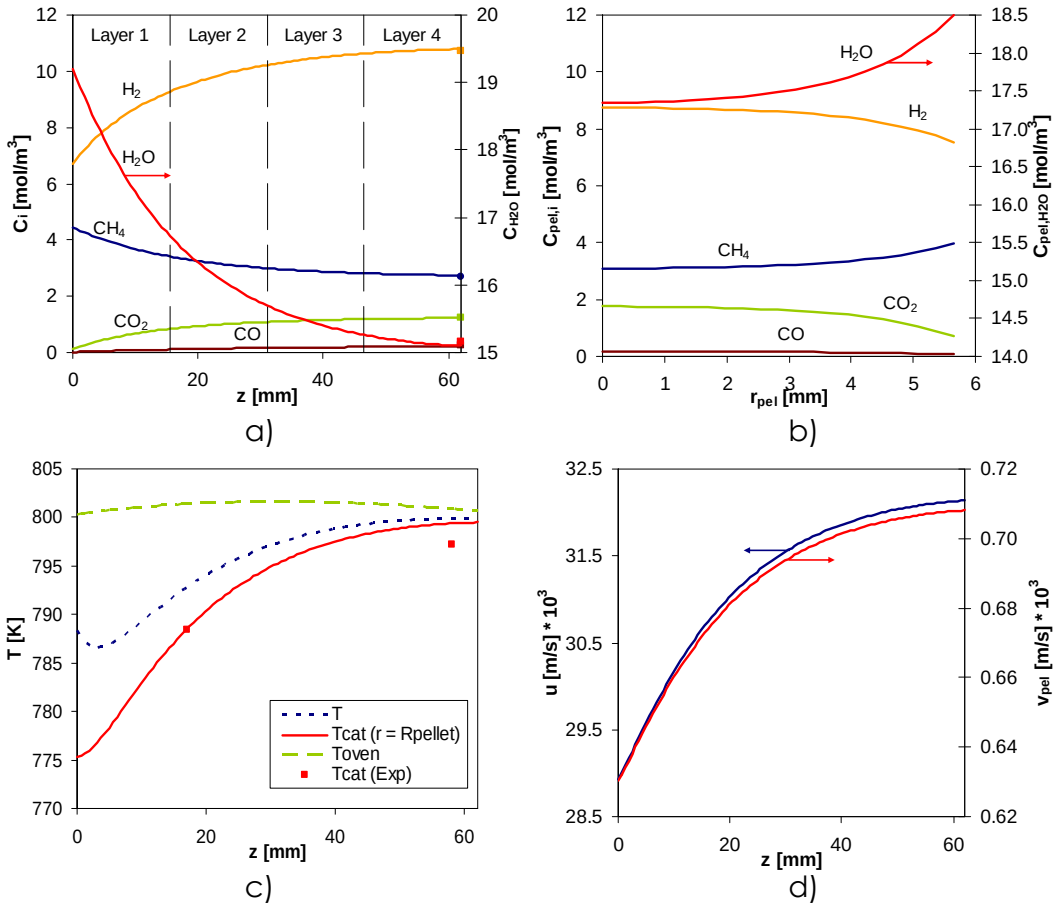

Figure 3.25. Simulation profiles obtained at t = 10 000 s for the steam methane reforming reference experiment at 800 K, 2 bar, 29.0 mmol/min (See Table 3.4 for experimental conditions). a) axial gas phase concentrations; b) radial concentration profiles inside the catalyst particle at z_{cat} = 0 and z = 0; c) gas and solid phase temperatures; d) superficial and intraparticle gas velocities.

A very interesting feature of the extrudates of catalyst A is that the overall mass transfer is enhanced by the convection inside the pores. The intraparticle velocity is shown in Figure 3.25d. It should be mentioned that the intraparticle velocity is around 40 times smaller than the

superficial velocity within the reactor (bed permeability = $3.3x10^{-7}$ m^2; particle permeability = $6.5x10^{-9}$ m^2). The effect of convection within the large pores enables a better utilization of the porous structure of the catalyst. Simulations without considering the convection term in equations 3.23 and 3.24 were performed to assess the effective contribution of the presence of large pores. In the case of the reference experiment (800 K, 29.0 mmol/min and 2 bar) a smaller methane conversion of 30.9 % was obtained. This value is considerably smaller compared with 34.1 % obtained in the simulations considering convection effect.

The simulations of the process with the mathematical model proposed allowed us to calculate the effectiveness factors of the set of reactions (equations 3.1-3.3). The effectiveness factors determined for the experiments at 29.0 mmol/min, 2 bar and different temperatures are shown in Figure 3.26. In all the experiments performed, the observed reaction rate is strongly limited by diffusional effects accompanied by limitations of heat transfer. Increasing the feed temperature decreased the effectiveness factor of the steam methane reforming and global steam methane reforming reactions while the feed flowrate had practically no effect. At 701 K, the diffusional limitations decrease the activity of the catalyst to the SMR and global SMR reactions by nearly 35 %, while at 800 K the value increases to about 55 %. Regarding the WGS reaction, the observed behavior of this reaction is strongly dependent of the SMR reactions, changing direction to comply with thermodynamic equilibrium. The effect is more pronounced when there are high temperature variations.

With the knowledge of the effectiveness factors at different temperatures, the mathematical model can be simplified by replacing

the mass and energy balance to the catalyst extrudates with the corresponding value of the effectiveness factor, saving computational time.

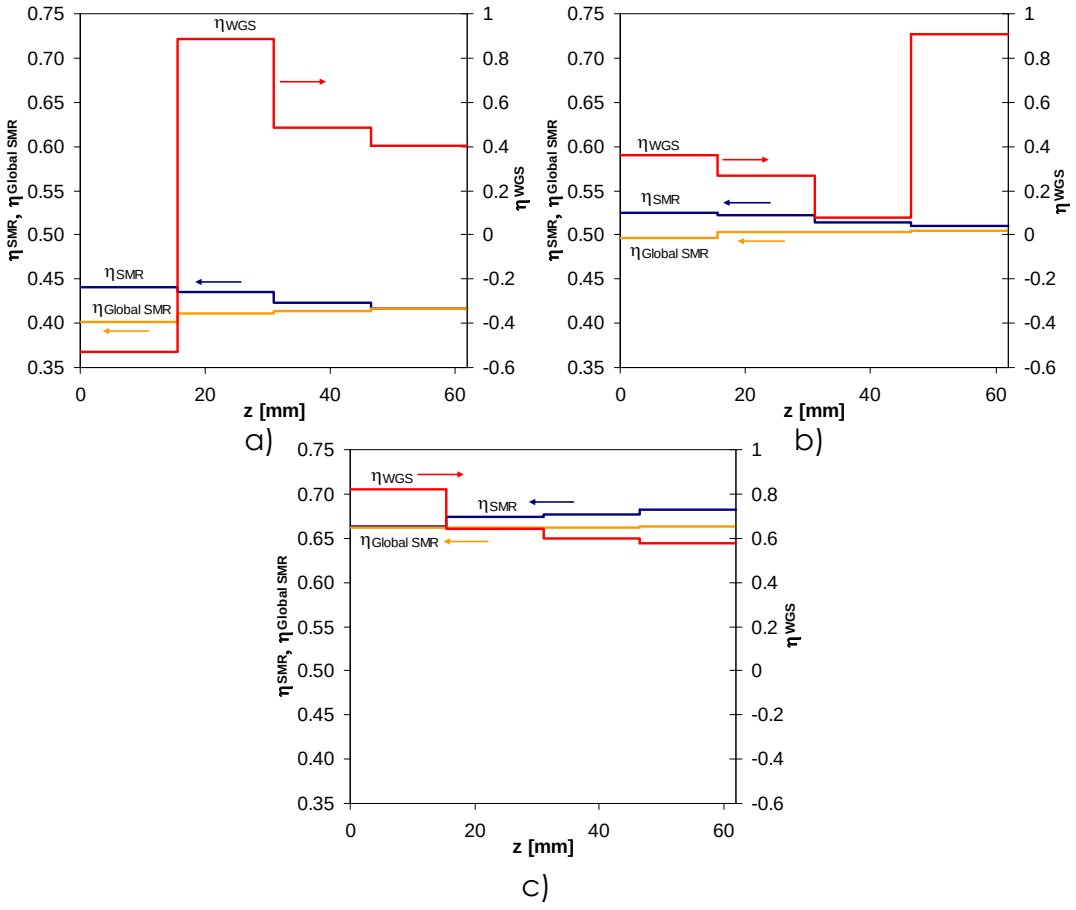

Figure 3.26. Variation of the effectiveness factor of SMR, WGS and global SMR reactions along the reactor length. Values were averaged for each extrudate and calculated for the experiments at 2 bar, 29.0 mmol/min and: a) 800 K; b) 749 K; c) 701 K. Simulation time is 10 000 s.

3.6. Conclusions

In this chapter, two Ni/Al_2O_3 catalysts were evaluated as selective catalysts for steam methane reforming (SMR) to produce hydrogen.

These materials are a commercial catalyst from Degussa (Germany) and "Catalyst A" containing large pores to enhance diffusion by convection within the extrudates. Different experiments using catalyst powder were performed to determine the true kinetics in both catalysts. Additional experiments using catalyst extrudates were also done to evaluate the effects of diffusion in the observed reaction rates and evaluate the effectiveness factors.

During the steam methane reforming experiments employing the Degussa catalyst, it was found that the carbon dioxide selectivity (F_{CO2}/F_{CO}) was always above 6. The result is important as the final goal is to use this catalyst for sorption enhanced reaction process (SERP) with carbon dioxide sorption. In the experiments with the extrudates, the effluent conversion was always close to equilibrium.

A non-isothermal, non-adiabatic fixed bed model was used to describe the experimental results obtained with the Degussa catalyst extrudates. The model indicated that, due to the endothermic steam methane reforming reactions, the temperature of the catalyst bed decreased near the feed end where the SMR reaction rates were higher.

The powder of Catalyst A was also used to determine the true SMR reaction kinetics. A carbon dioxide selectivity of 10 was measured in the powder experiments proving that this catalyst is also very suitable for SERP. It was found that the catalyst is very stable for steam methane reforming.

A non-isothermal, non-adiabatic fixed bed model including intraparticle convection within the extrudates was used to describe the experiments using Catalyst A extrudates. Simulations were performed with and without the intraparticle convection term. It was demonstrated

that the presence of large pores contributes to an increased methane conversion.

One of the major outputs of the mathematical models was the effectiveness factors of the reforming reactions. For both catalysts, simulations showed that there were large gas-solid heat transfer limitations and mass transfer limitations inside the catalyst particles.

The results presented in this work allow the complete description of the performance of the catalyst within hybrid reaction-separation systems like sorption enhanced reaction process for H_2 production.

3.7. References

1. Rostrup-Nielsen, J. R. Catalytic Steam Reforming. First ed, Springer-Verlag, Berlin, 1984.
2. Twigg, M. V. Catalyst Handbook. Second ed, Wolfe Publishing Ltd, England, 1989.
3. Xu, J.; Froment, G. F. Methane steam reforming, methanation and water-gas shift: I. Intrinsic kinetics. *AIChE J.* (1989), 35, 88.
4. Kirk, R. E.; Othmer, D. F.; Kroschwitz, J. I.; Howe-Grant, M. Kirk-Othmer Encyclopedia of Chemical Technology (Ammonia). Fifth ed, John Wiley & Sons, Inc., New York, 2001.
5. Kirk, R. E.; Othmer, D. F.; Kroschwitz, J. I.; Howe-Grant, M. Kirk-Othmer Encyclopedia of Chemical Technology (Methanol). Fifth ed, John Wiley & Sons, Inc., New York, 2001.
6. Aaron, D.; Tsouris, C. Separation of CO_2 from flue gas: A review. *Sep. Sci. Technol.* (2005), 40, 321-348.
7. Linde Engineering, http://www.linde-process-engineering.com/process_plants/gas_processing/rectisol_wash.php (Accessed June 2009).
8. Stöcker, J.; Whysall, M.; Miller, G. Q. 30 Years of PSA Technology for Hydrogen Purification, UOP, Des Plaines, Illinois, 1998.
9. Rostrup-Nielsen, T. Manufacture of hydrogen. In International Conference on Gas-Fuel 05, Amsterdam, November, *Catalysis Today* (2005), 293-296.
10. Ullmann, F. Ullmann's Encyclopedia of Industrial Chemistry (Gas Production). Seventh ed, John Wiley & Sons, Inc., New York, 2009.

11. Dirksen, H. A.; Riesz, C. H. Equilibrium in the steam reforming of natural gas. *Ind. Eng. Chem.* (1953), 45, 1562-1565.
12. Akers, W. W.; Camp, D. P. Kinetics of the methane-steam reaction. *AIChE J.* (1955), 1, 471-475.
13. Allen, D. W.; Gerhard, E. R.; Likins, M. R. Kinetics of the methane-steam reaction. *Ind. Eng. Chem. Proc. Des. Dev.* (1975), 14, 256-259.
14. Amphlett, J. C.; Evans, M. J.; F., M. R.; Weir, R. D. Hydrogen production by the catalytic steam reforming of methanol. Part 2: Kinetics of Methanol decomposition using GIRDLER G66B Catalyst. *Can. J. Chem. Eng.* (1985), 63, 605-611.
15. Amphlett, J. C.; Mann, R. F.; Weir, R. D. Hydrogen production by the catalytic steam reforming of methanol. Part 3: Kinetics of methanol decomposition using C18HC catalyst. *Can. J. Chem. Eng.* (1988), 66, 950-956.
16. Jiang, C. J.; Trimm, D. L.; Wainwright, M. S.; Cant, N. W. Kinetic mechanism for the reaction between methanol and water over a Cu-ZnO-Al_2O_3 catalyst. *Appl. Catal., A* (1993), 97, 145-158.
17. Cavallaro, S.; Freni, S. Ethanol steam reforming in a molten carbonate fuel cell. A preliminary kinetic investigation. *Int. J. Hydrogen Energy* (1996), 21, 465-469.
18. Borowiecki, T.; Golebiowski, A.; Stasinska, B. Effects of small MoO_3 additions on the properties of nickel catalysts for the steam reforming of hydrocarbons. *Appl. Catal., A* (1997), 153, 141-156.
19. Choudhary, V. R.; Mamman, A. S. Simultaneous oxidative conversion and CO_2 or steam reforming of methane to syngas over CoO-NiO-MgO catalyst. *J. Chem. Technol. Biotechnol.* (1998), 73, 345-350.
20. Wang, D.; Dewaele, O.; Froment, G. F. Methane adsorption on Rh/Al_2O_3. *J. Mol. Catal. A: Chem.* (1998), 136, 301-309.

21. Wolf, D.; Barre-Chassonnery, M.; Hoehenberger, M.; van Veen, A.; Baerns, M. Kinetic study of the water-gas shift reaction and its role in the conversion of methane to syngas over a Pt/MgO catalyst. *Catal. Today* (1998), 40, 147-156.
22. Peppley, B. A.; Amphlett, J. C.; Kearns, L. M.; Mann, R. F. Methanol-steam reforming on Cu/Zno/Al_2O_3. Part 1: The reaction network. *Appl. Catal., A* (1999), 179, 21-29.
23. Choudhary, T. V.; Goodman, D. W. CO-Free production of hydrogen via stepwise steam reforming of methane. *J. Catal.* (2000), 192, 316-321.
24. Froment, G. F. Production of synthesis gas by steam and CO_2-reforming of natural gas. *J. Mol. Catal. A: Chem.* (2000), 163, 147-156.
25. Hou, K.; Hughes, R. The kinetics of methane steam reforming over a Ni/α-Al_2O catalyst. *Chem. Eng. J.* (2001), 82, 311-328.
26. Agrell, J.; Birgersson, H.; Boutonnet, M. Steam reforming of methanol over a Cu/ZnO/Al_2O_3 catalyst: a kinetic analysis and strategies for suppression of CO formation. *J. Power Sources* (2002), 106, 249-257.
27. Choudhary, V. R.; Banerjee, S.; Rajput, A. M. Hydrogen from step-wise steam reforming of methane over Ni/ZrO_2: factors affecting catalytic methane decomposition and gasification by steam of carbon formed on the catalyst. *Appl. Catal., A* (2002), 234, 259-270.
28. Dong, W.-S.; Roh, H.-S.; Jun, K.-W.; Park, S.-E.; Oh, Y.-S. Methane reforming over Ni/Ce-ZrO_2 catalysts: effect of nickel content. *Appl. Catal., A* (2002), 226, 63-72.
29. Liu, Z.-W.; Jun, K.-W.; Roh, H.-S.; Park, S.-E. Hydrogen production for fuel cells through methane reforming at low temperatures. *J. Power Sources* (2002), 111, 283-287.
30. Marino, F.; Baronetti, G.; Jobbagy, M.; Laborde, M. Cu-Ni-K/Al_2O_3 supported catalysts for ethanol steam reforming: Formation of

hydrotalcite-type compounds as a result of metal-support interaction. *Appl. Catal., A* (2002), 238, 41-54.
31. Roh, H.-S.; Jun, K.-W.; Dong, W.-S.; Chang, J.-S.; Park, S.-E.; Joe, Y.-I. Highly active and stable Ni/Ce-ZrO_2 catalyst for H_2 production from methane. *J. Mol. Catal. A: Chem.* (2002), 181, 137-142.
32. Shen, J.-P.; Song, C. Influence of preparation method on performance of Cu/Zn-based catalysts for low-temperature steam reforming and oxidative steam reforming of methanol for H_2 production for fuel cells. *Catal. Today* (2002), 77, 89-98.
33. Wang, X.; Gorte, R. J. A study of steam reforming of hydrocarbon fuels on Pd/ceria. *Appl. Catal., A* (2002), 224, 209-218.
34. Cavallaro, S.; Chiodo, V.; Freni, S.; Mondello, N.; Frusteri, F. Performance of Rh/Al_2O_3 catalyst in the steam reforming of ethanol: H_2 production for MCFC. *Appl. Catal., A* (2003), 249, 119-128.
35. Oh, Y.-S.; Roh, H.-S.; Jun, K.-W.; Baek, Y.-S. A highly active catalyst, Ni/Ce-ZrO_2/θ-Al_2O_3, for on-site H_2 generation by steam methane reforming: pretreatment effect. *Int. J. Hydrogen Energy* (2003), 28, 1387-92.
36. Ramirez-Cabrera, E.; Laosiripojana, N.; Atkinson, A.; Chadwick, D. Methane conversion over Nb-doped ceria. *Catal. Today* (2003), 78, 433-438.
37. Zhang, J.; Wang, Y.; Ma, R.; Wu, D. Characterization of alumina-supported Ni and Ni-Pd catalysts for partial oxidation and steam reforming of hydrocarbons. *Appl. Catal., A* (2003), 243, 251-259.
38. Cao, C.; Xia, G.; Holladay, J.; Jones, E.; Wang, Y. Kinetic studies of methanol steam reforming over Pd/ZnO catalyst using a microchannel reactor. *Appl. Catal., A* (2004), 262, 19-29.

39. Frusteri, F.; Freni, S.; Chiodo, V.; Spadaro, L.; Di Blasi, O.; Bonura, G.; Cavallaro, S. Steam reforming of bio-ethanol on alkali-doped Ni/MgO catalysts: hydrogen production for MC fuel cell. *Appl. Catal., A* (2004), 270, 1-7.
40. Kaddouri, A.; Mazzocchia, C. A study of the influence of the synthesis conditions upon the catalytic properties of Co/SiO_2 or Co/Al_2O_3 catalysts used for ethanol steam reforming. *Catal. Commun.* (2004), 5, 339-345.
41. Matsumura, Y.; Nakamori, T. Steam reforming of methane over nickel catalysts at low reaction temperature. *Appl. Catal., A* (2004), 258, 107-114.
42. Purnama, H.; Girgsdies, F.; Ressler, T.; Schattka, J. H.; Caruso, R. A.; Schomacker, R.; Schlogl, R. Activity and selectivity of a nanostructured CuO/ZrO_2 catalyst in the steam reforming of methanol. *Catal. Lett.* (2004), 94, 61-68.
43. Takahashi, R.; Sato, S.; Sodesawa, T.; Yoshida, M.; Tomiyama, S. Addition of zirconia in Ni/SiO_2 catalyst for improvement of steam resistance. *Appl. Catal., A* (2004), 273, 211-215.
44. Li, D.; Atake, I.; Shishido, T.; Oumi, Y.; Sano, T.; Takehira, K. Self-regenerative activity of Ni/Mg(Al)O catalysts with trace Ru during daily start-up and shut-down operation of CH_4 steam reforming. *J. Catal.* (2007), 250, 299-312.
45. Bodrov, N. M.; Apel'baum, L. O.; Temkin, M. I. Kinetics of the reactions of methane with steam on the surface of nickel. *Kinet. Katal.* (1964), 5, 696-705.
46. Rodrigues, A. E.; Ahn, B. J.; Zoulalian, A. Intraparticle-forced convection effect in catalyst diffusivity measurements and reactor design. *AIChE J.* (1982), 28, 541-546.

47. Cogan, R.; Pipko, G.; Nir, A. Simultaneous intraparticle forced convection, diffusion and reaction in a porous catalyst - III: Depolymerization of paraldehyde *Chem. Eng. Sci.* (1982), 37, 147-151.
48. Nan, H. S.; Dias, M. M.; Rodrigues, A. E. Effect of forced convection on reaction with mole changes in porous catalysts. *Chem. Eng. J. Biochem. Eng. J.* (1995), 57, 101-114.
49. Nir, A.; Pismen, L. M. Simultaneous intraparticle forced convection, diffusion and reaction in a porous catalyst. *Chem. Eng. Sci.* (1977), 32, 35-41.
50. Rodrigues, A. E.; Lu, Z. P.; Lopes, J. C. B.; Dias, M. M.; Silva, A. M. Effect of intraparticle convection on conversion in heterogeneous isothermal fixed-bed reactors with large-pore catalysts for first-order reactions. *Chem. Eng. J. Biochem. Eng. J.* (1994), 54, 41-50.
51. Lopes, J. C. B.; Dias, M. M.; Mata, V. G.; Rodrigues, A. E. Flow field and non-isothermal effects on diffusion, convection, and reaction in permeable catalysts. *Ind. Eng. Chem. Res.* (1995), 34, 148-157.
52. Prince, C. L.; Bringi, V.; Shuler, M. L. Convective mass transfer in large porous biocatalysts. Plant organ cultures. *Biotechnol. Prog.* (1991), 7, 195-199.
53. Quinta Ferreira, R. M.; Marques, M. M.; Babo, M. F.; Rodrigues, A. E. Modelling of the methane steam reforming reactor with large-pore catalysts. *Chem. Eng. Sci.* (1992), 47, 2909-2914.
54. Quinta-Ferreira, R. M.; Simoes, P. M.; Rodrigues, A. E. Simulation of tubular reactors packed with large-pore catalysts with spherical geometry. *Comput. Chem. Eng.* (1995), 19, 351-356.
55. Farnan, D.; Frey, D. D.; Horvath, C. Intraparticle mass transfer in high-speed chromatography of proteins. *Biotechnol. Prog.* (1997), 13, 429-439.

56. Rodrigues, A. E. An Extended Van Deemter Equation (Rodrigues Equation) for Performing Chromatographic Processes Using Large-Pore, Permeable Packings. *LC-GC* (1993), 6, 20-29.
57. Rodrigues, A. E.; Lopes, J. C.; Lu, Z. P.; Loureiro, J. M.; Dias, M. M. Importance of intraparticle convection in the performance of chromatographic processes. *J. Chromatogr., A* (1992), 590, 93-100.
58. Shi, Q.-H.; Zhou, X.; Sun, Y. A novel superporous agarose medium for high-speed protein chromatography. *Biotechnol. Bioeng.* (2005), 92, 643-651.
59. Elnashaie, S. S. E. H.; Adris, A. M.; Al-Ubaid, A. S.; Soliman, M. A. On the non-monotonic behaviour of methane-steam reforming kinetics. *Chem. Eng. Sci.* (1990), 45, 491-501.
60. De Deken, J. C.; Devos, E. F.; Froment, G. F. Steam reforming of natural gas: intrinsic kinetics, diffusional influences, and reactor design. In American Chemical Society, Boston, Mass, USA, *ACS Symposium Series* (1982), 181-197.
61. Xu, J.; Froment, G. F. Methane steam reforming: II. Diffusional limitations and reactor simulation. *AIChE J.* (1989), 35, 97.
62. El-Bousiffi, M. A.; Gunn, D. J. A dynamic study of steam-methane reforming. *Int. J. Heat Mass Transfer* (2007), 50, 723-733.
63. Figueiredo, J. L.; Ribeiro, F. R.; Orfão, J. J. d. M.; Lemos, F.; Guisnet, M. Catálise heterogénea. Fundação Calouste Gulbenkian, Lisboa, 2007.
64. Ergun, S. Fluid flow through packed columns. *Chem. Eng. Prog.* (1952), 48, 89-94.
65. Bird, R. B.; Stewart, W. E.; Lightfoot, E. N. Transport Phenomena. Second ed, John Wiley & Sons, Inc, New York, 2002.
66. Rodrigues, A. E.; Loureiro, J. M.; Quinta Ferreira, R. M. Intraparticle convection revisited. *Chem. Eng. Commun.* (1991), 107, 21-33.

67. Rodrigues, A. E.; Lu, Z. P.; Loureiro, J. M. Residence time distribution of inert and linearly adsorbed species in a fixed bed containing 'large-pore' supports. Applications in separation engineering. *Chem. Eng. Sci.* (1991), 46, 2765-2773.
68. Semelsberger, T. A.; Brown, L. F.; Borup, R. L.; Inbody, M. A. M. A. Equilibrium products from autothermal processes for generating hydrogen-rich fuel-cell feeds. *Int. J. Hydrogen Energy* (2004), 29, 1047-1064.
69. Pedernera, M. N.; Pina, J.; Borio, D. O.; Bucala, V. Use of a heterogeneous two-dimensional model to improve the primary steam reformer performance. *Chem. Eng. J.* (2003), 94, 29-40.
70. Aparicio, L. M. Transient Isotopic Studies and Microkinetic Modeling of Methane Reforming over Nickel Catalysts. *J. Catal.* (1997), 165, 262-274.
71. Castro Luna, A.; Becerra, A. Kinetics of methane steam reforming on a Ni on alumina-titania catalyst. *React. Kinet. Catal. Lett.* (1997), 61, 369-374.
72. Comas, J.; Dieuzeide, M. L.; Baronetti, G.; Laborde, M.; Amadeo, N. Methane steam reforming and ethanol steam reforming using a Ni(II)-Al(III) catalyst prepared from lamellar double hydroxides. *Chem. Eng. J.* (2006), 118, 11-15.

4. Steam methane reforming sorption enhanced reaction process

4.1. Introduction

The kinetic and equilibrium properties of the high temperature CO_2 sorbents and the steam reforming catalysts were studied in Chapters 2 and 3.

The present chapter deals with the sorption enhanced reaction process (SERP) applied to the steam methane reforming (SMR) for H_2 production, termed herein as SMR-SERP. First, a summary of the developments in SERP and its application applied to steam methane reforming is given. Then, the experimental work focus on SMR-SERP using the two catalysts tested previously and MG30-K as selective CO_2 sorbent. The experimental work was necessary to validate a

mathematical model for SMR-SERP. This model was applied to simulate a previously published cycle consisting on a Skarstrom cycle including a reactive purge [1].

4.2. Hybrid reactors

The most important components of generic chemical plants are the reactor – where the raw materials are transformed to the desired products – and the separation processes – where impurities, unspent reagents and by-products are removed and the final products are obtained with high purity. The separation processes usually require the higher investment and operational costs [2].

The concept of hybrid reactors was developed to decrease separation costs [3, 4]. Hybrid reactors are the combination of reaction and separation in the same vessel [5]. The advantage of a hybrid reactor is the reduction (or even elimination) of the separation processes while obtaining high yields and purities of the desired products and conversions above thermodynamic equilibrium [5]. According to the Le Chatelier's principle, to exceed the thermodynamic equilibrium conversion it is necessary to remove *in situ* at least one of the reaction products [3, 4, 6]. For the particular case of SMR, when we consider the global steam methane reforming and water gas shift reaction, if the CO_2 is removed more H_2 is formed as shown below:

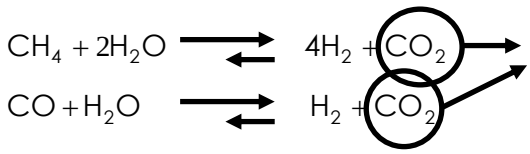

(4.1)

(4.2)

The possibility of applying a hybrid solution depends on the reaction as well as the properties of components used – products and reagents. Some examples of hybrid reactors are: reactive distillators [7-9], membrane reactors [10-12] and adsorptive or chromatographic reactors [1, 4, 6, 13-17].

Reactive distillation is used when the boiling point of the desired product is lower than the boiling point of the other by-products and reagents or when the resulting mixture forms an azeotrope [7, 8]. Some applications of reactive distillation are the production of methyl acetate [8], ethers (MTBE, ETBE, TAME and TAEE), ethylbenzene and cumene [18].

Membrane reactors are used to recover a product that has a high permeability and selectivity in a given membrane. Membrane reactors have been investigated for the production of H_2 by steam methane reforming (SMR) using a hydrogen selective membrane made of palladium [10, 19, 20] or palladium/silver [11]. A polymeric carbon dioxide selective membrane has also been investigated for the production of H_2 using the water gas shift (WGS) reaction [12].

Adsorptive reactors combine a catalyst and a sorbent selective to one or several of the reaction products [4]. Some examples of applications of adsorptive reactors are: hydrogen production by SMR [1, 4, 6, 13-17, 21-24] or WGS [25-28], the hydrolysis of aqueous methyl formate [29], catalytic oxidation of carbon monoxide [30], synthesis of dimethylether by adsorptive water removal [31], dehydrogenation of ethane to ethylene and hydrogen [32, 33] and producing ethene from propene [34]. At the LSRE, adsorptive reactors have been the subject of different PhD thesis such as metal recovery using resins [35], synthesis of diethylacetal [36] or dimethylacetal [37]. In fact, Lu *et al* [32] and later

Rawadieh and Gomes [34] proposed a layered configuration of catalyst and sorbent that were also used in the SMR-SERP experiments of this work.

4.2.1. Adsorptive reactors for hydrogen production

Adsorptive reactors for hydrogen production have been subject of research and development since the beginning of the 20th century. Around 1930, [3, 38]-[39], patents were issued for the production of hydrogen using a SMR catalyst and a calcium oxide-based sorbent selective for CO_2. Until almost the end of the century research in this field was limited to one patent by Gorin and Retallick in 1963 [40]. This little interest in the adsorptive reactors was most likely due to the low price of energy and reduced environmental concerns.

In 1997, the interest in adsorptive reactors for the production of H_2 restarted with the work of Mayorga *et al* for Air Products and Chemicals (USA) [4]. In this reference the name adsorptive reactor was replaced by sorption enhanced reaction process (SERP).

The idea of SERP is to use a reactor filled with a mixture of a SMR catalyst and a CO_2 sorbent. It is possible to achieve very high conversions in the temperature range of 673-873 K with ppm level concentrations of CO [4]. Removing carbon monoxide is very important if the hydrogen is going to be used in PEM (proton exchange membrane) fuel cells.

One technological challenge of SERP is its cyclic nature. The sorbent should be periodically regenerated without affecting the activity of the catalyst. On the other side, the main advantages of a SERP unit are the reduction of material and energy costs since lower

temperatures are used in the reactor and less separation processes are required to purify the H_2 stream [15]. Figure 4.1 shows a simplified schematic diagram of a steam methane reforming sorption enhanced reaction process plant.

Due to the cyclic operation of the SMR-SERP unit, each column with sorbent plus catalyst swings between two different states: reaction – where methane (natural gas) and steam are fed to the reactor to produce hydrogen and; regeneration – operating conditions are modified to partially regenerate the sorbent. Within the regeneration, CO_2 can be concentrated. The regeneration protocol depends on the operating conditions and on the desired specifications and comprise different steps that are designed to optimize the performance of the process [1, 4, 41-45].

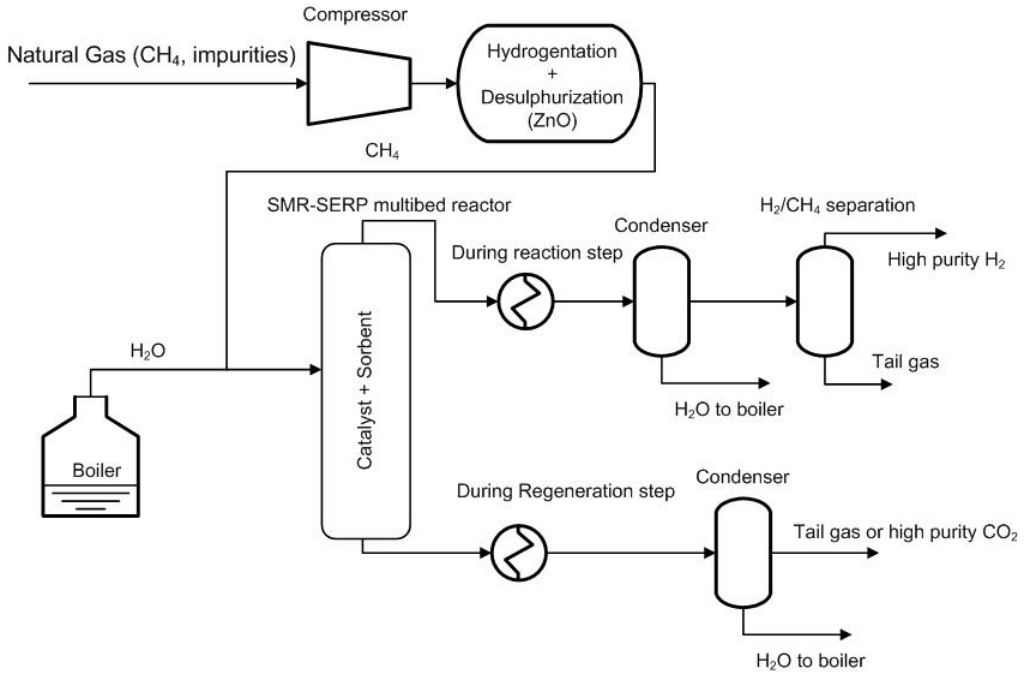

Figure 4.1. SMR-SERP plant for the production of hydrogen.

4.2.1.1. SERP using calcium-based sorbents

Calcium-based sorbents have been extensively researched for SMR-SERP since 1999 by the group of the Louisiana State University [13, 46-48]. In their first work they used a Ni/Al_2O_3 catalyst (30 %) mixed with a calcium oxide sorbent (70 %). Experimental results showed that at 923 K, steam to carbon ratio (S/C) of 4 and 15.2 bar total pressure, hydrogen was produced with 95 % purity during 90 min. Increasing the S/C ratio from 3 to 5 increased the conversion by 11 %.

Subsequent works by this group focused in the SERP multicycle stability using dolomite sorbents [46], applying a sulfur pretreatment to the sorbent [46] and using low temperature (673-753 K) and low pressure in the range 1-5 bar to produce H_2 with low carbon monoxide content [47, 48]. These experiments were made employing a powder mixture of reforming catalyst and $CaCO_3$ sorbent with sorbent/catalyst ratios in the range 2-20. The powder was supported in quartz wool. At 713 K, 5 bar and a S/C of 3, a stream containing 96 % H_2 and 7 ppm CO was produced [47]. When the temperature was changed to 753 K with S/C of 4, the effluent contained 98 % of H_2 and the 17 ppm of CO [48].

Satrio *et al* [49] developed a particle that acted both as sorbent and catalyst. The core of the material was made of limestone and dolomite that acted as CO_2 sorbent. The extrudates were covered with a mixture of dolomite (5 %) and alumina (95 %) and then impregnated with Ni that acted as catalyst. In fixed-bed experiments were made employing 6 g of extrudates. A methane conversion of 99 % and H_2 dry effluent concentration of 96 % were achieved at 873 K, 1.01 bar and S/C = 3.

The continuous production of hydrogen using a set of two parallel fixed bed reactors was investigated using powders of a Ni catalyst and a CaO based sorbent [23]. Hydrogen with a purity higher than 90 % was produced continuously for more than 7 hours using these reactors.

Other reactor concepts such as fluidized bed and moving bed reactors were also tested for SERP using calcium based sorbents. Hildebrand and coworkers [22] performed SERP using dolomite and Ni/Al_2O_4 catalyst in a fluidized bed reactor. They reported an initial induction period for the sorbent, where the H_2 concentration increases until reaching 90 %.

Simulations were performed by Lee *et al* [50] to determine the viability of the moving bed reactor for SERP. The catalyst and the sorbent were pneumatically carried along the reactor, co-currently with the feed. An effluent composition containing 1.3 % CO_2, 2.5 % CO, 94 % H_2 and 2.2 % CH_4 was obtained at 973 K, S/C of 3 and solids flowrate of 1.2 kg/h.

4.2.1.2. SERP using lithium salts

The group from NTNU in Norway developed a lithium zirconate that is able to sorb carbon dioxide at high temperature [16, 51-53]. In their first work, the simulation results indicated that it was possible to produce H_2 with a purity of 95 % at 848 K, 5 bar and using an S/C of 6. The S/C ratio used was quite high but a decrease from 6 to 4 decreased the H_2 purity to 90 % [16]. In 2007, simulations were reported [52, 53] comparing Li_2ZrO_3 and Li_4SiO_4 as carbon dioxide sorbents. Results showed that the Li_2ZrO_3 sorbent could reach hydrogen purities higher than 87 % at 848 K and 10 bar. However, higher reactor lengths are required when Li_2ZrO_3 is

used when compared to the orthosilicate, resulting in low productivities for the zirconate [52]. The advantage of the orthosilicate was due to the faster CO_2 capture kinetics [53].

The performance of lithium orthosilicate for SERP was measured in the temperature range of 773-873 K by Essaki *et al* [21]. A stream containing 93.6 % H_2, 6.23 % CH_4, 0.16 % CO_2 and 0.01 % CO was obtained after 30 min of reaction (switching time) at 823 K and S/C = 3.5. The orthosilicate showed very good cyclic stability showing that it is a good candidate for SERP.

4.2.1.3. SERP using sodium oxides

The use of sodium sorbents for SERP was reported by Lee *et al* [26, 54] and Bretado *et al* [25]. Both groups propose the shift of the SERP concept from the SMR reactor to the WGS reactor, as lower temperatures favor the CO_2 sorption in these sorbents.

Lee *et al* [26, 54] tested a Na_2O impregnated alumina sorbent for water gas shift SERP in the temperature range of 423-573 K. At 473 K and 1 bar, hydrogen was produced with a purity of 100 % and CO conversion of 100 % [26]. At 573 K, 100 % hydrogen was produced produced for less time since the sorption capacity of the impregnated alumina is lower than at 473 K [54].

These results show that using SERP in the water gas shift reactor is also an interesting example of hybrid reactor.

4.2.1.4. SERP using hydrotalcites

The first reference to the use of hydrotalcites for SERP was in a report of Air Products and Chemicals (USA) [4]. Their report showed that it was possible to produce a stream containing 60 % H_2 (dry composition) without CO nor CO_2 at 623 K, 4.8 bar, S/C of 2 and a catalyst/sorbent ratio of 1. These results were confirmed with a potassium modified hydrotalcite sorbent in benchscale [15] and in a pilot-scale reactor using a Skarstrom type cycle [2]. Results showed that at 723 K, 4.8 bar and using a S/C of 6 a stream containing 96 % hydrogen and 50 ppm of carbon oxides (CO + CO_2) was produced using the bench-scale reactor. To reach the obtained methane conversion of 82 % at 723 K, a conventional SMR reactor had to be operated at 918 K. Afterwards, cyclic SERP experiments were performed in a pilot-scale reactor [41]. The feed pressure was varied between 1.78-4.6 bar at 763 K and an S/C of 6. A hydrogen purity of 94 %, 40 ppm of CO_2, methane conversion of 73 % and no CO were obtained in the sorption-reaction step using a feed pressure of 1.8 bar. Approximately 30 cycles were necessary to reach cyclic steady state.

In 2000, Ding and Alpay [14] published their experimental results of sorption enhanced reaction using potassium modified hydrotalcites. It was found that there is an optimum temperature (718 K) that balances the slow kinetics of the SMR reaction at low temperature with the low carbon dioxide sorption capacity at higher temperatures. Increasing the pressure increases the CO_2 sorption capacity and therefore the methane conversion. Additionally, for smaller particle sizes (0.11-0.25 mm) an increase of methane conversion was observed due to faster diffusion.

In 2006, the group from ECN (Energy research Centre of the Netherlands) started publishing their results on SMR-SERP using hydrotalcites impregnated with 22 % K_2CO_3 [17]. The work reported cyclic SMR-SERP experiments at 673 K and S/C of 6. The cycle comprises two steps: reaction/sorption and desorption. An average methane conversion of 95 % was reported after 100 cycles. In 2007, the application of the SERP concept for energy production was reported [55]. Two systems were compared: SMR-SERP and autothermal reactor followed by a reactor filled with water gas shift catalyst and CO_2 sorbent (WGS-SERP). The efficiency of the conversion of CH_4 to electricity with SMR is 57.1 %. Results show that, with SMR-SERP the efficiency dropped to 51.6 % while with autothermal/WGS-SERP the efficiency was 48.5 %. The decrease in the efficiency is offset by the capture of 90 % of the CO_2 produced.

Dr. Shivaji Sircar at Lehigh University, continued to work in SMR-SERP with potassium modified hydrotalcites [56-58]. A new cycle (composed by two steps: sorption/reaction at 763 K and thermal regeneration at 863 K) was proposed instead of pressure swing for the regeneration of the sorbent material [56]. Simulations using this cycle showed that a stream containing 99.99 % H_2 can be produced with less than 15 ppm of carbon oxides [56]. Comparing the performance of the thermal swing regeneration with the pressure swing regeneration, the thermal swing process reached a H_2 purity of 99.99 % with a productivity of 0.39 mol/kg while using vacuum pressure swing the H_2 purity is 94.4 % at a productivity of 0.25 mol/kg (experimental results at pilot scale [41]). The catalyst content in the pressure swing experiments was 33 % while in the temperature swing simulations was only 10 %. Parametric studies were also performed to determine the optimum SERP conditions using the

temperature swing regeneration. Results indicate that the optimum sorbent/catalyst ratio is close to 13 and the optimum S/C was between 5 and 9 [57].

Koumpuras *et al* [59, 60] proposed a different reactor concept: a monolithic reactor with concurrent flow of the reactants and sorbent particles. The sorbent is then regenerated in a separate chamber. This concept is similar to the moving bed reactor proposed by Lee *et al* [50] that also proposed a separate chamber to regenerate the sorbent. One advantage of the configuration reported by Koumpuras *et al* [59, 60] is that the sorbent acts as a heat carrier to balance the heat used for the SMR reaction. Simulations show that this reactor configuration can reach a CH_4 conversion of 80 % at 800 K and 5 bar total pressure.

4.2.2. Cyclic PSA-SERP simulations

Most of the works mentioned in the previous sections showed the use of the SMR-SERP with different carbon dioxide sorbents. However, only very few reports have presented cyclic experimental results and only the group from Air Products and Chemicals (USA) [15, 41] reported a complete PSA cycle. Other authors limited their experimental cycles to reaction/sorption and purge.

In the particular case of hydrotalcites, pressure swing has been the most widely applied method of regeneration [1, 14, 15, 17, 41-45], with the exception of the most recent works of Lee *et al* [56-58] that proposed temperature swing.

Pressure swing operates cyclically with sequential steps to use and regenerate the sorbent in the most profitable way. Several different cycles were already proposed [1, 15, 41-45]. Here, a detailed

description of some results obtained with different strategies for the production of H_2 with SMR- SERP [1, 15, 41-45]. Xiu *et al* [1] used the sorbent CO_2 sorption properties reported by Ding and Alpay [61] and the catalyst kinetics reported by Xu and Froment [62] to simulate the a SMR-SERP unit [45].

An example of the behavior of the SERP concept is shown in Figure 4.2, where the feed contained a S/C ratio of 6. The transient nature of SERP is clear: in the first zone (I), the amount of CO_2 in the gas phase is very small allowing a conversion of methane higher than the equilibrium value, which can be also observed in Figure 4.2b. After some time, the sorbent becomes saturated with CO_2 and breaks through the column (zone II). In this zone, the sorption enhancement is less pronounced until CO_2 breakthrough where no enhancement is observed (see Figure 4.2b). After breakthrough (zone III) the reactor operates like a conventional SMR reactor. The cyclic steady state methane conversion reaches 24.5 % [45] which is in agreement with experimental results of Hufton *et al*

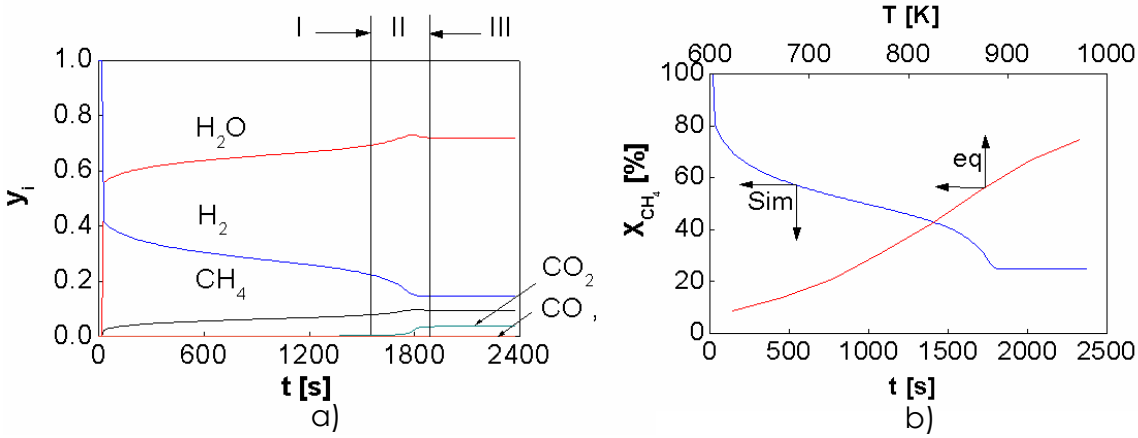

Figure 4.2. a) Effluent mole fraction vs time for SMR-SERP unit and b) methane conversion vs time for SMR-SERP unit. Results at P = 4.46 bar, T = 723 K, L = 2 m, S/C = 6, u = 0.05 m/s, sorbent/catalyst = 2 [45].

An important improvement of the SMR-SERP is the higher conversions achieved at much lower temperatures than conventional SMR. However, the operation temperature of SMR-SERP is narrow since there is a trade-off between conversion (favored by high temperatures) and CO_2 sorption capacity/stability of the hydrotalcite sorbent (favored by lower temperatures). Using hydrotalcites, the maximum temperature is fixed in 823 K (according to SASOL specifications) while temperatures lower than 673 K result in very small conversions.

4.2.2.1. Classical Skarstrom cycle vs reactive regeneration

In their first work, Xiu et al [1] compared the Skarstrom type PSA cycle proposed by Waldron *et al* [41] with a modified cycle that applied a reactive regeneration of the sorbent – reaction of the CO_2 with H_2 to produce CO through the reverse of the WGS reaction. Since CO does not sorb in the hydrotalcite, the regeneration is faster. This cycle was:

1. Reaction/sorption at high pressure;

2. Depressurization and reduction of the reactor temperature;

3. Low pressure purge at lower reactor temperature with a mixture of 10% H_2 in N_2 followed by purge with steam at the reaction temperature;

4. Pressurization with steam at feed temperature.

A graphical representation of a typical Skarstrom cycle [41] and the one proposed at the LSRE [1] is given in Figure 4.3.

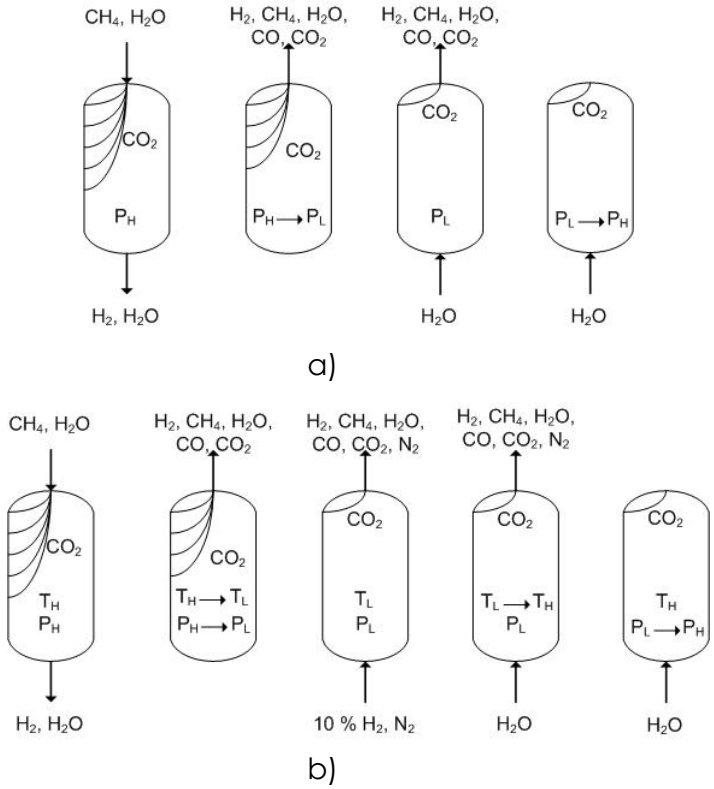

Figure 4.3. a) Skarstrom type PSA cycle with four steps: feed, depressurization, purge with steam and pressurization with steam[1, 41]. b) Cycle proposed by Xiu et al [1] including reactive regeneration purge with 10 % H_2.

The experimental results reported by Waldron *et al* [41] using a pilot-scale reactor (6 m column length and 25 mm diameter) show that an effluent stream containing 88-95 % H_2 was produced with methane as the main impurity and trace carbon oxides. Regeneration was performed at sub-atmospheric pressure (70~35 kPa). The simulations performed by Xiu *et al* [1] also confirm a hydrogen purity of 86.8 % with 587 ppm of CO_2 and 50 ppm CO. An important issue to consider in this process is that the amount of CO in the hydrogen stream should be controlled below 30 ppm to comply with PEM fuel cell specifications.

One drawback of the reactive regeneration is that desorption is endothermic and is not favored by the lower temperature. Simulations results using a column with 4 m indicated that the H_2 concentration in the product is 88 % with 28 ppm CO and 338 ppm CO_2. When the column size is increased to 6 m, the H_2 concentration in the product increases to 89 % with 28 ppm CO and 336 ppm CO_2.

4.2.2.2. Alternative design: sub-section controlled temperature

An alternative approach was developed by specific knowledge of what is happening inside the reactor: at the inlet section, reforming reactions are taking place intensively, while in the middle of the reactor the CO_2-selective sorption is enhancing the conversion and finally in the outlet portion of the reactor it is necessary to decrease the concentration of carbon oxides. Therefore, using a non-uniform packing ratio and different configurations of sorbent and catalyst, the performance of the process can be improved. Additionally, the outlet portion of the reactor can be set to a different operating temperature. If the temperature at the last portion of the reactor is reduced, the methanation and water gas shift reactions are promoted and also the CO_2 sorption capacity is increased. These two factors contribute to a total reduction of the concentration of carbon oxides in the gas phase allowing a longer feed step, improving the productivity of the process. This concept was developed by Xiu *et al* [43, 44] using a reactor divided into three sub-sections where the packing ratio of catalyst and sorbent changes and also where the temperature of the third sub-section may be different. This configuration is shown in Figure 4.4 [43, 44].

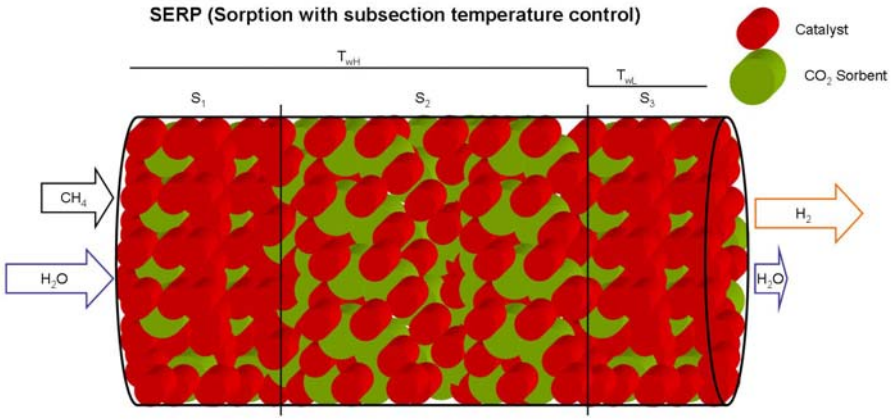

Figure 4.4. SMR-SERP reactor with 3 zones for subsection control. Zones S_1 and S_3 have a ratio of sorbent/catalyst = 2. Zone S_2 has a ratio of sorbent/catalyst = 4. Zone S_3 has a lower temperature to promote the conversion of carbon oxides to methane [43, 44].

With this strategy it was possible to obtain productivities of 1.27 mol/kg against 0.222 mol/kg without the sub-section controlled temperature. Some of the results of the simulations of the reactive regeneration and subsection-controlled temperature concepts are shown in Table 4.1. Comparing the results with and without the sub-section controlling temperature, it can be observed that the same unit productivity and can be maintained with a significant reduction in the CO and CO_2 contamination.

Table 4.1. Comparison of simulation results of a four step SMR-SERP unit using different operation strategies: base case (B), reactive regeneration with H_2 (R) and sub-section controlling temperature (S).

Nº	t_{feed} [s]	t_{depres} [s]	t_{purge} [s]	t_{pres} [s]	T [K]	y_{H2} [%]	y_{CH4} [%]	y_{CO2} [ppm]	y_{CO} [ppm]	X_{CH4} [%]	H_2 prod. [mol/kg]	Ref.
B1	250	150	450	100	723	86.03	13.91	546	42	61.05	0.103	[1]
B2	400	150	450	100	723	83.85	15.95	1254	82	56.55	0.166	
B3	500	150	450	100	723	82.41	17.29	2965	177	54.72	0.206	
R1	350	150	450	100	723/673	88.80	11.15	336	28	67.01	0.109	
R2	400	150	450	100	723/673	87.93	12.03	436	33	67.45	0.127	
R3	500	150	450	100	723/673	86.40	13.53	704	48	61.89	0.168	
S1	600	50	800	50	763	92.70	7.30	1525	198	78.40	0.197	[43]
S2	600	50	800	50	733	87.50	12.40	1136	86	65.20	0.184	
S3	600	50	800	50	763/713	92.50	7.50	204	18	75.90	0.213	
S4	600	50	800	50	733/693	87.60	12.40	270	16	65.10	0.184	
S5	400	50	600	50	763	93.80	6.20	717	95	82.60	0.130	
S6	400	50	600	50	733	88.80	11.10	825	69	71.60	0.113	
S7	1000	50	1100	50	763/713	91.40	8.60	284	23	71.20	0.356	
S8	1000	50	1100	50	733/693	86.30	13.70	373	21	60.90	0.307	

L_C = 6 m; R_C = 12.5 mm; P_H = 4.46 bar; P_L = 1.26 kPa; η(all) = 0.8; S/C = 6;

Purge step in regenerative purging: t_{purge} = 400 s (10 %H_2) at T_w = 673 K followed by 50 s (steam) at T_w = 723 K; Depressurization also performed at 673 K.

Sub-section controlling strategy: when temperature column has two numbers, the second value corresponds to the temperature in the third section of the reactor (see Figure 4.4) and of the depressurization, purge and pressurization steps.

4.2.2.3. Other cycle configurations

A cycle with 5 steps was also proposed by Xiu *et al* [45]. The new step was a low pressure purge with methane after the depressurization step. The new cycle was:

1. Reaction/sorption at high pressure;
2. Depressurization and reduction of the reactor temperature;
3. Low pressure purge with pure methane;
4. Low pressure purge with product hydrogen to displace the methane;
5. Pressurization with hydrogen at feed temperature.

The objective of this new step was to improve the regeneration time in order to have a continuous process with just two columns. As methane is a non-sorbing species, the regeneration would be faster. However, the reaction scheme does not take into account other reactions that take place when steam is not present: the methane reforming with CO_2 and the decomposition of methane or carbon dioxide to give coke. Therefore, the absence of steam might present a problem to this strategy.

A more complex mathematical model was also developed to determine the effect of the catalyst intraparticle diffusion limitations [42]. A mass balance to the catalyst particle was developed and the reaction effectiveness factors were calculated. The reaction effectiveness factor of the SMR reaction increased between 0.5 and 0.9 from the feed to the outlet end of the reactor. The water gas shift effectiveness factor is highly sensitive to the local carbon monoxide

concentration, varying in the range 0.4-1. Only the feed step was simulated.

4.3. Experimental

The equipment used previously to determine the steam methane reforming kinetics in Chapter 3 was employed with slight modifications to perform SERP experiments as shown in Figure 4.5.

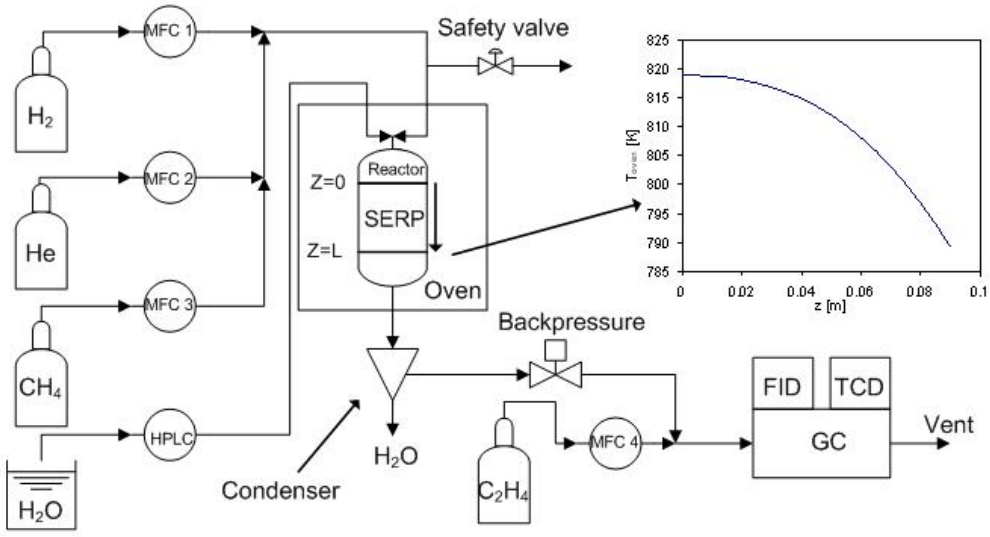

Figure 4.5. Experimental set-up employed for the SERP experiments.

To determine the temporal evolution of the exit flowrate, a stream of pure ethylene (C_2H_4) was added to the reactor effluent stream, after the backpressure regulator. Knowing the flowrate of pure ethylene (Q_{C2H4}) and the ethylene molar fraction in the resulting stream measured with the GC (y_{C2H4}), it is possible to calculate the flowrate of the stream exiting the reactor ($Q_{reactor}$) with the following equation [63]:

$$Q_{reactor} = \frac{Q_{C_2H_4}}{y_{C_2H_4,GC}} - Q_{C_2H_4} \quad (4.3)$$

For the SMR-SERP experiments, the reactor was loaded with alternating layers of catalyst and sorbent as shown in Figure 4.6.

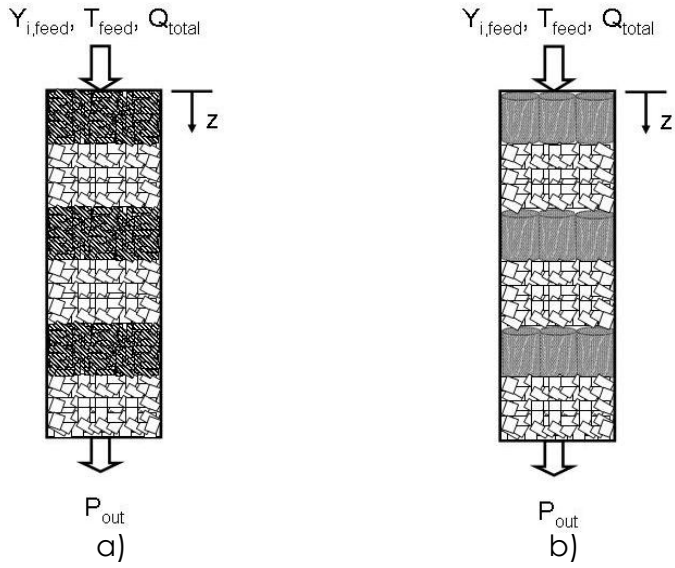

Figure 4.6. SMR-SERP Reactor configurations used in the experiments with extrudates: a) Alternating layers of Catalyst A and MG30-K sorbent; b) Alternating layers of Degussa Catalyst and MG30-K or MG30-Cs sorbent.

Prior to layer 1, an initial layer of quartz particles (5 mm) was used to accommodate flow variations. The composition of each layer is shown in Table 4.2. In order to compare the performance of each catalyst and sorbent, the length of each layer was maintained when the catalyst and sorbent were changed.

The reactor column was heated overnight to 776 K in He flow at 1 K/min. Prior to the SMR-SERP experiments it was necessary to remove all the CO_2 in the sorbent structure. A flow containing 10 % H_2 in steam at 1.01 bar was used until no CO_2 was detected in the effluent stream. Hydrogen was used to reduce the active metal of catalyst and prevent

its oxidation due to the presence of steam [62, 64]. Due to the exothermic sorption of steam in both the catalyst and the sorbent the flow of hydrogen and steam were started to the reactor 400 s prior to the methane flow. Helium was used to complete the total flowrate used.

Table 4.2. Reactor column solid composition employed for the SMR-SERP experiments using alternating layers of catalyst and sorbent extrudates.

Catalyst A/ MG30-K						
Layer	**1**	**2**	**3**	**4**	**5**	**6**
m_{cat} [kg] x 10^3	7.459	0.000	7.402	0.000	7.404	0.000
m_{sorb} [kg] x 10^3	0.000	18.592	0.000	16.041	0.000	17.832
L_{layer} [m] x 10^3	17	36	15	33	14	35
ε_c	0.53	0.50	0.47	0.53	0.44	0.53
Degussa/ MG30-K						
Layer	**1**	**2**	**3**	**4**	**5**	**6**
m_{cat} [kg] x 10^3	7.156	0.000	5.701	0.000	5.442	0.000
m_{sorb} [kg] x 10^3	0.000	19.282	0.000	16.083	0.000	16.410
L_{layer} [m] x 10^3	17	38	15	32	13	35
ε_c	0.40	0.50	0.46	0.51	0.41	0.54

In order to determine the response of layered system to different operating conditions (total pressure, feed temperature and feed flowrate), six experimental runs were performed using catalyst (Catalyst A or Degussa) and sorbent (MG30-K). The operating conditions of each of the experimental runs are reported in Table 4.3.

The reaction/sorption step of Run 1 was repeated in Run 2 in order to check the reproducibility of the experiments. Run 6 was a cyclic experiment with alternating reaction/regeneration steps. The reaction step was performed for 220 s and the regeneration step lasted 1200 s (~6 x reaction time). The pressurization took 50 s conditioning the column for the next cycle. The regeneration of the sorbent was made in the same direction as the reaction step (co-current regeneration).

Table 4.3. Operating conditions used in the SMR-SERP experiments employing layers of catalyst A or Degussa extrudates alternating with layers of MG30-K or MG30-Cs extrudates.

Reaction/Sorption						
Run	**1**	**2**	**3**	**4**	**5**	**6**
$y_{feed,\ CH4}$	0.189	0.189	0.189	0.189	0.189	0.184
$y_{feed,\ H2O}$	0.757	0.757	0.757	0.757	0.757	0.737
$y_{feed,\ H2}$	0.054	0.054	0.054	0.054	0.054	0.079
Q_{feed} [SLPM][a]	0.514	0.514	0.514	0.257	0.514	0.529
F_{feed} [mmol/min]	22.9	22.9	22.9	11.4	22.9	23.5
S/C	4.0	4.0	4.0	4.0	4.0	4.0
T_{oven} [K]	778	778	778	778	808	778
P_{out} [bar]	2.0	2.0	4.0	4.0	2.0	4.0
Regeneration						
Run	**1**	**2**	**3**	**4**	**5**	**6**
$y_{feed,\ CH4}$	0.000	0.000	0.000	0.000	0.000	0.000
$y_{feed,\ H2O}$	0.896	0.658	0.949	0.658	0.949	0.903
$y_{feed,\ H2}$	0.104	0.342	0.051	0.342	0.051	0.097
Q_{feed} [SLPM][a]	0.538	0.591	0.410	0.591	0.410	0.431
F_{feed} [mmol/min]	23.9	26.3	18.3	26.3	18.3	19.2
T_{oven} [K]	778	778	778	778	808	778
P_{out} [bar]	1.01					

a – Standard conditions are: 273 K and 1.01 bar.

All the experiments were performed in a vertical oven. The oven has a semi-parabolic temperature profile, with higher temperatures in the top of the oven. This profile was measured as a function of the axial position of the catalyst bed to describe $T_{\infty}(z)$ in the simulations performed (see Figure 4.5).

4.4. Theoretical

A mathematical model was developed to describe the SMR-SERP process. The following assumptions were made:

1. Axially dispersed plug flow;

2. Ideal gas behavior;
3. There are no mass or heat variations within the radial direction of the column;
4. There are film mass and heat transfer resistances in the external layer of the extrudates;
5. The mass transfer in the radial direction of the catalyst particles is described by pore diffusion;
6. The reaction takes place in the Ni crystallites present in the catalyst solid phase;
7. The column porosity is considered constant if the catalyst and sorbent extrudates are mixed. When there are different layers of catalyst or sorbent, the porosity within each layer is constant;
8. Sorption in the hydrotalcite pellets was only considered for CO_2;
9. The carbon dioxide sorption equilibrium was described by the bi-Langmuir model [65] proposed in Chapter 2.
10. There is no radial heat transfer resistance within the catalyst extrudates;
11. There is no radial heat transfer resistance within the sorbent extrudates.

In the case of the extrudates of catalyst A, there is a large pore network that increases the mass transfer. Therefore, in the case of catalyst A the additional assumption is:

12. The mass transfer in the axial direction of the catalyst particles is described by pore diffusion and also by convection within the catalyst.

The hydrotalcite sorbent particles were modeled as spheres since the radius and the height of the particle are identical.

As seen in section 2, the catalyst and sorbent extrudates can be loaded into the SMR-SERP reactor in different configurations. Therefore, it is necessary to determine how the total solid phase inside the reactor is divided:

$$V_{solid} = V_{cat} + V_{sorb} \tag{4.4}$$

Defining the catalyst fraction inside the reactor as the volume of catalyst in the total solid volume:

$$\alpha = \frac{V_{cat}}{V_{solid}} \tag{4.5}$$

and as a result, the sorbent fraction inside the reactor is:

$$(1-\alpha) = \frac{V_{sorb}}{V_{solid}} \tag{4.6}$$

These equations define how the solid phase in the SERP reactor is composed. In the case of layered configuration, α = 1 for the catalyst layer and $\alpha = 0$ for the sorbent layer. When using a layered configuration, the porosity (ε_c) is constant within each layer and may be different from layer to layer.

The mass balance to the gas phase within the reactor column filled with sorbent and catalyst particles is:

$$\varepsilon_c \frac{\partial C_i}{\partial t} = -\frac{\partial (uC_i)}{\partial z} + \varepsilon_c \frac{\partial}{\partial z}\left(D_{ax} C_T \frac{\partial y_i}{\partial z}\right) - (1-\varepsilon_c)\alpha a_{p,cat} k_{f,cat}\left(C_i - C_{cat,i}\big|_{r_{cat}=R_{cat}}\right) - (1-\varepsilon_c)(1-\alpha)\frac{a_{p,sorb} k_{f,sorb}}{Bi+1}\left(C_i - \overline{C}_{sorb,i}\right) \tag{4.7}$$

The energy transfer in the SMR-SERP reactor was described using a heterogeneous model with independent equations for the gas and solid phases and the reactor wall where energy is exchanged with the surroundings. As the catalyst and sorbent extrudates can have different

sizes, heat transfer to different solid particles was also taken into account in the reactor energy balance. The energy balance for the gas phase is:

$$\varepsilon_c C_T \hat{C}_{vg} \frac{\partial T}{\partial t} = \varepsilon_c \frac{\partial}{\partial z}\left(\lambda_{ax} \frac{\partial T}{\partial z}\right) - \upsilon C_T \hat{C}_{pg} \frac{\partial T}{\partial z} + \varepsilon_c R_g T \frac{\partial C_T}{\partial t} - 2\frac{h_w}{R_c}(T - T_w) - (1-\varepsilon_c)\alpha a_{p,cat} h_{f,cat}(T - T_{cat}) - (1-\varepsilon_c)(1-\alpha) a_{p,sorb} h_{f,sorb}(T - T_{sorb}) \quad (4.8)$$

The mass balance to the catalyst particle was developed considering convection, diffusion and reaction inside the catalyst particle [66]:

$$\varepsilon_{p,cat} \frac{\partial C_{cat,i}}{\partial t} = \varepsilon_{p,cat} D_{p,cat}\left(\frac{\partial^2 C_{cat,i}}{\partial r_{cat}^2} + \frac{1}{R_{cat}} \frac{\partial C_{cat,i}}{\partial r_{cat}} + \frac{\partial^2 C_{cat,i}}{\partial z_{cat}^2}\right) - v_{cat} \frac{\partial C_{cat,i}}{\partial z_{cat}} + \rho_{cat} \sum_{j=1}^{3} \upsilon_{j,i} R_j \quad (4.9)$$

In Chapter 3 it was shown that the temperature inside a catalyst particle was constant in the radial coordinate of the catalyst. It is therefore possible to simplify the energy balance by considering homogeneous particle in the radial coordinate. In the case of the large-pore particles, axial heat dispersion and convection were still considered.

$$\left(\varepsilon_{p,cat} \hat{C}_{vg} \overline{C}_{T,cat} + (1-\varepsilon_{p,cat}) \rho_{solid,cat} \hat{C}_{ps,cat}\right) \frac{\partial T_{cat}}{\partial t} = -v_{cat} \hat{C}_{pg} \overline{C}_{T,cat} \frac{\partial T_{cat}}{\partial z_{cat}} + \lambda_{cat} \frac{\partial^2 T_{cat}}{\partial z_{cat}^2} + a_{p,cat} h_{f,cat}(T - T_{cat}) + \varepsilon_{p,cat} R_g T_{cat} \frac{\partial \overline{C}_{T,cat}}{\partial t} + \rho_{cat} \sum_{j=1}^{3} \overline{R}_j (-\Delta H_j) \quad (4.10)$$

where $\overline{C}_{T,cat}$ is the average total concentration in the in the radial direction and $\overline{R}_j$ is the average reaction rate in the radial direction. These variables are calculated using the following equations:

$$\overline{C}_{T,cat} = \frac{2\int_{r_{cat}=0}^{r_{cat}=R_{cat}} r_{cat}\sum_{i=1}^{5}(C_{cat,i})dr_{cat}}{R_{cat}^2} \tag{4.11}$$

$$\overline{R}_j = \frac{2\int_{r_{cat}=0}^{r_{cat}=R_{cat}} r_{cat}R_j dr_{cat}}{R_{cat}^2} \tag{4.12}$$

The mass transfer from the gas phase to the pore network of the sorbent was approximated using the linear driving force model [67].

$$\frac{\partial\overline{C}_{sorb,i}}{\partial t} = \frac{15D_{p,sorb}}{R_{sorb}^2}\frac{Bi}{Bi+1}\left(C_i - \overline{C}_{sorb,i}\right) - \frac{\rho_{sorb}}{\varepsilon_{p,sorb}}\frac{\partial\overline{q}_i}{\partial t} \tag{4.13}$$

The temperature inside the sorbent particle was considered constant in the radial coordinate. The temperature in the sorbent particles is described by:

$$\left[\varepsilon_{p,sorb}\hat{C}_{vg}\overline{C}_{T,sorb} + (1-\varepsilon_{p,sorb})\rho_{solid,sorb}\hat{C}_{ps,sorb} + (1-\varepsilon_{p,sorb})\frac{\rho_{sorb}}{(1-\varepsilon_{p,sorb})}\left(\sum_{i=1}^{5}\overline{q}_i\right)\hat{C}_{vg}\right]$$
$$(1-\varepsilon_c)\frac{\partial T_{sorb}}{\partial t} = (1-\varepsilon_c)a_{p,sorb}h_{f,sorb}(T-T_{sorb}) + (1-\varepsilon_c)\varepsilon_{p,sorb}R_g T_{sorb}\frac{\partial\overline{C}_{T,sorb}}{\partial t} + \tag{4.14}$$
$$(1-\varepsilon_c)\rho_{sorb}\sum_{i=1}^{5}\frac{\partial\overline{q}_i}{\partial t}(\beta(-\Delta H_1) + (1-\beta)E_2)$$

The energy exchange with the surroundings is described by the following equation:

$$\rho_w\hat{C}_{pw}\frac{\partial T_w}{\partial t} = \frac{2R_c}{(w_{thick}(2R_c + w_{thick}))}h_w(T-T_w) -$$
$$-\frac{1}{\left((2R_c + w_{thick})\ln\left(\frac{2R_c + w_{thick}}{2R_c}\right)\right)}U(T_w - T_\infty) \tag{4.15}$$

The Ergun equation was used to describe the pressure drop inside the reactor [68].

$$-\frac{\partial P_T}{\partial z} = 150\frac{\mu_{gas}(1-\varepsilon_c)^2}{4\bar{R}_p^2\varepsilon_c^3}u + 1.75\frac{\rho_{gas}(1-\varepsilon_c)}{2\bar{R}_p\varepsilon_c^3}|u|u \quad (4.16)$$

The Ergun equation was originally derived considering a bed of particles of the same size. As the catalyst and sorbent extrudates have different sizes the following equation was used to calculate the average particle radius [69].

$$\frac{1}{\bar{R}_p} = \frac{x_{cat}}{R_{cat}} + \frac{x_{sorb}}{R_{sorb}} = \frac{x_{cat}}{R_{cat}} + \frac{(1-x_{cat})}{R_{sorb}} \quad (4.17)$$

where x_{cat} and x_{sorb} are the weight fraction of the particles of catalyst and sorbent in the mixture of solids.

In the case of catalyst A, the intraparticle velocity was calculated using the following equation (as shown in Chapter 3) [70-72]:

$$v_{cat} = \frac{(1-\varepsilon_c)^2\varepsilon_{p,cat}^3 d_{microsphere,cat}^2}{(1-\varepsilon_{p,cat})^2\varepsilon_c^3(2R_{cat})^2}u + \frac{1.75(1-\varepsilon_c)\rho_{gas}\varepsilon_{p,cat}^3 d_{microsphere,cat}^2}{150(1-\varepsilon_{p,cat})^2\mu_{gas}\varepsilon_c^3(2R_{cat})}|u|u \quad (4.18)$$

The steam methane reforming is described by the set of three reactions, as proposed by Xu and Froment [62] with the corresponding reaction rate expressions already given in Chapter 3. Only carbon dioxide is considered to sorb in the hydrotalcite extrudates with first order sorption kinetics.

The performance of the SMR-SERP will be evaluated with four different variables: SERP enhancement factor (% SERP), hydrogen purity (Purity), productivity and gain.

The SERP enhancement factor is the ratio of the average conversion during the reaction step to the equilibrium conversion at

feed conditions, indicating what is the advantage of SERP when compared to the equilibrium conversion at the same feed temperature.

$$\%\ \text{SERP} = \frac{\int_0^{tfeed} X_{CH4}\, dt_{feed}}{X_{CH4}\, t_{feed}} \times 100 \tag{4.19}$$

The purity is an important parameter as it indicates the quality of hydrogen produced during the reaction step. This parameter will be evaluated using the dry effluent molar flowrates.

$$\text{Purity} = \frac{\int_0^{tfeed} F_{H2,out}\, dt_{feed}}{\int_0^{tfeed} \left(F_{H2,out} + F_{CH4,out} + F_{CO2,out} + F_{CO,out}\right) dt_{feed}} \tag{4.20}$$

The productivity measures how much high purity hydrogen is in fact produced by the SMR-SERP reactor. The value of the productivity is normalized by the reactor volume to provide a basis for comparison with other works.

$$\text{Productivity}\left[\frac{mol}{m^3 h}\right] = \frac{\int_0^{tfeed} F_{H2} dt_{feed} - \left(F_{H2,feed} t_{feed} + F_{H2,regeneration} t_{regeneration}\right)}{A_{col} L_c t_{cycle}} \tag{4.21}$$

Finally, the gain is defined as the amount of high purity hydrogen produced per mol of methane fed. The equation is normalized by the maximum amount of hydrogen that can be produced using 1 mol of methane.

$$\text{Gain}\left[\frac{mol_{H2}}{4 mol_{CH4}}\right] = \frac{\int_0^{tfeed} F_{H2} dt_{feed} - \left(F_{H2,feed} t_{feed} + F_{H2,regeneration} t_{regeneration}\right)}{4 F_{CH4,feed} t_{feed}} \tag{4.22}$$

The centered finite difference method with second order approximation was used for the discretisation of the differential equations using at least 200 elements for the axial coordinate of the reactor and 20 elements for the radial coordinate of the catalyst extrudates. The software package gPROMS was used to solve this model.

4.4.1. Boundary conditions

A set of boundary conditions is necessary to solve the mass and energy balances to the catalyst particles. For the radial coordinate (Catalyst A and Degussa) the boundary conditions are:

$$\left.\frac{\partial C_{cat,i}}{\partial r_{cat}}\right|_{r_{cat}=0} = 0.0 \tag{4.23}$$

$$\varepsilon_{P,cat} D_{p,cat} \left.\frac{\partial C_{cat,i}}{\partial r_{cat}}\right|_{r=R_{cat}} = k_{f,cat}\left(C_i - C_{cat,i}\big|_{r_{cat}=R_{cat}}\right) \tag{4.24}$$

$$\left.\frac{\partial T_{cat}}{\partial r_{cat}}\right|_{r_{cat}=0} = 0.0 \tag{4.25}$$

$$\lambda_{cat} \left.\frac{\partial T_{cat}}{\partial r_{cat}}\right|_{r_{cat}=R_{cat}} = h_{f,cat}\left(T - T_{cat}\big|_{r_{cat}=R_{cat}}\right) \tag{4.26}$$

In the case of the large-pore extrudates (Catalyst A), boundary conditions are also necessary for the particle axial coordinate:

$$-\varepsilon_{P,cat} D_{p,cat} \left.\frac{\partial C_{cat,i}}{\partial z_{cat}}\right|_{z_{cat}=0} + v_{cat} C_{cat,i}\big|_{z_{cat}=0} = k_{f,cat}\left(C_i - C_{cat,i}\big|_{z_{cat}=0}\right) \tag{4.27}$$

$$-\varepsilon_{P,cat} D_{p,cat} \left.\frac{\partial C_{catj}}{\partial z_{cat}}\right|_{z_{,cat}=L_{cat}} + v_{cat} C_{catj}\big|_{z_{cat}=L_{cat}} = k_{f,cat}\left(C_i - C_{catj}\big|_{z_{cat}=L_{cat}}\right) \tag{4.28}$$

$$-\lambda_{cat}\left.\frac{\partial T_{cat}}{\partial z_{cat}}\right|_{z_p=0}+v_{cat}\hat{C}_{pg}\sum C_{cat,i}T_{cat}\big|_{z_{cat}=0}=h_{f,cat}\left(T-T_{cat}\big|_{z_{cat}=0}\right) \quad (4.29)$$

$$-\lambda_{cat}\left.\frac{\partial T_{cat}}{\partial z_{cat}}\right|_{z_{cat}=L_{cat}}+v_{cat}\hat{C}_{pg}\sum C_{cat,i}T_{cat}\big|_{z_{cat}=L_{cat}}=h_{f,cat}\left(T-T_{cat}\big|_{z_{cat}=L_{cat}}\right) \quad (4.30)$$

To solve the mass, energy and momentum balances to the SMR-SERP reactor, different sets of boundary conditions are necessary depending on the cycle step. Four different cycle steps will be considered: reaction, depressurization, purge and pressurization. In the SMR-SERP experiments the depressurization, purge and pressurization steps were made co-currently to the reaction step. In the SMR-SERP simulations the depressurization, purge and pressurization steps can also be performed in counter-current fashion. The complete set of boundary conditions to the SMR-SERP reactor column are:

Reaction

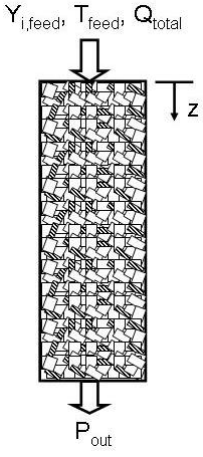

$$\varepsilon_c D_{ax}\left.\frac{\partial C_i}{\partial z}\right|_{z=0}=-u_{feed}\left(\frac{y_{i,feed}P_T}{R_g T}\Big|_{z=0}-C_i\big|_{z=0}\right) \quad (4.31)$$

$$\lambda_{ax}\left.\frac{\partial T}{\partial z}\right|_{z=0}=-u_{feed}C_T\hat{C}_{pg}\left(T_{feed}-T\big|_{z=0}\right) \quad (4.32)$$

$$u_{z=0}=\frac{Q_{total}}{A_{col}} \quad (4.33)$$

$$\left.\frac{\partial C_i}{\partial z}\right|_{z=L_c}=0.0 \quad (4.34)$$

$$\left.\frac{\partial T}{\partial z}\right|_{z=L_c}=0.0 \quad (4.35)$$

$$P_T\big|_{z=L_c}=P_{out} \quad (4.36)$$

Co-current depressurization

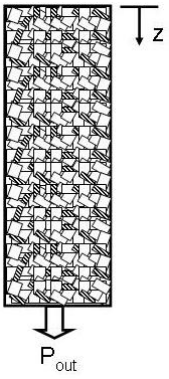

$$\left.\frac{\partial C_i}{\partial z}\right|_{z=0} = 0.0 \quad (4.37)$$

$$\left.\frac{\partial T}{\partial z}\right|_{z=0} = 0.0 \quad (4.38)$$

$$u_{z=0} = 0.0 \quad (4.39)$$

$$\left.\frac{\partial C_i}{\partial z}\right|_{z=L_C} = 0.0 \quad (4.40)$$

$$\left.\frac{\partial T}{\partial z}\right|_{z=L_C} = 0.0 \quad (4.41)$$

$$P_T\big|_{z=L_c} = P_{out} \quad (4.42)$$

Counter-current depressurization

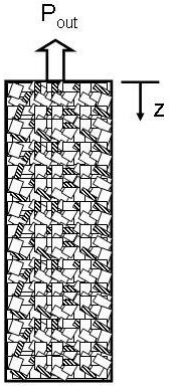

$$\left.\frac{\partial C_i}{\partial z}\right|_{z=0} = 0.0 \quad (4.43)$$

$$\left.\frac{\partial T}{\partial z}\right|_{z=0} = 0.0 \quad (4.44)$$

$$P_T\big|_{z=0} = P_{out} \quad (4.45)$$

$$\left.\frac{\partial C_i}{\partial z}\right|_{z=L_C} = 0.0 \quad (4.46)$$

$$\left.\frac{\partial T}{\partial z}\right|_{z=L_C} = 0.0 \quad (4.47)$$

$$u_{z=L_c} = 0.0 \quad (4.48)$$

Co-current purge

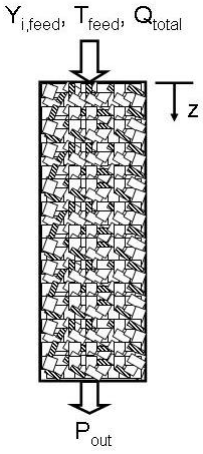

$$\varepsilon_c D_{ax} \left.\frac{\partial C_i}{\partial z}\right|_{z=0} = -u_{feed}\left(\frac{y_{i,feed}P_T}{R_g T}\bigg|_{z=0} - C_i\big|_{z=0}\right) \tag{4.49}$$

$$\lambda_{ax} \left.\frac{\partial T}{\partial z}\right|_{z=0} = -u_{feed} C_T \hat{C}_{pg}\left(T_{feed} - T\big|_{z=0}\right) \tag{4.50}$$

$$u_{z=0} = \frac{Q_{total}}{A_{col}} \tag{4.51}$$

$$\left.\frac{\partial C_i}{\partial z}\right|_{z=L_C} = 0.0 \tag{4.52}$$

$$\left.\frac{\partial T}{\partial z}\right|_{z=L_C} = 0.0 \tag{4.53}$$

$$P_T\big|_{z=L_c} = P_{out} \tag{4.54}$$

Contra-current purge

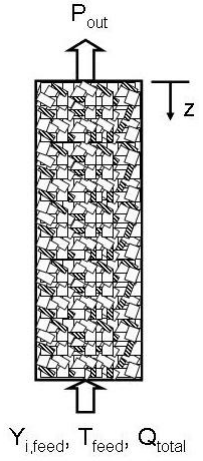

$$\left.\frac{\partial C_i}{\partial z}\right|_{z=0} = 0.0 \tag{4.55}$$

$$\left.\frac{\partial T}{\partial z}\right|_{z=0} = 0.0 \tag{4.56}$$

$$P_T\big|_{z=0} = P_{out} \tag{4.57}$$

$$\varepsilon_c D_{ax} \left.\frac{\partial C_i}{\partial z}\right|_{z=L_c} = -u_{feed}\left(\frac{y_{i,feed}P_T}{R_g T}\bigg|_{z=L_c} - C_i\big|_{z=L_c}\right) \tag{4.58}$$

$$\lambda_{ax} \left.\frac{\partial T}{\partial z}\right|_{z=L_c} = -u_{feed} C_T \hat{C}_{pg}\left(T_{feed} - T\big|_{z=L_c}\right) \tag{4.59}$$

$$u_{z=L_c} = -\frac{Q_{total}}{A_{col}} \tag{4.60}$$

Co-current pressurization

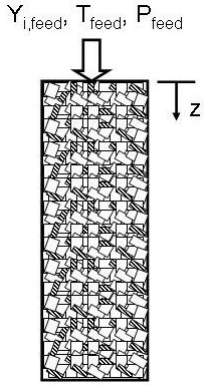

$$\varepsilon_c D_{ax} \left.\frac{\partial C_i}{\partial z}\right|_{z=0} = -u_{feed}\left(\frac{y_{i,feed}P_T}{R_g T}\bigg|_{z=0} - C_i\big|_{z=0}\right) \tag{4.61}$$

$$\lambda_{ax} \left.\frac{\partial T}{\partial z}\right|_{z=0} = -u_{feed} C_T \hat{C}_{pg}\left(T_{feed} - T\big|_{z=0}\right) \tag{4.62}$$

$$P_T\big|_{z=0} = P_{feed} \tag{4.63}$$

$$\left.\frac{\partial C_i}{\partial z}\right|_{z=L_C} = 0.0 \tag{4.64}$$

$$\left.\frac{\partial T}{\partial z}\right|_{z=L_C} = 0.0 \tag{4.65}$$

$$u_{z=L_c} = 0.0 \tag{4.66}$$

Counter-current pressurization

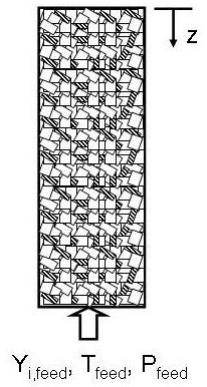

$$\left.\frac{\partial C_i}{\partial z}\right|_{z=0} = 0.0 \tag{4.67}$$

$$\left.\frac{\partial T}{\partial z}\right|_{z=0} = 0.0 \tag{4.68}$$

$$u_{z=0} = 0.0 \tag{4.69}$$

$$\varepsilon_c D_{ax} \left.\frac{\partial C_i}{\partial z}\right|_{z=L_c} = -u_{feed}\left(\frac{y_{i,feed}P_T}{R_g T}\bigg|_{z=L_c} - C_i\big|_{z=L_c}\right) \tag{4.70}$$

$$\lambda_{ax} \left.\frac{\partial T}{\partial z}\right|_{z=L_c} = -u_{feed} C_T \hat{C}_{pg}\left(T_{feed} - T\big|_{z=L_c}\right) \tag{4.71}$$

$$P_T\big|_{z=L_c} = P_{feed} \tag{4.72}$$

4.5. Results and discussion

In this section, several steam methane reforming sorption enhanced reaction process experiments were made using the MG30-K sorbent reported in Chapter 2 and the catalysts reported in Chapter 3 (Degussa and catalyst A). The objective of these experiments was to measure experimental results of SMR-SERP with a commercial and a large-pore catalyst as well as to evaluate the predictive capabilities of the mathematical model. Then, the SMR-SERP mathematical model was used to simulate the cyclic process proposed by Xiu *et al* [1] including a reactive regeneration purge. Preliminary experiments performed to test the SMR-SERP concept are reported in Appendix B.

4.5.1. SMR-SERP experiments using Catalyst A and MG30-K sorbent

The SMR-SERP reactor was filled with alternating layers (a total of 6) of catalyst A and MG30-K sorbent as shown in Figure 4.6a). The layered configuration was already proposed for the dehydrogenation of ethane to ethylene and hydrogen by Lu *et al* [32] and by Rawadieh and Gomes [34] the production of ethene from propene .

After heating the reactor to 778 K, reducing the catalyst using H_2 and desorbing the CO_2 present in the interlayer of the sorbent, six SMR-SERP experimental runs were performed, employing the experimental conditions reported in Table 4.3. The mathematical model was used to simulate the experimental conditions using the parameters shown in Table 4.4. The reaction rate kinetic constants of Catalyst A and the CO_2

sorption equilibrium and kinetics determined in previous chapters were used in the mathematical model. No fitting parameters were used to simulate the experimental results. Additionally, simulations were made using the mathematical model developed for SMR with catalyst extrudates reported in Chapter 3, employing the same total catalyst mass and catalytic bed length used in the SMR-SERP experiments. The objective is to determine if after the sorbent is saturated with carbon dioxide the SMR-SERP reactor gives the same result as a SMR reactor. The transport parameters in Table 4.4 were calculated using the correlations in Appendix A.

Table 4.4. Parameters used in the simulations of the non-isothermal SMR-SERP reactor composed of 6 alternating layers of catalyst A and MG30-K extrudates.

Column		**Catalyst A**	
R_c [m]	0.0133	**R_{cat} [mm]**	5.6
w_{thick} [m]	0.0091	**$L_{p,cat}$ [mm]**	15.5
h_w [W/(m².K)]	400	**$r_{pore,cat}$ [mm]**	0.4
U [W/(m².K)]	200	**ρ_{cat} [kg/m³]**	1687
$\hat{C}p_w$ [J/(kg.K)]	500	**$\varepsilon_{p,cat}$**	0.57
ρ_w [kg/m³]	7750	**τ_p**	1.76
ρ_{gas} [kg/m³][a]	0.52	**$a_{p,cat}$ [m⁻¹]**	354
μ_{gas} [Pa.s][a]	2.69×10^{-5}	**$\hat{C}_{ps,cat}$ [J/(kg.K)]**[a]	1096
λ_{ax} [W/m.K][a]	0.50	**$h_{f,cat}$ [W/(m².K)]**[a]	335.1
D_{ax} [m²/s][a]	0.70×10^{-4}	**$k_{f,cat}$ [m/s]**[a]	0.033
D_m [m²/s][a]	0.84×10^{-4}	**$D_{k,cat}$ [m²/s]**[a]	2854×10^{-4}
		$D_{p,cat}$ [m²/s][a]	0.476×10^{-4}
MG30-K hydrotalcite		**MG30-K hydrotalcite**	
r_{sorb} [mm]	2.215	**$a_{p,sorb}$ [m⁻¹]**	1354
$r_{pore,sorb}$ [nm]	4.55	**$\hat{C}_{ps,sorb}$ [J/(kg.K)]**	850
ρ_{sorb} [kg/m³]	1845	**$h_{f,sorb}$ [W/(m².K)]**[a]	49.8
$\varepsilon_{p,sorb}$	0.27	**$k_{f,sorb}$ [m/s]**[a]	0.067

a – Calculated for the reaction conditions at 778 K and 2 bar.

As previously observed in the SMR experiments, there is a strong decrease in the temperature inside the reactor due to the endothermic

natured of the SMR reactions. The CO_2 sorption in hydrotalcites is exothermic, therefore the different layers will have different temperatures. The temperature was measured by three thermocouples inserted into the reactor at the following positions from the feed end: 6 mm (first catalyst layer); 46 mm (first sorbent layer) and 87 mm (second sorbent layer).

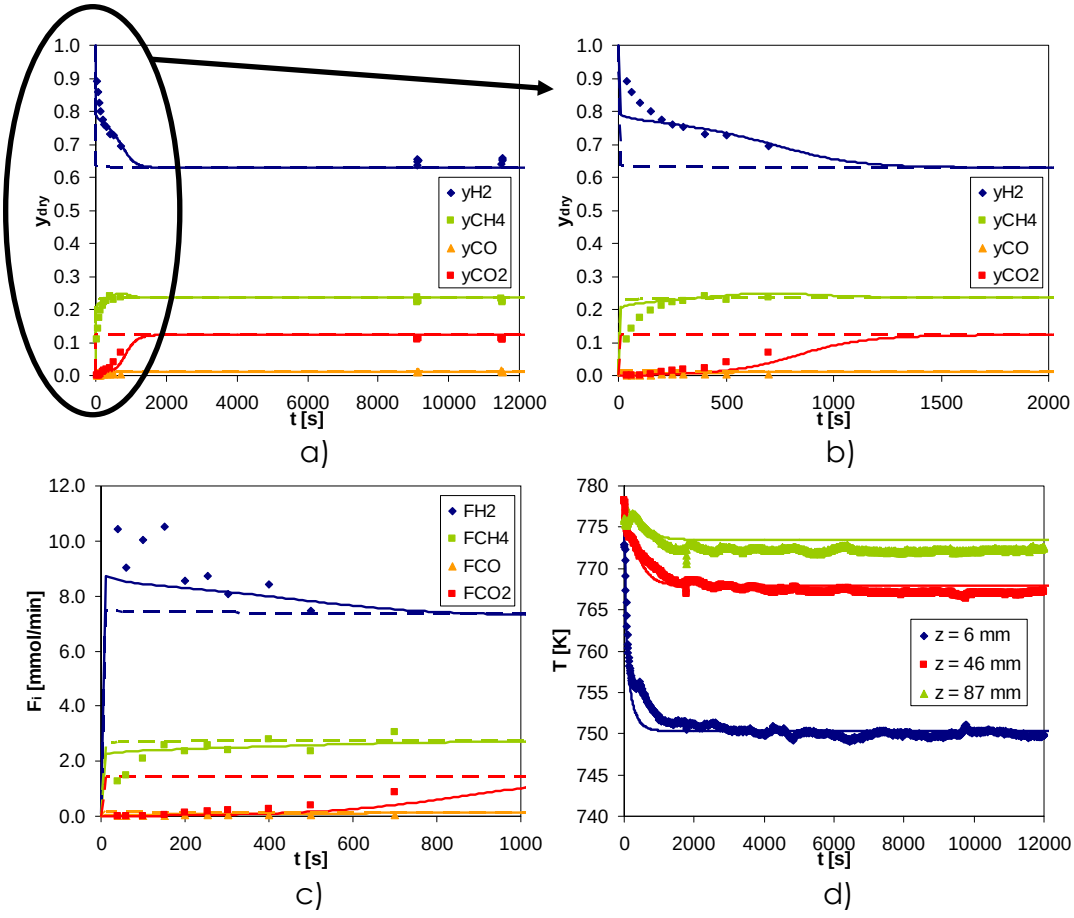

Figure 4.7. Dry-basis molar fractions (a-b), molar flowrates (c) and temperature (d) histories measured during the reaction step of Run 1 (2 bar, 778 K and 22.9 mmol/min total molar flowrate) of SMR-SERP using alternate layers of Catalyst A and MG30-K sorbent. Solid points are experimental results, lines are simulated results and dotted lines are SMR results using the same amount of catalyst.

The experimental and simulated dry basis molar fractions, molar flowrates and temperature histories of Run 1 are reported in Figure 4.7.

During the operation of the SMR-SERP, the hydrogen dry basis molar fraction continuously decreases with time as shown in Figure 4.7b. In the layered configuration used in this work this means that, when each sorbent layer becomes saturated with CO_2, the following catalyst layer comes in contact with more CO_2, decreasing the sorption enhancement effect. In Run 1, the SERP effect lasts less than 1600 s after which the SMR-SERP reactor works as a regular SMR reactor – SMR-SERP simulation overlaps SMR simulation.

At the start of the experimental run, the methane dry basis molar fraction slowly increases while the simulated CH_4 molar fraction takes less than 10 s to reach a value close to 0.2. After less than 100 s, the experimental and simulated values overlap. A similar lag happens between the experimental and simulated hydrogen dry basis molar fractions. This delay effect is due to the large dead-volume (over 50 ml) of the ice-trap used to remove H_2O from the effluent stream. However, it is noticeable that the breakthrough of methane is much faster than CO or CO_2 indicating that methane is the primary contaminant (20-25 %) of the high purity hydrogen produced.

The experimental results of Run 1 in Figure 4.7 and Run 2 in Figure 4.9 also indicate that the CO_2 breakthrough happens between 100 and 150 s after the reaction starts. The carbon dioxide dry basis molar fraction then takes more than 1500 s to reach the final value of 0.12. Experimental results also show that the CO breakthrough is almost simultaneous with CO_2 which is good for cyclic operation since controlling the feed time will prevent breakthrough of both carbon oxides. Finally, in Figure 4.7c and d it can be observed that the mathematical model is able to describe both molar flowrates and temperatures variations during the reaction step.

After almost 4 h of reaction, the regeneration was initiated by changing the operating conditions (P_T = 1.0 bar; $y_{CH4,feed}$ = 0.0; $y_{H2O,feed}$ = 0.90; $y_{H2,feed}$ = 0.10; F_{feed} = 23.9 mmol/min). The experimental and simulation results are shown in Figure 4.8.

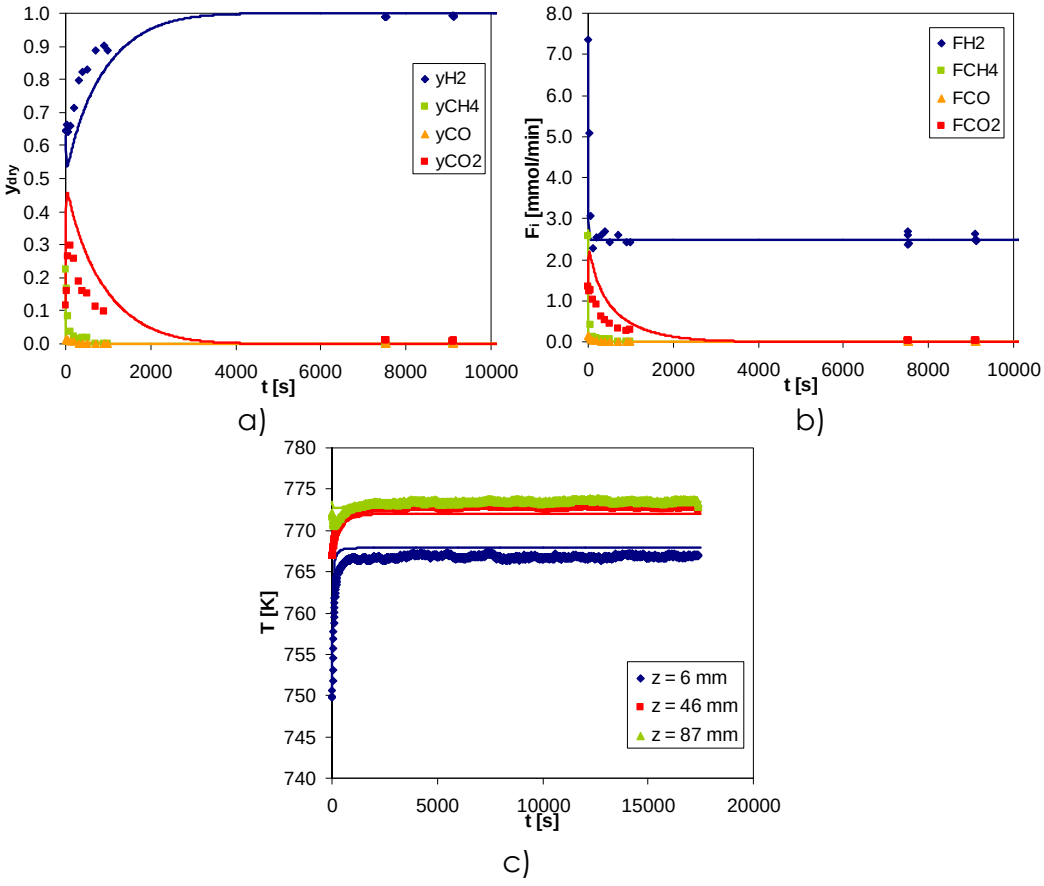

Figure 4.8. Dry-basis molar fractions (a), molar flowrates (b) and temperature (c) histories measured during the sorbent regeneration step of Run 1 using 10 % H_2 in H_2O (1.01 bar, 778 K and 23.9 mmol/min total molar flowrate). Alternate layers of Catalyst A and MG30-K sorbent were employed in the SMR-SERP experiment. Solid points are experimental results, lines are simulated results.

The complete regeneration of the sorbent took more than 5 h, which was 9 times longer than the complete breakthrough of CO_2. In Chapter 2 it was already reported that the desorption of carbon dioxide from the hydrotalcite was slow due to the strong steepness of the CO_2

sorption equilibrium isotherm. Figure 4.8 shows that the mathematical model was able to predict the trend of the experimental H_2 and CO_2 data but overestimates the CO_2 effluent molar fraction. In this work, the same LDF constant was employed for the sorption and desorption of CO_2. However, these results show that the desorption of CO_2 is slower than the sorption. This result has to be taken into account in the design of the cyclic process.

The difference between the sorbent regeneration step of Runs 1 and 2 is the H_2 molar fraction used during the regeneration: 0.10 and 0.34, respectively. For the case of using 10 % of H_2, methane was detected in the first 700 s of the regeneration, indicating that some H_2 was reacting with CO_2. For the case of 34 % H_2, methane was detected until 1900 s. The utilization of this reaction (reverse WGS) was proposed by Xiu *et al* [1] as a "reactive regeneration". It is important to notice that using hydrogen in the regeneration step decreases productivity and gain. Therefore, the amount of H_2 employed during the regeneration step should be limited. After the regeneration started, the temperature in the reactor increased as the SMR reactions were no longer taking place (see Figure 4.8d).

The reaction step of Run 1 was repeated in Run 2 to check its reproducibility. The mathematical model employed in the simulations (see Figure 4.9a), could satisfactorily describe the two different effects taking place with the SMR-SERP: the total amount of CO_2 formed (and methane converted) by the catalyst as well as the sorption of CO_2 by the sorbent.

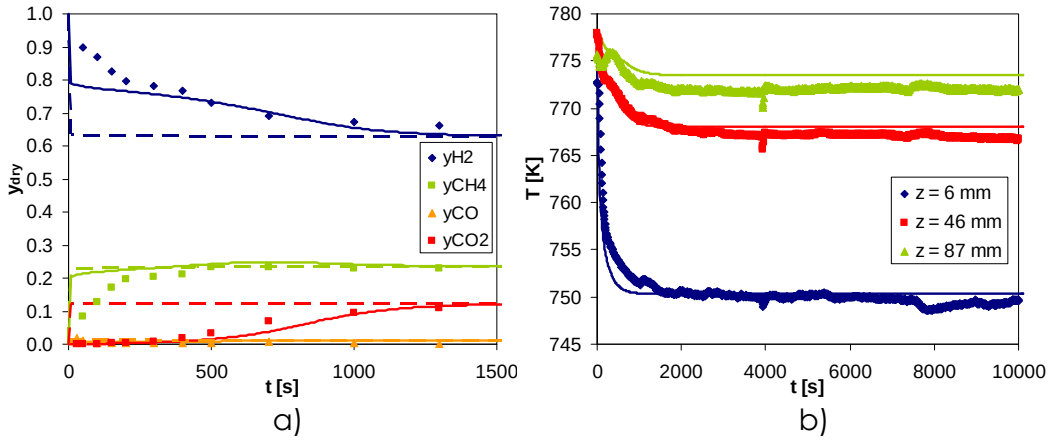

Figure 4.9. Dry-basis molar fractions (a) and temperature (b) histories measured during the reaction step of Run 2 (2 bar, 778 K and 22.9 mmol/min total molar flowrate). The SMR-SERP reactor was filled with alternate layers of Catalyst A and MG30-K sorbent. Solid points are experimental results, lines are simulated results and dotted lines are SMR results using the same amount of catalyst.

The objective of Runs 3-5 was to determine the influence of total pressure, feed flowrate and temperature (feed molar fractions were maintained constant). In Run 3 a total pressure of 4.0 bar was used while maintaining constant the other operating conditions of Run 2 (22.9 mmol/min and 778 K). In Run 4, the total pressure and feed temperature of Run 3 were used but the feed flowrate was reduced to 11.4 mmol/min. To check the effect of feed temperature, in Run 5 the feed flowrate and total pressure of Run 2 (22.9 mmol/min and 2.0 bar) were maintained but the feed temperature was increased to 808 K. The dry basis effluent molar fractions and temperatures of the reaction step of those runs are reported in Figure 4.10. The experimental and simulated results obtained for the regeneration step of runs 3-5 are shown in Figure 4.12.

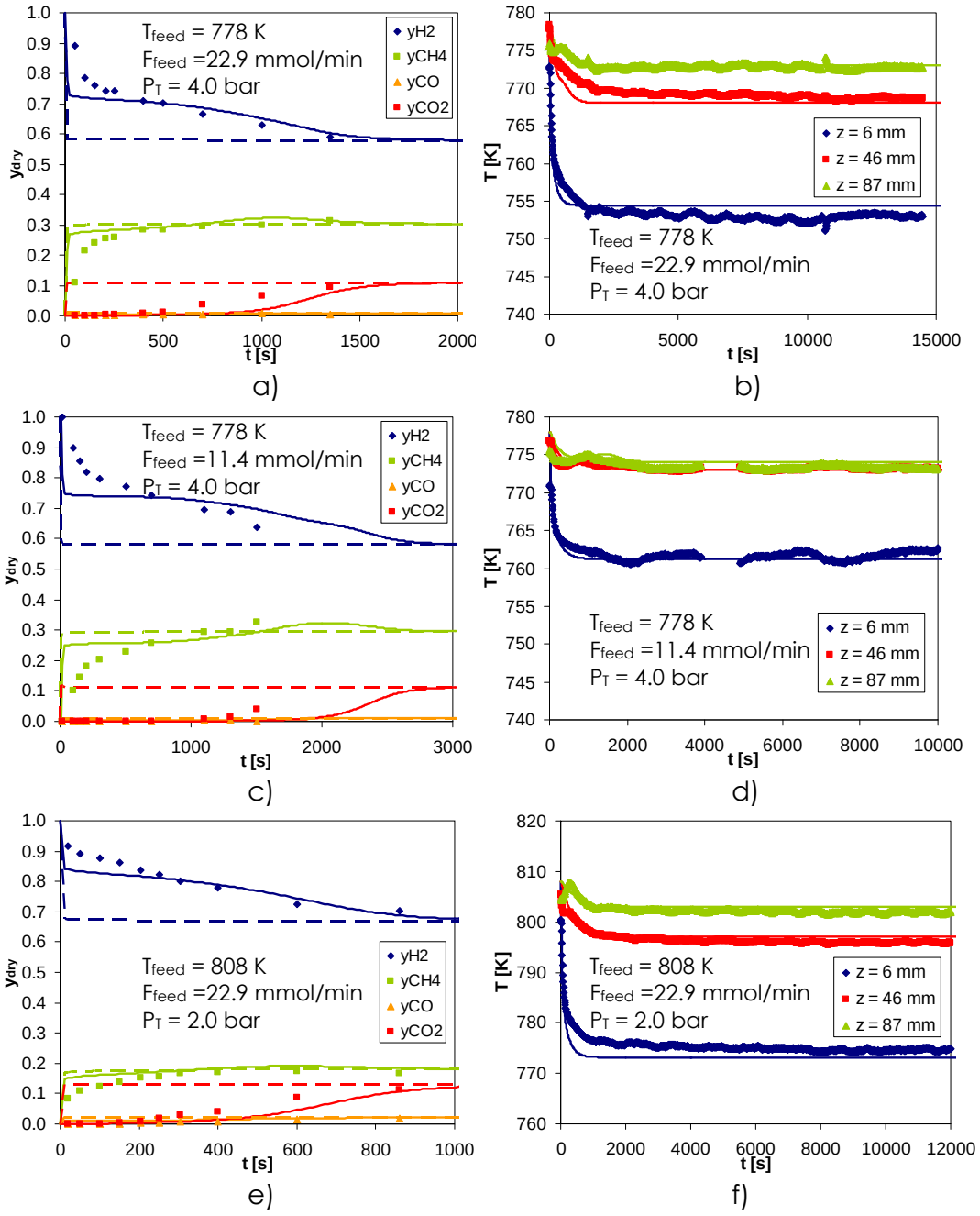

Figure 4.10. Dry-basis molar fractions and temperature histories of Run 3 (a-b), Run 4 (c-d) and Run 5 (e-f) obtained during the reaction step of the SMR-SERP experiments employing alternate layers of Catalyst A and MG30-K sorbent. Solid points are experimental results, lines are simulated results and dotted lines are SMR results using the same amount of catalyst.

Comparing Runs 2 (Figure 4.9) and 3 (Figure 4.10a-b) we can see that the operating pressure has two different effects in the SMR-SERP: increasing the total pressure decreases the conversion of SMR reactions; on the other side, increasing the total pressure also increases the CO_2 partial pressure and therefore a higher CO_2 sorption capacity is available. Thus there is a balance between producing less CO_2 but at higher partial pressure. Experimental results indicate that increasing the total pressure from 2.0 to 4.0 bar (as shown in Figure 4.10a) was favorable since the CO_2 breakthrough time was delayed.

The effect of decreasing the total flowrate by a factor of 2 to 11.4 mmol/min at a total pressure of 4.0 bar can be observed comparing Run 3 with Run 4 in Figure 4.10. Experimental data shows that hydrogen free of carbon oxides was produced during the first 700 s. This value is more than 3 times higher than the time obtained in a similar experiment with 22.9 mmol/min flowrate (Run 3, ~200 s with production of hydrogen free of carbon oxides).

The steam methane reforming process is globally endothermic and thus increasing the feed temperature in 30 K increases the reaction rate. As a consequence more CO_2 is produced. However, the capacity of the sorbent decreases and the sorbent takes less time to saturate. On the other side, an increase of 30 K also has some effect in the sorption kinetics, increasing the value of the kinetic constant exponentially. Experimental results of Run 5 (see Figure 4.10e) already show traces of CO_2 in the effluent (~100 ppm) at 100 s of reaction. In Run 2 (see Figure 4.9), CO_2 was only detected at 150 s of reaction (~4300 ppm). Therefore, increasing the temperature decreases the time of sorption enhancement.

A roll up effect was noticed in the methane and hydrogen molar fractions immediately before the carbon dioxide breakthrough during the reaction step of Runs 1-5 but is more noticeable in Run 4 Figure 4.10c. A roll up in a sorber column is when the lighter components (CH_4, H_2, CO or H_2O) increase its concentration above the feed concentration as it is being displaced by the sorption of the heavy component in the sorbent [73-75]. In the case of the layered SMR-SERP, the roll-up effect is only noticeable due to selective sorption of CO_2 in the last layer of hydrotalcite: when CO_2 starts to break through, the methane concentration decreases to the steady state values.

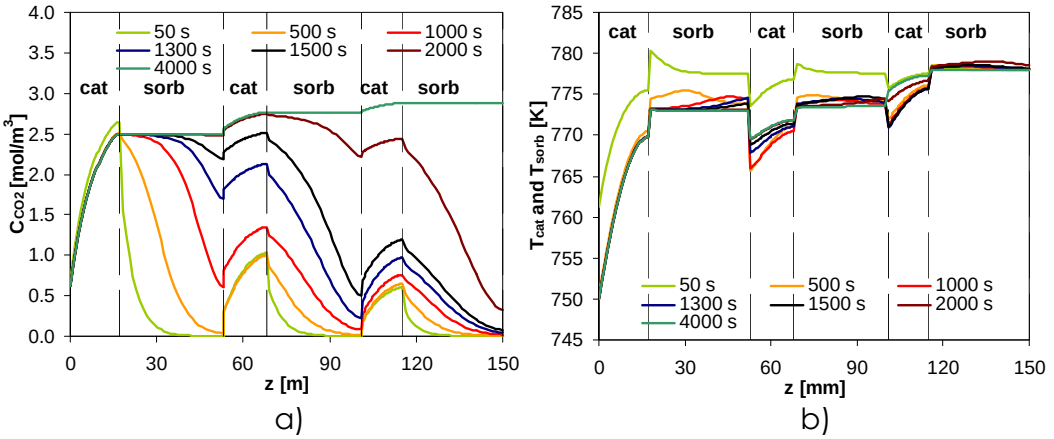

Figure 4.11. SMR-SERP simulated carbon dioxide concentration profile (a) and solid temperature profiles (b) inside the reactor at different reaction times of Run 4 (4.0 bar, 778 K and 11.4 mmol/min total molar flowrate) using alternate layers of Catalyst A and MG30-K sorbent.

Figure 4.11 shows the simulated profiles of carbon dioxide gas phase concentration and solid temperature inside the SMR-SERP column during Run 4 at different reaction times until the end of the CO_2 breakthrough (times indicated in Figure 4.11). It can be observed that the temperature decrease is significant in the catalyst beds, especially in the first one where the bulk of methane conversion takes place. Additionally, in the concentration profiles of CO_2 it can be observed

that there is an important resistance in the diffusion of CO_2 within the sorbent material that will seriously limit the performance of the SMR-SERP process.

The regeneration of the hydrotalcite sorbent was carried out immediately after the reaction step. The regeneration stream conditions were to a lower pressure (1.01 bar) and higher feed flowrate composed by H_2 and steam, keeping T constant (conditions detailed in Table 4.3). The effluent molar flowrates and temperature profiles during the regeneration step are reported in Figure 4.12.

At the start of the regeneration step, Figure 4.12 shows that the temperature inside the reactor increases. This increase results from a trade-off between the heat needed for desorption and less heat consumed by the catalyst since SMR reactions are not active.

The regeneration step was carried out using stream with different amounts of hydrogen (balanced by steam) – 5 % in runs 3 and 5; 34 % in Run 4. The desorption of carbon dioxide from the sorbent was always very slow, taking more than 2 h.

In all runs the conversion was always above equilibrium: between 11 % (Run 5) and 36 % (Run 4). Increasing the temperature resulted in a lower sorption enhancement due to the combination of a higher CO_2 production by the catalyst (higher reaction rate) and lower CO_2 capacity of the sorbent.

Increasing the total pressure from 2.0 to 4.0 bar decreased the H_2 purity because less methane is converted. However, less carbon oxides are produced during the enhancement of equilibrium due to selective sorption of CO_2.

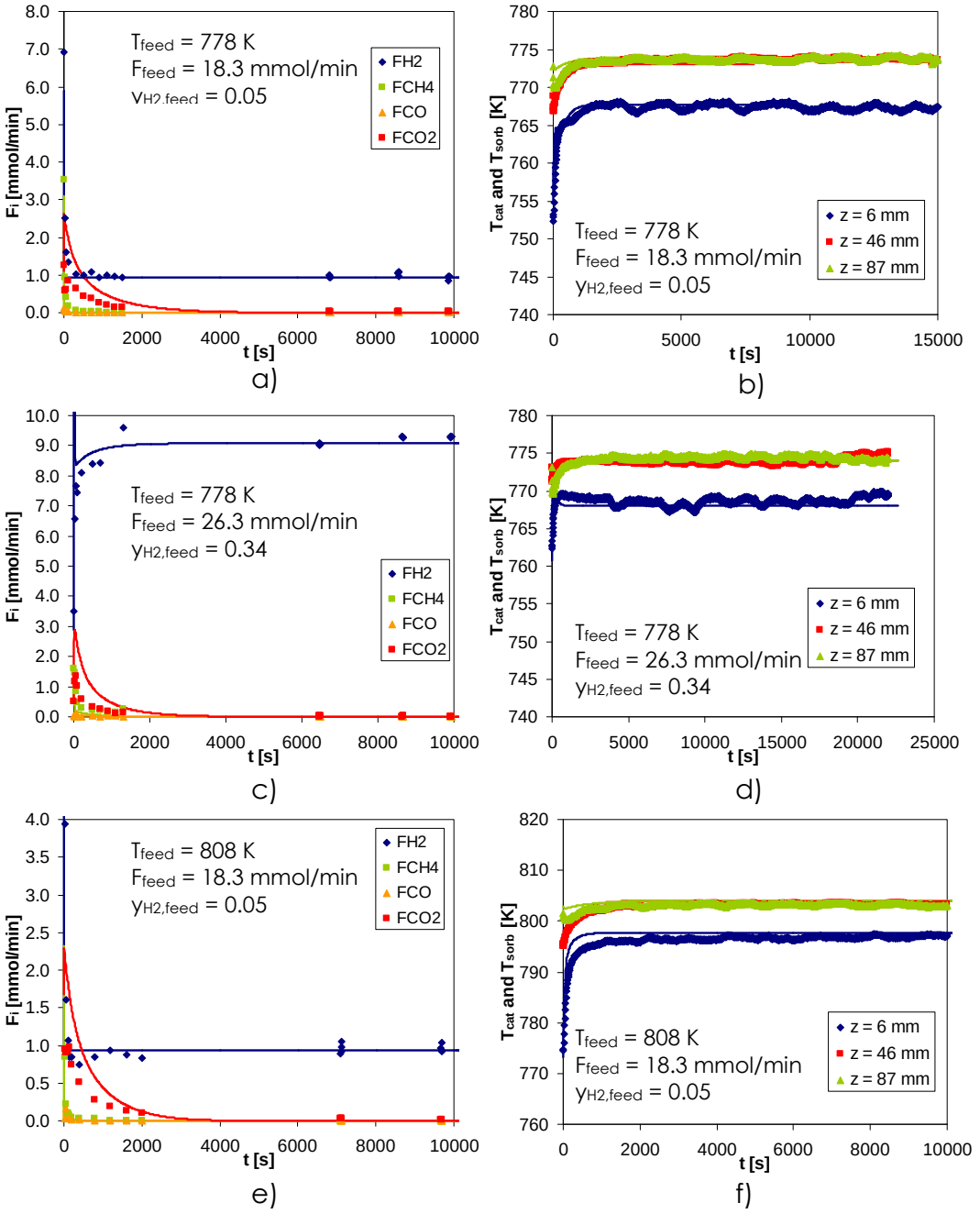

Figure 4.12. Molar fractions and temperature histories of Run 3 (a-b), Run 4 (c-d) and Run 5 (e-f) measured during the regeneration step at 1.01 bar total pressure. The SMR-SERP reactor was filled with alternate layers of Catalyst A and MG30-K sorbent. Solid points are experimental results, lines are simulated results.

The temperature has a positive effect in the purity mainly because increasing the temperature increases the methane conversion and thus the amount of H_2 produced. Also, as the effluent contains less methane, the hydrogen purity is higher before CO_2 and CO breakthrough.

The most important restriction to the SMR-SERP is the slow diffusion of CO_2 within the extrudates of the sorbent. These kinetic effects are problematic in the reaction step, reducing drastically the overall column capacity for CO_2. In the regeneration step, the CO_2 desorption is slow due to these diffusional problems and also due to the strong non-linearity of the isotherm.

In Run 6, seven reaction/regeneration cycles were performed. Each cycle takes a total time of 1400 s. The experiment was composed by four different steps:

1. Reaction (220 s) – where methane and steam are fed at 4.0 bar;
2. Depressurization (~15 s) – the pressure is reduced from 4.0 to 1.01 bar;
3. Purge (1115 s) – the reactor is purged co-currently with H_2O and H_2;
4. Pressurization (50 s) – the pressure is increased from 1.01 to 4.0 bar;

The experimental and simulation results of Run 6 are reported in Figure 4.13.

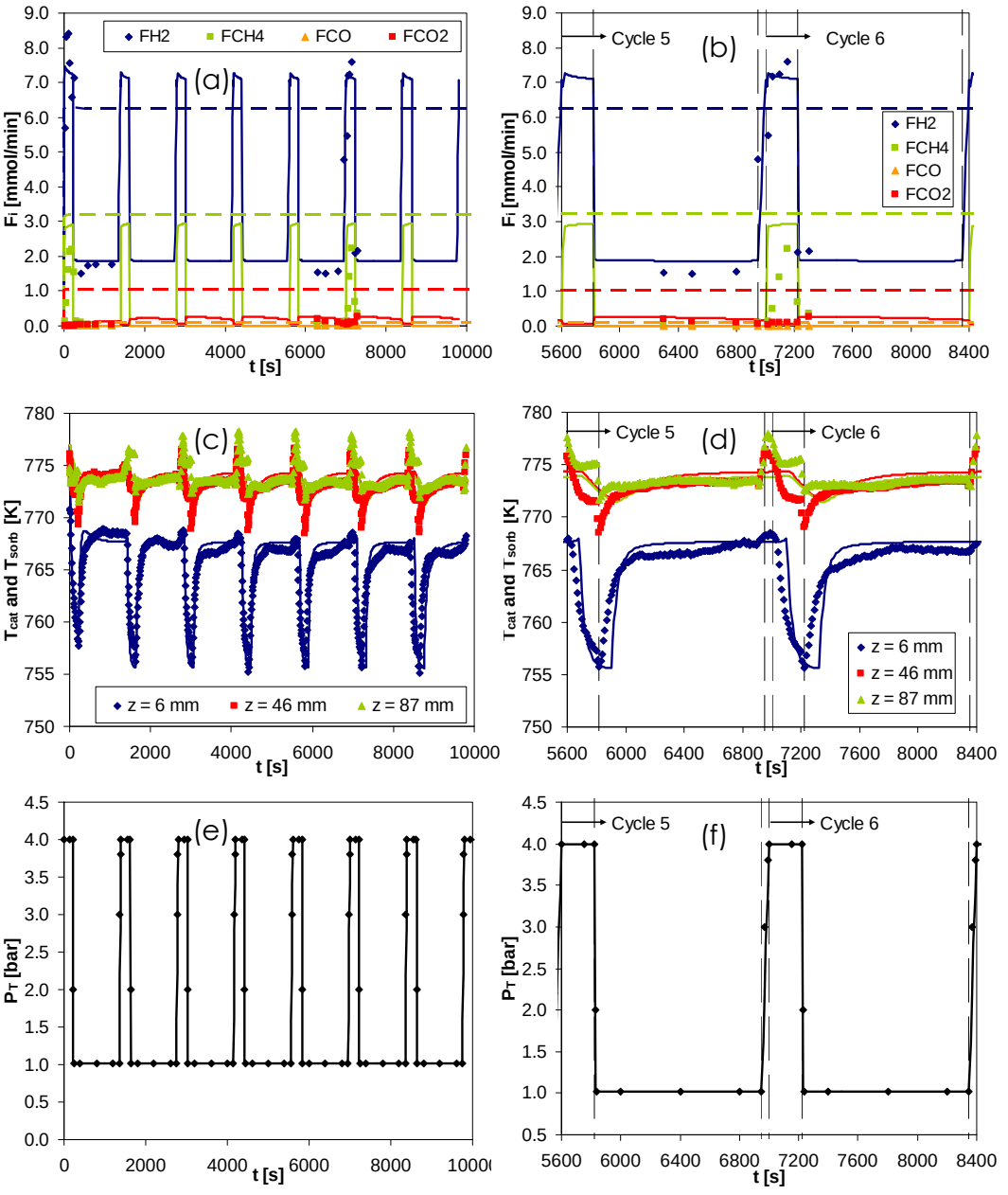

Figure 4.13. Molar flowrates (a-b), catalyst and sorbent temperatures (c-d) and total pressure (e-f) measured during the cyclic reaction/regeneration SMR-SERP experiments employing alternate layers of Catalyst A and MG30-K sorbent (Run 6). The reaction step was performed at 4.0 bar, 778 K and 22.9 mmol/min. During the regeneration step the conditions were: 1.01 bar, 778 K, 19.2 mmol/min and $y_{H2,feed}$ = 0.1. Solid points are experimental results, lines are simulated results.

Cyclic steady state (CSS) is reached when the temperature and composition of one cycle is repeated in the following cycles [76]. Observing the temperature and pressure profiles in Figure 4.13 we can say that the cyclic steady state was achieved after the third cycle. This result indicates that the regeneration of the sorbent layers was sufficient to compensate the amount of CO_2 produced during the reaction step. Also, in the cyclic experiments a low amount of CO was detected during the reaction step. This is an important result since the objective is to produce fuel cell grade hydrogen (less than 30 ppm of CO).

The SERP enhancement and hydrogen purity were calculated for each cycle of Run 6 using the simulation results and are reported in Table 4.5.

Table 4.5. Cycle performance of SMR-SERP Run 6 employing Catalyst A and MG30-K hydrotalcite. Operating conditions: Reaction (220 s) – 4.0 bar, 23.5 mmol/min and 778 K; Purge (1115 s) – 1.01 bar, 19.2 mmol/min and 778 K.

Cycle	% SERP	Purity
1	128	72.5
2	124	71.4
3	123	71.2
4	123	71.2
5	123	71.2
6	123	71.2
7	123	71.1

The SERP enhancement and hydrogen purity values indicate that the CSS was reached in cycle 3. Hydrogen was produced with a purity of 71 %, which is 22 percentage points higher than the thermodynamic equilibrium (59 %). In CSS, simulation results show that the main contaminant is methane (27.2 %) followed by carbon dioxide (0.9 %) and CO (0.4 %).

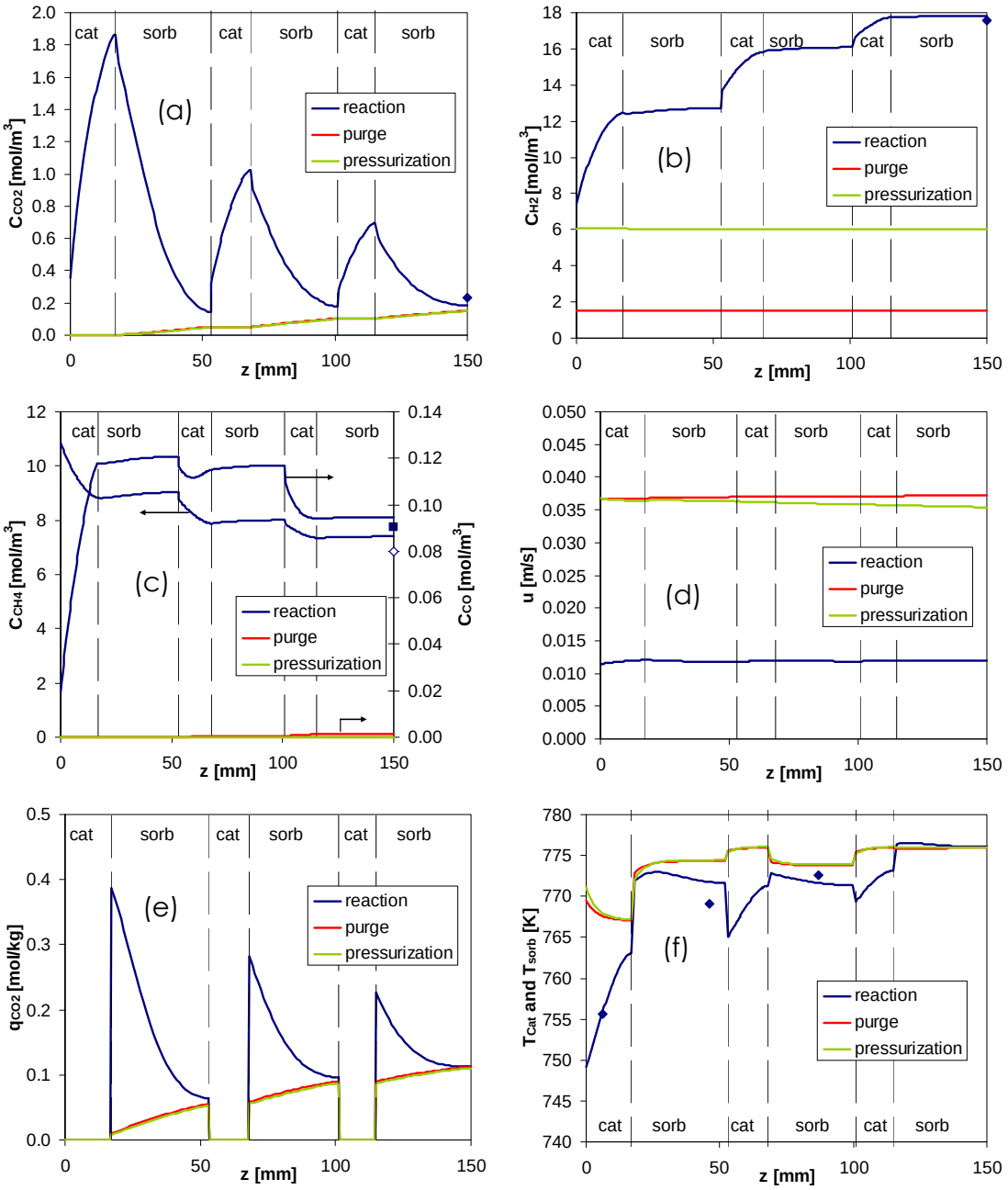

Figure 4.14. Gas phase concentration profiles of CO_2 (a), H_2 (b), CO and CH_4 (c); superficial velocity (d), CO_2 sorbed concentration (e) and solid temperature profiles (f). Simulated CSS (cycle 6) profiles determined for the SMR-SERP layered reactor (Catalyst A and MG30-K) at the end of the reaction, purge and pressurization steps.

The mathematical model was used to observe what is happening inside the SMR-SERP reactor in cyclic steady state (cycle 6 of Run 6). Figure 4.14 shows the concentration profiles, superficial gas velocity, carbon dioxide sorbed concentration in the hydrotalcite material and temperatures of the solid extrudates (catalyst and sorbent) at the end of the reaction, purge and pressurization steps.

Due to limitations in the experimental system, in this work the regeneration of the sorbent was performed co-currently with the reaction. Figure 4.13 (a and e) shows the main drawback of co-current regeneration: at the end of the purge step, the concentration of carbon dioxide in the gas and solid phases is highest at the effluent end. This means that when the next cycle starts, CO_2 from the previous cycle will contaminate the effluent. In order to improve the cyclic results, the regeneration should be performed counter-currently to the reaction step. In Figure 4.13e the mass transfer zone of CO_2 can be observed. This is the most negative aspect of the sorbent material that should be improved to achieve high performance of SMR-SERP. The objective of the SMR-SERP experiments is to validate the mathematical model and to determine the response of the SMR-SERP to different feed conditions. The counter-current regeneration will be simulated in Section 4.5.3.

Other important feature that can be observed in Figure 4.13 is the conversion of CO in the last layer of the catalyst. In fact, some CO is converted; however, its conversion is not favored by temperature. Xiu *et al* proposed a sub-section temperature controlled strategy to reduce formation of CO where the last portion of the reactor is operated at a lower temperature [44].

The maximum CO_2 sorbed concentration at the end of the reaction step (Figure 4.14e) is different in all the sorbent layers. The SMR

reaction rates are highest near the feed end. Therefore, the rate of CO_2 and H_2 production (Figure 4.14a-b) will also be higher in the first catalyst layer and then decrease in the subsequent catalyst layers. The decrease in the SMR reaction rates is also visible in the temperature profiles of Figure 4.14f, where the temperature drop is highest in the catalyst bed near the feed end (endothermic reaction).

The CO_2 sorption equilibrium isotherm of the MG30-K hydrotalcite is non-linear and unfavorable for desorption. In Runs 1-5 it was already seen that the desorption of CO_2 from the hydrotalcite was very slow. In Figure 4.14a and e we can see that the CO_2 concentration at the end of the purge step increases almost linearly in each sorbent layer, from the feed end to the effluent end confirming a slow desorption of CO_2. In a sorbent with a more linear isotherm and a faster diffusion we would expect a faster CO_2 desorption.

The layered distribution of catalyst and sorbent reduces the energy integration between the endothermic reaction in the catalyst and the exothermic CO_2 sorption in the hydrotalcite material (Figure 4.14f) when compared to a mixed distribution.

One advantage of the layered distribution is that each catalyst layer comes in contact with a stream with a low CO_2 concentration, maximizing the hydrogen production rate (Figure 4.14b). Also, the most important advantage of the layered configuration in this SMR-SERP is that the use of a sorbent only layer at the end of the reactor delays the CO_2 breakthrough and allows a longer reaction step time.

4.5.2. SMR-SERP experiments using Degussa catalyst and MG30-K sorbent

The SMR-SERP reactor was filled with alternating layers (a total of 6) of Degussa catalyst and MG30-K sorbent as shown in Figure 4.6b. The two catalysts used in this work have different particle sizes and Ni contents. In order to provide a basis for comparison, the length of the catalyst and sorbent layers was the same in the SMR-SERP experiments employing Catalyst A or Degussa catalyst (see Table 4.2). Three thermocouples were placed at 6 mm (first catalyst layer), 46 mm (first sorbent layer) and 87 mm (second sorbent layer) from the feed end.

The catalyst was reduced and the CO_2 was removed from the sorbent employing a stream of 5 % H_2 in steam. Four SMR-SERP experiments were performed: Runs 2, 3, 5 and 6 of Table 4.3. The mathematical model of Section 4.4 was employed to simulate the experimental runs using the parameters reported in Table 4.6, the CO_2 sorption equilibrium and kinetic constants determined in Chapter 2 for the MG30-K hydrotalcite and the kinetic constants determined in Chapter 3 for the Degussa catalyst. No fitting parameters were used to simulate the experimental results. Simulations were also performed considering only the catalyst extrudates in order to determine the output of a SMR reactor with the same amount of catalyst.

The SMR-SERP experimental and simulation results for the reaction step of Run 2 (2.0 bar total pressure, 778 K and 22.9 mmol/min) as well as the catalyst only simulations are reported in Figure 4.15.

Table 4.6. Parameters used in the simulations of the non-isothermal SMR-SERP reactor composed of 6 alternating layers of Degussa catalyst and MG30-K extrudates.

Column		**Degussa catalyst**	
R_c [m]	0.0133	R_{cat} [mm]	0.80
w_{thick} [m]	0.0091	$L_{p,cat}$ [mm]	5.0
h_w [W/(m².K)]	400	$r_{pore,cat}$ [nm]	4.25
U [W/(m².K)]	200	ρ_{cat} [kg/m³]	1274
$\hat{C}p_w$ [J/(kg.K)]	500	$\varepsilon_{p,cat}$	0.64
ρ_w [kg/m³]	7750	τ_p	1.56
ρ_{gas} [kg/m³][a]	0.52	$a_{p,cat}$ [m⁻¹]	2500
μ_{gas} [Pa.s][a]	2.69×10^{-5}	$\hat{C}_{ps,cat}$ [J/(kg.K)][a]	1063
λ_{ax} [W/m.K][a]	0.46	$h_{f,cat}$ [W/(m².K)][a]	109
D_{ax} [m²/s][a]	0.64×10^{-4}	$k_{f,cat}$ [m/s][a]	0.162
D_m [m²/s][a]	0.84×10^{-4}	$D_{k,cat}$ [m²/s][a]	3.03×10^{-6}
		$D_{p,cat}$ [m²/s][a]	1.87×10^{-6}
MG30-K hydrotalcite		**MG30-K hydrotalcite**	
r_{sorb} [mm]	2.215	$a_{p,sorb}$ [m⁻¹]	1354
$r_{pore,sorb}$ [nm]	4.55	$\hat{C}_{ps,sorb}$ [J/(kg.K)]	850
ρ_{sorb} [kg/m³]	1845	$h_{f,sorb}$ [W/(m².K)][a]	49.8
$\varepsilon_{p,sorb}$	0.27	$k_{f,sorb}$ [m/s][a]	0.067

a – Calculated for the reaction conditions at 778 K and 2 bar.

There is good agreement between the experimental and simulated results. The mathematical model was able to describe both the CO_2 sorption in the MG30-K material and the SMR reaction in the catalyst extrudates.

Employing the Degussa catalyst, a slightly higher amount of CO_2 is formed. The reason for this is the higher amount of catalyst employed in each layer (to comply with the same layer dimensions). In Figure 4.15b we can also observe that the CO_2 breakthrough ends at 1400 s and the SMR-SERP results overlap the simulations of the regular SMR reactor (catalyst only).

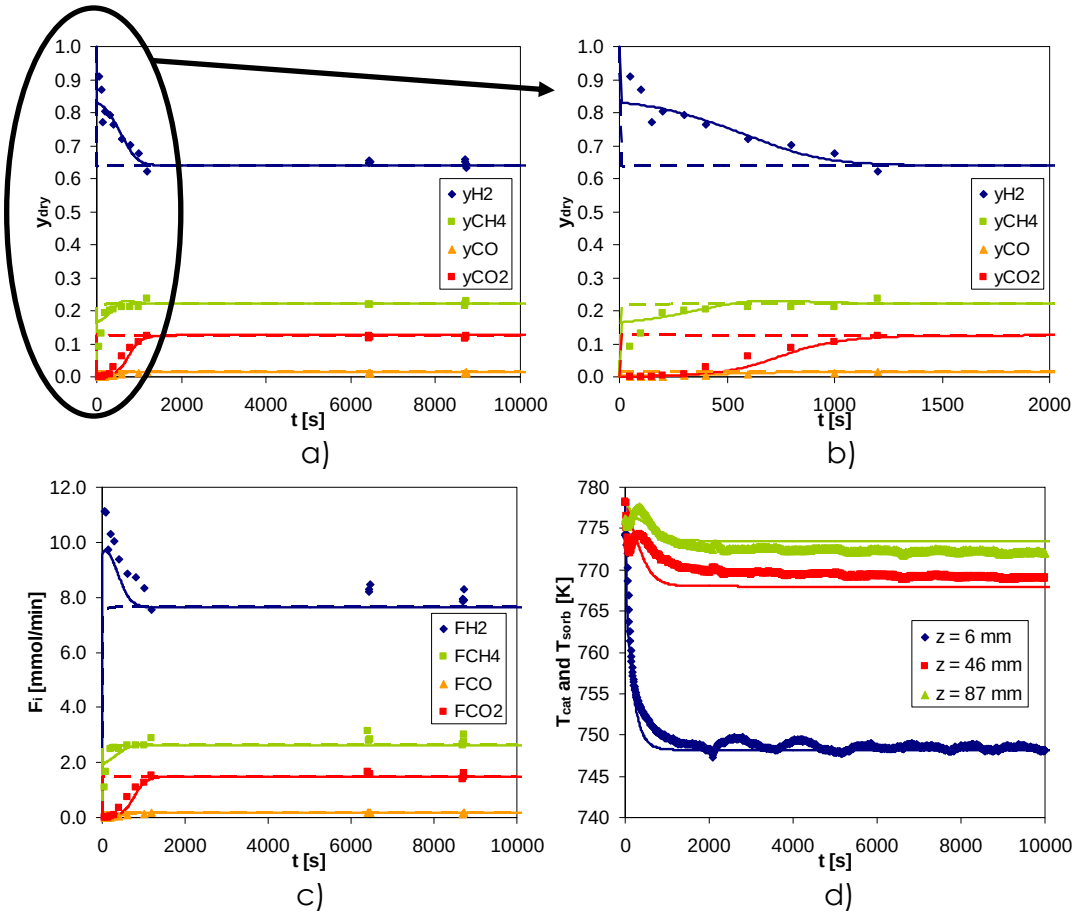

Figure 4.15. Dry-basis molar fractions (a-b), molar flowrates (c) and temperature (d) histories measured during the reaction step of Run 2 (2 bar, 778 K and 22.9 mmol/min total molar flowrate) of SMR-SERP using alternate layers of Degussa catalyst and MG30-K sorbent. Solid points are experimental results, lines are simulated results and dotted lines are SMR results using the same amount of catalyst.

After more than 3 h, the feed stream was switched to the regeneration conditions. Figure 4.16 shows the experimental and simulated results of the regeneration step of Run 2. The complete regeneration of the MG30-K hydrotalcite using 34 % H_2 in steam took less than 3 h. During the same time, methane was always detected in the effluent stream indicating that CO_2 was reacting with the hydrogen present in the feed stream.

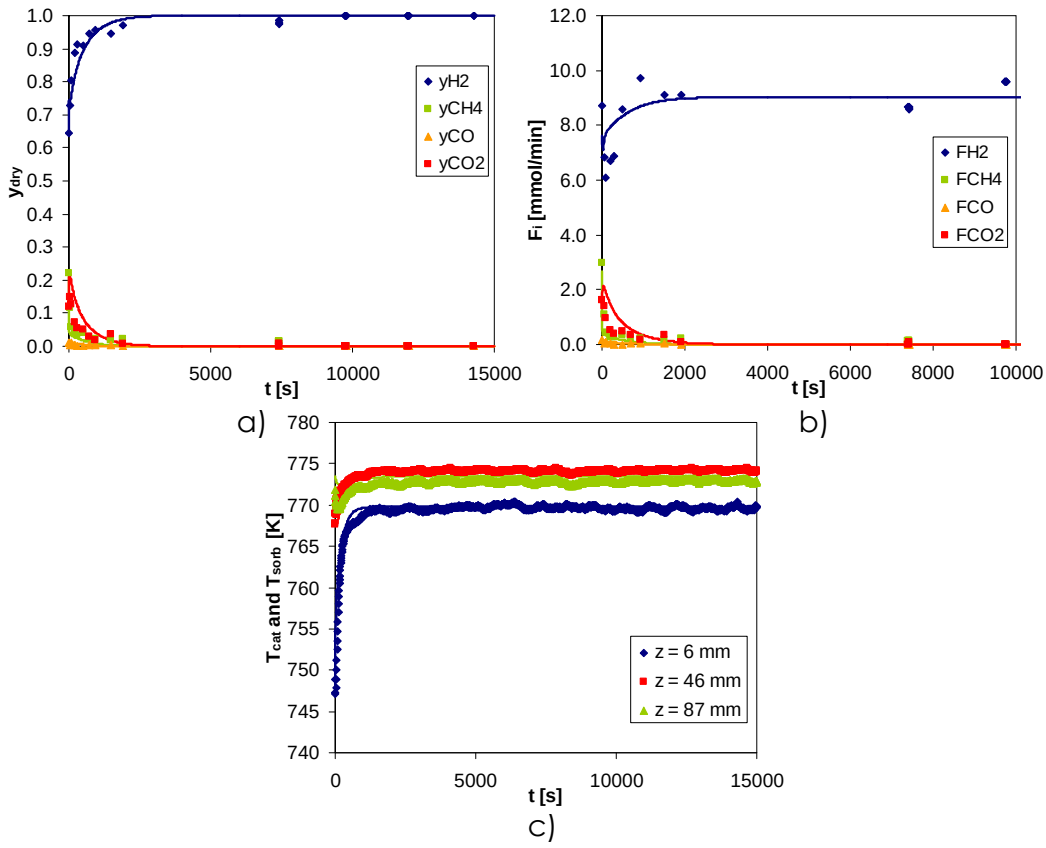

Figure 4.16. Dry-basis molar fractions (a), molar flowrates (b) and temperature (c) histories measured during the sorbent regeneration step of Run 2 using 34 % H_2 in H_2O (1.01 bar, 778 K and 26.3 mmol/min total molar flowrate). Alternate layers of Degussa catalyst and MG30-K sorbent were employed in the SMR-SERP experiment. Solid points are experimental results, lines are simulated results.

Previously, when Catalyst A was employed for Run 2, methane was only detected until 1900 s. This is the reason why, when Catalyst A was employed, the regeneration of the sorbent took more than 4 h. The Degussa catalyst is more active for the reverse SMR reactions (reactive regeneration) most likely due to its higher Ni content (15 %) when compared to Catalyst A (10 %).

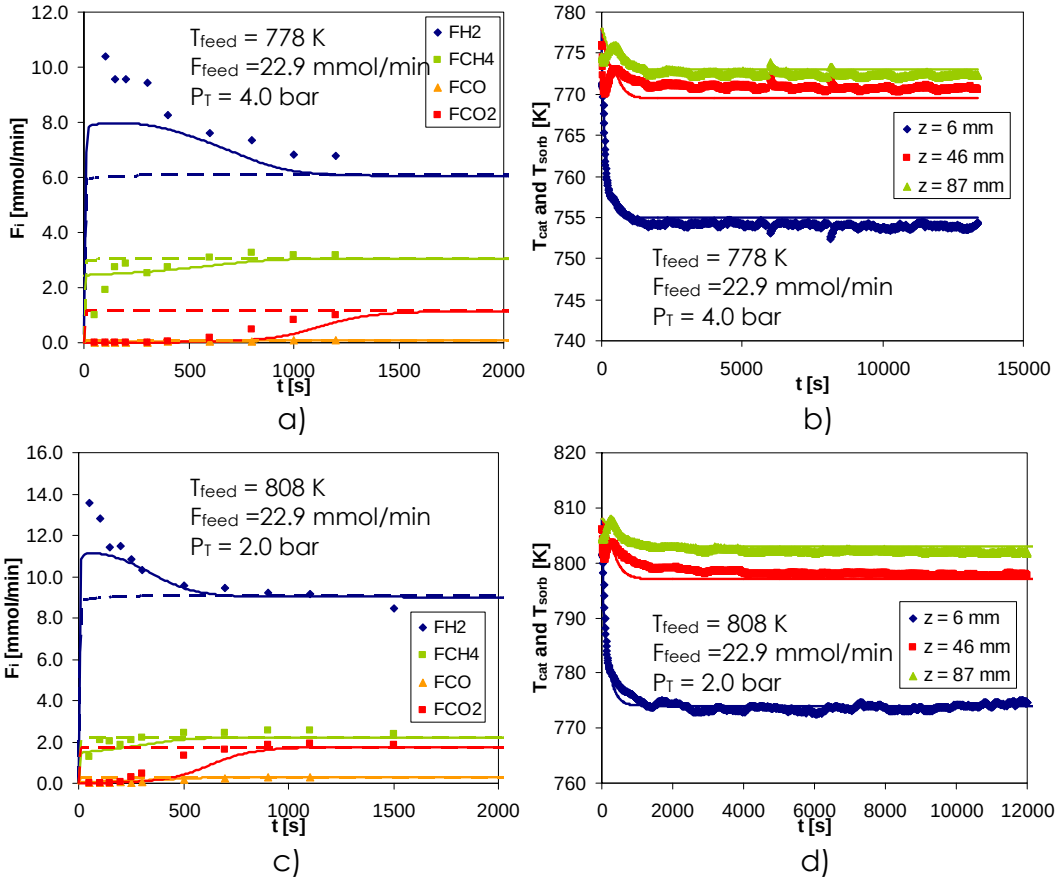

Figure 4.17. Molar flowrates and temperature histories of Run 3 (a-b) and Run 5 (c-d) obtained during the reaction step of the SMR-SERP experiments employing alternate layers of Degussa catalyst and MG30-K sorbent. Solid points are experimental results, lines are simulated results and dotted lines are SMR results using the same amount of catalyst.

Two experiments were then made to study the effect of feed temperature and the effect of the total pressure in the reaction step. In Run 3, a total pressure of 4.0 bar was used while maintaining all the other feed conditions of Run 2. In Run 5, a feed temperature of 808 K was used. The experimental and simulated results are shown in Figure 4.17 for the reaction step and in Figure 4.18 for the regeneration step.

When a total pressure of 4.0 bar was used, carbon dioxide was only detected after 400 s of reaction and the hydrogen molar fraction in the

effluent stream was always higher than 76 %. Increasing the total pressure increases the available CO_2 sorption capacity of the sorbent, allowing longer SMR-SERP carbon oxides free operation. When Catalyst A was used at 4.0 bar, carbon oxides free hydrogen was produced during less than 200 s.

In the experiments employing the Degussa catalyst and MG30-K sorbent, the initial breakthrough of CO and CO_2 was approximately the same at 778 K (in Figure 4.15) and at 808 K (Figure 4.17c). However, at 808 K the effluent H_2 molar flowrate before the breakthrough of carbon oxides was 19 % higher. The increase in the H_2 molar flowrate was caused by the increase in the SMR reaction rates.

A stream containing 5 % H_2 in steam (1.01 bar, 18.3 mmol/min) was employed in the regeneration step of Runs 3 and 5. In Run 3 (in Figure 4.18a), carbon monoxide was detected up to 1800 s after the beginning of the regeneration step. At 808 K, methane was detected even at 2300 s, indicating that the hydrogen feed during the regeneration step increases the CO_2 desorption rate.

In the desorption step of Runs 2, 3 and 5 it was also found that the methane molar flowrate decreases exponentially in the first 300 s. After the initial 300 s, the decrease is linear. This result is important because it shows that, after the initial 300 s, the benefit of the reactive regeneration is lower than the disadvantage of decreasing the hydrogen productivity of the process.

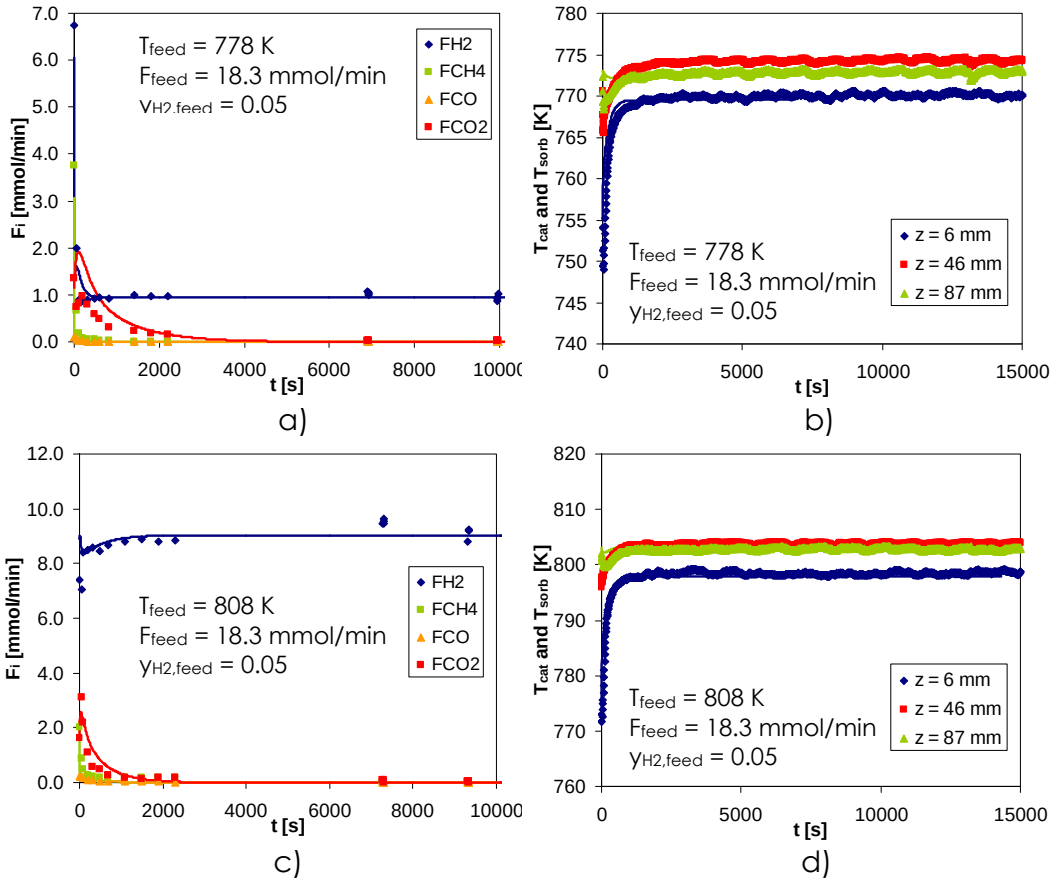

Figure 4.18. Molar flowrates and temperature histories of Run 3 (a-b) and Run 5 (c-d) measured during the regeneration step at 1.01 bar total pressure. The SMR-SERP reactor was filled with alternate layers of Degussa catalyst and MG30-K sorbent. Solid points are experimental results, lines are simulated results.

In the SMR-SERP experiments employing the Degussa catalyst and MG30-K sorbent, using a higher pressure increased the SERP effect while increasing the temperature decreased the SERP effect. The opposite happened to the hydrogen purity: decreased when the feed pressure was increased to 4.0 bar and increased when the feed temperature was increased to 808 K. At higher pressures, the decrease in the equilibrium methane conversion is compensated by a higher CO_2 sorption capacity – higher SERP effect. However, as the methane

conversion is lower, the hydrogen purity decreases – more methane in the effluent. Increasing the feed temperature increases the methane conversion and therefore more hydrogen and less methane are present in the effluent (higher hydrogen purity). At higher temperature the methane conversion is higher. However, the thermodynamic equilibrium methane conversion is also higher and thus the value of the SERP parameter is lower at higher temperature.

Despite the large-pore network of Catalyst A that reduces the mass transfer limitations in the pore network, the Degussa catalyst has a higher Ni content (15 %) when compared to Catalyst A (10 %). Thus, the reaction rate is higher in the Degussa catalyst. In the current laboratory experiments the pressure drop is negligible but for industrial applications the larger extrudates of Catalyst A (R_{cat} = 5.6 mm) will produce a much lower pressure drop than the Degussa catalyst (R_{cat} = 0.8 mm).

In Run 6, fourteen reaction/regeneration cycles were performed with a total cycle time of 1400 s. The experiment was composed of four different steps:

1. Reaction (220 s) – where methane and steam are fed at 4.0 bar;
2. Depressurization (~15 s) – the pressure is reduced from 4.0 to 1.01 bar;
3. Purge (1115 s) – the reactor is purged co-currently with H_2O and H_2;
4. Pressurization (50 s) – the pressure is increased from 1.01 to 4.0 bar;

The experimental and simulation results of Run 6 are reported in Figure 4.19. The temperature profiles indicate that cyclic steady state was reached in the fourth cycle.

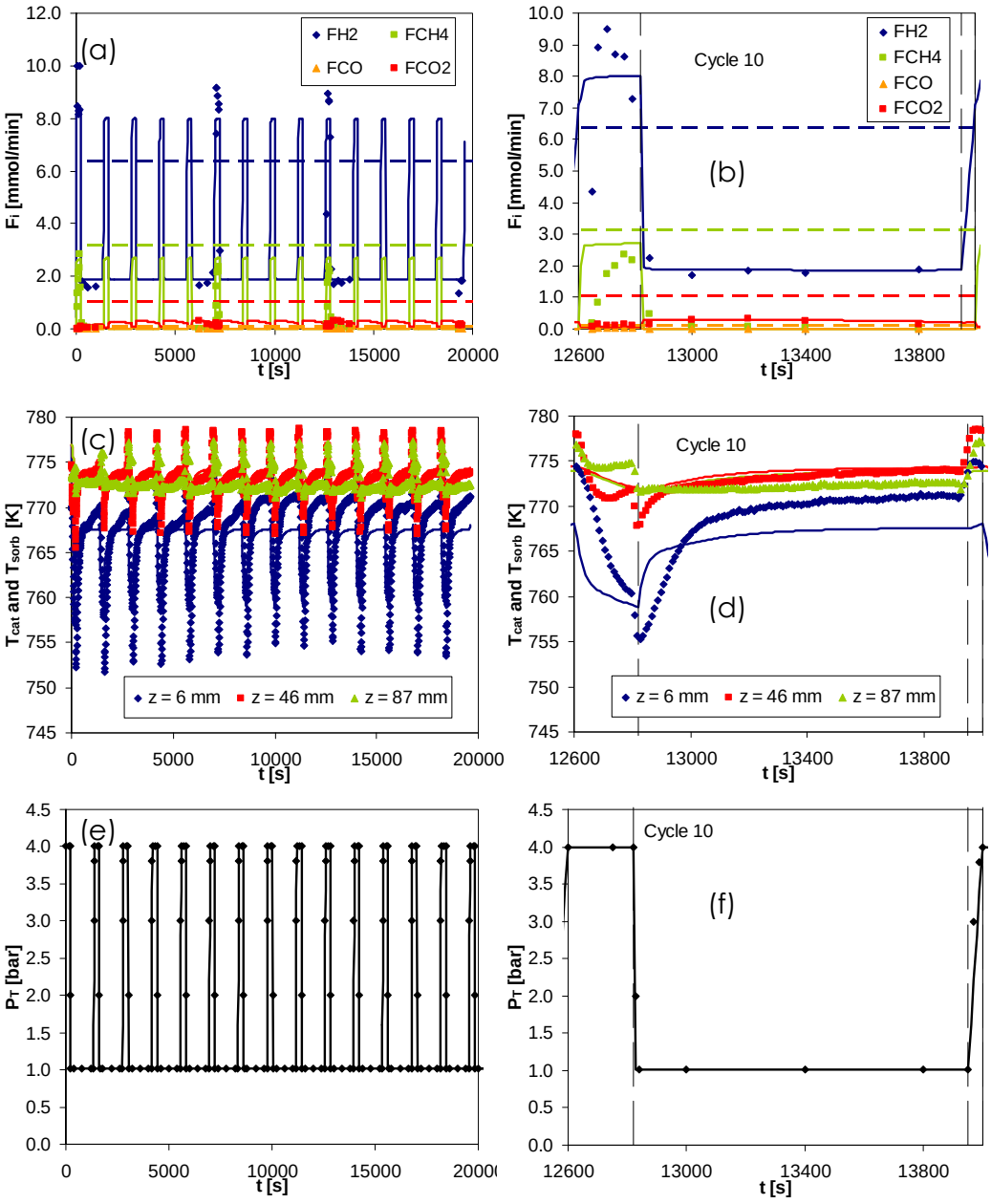

Figure 4.19. Molar flowrates (a-b), catalyst and sorbent temperatures (c-d) and total pressure (e-f) measured during the cyclic reaction/regeneration SMR-SERP experiments employing alternate layers of Degussa catalyst and MG30-K sorbent (Run 6). The reaction step was performed at 4.0 bar, 778 K and 22.9 mmol/min. During the regeneration step the conditions were: 1.01 bar, 778 K, 19.2 mmol/min and $y_{H2,feed}$ = 0.1. Solid points are experimental results, lines are simulated results.

In the SMR-SERP process, the CO_2 equilibrium sorption capacity and sorption kinetics of the sorbent material restrict the performance of the process. If the sorbent cannot be adequately regenerated, the sorption enhancement will decrease in each cycle, decreasing the methane conversion and more importantly, the hydrogen purity.

Due to the experimental limitation of performing co-current regeneration, carbon dioxide is always present in the effluent stream of the reaction step in CSS. For this reason, at the start of the reaction step, there is CO_2 in the gas phase of the reactor near the effluent end. The most important result taken from this experiment is that the mathematical model can predict the cyclic behavior of a fixed-bed arranged by layers of catalyst and sorbent.

During the reaction step in cyclic steady state, carbon oxide was always present in the effluent. A maximum of 0.3 % was measured in several cycles. In the previous SMR-SERP experiments employing Catalyst A, low CO content was detected during the reaction step. In Chapter 3 it was already reported that Catalyst A was more selective for CO_2 than the Degussa catalyst. As carbon oxide does was assumed not sorb in the hydrotalcite material [14], a catalyst that is more selective for CO_2 helps in the control the CO contamination of the hydrogen produced in the reaction step.

The performance variables introduced in Section 4.4 were calculated using the simulated results of each cycle of Run 6 and are reported in Table 4.7.

Table 4.7. Cycle performance of SMR-SERP Run 6 employing the Degussa catalyst and MG30-K hydrotalcite. Operating conditions: Reaction (220 s) – 4.0 bar, 23.5 mmol/min and 778 K; Purge (1115 s) – 1.01 bar, 19.2 mmol/min and 778 K.

Cycle	% SERP	Purity
1	148.5	76.4
2	143.1	75.0
3	142.7	74.8
4	142.6	74.8
5	142.6	74.8
6	142.6	74.8
7	142.6	74.8
8	142.6	74.8
9	142.6	74.8
10	142.6	74.8
11	142.6	74.8
12	142.6	74.8
13	142.6	74.8
14	142.6	74.8
15	142.6	74.8

The hydrogen purity and SERP enhancement values indicate that CSS was reached in the fourth cycle. Higher hydrogen purity was achieved in the SMR-SERP experiments with the Degussa catalyst (75 %) when compared to the results using Catalyst A (71 %). The main contaminant was once again methane (24 %) followed by carbon dioxide (0.8 %) and carbon monoxide (0.3 %). The carbon oxides content was lower than what is expected in a typical SMR reactor operated using the same operating conditions.

The simulated concentration, temperature and superficial velocity profiles in cyclic steady state (cycle 10) at the end of the reaction, purge and pressurization steps are detailed in Figure 4.20.

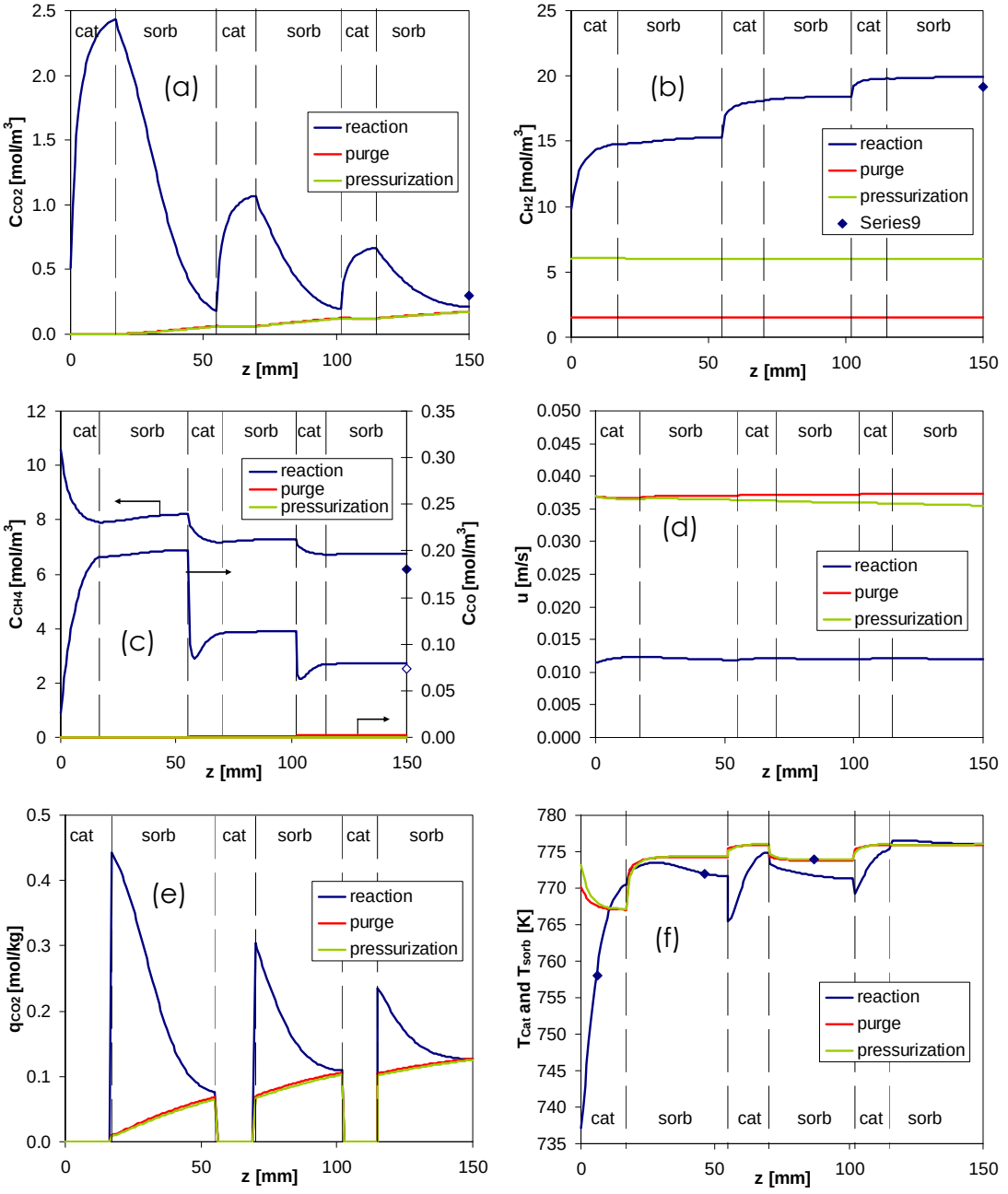

Figure 4.20. Gas phase concentration profiles of CO_2 (a), H_2 (b), CO and CH_4 (c); superficial velocity (d), CO_2 sorbed concentration (e) and solid temperature profiles (f). Simulated CSS (cycle 10) profiles determined for the SMR-SERP layered reactor (Degussa catalyst and MG30-K) at the end of the reaction, purge and pressurization steps.

The carbon dioxide and hydrogen concentration profiles in Figure 4.20a and b show that more CO_2 and H_2 were produced by the first catalyst layer when compared with the results obtained with Catalyst A. As the sorption capacity of the hydrotalcite is related to the concentration of CO_2, the carbon dioxide sorbed concentration is also higher (Figure 4.20e). In the case of the co-current regeneration, the drawback is that, at the end of the regeneration, 13 % more CO_2 is present near the effluent end (lower purity) when the Degussa catalyst is used. To solve this problem, counter-current regeneration can be employed.

The cyclic steady state simulation results also indicate that in a reactor of fixed size, since the Degussa catalyst is more active than Catalyst A, smaller catalyst layers can be used. The extra reactor length can be used to increase the sorbent layer, increasing the reaction time or reducing the regeneration time.

When comparing the two catalysts for SMR-SERP, the Degussa is more active but Catalyst A causes less pressure drop. In laboratory applications, the pressure drop is not important but in the scale-up of SMR-SERP this problem cannot be neglected. However, the efficiency of the steam methane reforming sorption enhanced reaction process is much more dependent on the sorbent than the catalyst and the regeneration is difficult, decreasing the overall productivity and gain of the process.

The most important problem observed in the SMR-SERP experiments was the slow diffusion constants of CO_2 in the MG30-K hydrotalcites. The slow diffusion coefficients are detrimental both in reaction and in desorption steps. Additionally, in the desorption steps, the

thermodynamic is also not favorable: strong non-linearity of the sorption equilibrium.

In the SMR-SERP cyclic experiments with Degussa catalyst and potassium modified hydrotalcite, hydrogen was produced in CSS at 778 K with a purity of 75 %. When Catalyst A was employed with MG30-K hydrotalcite the purity was 71 %. These results are 25 % higher than the SMR equilibrium at 778 K. It is also significant that the temperature is much lower than the 1060 K of an industrial steam methane reformer.

4.5.3. Simulation of SMR-SERP with reactive regeneration

In the previous sections we have evaluated the column behavior of a column where a SMR catalyst and a CO_2-selective material are coupled to produce H_2 by SMR-SERP.

In this section, numerical simulations of a specific cycle are carried out. The cycle proposed by Xiu *et al* [1] is a Skarstrom–type cycle splitting the purge into two steps, first using H_2-N_2 and then using H_2O. The use of H_2 in the purge stream developed the concept of a "reactive purge" with H_2 to promote conversion of CO_2 to CO facilitating its desorption [1]. The simulations performed in this work intends to compare the results obtained by Xiu *et al* [1] (based on SMR kinetics and CO_2 data previously reported [14, 62]) with new results based on experimental data obtained at LSRE.

The simulations of Xiu *et al* [1] were performed using a random distribution of catalyst and sorbent in a reactor with 2 m length and 12.5 mm radius. Since the radius of Catalyst A is 5.6 mm, a true random distribution will not be possible and thus only the data obtained in Degussa catalyst was employed for a direct comparison. The

performance of Catalyst A in SMR-SERP was evaluated afterwards using a larger reactor.

The reactive regeneration cycle is composed of five steps: feed or reaction where H_2 is obtained as product; conter-current blowdown or depressurization where the pressure of the reactor is reduced and some CO_2 is desorbed; conter-current reactive purge to promote CO_2 desorption; conter-current steam purge and pressurization. During the reactive regeneration step, 10 % H_2 is used (balanced by nitrogen) to promote the reverse WGS and SMR reactions and increase the desorption rate. The operating conditions employed in the simulations are shown in Table 4.8 while the parameters used in the simulations are reported in Table 4.9.

Table 4.8. Operating conditions used in the SMR-SERP experiments employing Degussa catalyst and MG30-K sorbent with a sorbent/catalyst volumetric ratio of 3 (m_{cat} = 0.16 kg and m_{sorb} = 0.71 kg). Conditions are identical to Xiu et al. [1].

	Reaction	Depress	Reactive Purge	Steam Purge	Press
t [s]	500	150	400	50	100
$y_{feed, CH4}$	0.143	0.000	0.000	0.000	0.000
$y_{feed, H2O}$	0.857	0.000	0.000	1.000	1.000
$y_{feed, H2}$	0.000	0.000	0.100	0.000	0.000
$y_{feed, N2}$	0.000	0.000	0.900	0.000	0.000
u_{feed} [m/s]	0.08	0.00	0.30	0.30	-
T_{feed} [K]	723	673	673	723	723
T_w [K]	723	673	673	723	723
P_{out} [bar]	4.457	1.257	1.257	1.257	4.457

In the case of SMR-SERP, the steam methane reforming reactions are enhanced by the use of a high temperature sorbent selective for CO_2 as shown in Figure 4.21.

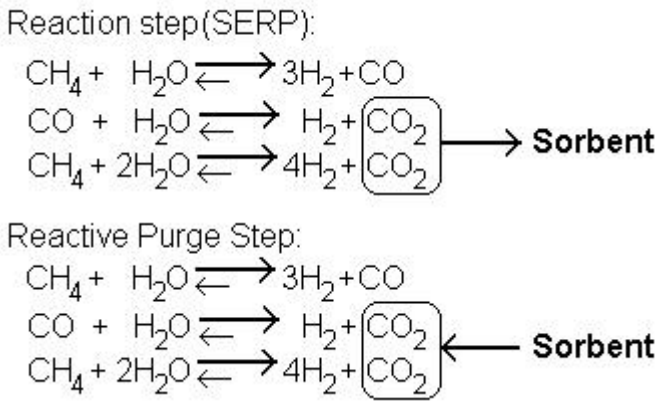

Figure 4.21. Effect of reaction and reactive purge steps of the SMR-SERP cycle proposed by Xiu et al [1] on reforming and water gas shift chemical reactions.

In their study, Xiu *et al* [1] employed the SMR-SERP concept to produce hydrogen during the reaction step of a pressure swing cycle. In order to increase the desorption rate of CO_2 from the sorbent, the reactive regeneration concept was proposed: hydrogen was used to promote the reverse of the WGS and Global SMR reactions, increasing the CO_2 desorption rate as shown in Figure 4.21. Xiu *et al* [1] proposed the use of 10 % H_2 in N_2 instead of employing steam because steam is a product of the reverse reactions and would decrease the reaction rate. Following the reactive purge, the reactor is purged with steam to avoid contamination of the hydrogen produced during the reaction with nitrogen.

The simulation results of the SMR-SERP reactive regeneration employing the Degussa catalyst and MG30-K sorbent are shown in Figure 4.22. In the initial cycle, during the reaction step the effluent was composed mostly of hydrogen (81.7 %) and methane (18.1 %) with traces of CO_2 (0.002 %) and CO (160 ppm). However, in cyclic steady state the hydrogen purity was reduced to 71.1 % while the CO_2 and CO

content rose to 0.008 % and 308 ppm, respectively. Xiu *et al* [1] obtained an effluent with 80.5 % H_2 with 19.3 % methane, 0.2 % CO_2 and 109 ppm of CO.

Table 4.9. Parameters used in the simulations of the non-isothermal SMR-SERP reactor employing a random mixture of Degussa catalyst and MG30-K sorbent .

Column		**Degussa catalyst**	
R_c [m]	0.0125	**R_{cat} [mm]**	0.80
L_c [m]	2.0	**$L_{p,cat}$ [mm]**	5.0
ε_c	0.48	**$r_{pore,cat}$ [nm]**	4.25
U [W/(m².K)]ª	7.71	**ρ_{cat} [kg/m³]**	1274
ρ_{gas} [kg/m³]ª	1.32	**$\varepsilon_{p,cat}$**	0.64
μ_{gas} [Pa.s]ª	2.53×10^{-5}	**τ_p**	1.56
λ_{ax} [W/m.K]ª	0.73	**$\hat{C}_{ps,cat}$ [J/(kg.K)]ª**	1040
D_{ax} [m²/s]ª	8.81×10^{-5}	**$h_{f,cat}$ [W/(m².K)]ª**	165
D_m [m²/s]ª	2.6×10^{-5}	**$k_{f,cat}$ [m/s]ª**	0.111
Re	14	**$D_{k,cat}$ [m²/s]ª**	2.63×10^{-6}
Pe	3784	**$D_{p,cat}$ [m²/s]ª**	1.53×10^{-6}
MG30-K hydrotalcite			
r_{sorb} [mm]	2.215	**$a_{p,sorb}$ [m⁻¹]**	1354
$r_{pore,sorb}$ [nm]	4.55	**$\hat{C}_{ps,sorb}$ [J/(kg.K)]**	850
ρ_{sorb} [kg/m³]	1845	**$h_{f,sorb}$ [W/(m².K)]ª**	92
$\varepsilon_{p,sorb}$	0.27	**$k_{f,sorb}$ [m/s]ª**	0.04

a – Calculated for the reaction step conditions at 723 K and 4.457 bar.

The main reason for the lower hydrogen purity obtained using the experimental data collected at LSRE is that the regeneration of the MG30-K hydrotalcite sorbent is much slower than the material reported by Ding and Alpay [14]. The CO_2 sorbed concentrations at the end of the reaction, depressurization and reactive purge steps in CSS, obtained in this work and reported by Xiu *et al* [1] are compared in Figure 4.23. It can be seen that, in this work, the reactive regeneration was not able to desorb substantial amounts of CO_2.

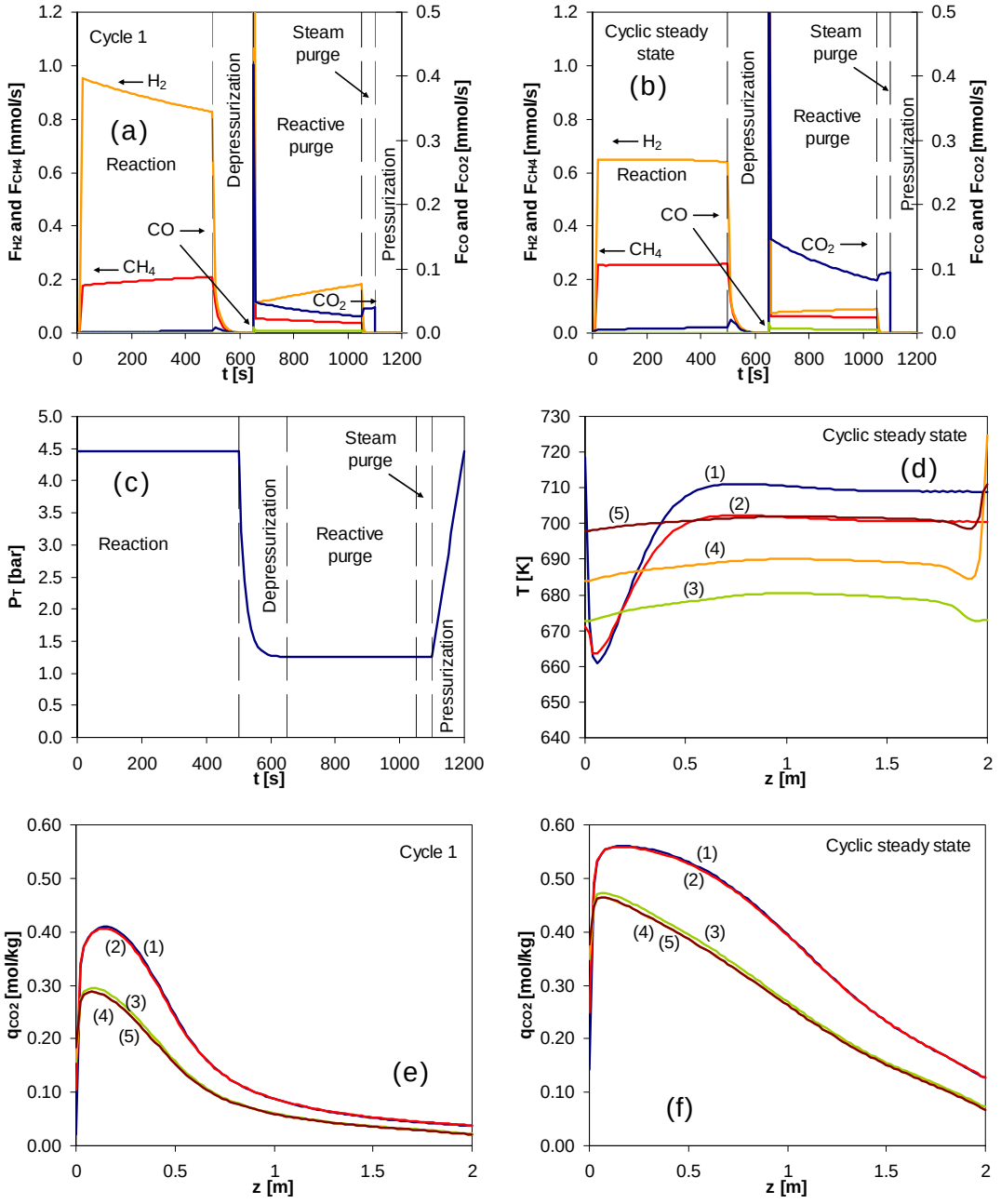

Figure 4.22. Effluent molar flowrates in cycle 1 (a) and CSS (b); pressure histories (c); temperature profiles (d) and CO_2 sorbed concentration profiles in cycle 1 (e) and CSS (f) at the end of the reaction (1), depressurization (2), reactive purge (3), steam purge (4) and pressurization (5) steps in CSS (Cycle 30). Simulation of the SMR-SERP cycle with reactive regeneration (simulation L2-1).

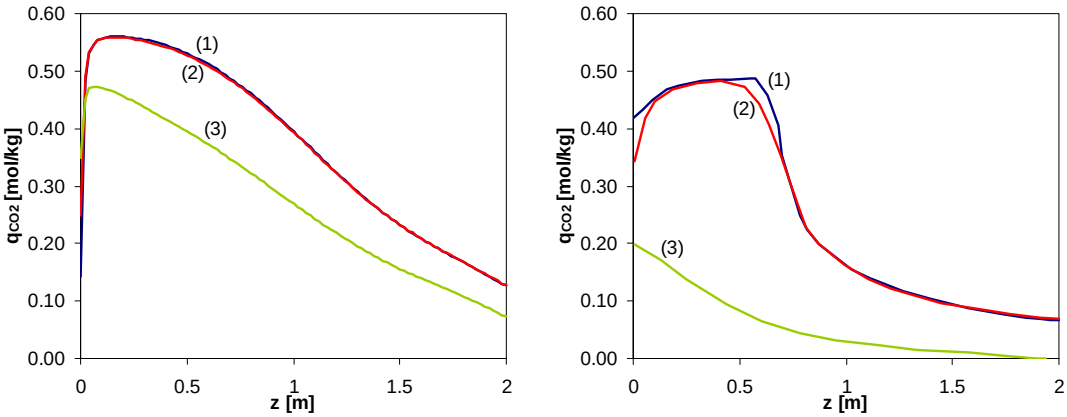

Figure 4.23. CO_2 sorbed concentration profiles obtained in this work (a) and reported by Xiu et al [1] at the end of the reaction (1), depressurization (2) and reactive purge (3) in CSS. Simulations of SMR-SERP with reactive regeneration.

The reactive regeneration was carried out at lower temperature (673 K) in order to promote the reverse of the WGS and SMR reactions. However, the desorption rate of CO_2 in the hydrotalcite material decreases exponentially with temperature and the decrease is much more marked in this work than in the data from Alpay [14]. This means that using the MG30-K prepared at LSRE, decreasing the temperature is detrimental to the regeneration of the sorbent.

It is also important to determine the rates of production and uptake of CO_2 in the reaction step. The results obtained during the reaction step of Cycle 1 and CSS are compared in Figure 4.24. The carbon dioxide production rate is roughly 5 times higher than the CO_2 sorption rate in the hydrotalcite. Near the feed end of the reactor the ratio between production and sorption of CO_2 can reach two orders of magnitude. In order to compensate for the difference in the CO_2 production/sorption ratio, many authors employed sorbent/catalyst ratios higher than 2 [1, 14, 15]. In this work, a sorbent/catalyst volumetric

ratio of 3 was used but may be higher values could have improved process performance.

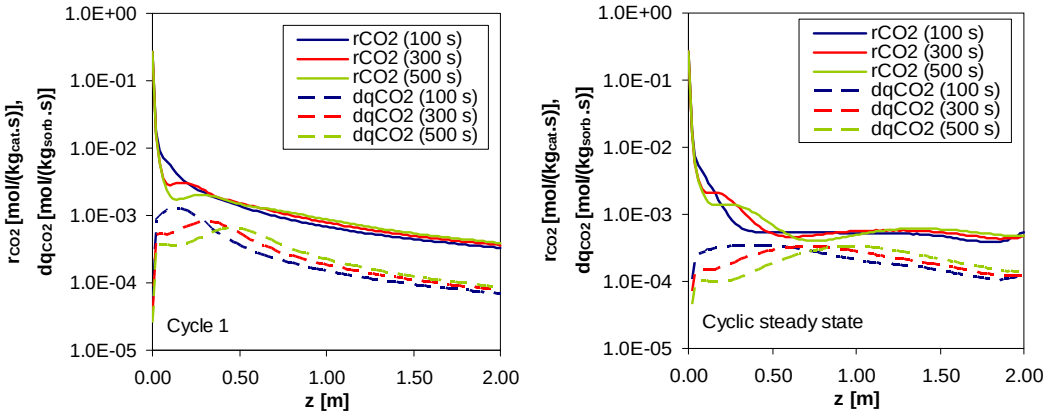

Figure 4.24. Simulation of production and sorption rates of CO_2 during the reaction step of Cycle 1 (a) and at CSS (b) for the SMR-SERP with reactive regeneration employing the Degussa catalyst and the MG30-K hydrotalcite.

Other key parameter of the SMR-SERP is the CO content in the hydrogen produced. The carbon monoxide dry-basis molar fraction evolution during the reaction step of the SMR-SERP with reactive regeneration in CSS is shown in Figure 4.25. The carbon monoxide content in the effluent was above 100 ppm during the reaction step of Cycle 1 – average of 160 ppm. In cyclic steady state the average increased to 308 ppm. Using the same operating conditions and the CO_2 sorption kinetics proposed by Ding and Alpay [14], Xiu *et al* [1] reported an average concentration of 102 ppm of CO.

The hydrotalcite material employed in this work has slower CO_2 sorption kinetics and thus the production of CO is higher because of a lower sorption enhancement of the WGS reaction. To obtain an average CO content of 28 ppm, Xiu *et al* [1] proposed the use of a reactor with 6 m and a shorter reaction step (350 s). Simulation results of the 6 m reactor using the operating conditions proposed by Xiu *et al* [1]

are reported in Table 4.10. The simulation of the 6 m reactor with $t_{reaction}$ = 350 s (L6-1) resulted in a hydrogen purity of 82.4 % with 89 ppm of CO. The hydrogen purity is much higher than the one obtained with the 2 m long reactor (L2-1), with the expense of a strong decrease in the hydrogen productivity (increase in column size and reduction of reaction step). However, the CO concentration is much higher than the value reported by Xiu *et al* [1] that comply with the 30 ppm restriction for PEM fuel cells.

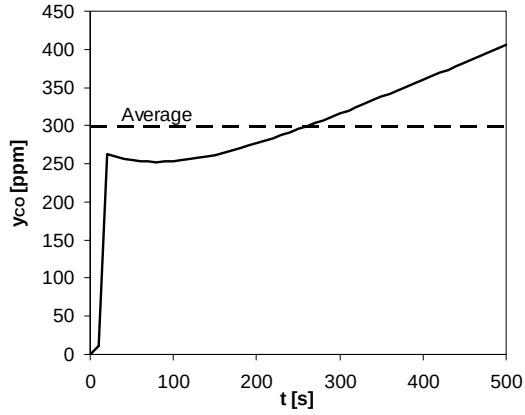

Figure 4.25. Simulated carbon monoxide dry-basis molar fraction in the effluent stream obtained during the reaction step of the SMR-SERP reactive regeneration in CSS, employing the Degussa catalyst and the MG30-K hydrotalcite.

Based on the analysis of Runs L2-1 and L6-1, the operating conditions were modified with the objective of increasing hydrogen purity, productivity and lowering the CO content in the effluent during the reaction step.

Table 4.10. Operating conditions and results of the SMR-SERP simulations employing Degussa catalyst and MG30-K sorbent with a sorbent/catalyst volumetric ratio of 3.

Run	L2-1	L6-1	L2-2	L2-3	L6-2	L6-3
L_c [m]	2.0	6.0	2.0	2.0	6.0	6.0
$t_{reaction}$ [s]	500	350	500	400	350	350
$t_{depress}$ [s]	150	150	150	100	150	100
$t_{reactive\ purge}$ [s]	400	400	400	350	400	400
$t_{steam\ purge}$ [s]	50	50	50	250	50	250
t_{press} [s]	100	100	100	100	100	100
u_{feed} [m/s] [a]	0.08/0.3	0.08/0.3	0.08/0.3	0.08/0.3/0.5[b]	0.08/0.3	0.08/0.3/0.5[b]
T_{feed} [K][a]	723/673	723/673	723	723/740	723	680
T_w [K][a]	723/673	723/673	723	723/740	723	680/740
P_{out} [bar][a]	4.46/1.26	4.46/1.26	4.46/1.26	4.46/1.26	4.46/1.26	4.46/1.26
Simulation results (Cyclic Steady State)						
$y_{CH4,reaction}$	0.281	0.174	0.234	0.198	0.144	0.216
$y_{CO2,reaction}$	0.008	0.001	0.007	0.003	0.001	0.0007
$y_{CO,reaction}$ [ppm]	308	89	370	227	101	30
Purity [%]	71.1	82.4	75.9	79.9	85.5	78.3
% SERP	141	210	162	182	226	257
Productivity [$mol_{H2}/(m^3_{col}.h)$]	555	166	732	665	211	137
Gain [$mol_{H2}/(4mol_{CH4})$]	0.218	0.245	0.288	0.327	0.311	0.221

a – reaction/reactive purge;

b – reaction/reactive purge/steam purge.

In Run L2-2, the feed and wall temperatures were maintained constant in all the steps. This change modified the temperature profile inside the reactor, especially at the start of each cycle as shown in Figure 4.26. In CSS, the hydrogen purity of Run L2-2 was 75.9 %. This value is higher than in Run L2-1 but CO content was higher (370 ppm) due to the faster SMR reaction rates.

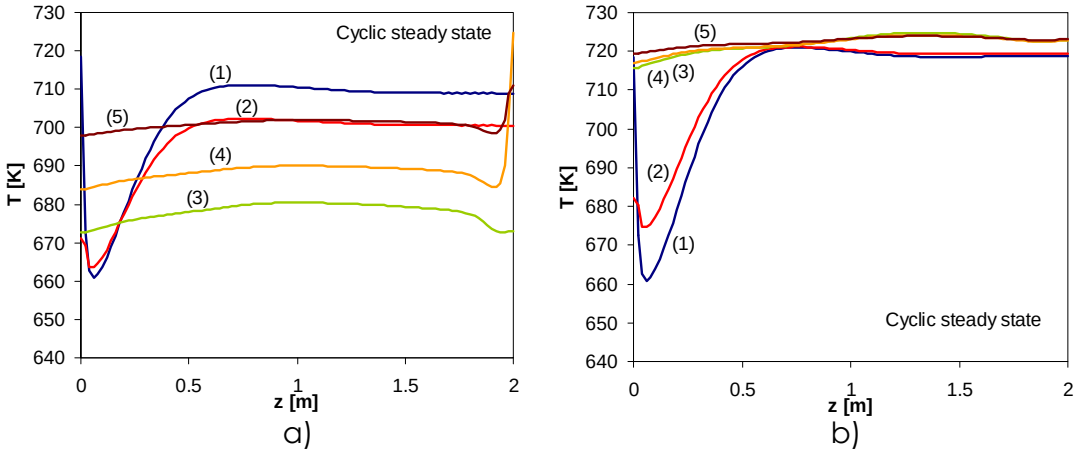

Figure 4.26. Simulated temperature profiles of Run L2-1 (a) and L2-2 (b) in CSS at the end of the reaction (1), depressurization (2), reactive purge (3), steam purge (4) and pressurization (5) steps in CSS (Cycle 30). Operating conditions are detailed in Table 4.10 [1].

In Run L2-3, the reactive purge temperature was increased to 740 K. The steam purge time and flowrate were also increased in order to further improve the CO_2 desorption. The reaction step time was decreased to 400 s to reduce the amount of CO_2 produced and compensate for the slower sorption kinetics. To balance the lower amount of hydrogen produced during the reaction step, the reactive purge step time was also reduced.

The modifications of the operating parameters in Run L2-3 resulted in an overall improvement of the performance parameters: improved CO_2 desorption and thus the hydrogen purity. However, the CO content

was only reduced to 227 ppm. The solution proposed by Xiu *et al* [1] to reduce the CO concentration in the effluent was to decrease the reaction step time and increase the reactor length (Run L6-1).

In Run L6-2 the feed and wall temperatures were kept constant during the complete cycle. This resulted in an increase of the hydrogen purity and productivity. However, as seen in Run L2-2, the CO concentration also increased due to the higher SMR reaction rate.

In Run L6-3, the temperature of the reaction step was reduced to 680 K and the purge times and flowrates were modified based on the data obtained in Run L2-3. With these modifications to the cycle, a stream with a hydrogen purity of 78.3 % and with 30 ppm of CO was obtained in CSS. This value is within the limit for PEM fuel cells. The hydrogen purity is lower than the one obtained in Run L6-2 due to the decrease in the SMR reaction rate necessary to reduce the CO content. This means that, a separation step is necessary to recover and recycle the unconverted methane.

The performance of Catalyst A extrudates for SMR-SERP with reactive regeneration was evaluated by simulating a reactor with L_c = 6 m and R_c = 0.025 m. The large column radius was employed to increase the realistic assumption of obtaining a random distribution of Catalyst A extrudates and hydrotalcite sorbent, since the catalyst particles are very large (R_{cat} = 5.6 mm).

Catalyst A has two advantages when compared to the commercial Degussa catalyst: large-pore network that enhances the mass transfer inside the catalyst; large particle size that decreases the pressure drop inside the reactor. On the other side, the Degussa catalyst has higher Ni content that results in higher true kinetics. Due to the

different characteristics of the two catalysts, two sets of operating conditions were employed in order to obtain a hydrogen stream with less than 30 ppm of CO with each catalyst. The parameters employed in the simulations of Catalyst A and MG30-K sorbent can be seen in Table 4.11. The operating conditions and results of the SMR-SERP simulations are reported in Table 4.12. Due to the different densities of Catalyst A and Degussa extrudates, the mass of catalyst employed was different in order to obtain a sorbent/catalyst volumetric ratio of 3.

Table 4.11. Parameters used in the simulations of the non-isothermal SMR-SERP reactor employing a random mixture of Catalyst A and MG30-K sorbent.

Column		**Catalyst**	**Catalyst A**
R_c [m]	0.025	**R_{cat} [mm]**	5.6
L_c [m]	6.0	**$L_{p,cat}$ [mm]**	15.5
U [W/(m².K)]ª	7.06	**$r_{pore,cat}$ [nm]**	4.0×10^5
ρ_{gas} [kg/m³]ª	1.36	**ρ_{cat} [kg/m³]**	1687
μ_{gas} [Pa.s]ª	2.45×10^{-5}	**$\varepsilon_{p,cat}$**	0.57
λ_{ax} [W/m.K]ª	0.98	**τ_p**	1.76
D_{ax} [m²/s]ª	1.59×10^{-4}	**$\hat{C}_{ps,cat}$ [J/(kg.K)]ª**	1062
D_m [m²/s]ª	2.45×10^{-5}	**$h_{f,cat}$ [W/(m².K)]ª**	494
Re	24	**$k_{f,cat}$ [m/s]ª**	0.0188
Pe	6302	**$D_{k,cat}$ [m²/s]ª**	2854×10^{-4}
Sc	0.74	**$D_{p,cat}$ [m²/s]ª**	1.39×10^{-5}
MG30-K hydrotalcite			
r_{sorb} [mm]	2.215	**$a_{p,sorb}$ [m⁻¹]**	1354
$r_{pore,sorb}$ [nm]	4.55	**$\hat{C}_{ps,sorb}$ [J/(kg.K)]**	850
ρ_{sorb} [kg/m³]	1845	**$h_{f,sorb}$ [W/(m².K)]ª**	90
$\varepsilon_{p,sorb}$	0.27	**$k_{f,sorb}$ [m/s]ª**	0.05

a – Calculated for the reaction step conditions at 700 K and 4.457 bar.

Table 4.12. Operating conditions and results of the SMR-SERP simulations employing Catalyst A or Degussa catalyst and MG30-K sorbent with a sorbent/catalyst volumetric ratio of 3 (L_c = 6 m; R_c = 0.025 m).

Run	Catalyst A-1	Degussa-1	Catalyst A-2	Degussa-2
m_{cat} [kg]	2.58	1.95	2.58	1.95
m_{sorb} [kg]	8.48	8.48	8.48	8.48
$t_{reaction}$ [s]	350	350	1100	1100
$t_{depress}$ [s]	100	100	100	100
$t_{reactive\ purge}$ [s]	400	400	200	200
$t_{steam\ purge}$ [s]	270	270	470	470
t_{press} [s]	100	100	100	100
u_{feed} [m/s][a]	0.08/0.3/0.5	0.08/0.3/0.5	0.013/0.3/0.7	0.013/0.3/0.7
T_{feed} [K][a]	680/740/680	680/740/680	680/740/680	680/740/680
T_w [K][a]	680/740/680	680/740/680	680/740/680	680/740/680
P_{out} [bar]	4.46/1.26	4.46/1.26	4.46/1.26	4.46/1.26
Simulation results (Cyclic Steady State)				
$y_{CH4,reaction}$	0.269	0.190	0.197	0.139
$y_{CO2,reaction}$	0.0007	0.0006	0.0002	0.0002
$y_{CO,reaction}$ [ppm]	130	29	25	10
Purity [%]	73.1	80.9	80.0	86.0
% SERP	241	290	324	366
Productivity [$mol_{H2}/(m^3_{col}.h)$]	98	158	35.9	51.2
Gain [$mol_{H2}/(4mol_{CH4})$]	0.158	0.255	0.180	0.259

a – reaction/reactive purge/steam purge;

Reaction: y_{CH4} = 0.143 and y_{H2O} = 0.857; Reactive purge: y_{N2} = 0.90 and y_{H2} = 0.10;

Steam Purge and Pressurization: y_{H2O} = 1.0

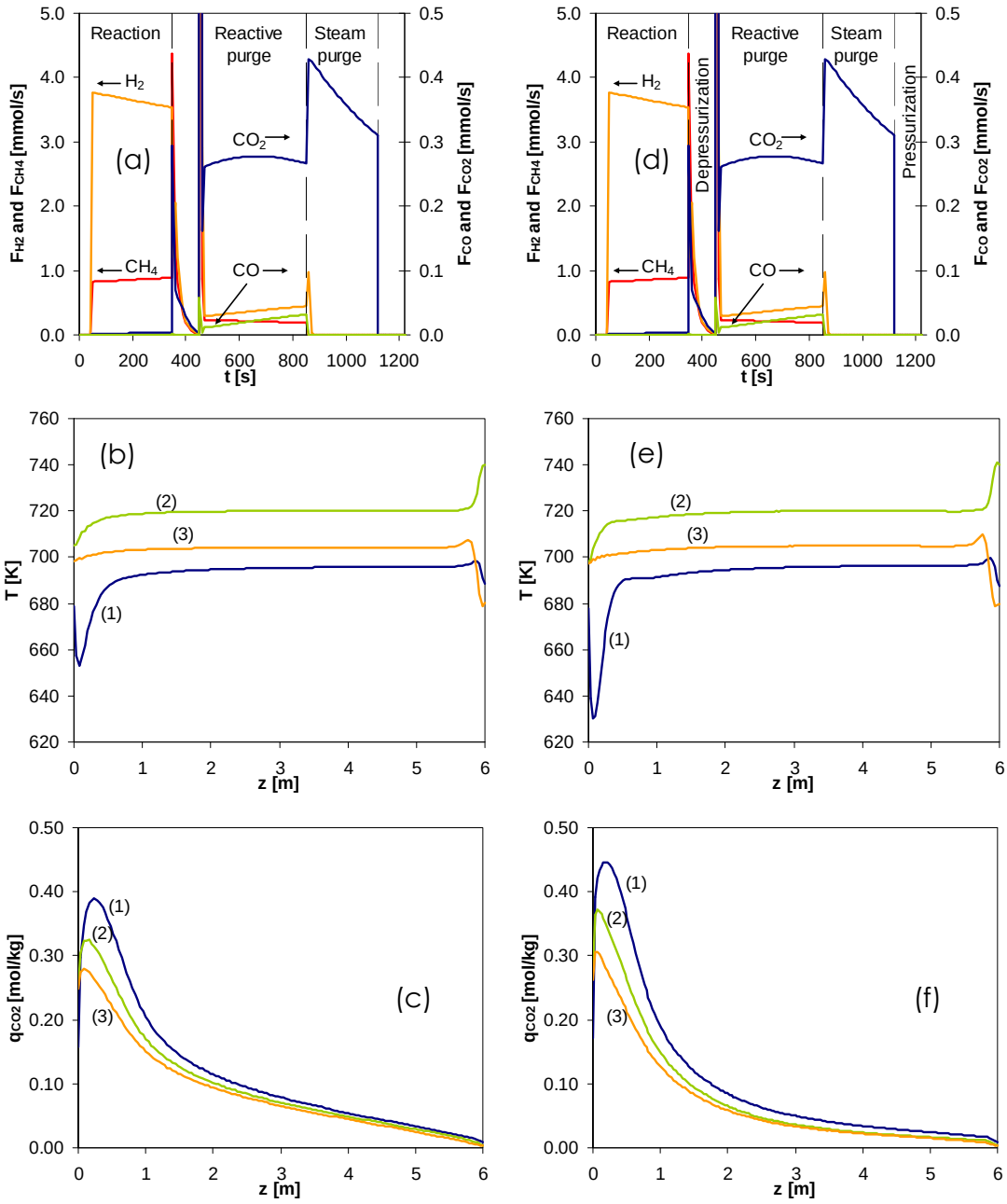

Figure 4.27. Effluent molar flowrates (a), temperature profiles (b) and CO_2 sorbed concentration (c) obtained in CSS in Run "Catalyst A-1". Effluent molar flowrates (d), temperature profiles (e) and CO_2 sorbed concentration (f) obtained in CSS in Run "Degussa-1". Results obtained at the end of the reaction (1), reactive purge (2) and steam purge (3) steps of the SMR-SERP cycle with reactive regeneration.

The operating conditions of Run L6-3 were employed in the SMR-SERP simulations of the larger reactor – Runs Catalyst A-1 and Degussa-1. The results are shown in Figure 4.27.

In the simulations employing Degussa catalyst, a stream with 29 ppm of CO and 80.9 % H_2 was produced. In the SMR-SERP employing Catalyst A, the CO content was 130 ppm. The temperature drop near the feed end of the reactor is caused by the endothermic SMR reactions. In the case of the Degussa catalyst this decrease was bigger than with Catalyst A, indicating a higher SMR reaction rate. The lower temperature in that section of the reactor increases the hydrogen purity since on the one hand, more CO is converted to CO_2 and hydrogen by the WGS reaction, increasing the purity and productivity; and on the other hand, the MG30-K sorbent has a maximum in sorption capacity at 673 K, and therefore higher sorption capacity is available in the sorbent, increasing the sorption enhancement. By comparing Figure 4.27c (Catalyst A-1) with Figure 4.27e (Degussa-1) it can be observed that more CO_2 was sorbed in the hydrotalcite when Degussa catalyst was employed.

In Figure 4.27, it can also be observed that, during the reactive purge step, the CO effluent molar flowrate increases monotonically. During this step the wall temperature was increased to 740 K, increasing both the desorption rate of CO_2 and the reaction rate of the reverse water gas shift reaction.

The extrudates of Catalyst A are 7 times larger than the Degussa extrudates. Larger particles create a lower the pressure drop inside the reactor. In order to apply the Ergun equation to calculate the pressure drop, the average particle radius inside the reactor was calculated

according to equation 4.17. Since a sorbent/catalyst ratio of 3 was employed in these simulations, the average radius in Run Catalyst A-1 is only 1.5 times larger than the average radius employed in Run Degussa-1. Despite the smaller difference, the pressure drop when Catalyst A was employed was half of the pressure drop when Degussa catalyst was used, showing the advantage of Catalyst A over Degussa catalyst.

The carbon monoxide dry-basis molar fraction profile obtained at the end of the reaction step in Run Catalyst A-1 is shown in Figure 4.28.

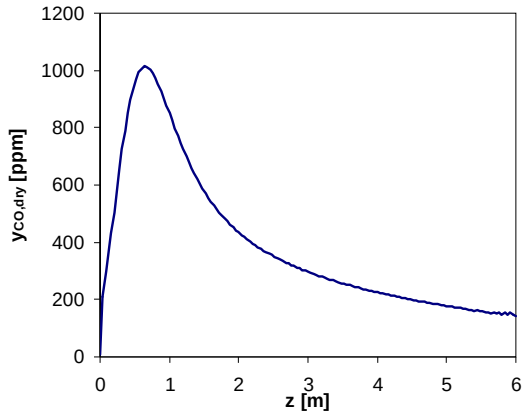

Figure 4.28. Carbon monoxide dry-basis molar fraction profile at the end of the reaction step of Run Catalyst A-1. Simulation of the SMR-SERP reactor with L_c = 6 m and R_c = 0.025 m (see operating conditions and simulation results in Table 4.12).

In the initial section of the reactor, the CO molar fraction increases to a maximum of 1013 ppm, produced by the conversion of methane by the SMR reaction. The molar fraction then drops as CO is converted to CO_2 by the WGS reaction, but at the effluent end it is still higher than 30 ppm. In Run Catalyst A-2, the operating conditions were optimized to obtain an effluent with less than 30 ppm of CO. The main modification was the reduction of the feed flowrate in order to promote the WGS reaction. At lower flowrates, the contact time of CO with the catalyst

and of CO_2 with the hydrotalcite sorbent is increased, promoting a sorption enhancement effect of the water gas shift reaction. To compensate for the decrease in the flowrate, the time of the reaction step was increased to 1100 s (see Table 4.12 for other operating conditions and simulation results).

In Run Catalyst A-2, a stream with a hydrogen purity of 80 % was produced with 25 ppm of CO. There was also an increase in the SERP effect when compared to Run Catalyst A-1 since the same feed temperature, pressure and composition were employed (same equilibrium conversion) but contact time of CO_2 with the sorbent was increased, promoting the CO_2 sorption kinetics. The drawback of reducing the feed flowrate is that less hydrogen is produced during the reaction step despite the increased reaction time. To compensate, in Run Catalyst A-2 the reactive purge time was decreased and the steam purge was increased.

In the present study, due to low sorption kinetics of the MG30-K hydrotalcite, the feed temperature was decreased to 680 K to limit the amount of CO produced by the catalyst to less than 30 ppm. At this temperature, the equilibrium methane conversion of a traditional SMR is 19 % but with the SMR-SERP the conversion was 47 % (Run Degussa-1).

4.6. Conclusions

In this Chapter, the two Ni/Al_2O_3 catalysts (Catalyst A and Degussa) were employed for steam methane reforming sorption enhanced reaction process (SMR-SERP). Experiments were performed using a layered configuration of catalyst and sorbent extrudates to evaluate

the SMR-SERP under different operating conditions (feed flowrate, feed temperature and pressure). Cyclic reaction/regeneration experiments were also performed to check the stability of the SMR-SERP.

A total of six alternating layers of Catalyst A and MG30-K sorbent were used for SMR-SERP. In all experiments, before CO_2 breakthrough, the methane conversion and hydrogen purity were higher than equilibrium values for a SMR only reactor. Using hydrogen during the regeneration of the sorbent material increased the CO_2 desorption rate (reactive regeneration). However, the effect decreases with time. During the cyclic experiments a hydrogen purity of 71 % was obtained with low CO content.

With the commercial Degussa catalyst, higher methane conversions and hydrogen purities were reached compared with the experiments employing Catalyst A. This was attributed to the higher Ni content of the Degussa catalyst even though Catalyst A has lower mass transfer resistances due to the large-pore network. A hydrogen purity of 75 % was obtained in cyclic steady state with unreacted methane as the main contaminant (24 %)

From the experimental work it was confirmed: increasing the total pressure of the reaction step decreases the conversion of methane but increases the sorption capacity of the sorbent material; increasing the feed temperature increases the methane conversion and the sorption and desorption kinetics but decreases the CO_2 sorption capacity of the hydrotalcite. Therefore, for the SMR-SERP, there is an optimum set of operating conditions to maximize both the hydrogen production and the hydrogen purity.

The performance of the SMR-SERP was far from ideal due to the slow CO_2 sorption kinetics of the hydrotalcite material. These kinetic

effects reduce the displacement of the equilibrium during the reaction step and also increase the time required to regenerate the sorbent.

A mathematical model was developed to describe the SMR-SERP. Employing the parameters determined in Chapter 2 and Chapter 3, the model was able to describe the SMR-SERP experiments without any fitting parameter.

After validation by SMR-SERP experiments, the mathematical model was employed to simulate the reactive regeneration cycle proposed by Xiu *et al* [1]. As a consequence of the slow CO_2 sorption kinetics in the MG30-K hydrotalcite, lower hydrogen purities and higher CO contents were obtained if compared to the results of Xiu *et al* [1]. After optimization of the operating conditions of the reactive regeneration cycle, simulations show that it is possible to produce a stream with 30 ppm of CO and a hydrogen purity of 78 % at the expense of decrease in the process productivity.

In order to determine the performance of Catalyst A for the SMR-SERP with reactive regeneration, the SMR-SERP mathematical model was also employed to simulate a reactor with R_c = 25 mm. In this reactor, a stream with 29 ppm of CO was obtained at 680 K.

Industrial steam methane reformers are operated at temperatures higher than 1000 K in order to reach thermodynamic equilibrium. In this work, the SMR-SERP was operated at much lower temperatures while obtaining methane conversions higher than thermodynamic equilibrium. Also, hydrogen purities over 80 % were obtained without any extra separation steps. This shows that the SMR-SERP is an alternative to conventional steam methane reformers.

4.7. References

(1) Xiu, G.-h.; Li, P.; Rodrigues, A. E. Sorption-enhanced reaction process with reactive regeneration. *Chem. Eng. Sci.* (2002), 57.
(2) Yang, R. T. Gas separation by adsorption processes. First ed, Imperial College Press, London, 1987.
(3) Gulker, F. Method of producing hydrogen. GB275273, 1928.
(4) Mayorga, S. G.; Hufton, J. R.; Sircar, S.; Gaffney, T. R. Sorption Enhanced Reaction Process for the production of hydrogen. Phase I Final Report, Proceedings of U.S. DOE Hydrogen program Review, Washington DC, 1997.
(5) Aida, T.; Silveston, P. L. Cyclic Separating Reactors. First ed, Wiley-Blackwell, New York, 2005.
(6) Yong, Z.; Mata, V.; Rodrigues, A. E. Adsorption of carbon dioxide at high temperature - a review. *Sep. Purif. Technol.* (2002), 26, 195-205.
(7) Duarte, C. F. M. Production of TAME and n-Propyl propionate by reactive distillation. PhD thesis, University of Porto, Porto, 2006.
(8) Agreda, V. H.; Partin, L. R.; Heise, W. H. High-purity methyl acetate via reactive distillation. *Chem. Eng. Prog.* (1990), 86, 40-46.
(9) Oliveira, M. M. V. F. d. TAME : Cinética em reactor fechado e simulação da produção em contínuo. PhD thesis, University of Porto, Porto, 2004.
(10) Bottino, A.; Comite, A.; Capannelli, G.; Di Felice, R.; Pinacci, P. Steam reforming of methane in equilibrium membrane reactors for integration in power cycles. *Catal. Today* (2006), 118, 214-222.
(11) Mori, N.; Nakamura, T.; Noda, K.-I.; Sakai, O.; Takahashi, A.; Ogawa, N.; Sakai, H.; Iwamoto, Y.; Hattori, T. Reactor configuration and

concentration polarization in methane steam reforming by a membrane reactor with a highly hydrogen-permeable membrane. *Ind. Eng. Chem. Res.* (2007), 46, 1952-1958.

(12) Zou, J.; Huang, J.; Ho, W. S. W. CO_2-selective water gas shift membrane reactor for fuel cell hydrogen processing. *Ind. Eng. Chem. Res.* (2007), 46, 2272-2279.

(13) Balasubramanian, B.; Lopez Ortiz, A.; Kaytakoglu, S.; Harrison, D. P. Hydrogen from methane in a single-step process. *Chem. Eng. Sci.* (1999), 54, 3543-3552.

(14) Ding, Y.; Alpay, E. Adsorption-enhanced steam-methane reforming. *Chem. Eng. Sci.* (2000), 55, 3929-3940.

(15) Hufton, J. R.; Mayorga, S.; Sircar, S. Sorption-enhanced reaction process for hydrogen production. *AIChE J.* (1999), 45, 248-256.

(16) Ochoa-Fernandez, E.; Rusten, H. K.; Jakobsen, H. A.; Ronning, M.; Holmen, A.; Chen, D. Sorption enhanced hydrogen production by steam methane reforming using Li_2ZrO_3 as sorbent: Sorption kinetics and reactor simulation. In International Conference on Gas-Fuel 05, Brugge, November, *Catalysis Today* (2005), 41-46.

(17) Reijers, H. T. J.; Valster-Schiermeier, S. E. A.; Cobden, P. D.; van den Brink, R. W. Hydrotalcite as CO_2 Sorbent for Sorption-Enhanced Steam Reforming of Methane. *Ind. Eng. Chem. Res.* (2006), 45, 2522-2530.

(18) Ullmann, F. Ullmann's Encyclopedia of Industrial Chemistry (Online version: http://mrw.interscience.wiley.com/emrw/9783527306732/ueic/article/a13_297/current/html#a13_297-sec1-0004). 7th ed, John Wiley & Sons, Inc., New York, 2009.

(19) Chen, Y.; Xu, H.; Wang, Y.; Xiong, G. Hydrogen production from the steam reforming of liquid hydrocarbons in membrane reactor. *Catal. Today* (2006), 118, 136-143.
(20) Tong, J.; Matsumura, Y. Pure hydrogen production by methane steam reforming with hydrogen-permeable membrane reactor. In Amsterdam, 1000 AE, Netherlands, *Catalysis Today* (2006), 147-152.
(21) Essaki, K.; Muramatsu, T.; Kato, M. Effect of equilibrium shift by using lithium silicate pellets in methane steam reforming. *Int. J. Hydrogen Energy* (2008), 33, 4555-4559.
(22) Hildenbrand, N.; Readman, J.; Dahl, I. M.; Blom, R. Sorbent enhanced steam reforming (SESR) of methane using dolomite as internal carbon dioxide absorbent: Limitations due to $Ca(OH)_2$ formation. *Appl. Catal., A* (2006), 303, 131-137.
(23) Li, Z.-S.; Cai, N.-S.; Yang, J.-B. Continuous production of hydrogen from sorption-enhanced steam methane reforming in two parallel fixed-bed reactors operated in a cyclic manner. *Ind. Eng. Chem. Res.* (2006), 45, 8788-8793.
(24) Mayorga, S. G.; Gaffney, T. R.; Brzozowski, J. R.; Weigel, S. J. Carbon dioxide adsorbents containing magnesium oxide suitable for use at high temperatures. European Patent 1074297, 2001.
(25) Bretado, M. E.; Vigil, M. D. D.; Collins-Martinez, V.; Ortiz, A. L. Thermodynamic Analysis for the Production of Hydrogen through Sorption Enhanced Water Gas Shift (SEWGS). *Int. J. Chem. Reactor Eng.* (2008), 6, A51.
(26) Lee, K. B.; Beaver, M. G.; Caram, H. S.; Sircar, S. Reversible chemisorption of carbon dioxide: Simultaneous production of fuel-cell grade H_2 and compressed CO_2 from synthesis gas. *Adsorption* (2007), 13, 385-397.

(27) van Selow, E. R.; Cobden, P. D.; van den Brink, R. W.; Hufton, J. R.; Wright, A. Performance of sorption-enhanced water-gas shift as a pre-combustion CO_2 capture technology. *Energy Procedia* (2009), 1, 689-696.
(28) Wright, A.; White, V.; Hufton, J.; Selow, E. v.; Hinderink, P. Reduction in the cost of pre-combustion CO_2 capture through advancements in sorption-enhanced water-gas-shift. *Energy Procedia* (2009), 1, 707-714.
(29) Cho, B. K.; Carr, R. W., Jr.; Aris, R. Continuous chromatographic reactors. *Chem. Eng. Sci.* (1980), 35, 74-81.
(30) Takeuchi, K.; Uraguchi, Y. Experimental studies of a chromatographic moving-bed reactor. Catalytic oxidation of carbon monoxide on activated alumina as a model reaction. *J. Chem. Eng. Jpn.* (1977), 10, 455-460.
(31) Ressler, S.; Agar, D. W. Enhancement of the syngas-to-dimethyl ether process by adsorptive water removal. In 4th International Symposium on Multifunctional Reactors, Portorož-Portorose, Slovenia, June 15−18, (2005).
(32) Lu, Z. P.; Loureiro, J. M.; Rodrigues, A. E. Simulation of Pressure Swing Adsorption Reactors. In CHEMPOR'93, International Chemical Engineering Conference, Porto, April 4-6, (1993), 75-82.
(33) Lu, Z. P.; Rodrigues, A. E. Pressure swing adsorption reactors: simulation of three-step one-bed process. *AIChE J.* (1994), 40, 1118-1137.
(34) Rawadieh, S.; Gomes, V. G. Catalyst-adsorbent configurations in enhancing adsorptive reactor performance. *Int. J. Chem. Reactor Eng.* (2007), 5, 18 pp.
(35) Loureiro, J. M. Adsorção e reacção química simultâneas em partículas porosas : Aplicação ao estudo da recuperação de metais com resinas complexantes. PhD thesis, University of Porto, Porto, 1986.

(36) Silva , V. M. T. M. d. Diethylacetal synthesis in simulated moving bed reactor. PhD thesis, University of Porto, Porto, 2003.
(37) Gandi, G. K. Process development for fine chemicals (Acetaldehyde Dimethylacetal) synthesis. PhD thesis, University of Porto, Porto, 2006.
(38) Gulker, F. Improvements in and relating to the preparation of hydrogen and to the absorption of carbon dioxide from gas mixtures. GB301499, 1930.
(39) Williams, R. Hydrogen production. US1938202 1933.
(40) Gorin, E.; Retallick, W. B. Method for the production of Hydrogen. US3108857, 1963.
(41) Waldron, W. E.; Hufton, J. R.; Sircar, S. Production of hydrogen by cyclic sorption enhanced reaction process. *AIChE J.* (2001), 47, 1477-1479.
(42) Xiu, G.-h.; Li, P.; Rodrigues, A. E. Adsorption-enhanced steam-methane reforming with intraparticle-diffusion limitations. *Chem. Eng. J.* (2003).
(43) Xiu, G.-h.; Li, P.; Rodrigues, A. E. New generalized strategy for improving sorption-enhanced reaction process. *Chem. Eng. Sci.* (2003), 58, 3425-3437.
(44) Xiu, G.-h.; Li, P.; Rodrigues, A. E. Subsection-controlling strategy for improving sorption-enhanced reaction process. *Chem. Eng. Res. Des.* (2004), 82, 192-202.
(45) Xiu, G.-h.; Soares, J. L.; Li, P.; Rodrigues, A. E. Simulation of five-step one-bed sorption-enhanced reaction process. *AIChE J.* (2002), 48, 2817.
(46) Ortiz, A. L.; Harrison, D. P. Hydrogen production using sorption-enhanced reaction. *Ind. Eng. Chem. Res.* (2001), 40, 5102-5109.

(47) Kwang, B. Y.; Harrison, D. P. Low-pressure sorption-enhanced hydrogen production. *Ind. Eng. Chem. Res.* (2005), 44, 1665-1669.
(48) Peng, Z.; Harrison, D. P. Low-Carbon Monoxide Hydrogen by Sorption-Enhanced Reaction. *Int. J. Chem. Reactor Eng.* (2003), 1, A37.
(49) Satrio, J. A.; Shanks, B. H.; Wheelock, T. D. Development of a novel combined catalyst and sorbent for hydrocarbon reforming. *Ind. Eng. Chem. Res.* (2005), 44, 3901-3911.
(50) Lee, D. K.; Baek, I. H.; Yoon, W. L. A simulation study for the hybrid reaction of methane steam reforming and in situ CO_2 removal in a moving bed reactor of a catalyst admixed with a CaO-based CO_2 acceptor for H_2 production. *Int. J. Hydrogen Energy* (2006), 31, 649-657.
(51) Ochoa-Fernandez, E.; Haugen, G.; Zhao, T.; Ronning, M.; Aartun, I.; Børresen, B.; Rytter, E.; Rønnekleiv, M.; Chen, D. Process design simulation of H_2 production by sorption enhanced steam methane reforming: evaluation of potential CO_2 acceptors. *Green Chem.* (2007), 9, 654 - 662.
(52) Rusten, H. K.; Ochoa-Fernandez, E.; Chen, D.; Jakobsen, H. A. Numerical investigation of sorption enhanced steam methane reforming using Li_2ZrO_3 as CO_2-acceptor. *Ind. Eng. Chem. Res.* (2007), 46, 4435-4443.
(53) Rusten, H. K.; Ochoa-Fernandez, E.; Lindborg, H.; Chen, D.; Jakobsen, H. A. Hydrogen production by sorption-enhanced steam methane reforming using lithium oxides as CO_2-acceptor. *Ind. Eng. Chem. Res.* (2007), 46, 8729-8737.
(54) Lee, K. B.; Beaver, M. G.; Caram, H. S.; Sircar, S. Performance of Na_2O promoted alumina as CO_2 chemisorbent in sorption-enhanced reaction process for simultaneous production of fuel-cell grade H_2 and

compressed CO_2 from synthesis gas. *J. Power Sources* (2008), 176, 312-319.
(55) Cobden, P. D.; van Beurden, P.; Reijers, H. T. J.; Elzinga, G. D.; Kluiters, S. C. A.; Dijkstra, J. W.; Jansen, D.; van den Brink, R. W. Sorption-enhanced hydrogen production for pre-combustion CO_2 capture: Thermodynamic analysis and experimental results. *Int. J. Greenhouse Gas Control* (2007), 1, 170-179.
(56) Lee, K. B.; Beaver, M. G.; Caram, H. S.; Sircar, S. Novel thermal-swing sorption-enhanced reaction process concept for hydrogen production by low-temperature steam-methane reforming. *Ind. Eng. Chem. Res.* (2007), 46, 5003-5014.
(57) Lee, K. B.; Beaver, M. G.; Caram, H. S.; Sircar, S. Production of fuel-cell grade hydrogen by thermal swing sorption enhanced reaction concept. *Int. J. Hydrogen Energy* (2008), 33, 781-790.
(58) Lee, K. B.; Verdooren, A.; Caram, H. S.; Sircar, S. Chemisorption of carbon dioxide on potassium-carbonate-promoted hydrotalcite. *J. Colloid Interface Sci.* (2007), 308, 30-39.
(59) Koumpouras, G. C.; Alpay, E.; Lapkin, A.; Ding, Y.; Stepanek, F. The effect of adsorbent characteristics on the performance of a continuous sorption-enhanced steam methane reforming process. *Chem. Eng. Sci.* (2007), 62, 5632-5637.
(60) Koumpouras, G. C.; Alpay, E.; Stepanek, F. Mathematical modelling of low-temperature hydrogen production with in situ CO_2 capture. *Chem. Eng. Sci.* (2007), 62, 2833-2841.
(61) Ding, Y.; Alpay, E. Equilibria and kinetics of CO_2 adsorption on hydrotalcite adsorbent. *Chem. Eng. Sci.* (2000), 55, 3461-3474.
(62) Xu, J.; Froment, G. F. Methane steam reforming, methanation and water-gas shift: I. Intrinsic kinetics. *AIChE J.* (1989), 35, 88.

(63) da Silva, F. A. Cyclic Adsorption Processes: Application to Propane/Propylene Separation. PhD thesis, University of Porto, Porto, 2003.
(64) Li, D.; Atake, I.; Shishido, T.; Oumi, Y.; Sano, T.; Takehira, K. Self-regenerative activity of Ni/Mg(Al)O catalysts with trace Ru during daily start-up and shut-down operation of CH_4 steam reforming. *J. Catal.* (2007), 250, 299-312.
(65) Ruthven, D. M. Principles of Adsorption and Adsorption Processes. First ed, John Wiley and Sons, Inc, USA, 1984.
(66) Nan, H. S.; Dias, M. M.; Rodrigues, A. E. Effect of forced convection on reaction with mole changes in porous catalysts. *Chem. Eng. J. Biochem. Eng. J.* (1995), 57, 101-114.
(67) Glueckauf, E. Theory of chromatography. Part 10. - Formulae for diffusion into spheres and their application to chromatography. *Trans. Faraday Soc.* (1955), 51, 1540-1551.
(68) Bird, R. B.; Stewart, W. E.; Lightfoot, E. N. Transport Phenomena. Second ed, John Wiley & Sons, Inc, New York, 2002.
(69) Perry, R. H.; Green, D. W. Perry's Chemical Engineers' Handbook. Seventh ed, McGraw-Hill, New York, 1997.
(70) Quinta Ferreira, R. M.; Marques, M. M.; Babo, M. F.; Rodrigues, A. E. Modelling of the methane steam reforming reactor with large-pore catalysts. *Chem. Eng. Sci.* (1992), 47, 2909-2914.
(71) Rodrigues, A. E.; Loureiro, J. M.; Quinta Ferreira, R. M. Intraparticle convection revisited. *Chem. Eng. Commun.* (1991), 107, 21-33.
(72) Rodrigues, A. E.; Lu, Z. P.; Loureiro, J. M. Residence time distribution of inert and linearly adsorbed species in a fixed bed containing 'large-pore' supports. Applications in separation engineering. *Chem. Eng. Sci.* (1991), 46, 2765-2773.

(73) Silva, J. A. C.; Rodrigues, A. E. Fixed-bed adsorption of two linearly adsorbed components in presence of an inert. *Chem. Eng. Sci.* (1998), 53, 3513-3520.
(74) Doong, S. J.; Yang, R. T. Bulk separation of multicomponent gas mixtures by pressure swing adsorption: Pore/surface diffusion and equilibrium models. *AIChE J.* (1986), 32, 397-410.
(75) Silva, J. A. C.; Rodrigues, A. E. Separation of n/iso-paraffins mixtures by pressure swing adsorption. *Sep. Purif. Technol.* (1998), 13, 195-208.
(76) Unger, J.; Kolios, G.; Eigenberger, G. On the efficient simulation and analysis of regenerative processes in cyclic operation. *Comput. Chem. Eng.* (1997), 21, 167-72.

5. Conclusions and suggestions for future work

5.1. Conclusions of PhD work

In this work, production of hydrogen by the steam methane reforming sorption enhanced reaction process (SMR-SERP) was studied. Previously, SMR-SERP simulations were carried out at the LSRE by Xiu *et al* [1-5] using the steam methane reforming kinetics reported by Xu and Froment [6] and the carbon dioxide (CO_2) sorption equilibria and kinetics determined by Ding and Alpay [7] in a potassium impregnated hydrotalcite. Different operating conditions were proposed by Xiu *et al* [1-5] to achieve high hydrogen purities and low CO concentrations in the effluent stream. The objective of this work was to obtain experimental data on SMR-SERP employing steam reforming catalysts and high temperature carbon dioxide sorbents.

The first steps of this study were related to obtain high temperature carbon dioxide equilibrium data on hydrotalcite extrudates in the presence of large amounts of steam. For this purpose, an equipment was built at the LSRE that was able to measure sorption equilibrium at high temperatures (T > 573 K) in the presence of steam. The same unit with slight modifications was also employed in measuring steam methane reforming and sorption enhanced reaction. Hydrotalcites were selected as sorbent material since several reports showed that it has good CO_2 sorption capacity at high temperatures and good stability in the presence of steam [8-10].

Three hydrotalcite samples, with different magnesium/aluminum ratios, were offered by Sasol (Germany) – MG30, MG50 and MG70 – for this work. Carbon dioxide sorption equilibrium was measured at 673 K in the pure extrudates and it was found that the sorption capacity was too low (~0.1 mol/kg). In order to increase the sorption capacity of the materials, the three pure hydrotalcite samples were impregnated with potassium and with cesium.

After impregnation, CO_2 sorption equilibrium was measured at 673 K, P_{CO2} = 0.40 bar and y_{H2O} = 0.265 (balanced with helium) to determine the best candidate for SMR-SERP. The potassium modified samples showed the highest CO_2 equilibrium sorption capacity. All the impregnated samples showed a CO_2 sorption capacity higher than 0.3 mol/kg. The potassium and the cesium modified samples with the highest CO_2 sorption capacities – MG30-K and MG30-Cs – were selected for the measurement of CO_2 sorption equilibrium isotherms at different temperatures.

The sorption equilibrium isotherms of both materials showed a maximum in the CO_2 equilibrium sorption capacity at 673 K [11]. This

maximum was described with a Bi-Langmuir model combining two different sorption mechanisms: endothermic physical sorption and exothermic chemical reaction.

The cyclic stability of the MG30-K sample was investigated in an experiment where 75 carbon dioxide sorption/desorption cycles in the presence of steam were performed. Comparing the capacity between the first cycle and the last one, there was a slight decrease in the sorption capacity (7 %).

A mathematical model was developed to simulate the carbon dioxide sorption/desorption breakthrough experiments and determine CO_2 the sorption kinetics on the hydrotalcite materials. At 783 K, the LDF constant determined for the cesium impregnated sample (MG30-Cs) was twice the value of the potassium modified sample. Since the MG30-K hydrotalcite showed a much higher CO_2 sorption capacity, it was selected for SMR-SERP.

The second part of this PhD work was dedicated to the steam methane reforming reaction. Two Ni/Al_2O_3 catalysts were selected for the experimental work: a commercial extrudate from Degussa (Germany) and a large-particle material containing large pores in its structure that was termed "Catalyst A".

Experiments were performed using catalyst powder (R_{cat} < 150 μm) to determine the true kinetic parameters of the catalyst. Afterwards, experiments using catalyst extrudates were performed to determine the diffusional limitations of the particles. The reaction rate equations proposed by Xu and Froment [6] were employed to describe the true reaction kinetics. One important characteristic of a catalyst for SMR-SERP is a high CO_2 selectivity (F_{CO2}/F_{CO}) since CO_2 is removed to enhance the SMR reaction. In the powder experiments, the CO_2

selectivity of the Degussa catalyst was always above 6 [12]. In Catalyst A experiments, the CO_2 selectivity was always higher than 10 [13].

A non-adiabatic, non-isothermal fixed bed model was developed to describe the experiments with the extrudates. The model was able to describe the effluent concentrations measured in the SMR experiments with Degussa [12] and Catalyst A extrudates under different operating conditions. To account for the large-pore network in Catalyst A, the mass and energy balances to the catalyst extrudates were based on the model reported by Nan *et al* [14]; a convection term was included in the balances within the extrudates particle. The enhanced mass transfer due to the large-pore network was demonstrated by steam methane reforming simulations with and without the intraparticle convection term. A higher methane conversion was obtained with the intraparticle convection [13]. An important result from the simulations was that the reaction rates are higher near the feed end, causing a large temperature drop in this zone of the reactor.

The mathematical model was employed to calculate the reaction effectiveness factors of each catalyst. In the experiments with Degussa extrudates, the SMR effectiveness factor was 0.4 at 747 K. The large-pore network of Catalyst A resulted in an SMR effectiveness factor of 0.52 at the same temperature. The reaction effectiveness factor is a measure of the mass transfer limitations within the catalyst extrudates. Thus, higher effectiveness factors mean that a lower amount of catalyst is required to reach the same conversion. In the case of the WGS reaction, an asymptote was observed in the reaction effectiveness factor near the feed end. In this section of the reactor the temperature decreases due to the SMR reaction and this causes a change in direction of the

reaction rate of the WGS reaction to comply with thermodynamic equilibrium.

In recent years, SMR-SERP has been widely researched [1-5, 9, 15-29]. In this thesis, the major novelty was related to the the application of large-pore catalyst extrudates for SMR-SERP and to the evaluation of a previously proposed cycle [1] using experimental data collected at LSRE.

With the objective of understanding the influence of operating conditions – temperature, pressure and feed flowrate – in the performance of SMR-SERP, experiments were performed with catalyst (Catalyst A and Degussa) and sorbent (MG30-K hydrotalcite) extrudates. A layered distribution catalyst and sorbent was employed in the experimental runs [30, 31]. This configuration allows a direct comparison of catalysts with completely different structural properties like particle size and density. With the layered distribution, each catalyst layer comes in contact with a CO_2-free stream, enhancing the SMR and WGS reactions. Also, the last sorbent layer acts as a guard bed that delays the CO_2 breakthrough.

In all the experiments the methane conversion and hydrogen purities were higher than equilibrium values prior to CO_2 breakthrough. When the sorbent was saturated with CO_2, the SMR-SERP reactor worked as a classical SMR reactor. After the reaction step, sorbent regeneration was performed decreasing the pressure to 1.01 bar and purging the reactor with a mixture of steam and hydrogen. It was confirmed that hydrogen promotes the reverse WGS and SMR reactions, increasing the CO_2 desorption rate: reactive regeneration [1].

The cyclic performance of the SMR-SERP was determined by performing several reaction/regeneration cycles. The reaction step was

performed at 4.0 bar, 778 K and S/C ratio of 4.0. During the regeneration step, the reactor was purged with 10 % H_2 in steam at atmospheric pressure. Cyclic steady state was reached within 4 cycles. When Catalyst A and MG30-K hydrotalcite were employed, a hydrogen purity of 71.4 % with low CO content was obtained at 778 K and 4.0 bar. This value is 20 % higher than thermodynamic equilibrium (59.6 %). In the cyclic experiments with Degussa catalyst and MG30-K sorbent, a hydrogen purity of 75 % was obtained with methane as the main impurity (24 %).

When Degussa catalyst and MG30-K sorbent were employed for SMR-SERP, higher methane conversions and hydrogen purities were obtained than in the experiments with Catalyst A. The difference in performance is due to the higher Ni content of the Degussa catalyst (15 %), since it is in these sites that the reactions take place. The sorbent regeneration was performed at atmospheric pressure by purging the reactor with a stream of hydrogen and steam. The use of hydrogen increased the desorption rate due to the reactive regeneration effect [1]. However, the CO_2 desorption rate of the MG30-K hydrotalcite was slower than the values reported by Ding and Alpay [7]. This is important since a difficult sorbent regeneration decreases the performance of a cyclic sorption process.

The aim of the SMR-SERP experimental work was to determine predictive capabilities of the mathematical model at different operating conditions: temperature, pressure and flowrate. The non-adiabatic, non-isothermal fixed bed mathematical model was able to describe the effluent concentrations and temperatures without any fitting parameters. It was found that each operating conditions has opposite effects in the performance of the sorbent and catalyst

extrudates. For example: increasing the temperature increases the SMR reaction rates but decreases the CO_2 sorption capacity; increasing the pressure increases the sorption capacity of the hydrotalcite but decreases the SMR reaction rate in the catalyst. Therefore, there is an optimum set of operating conditions to reach maximum hydrogen purity in SMR-SERP.

The SMR-SERP mathematical model was employed to simulate the reactive regeneration cycle proposed by Xiu *et al* [1] with the Degussa catalyst and MG30-K sorbent. A first set of simulations was made in the conditions reported by Xiu *et al.* [1] for direct comparison of the results. Due to the slower sorption kinetics of the MG30-K hydrotalcite, the hydrogen purities were lower than the previously reported values [1]. Also, in the simulation of a 6 m SMR-SERP reactor, the CO content was more than double of the 30 ppm restriction for PEM fuel cells. To meet this target, the reactive regeneration temperature was increased to 740 K to increase the desorption kinetics. Simulation results of the reactive regeneration cycle indicate that, at 4.46 bar and 680 K, a stream with 28 ppm of CO can be produced with a hydrogen purity of 77 %.

Finally, a reactor with R_c = 25 mm was simulated in order to compare the performance of Catalyst A and Degussa catalyst for the reactive regeneration cycle. The operating conditions were optimized to produce a stream with less than 30 ppm of CO. Higher hydrogen purities and lower CO contents were obtained when Degussa catalyst was employed. Simulation results show that, in the SMR-SERP with the Degussa catalyst there is a larger temperature drop near the feed end of the reactor than with Catalyst A. The lower temperature promotes the WGS reaction and the sorption enhancement effect, since the hydrotalcite has a maximum in the CO_2 sorption capacity at 676 K.

This work showed that the SMR-SERP, employing Ni/Al_2O_3 catalyst and K-promoted hydrotalcite sorbent, is able to produce hydrogen with purities higher than 80 % and ppm level of CO and CO_2 at much lower temperatures than the traditional SMR. The use of lower temperature represents substantial reduction in energy and material costs while low carbon oxides content means a reduction in the separation costs. The main impurity is methane should be recycled to reduce production costs. Thus, the SMR-SERP is a viable alternative to the steam methane reforming process.

5.2. Suggestions for future work

The experiments and simulations reported in this work indicate that the performance of the SMR-SERP is limited by the sorption kinetics of the CO_2 sorbent. Experimental results showed that, CO_2 sorption capacity of the pure hydrotalcite is very low and that it was necessary to modify the material with alkali metals (K or Cs) to improve the sorption capacity. Impregnation with potassium resulted in higher sorption capacity but the cesium modified hydrotalcite showed higher sorption kinetics. It would be interesting to determine if a material with intermediate properties can be produced by impregnation with rubidium since this alkali metal is between potassium and cesium in the periodic table and can therefore result in a material with intermediate properties.

Different authors have proposed different CO_2 sorption mechanisms [7, 11, 32-34] based on their experimental results. There is no consensus on how the CO_2 is sorbed in the hydrotalcite material and what is the role of the alkali-metal. Therefore, a detailed study of the

CO_2 sorption mechanism may allow to proceed with modification of the impregnation protocol in order to obtain materials with faster sorption kinetics.

The SMR-SERP is a promising technology for hydrogen production. However, there are other possible applications of the SERP concept for hydrogen production. In recent years, some publications have focused on the water gas shift sorption enhanced process (WGS-SERP) [35, 36]. Lee *et al* [35] employed a simulated stream composed of CO and H_2O and van Selow *et al* [36] studied the WGS-SERP reactor placed after the high temperature shift reactor. Therefore, there is an opportunity to study a WGS-SERP placed after the SMR reactor. In this case, since the reaction can be carried out at lower temperatures than the SMR, different sorbent materials can be employed.

Another possible application of SERP is the steam reforming of ethanol. Ethanol can be produced from renewable sources, reducing the carbon footprint of the process. Comas *et al* [37] proposed the use of CaO as sorbent for this application. Other sorbents and operating conditions can be studied for this application.

5.3. References

1. Xiu, G.-h.; Li, P.; Rodrigues, A. E. Sorption-enhanced reaction process with reactive regeneration. *Chem. Eng. Sci.* (2002), 57.
2. Xiu, G.-h.; Li, P.; Rodrigues, A. E. Adsorption-enhanced steam-methane reforming with intraparticle-diffusion limitations. *Chem. Eng. J.* (2003).
3. Xiu, G.-h.; Li, P.; Rodrigues, A. E. New generalized strategy for improving sorption-enhanced reaction process. *Chem. Eng. Sci.* (2003), 58, 3425-3437.
4. Xiu, G.-h.; Li, P.; Rodrigues, A. E. Subsection-controlling strategy for improving sorption-enhanced reaction process. *Chem. Eng. Res. Des.* (2004), 82, 192-202.
5. Xiu, G.-h.; Soares, J. L.; Li, P.; Rodrigues, A. E. Simulation of five-step one-bed sorption-enhanced reaction process. *AIChE J.* (2002), 48, 2817.
6. Xu, J.; Froment, G. F. Methane steam reforming, methanation and water-gas shift: I. Intrinsic kinetics. *AIChE J.* (1989), 35, 88.
7. Ding, Y.; Alpay, E. Equilibria and kinetics of CO_2 adsorption on hydrotalcite adsorbent. *Chem. Eng. Sci.* (2000), 55, 3461-3474.
8. Mayorga, S. G.; Gaffney, T. R.; Brzozowski, J. R.; Weigel, S. J. Carbon dioxide adsorbents containing magnesium oxide suitable for use at high temperatures. European Patent 1074297, 2001.
9. Mayorga, S. G.; Hufton, J. R.; Sircar, S.; Gaffney, T. R. Sorption Enhanced Reaction Process for the production of hydrogen. Phase I Final Report, Proceedings of U.S. DOE Hydrogen program Review, Washington DC, 1997.

10. Yong, Z.; Mata, V.; Rodrigues, A. E. Adsorption of carbon dioxide at high temperature - a review. *Sep. Purif. Technol.* (2002), 26, 195-205.
11. Oliveira, E. L. G.; Grande, C. A.; Rodrigues, A. E. CO_2 sorption on hydrotalcite and alkali-modified (K and Cs) hydrotalcites at high temperatures. *Sep. Purif. Technol.* (2008), 62, 137-147.
12. Oliveira, E. L. G.; Grande, C. A.; Rodrigues, A. E. Steam Methane Reforming in a Ni/Al_2O_3 catalyst: kinetics and diffusional limitations in extrudates. *Can. J. Chem. Eng.* (2009), in press.
13. Oliveira, E. L. G.; Grande, C. A.; Rodrigues, A. E. Methane steam reforming in large pore catalyst. *Chem. Eng. Sci.* (2009), submitted for publication.
14. Nan, H. S.; Dias, M. M.; Rodrigues, A. E. Effect of forced convection on reaction with mole changes in porous catalysts. *Chem. Eng. J. Biochem. Eng. J.* (1995), 57, 101-114.
15. Balasubramanian, B.; Lopez Ortiz, A.; Kaytakoglu, S.; Harrison, D. P. Hydrogen from methane in a single-step process. *Chem. Eng. Sci.* (1999), 54, 3543-3552.
16. Cobden, P. D.; van Beurden, P.; Reijers, H. T. J.; Elzinga, G. D.; Kluiters, S. C. A.; Dijkstra, J. W.; Jansen, D.; van den Brink, R. W. Sorption-enhanced hydrogen production for pre-combustion CO_2 capture: Thermodynamic analysis and experimental results. *Int. J. Greenhouse Gas Control* (2007), 1, 170-179.
17. Ding, Y.; Alpay, E. Adsorption-enhanced steam-methane reforming. *Chem. Eng. Sci.* (2000), 55, 3929-3940.
18. Hildenbrand, N.; Readman, J.; Dahl, I. M.; Blom, R. Sorbent enhanced steam reforming (SESR) of methane using dolomite as internal carbon dioxide absorbent: Limitations due to $Ca(OH)_2$ formation. *Appl. Catal., A* (2006), 303, 131-137.

19. Hufton, J. R.; Mayorga, S.; Sircar, S. Sorption-enhanced reaction process for hydrogen production. *AIChE J.* (1999), 45, 248-256.
20. Koumpouras, G. C.; Alpay, E.; Lapkin, A.; Ding, Y.; Stepanek, F. The effect of adsorbent characteristics on the performance of a continuous sorption-enhanced steam methane reforming process. *Chem. Eng. Sci.* (2007), 62, 5632-7.
21. Kwang, B. Y.; Harrison, D. P. Low-pressure sorption-enhanced hydrogen production. *Ind. Eng. Chem. Res.* (2005), 44, 1665-1669.
22. Lee, D. K.; Baek, I. H.; Yoon, W. L. A simulation study for the hybrid reaction of methane steam reforming and in situ CO_2 removal in a moving bed reactor of a catalyst admixed with a CaO-based CO_2 acceptor for H_2 production. *Int. J. Hydrogen Energy* (2006), 31, 649-657.
23. Lee, K. B.; Beaver, M. G.; Caram, H. S.; Sircar, S. Novel thermal-swing sorption-enhanced reaction process concept for hydrogen production by low-temperature steam-methane reforming. *Ind. Eng. Chem. Res.* (2007), 46, 5003-5014.
24. Ochoa-Fernandez, E.; Haugen, G.; Zhao, T.; Ronning, M.; Aartun, I.; Børresen, B.; Rytter, E.; Rønnekleiv, M.; Chen, D. Process design simulation of H_2 production by sorption enhanced steam methane reforming: evaluation of potential CO_2 acceptors. *Green Chem.* (2007), 9, 654 - 662.
25. Ochoa-Fernandez, E.; Rusten, H. K.; Jakobsen, H. A.; Ronning, M.; Holmen, A.; Chen, D. Sorption enhanced hydrogen production by steam methane reforming using Li_2ZrO_3 as sorbent: Sorption kinetics and reactor simulation. In International Conference on Gas-Fuel 05, Brugge, November, *Catalysis Today* (2005), 41-46.
26. Peng, Z.; Harrison, D. P. Low-Carbon Monoxide Hydrogen by Sorption-Enhanced Reaction. *Int. J. Chem. Reactor Eng.* (2003), 1, A37.

27. Reijers, H. T. J.; Valster-Schiermeier, S. E. A.; Cobden, P. D.; van den Brink, R. W. Hydrotalcite as CO_2 Sorbent for Sorption-Enhanced Steam Reforming of Methane. *Ind. Eng. Chem. Res.* (2006), 45, 2522-2530.
28. Rusten, H. K.; Ochoa-Fernandez, E.; Chen, D.; Jakobsen, H. A. Numerical investigation of sorption enhanced steam methane reforming using Li_2ZrO_3 as CO_2-acceptor. *Ind. Eng. Chem. Res.* (2007), 46, 4435-4443.
29. Waldron, W. E.; Hufton, J. R.; Sircar, S. Production of hydrogen by cyclic sorption enhanced reaction process. *AIChE J.* (2001), 47, 1477-1479.
30. Lu, Z. P.; Loureiro, J. M.; Rodrigues, A. E. Simulation of Pressure Swing Adsorption Reactors. In CHEMPOR'93, International Chemical Engineering Conference, Porto, April 4-6, (1993), 75-82.
31. Rawadieh, S.; Gomes, V. G. Catalyst-adsorbent configurations in enhancing adsorptive reactor performance. *Int. J. Chem. Reactor Eng.* (2007), 5, 18 pp.
32. Ebner, A. D.; Reynolds, S. P.; Ritter, J. A. Understanding the Adsorption and Desorption Behavior of CO_2 on a K-Promoted Hydrotalcite-like Compound (HTlc) through Nonequilibrium Dynamic Isotherms. *Ind. Eng. Chem. Res.* (2006), 45, 6387-6392.
33. Ebner, A. D.; Reynolds, S. P.; Ritter, J. A. Nonequilibrium kinetic model that describes the reversible adsorption and desorption behavior of CO_2 in a K-promoted hydrotalcite-like compound. *Ind. Eng. Chem. Res.* (2007), 46, 1737-1744.
34. Lee, K. B.; Verdooren, A.; Caram, H. S.; Sircar, S. Chemisorption of carbon dioxide on potassium-carbonate-promoted hydrotalcite. *J. Colloid Interface Sci.* (2007), 308, 30-39.

35. Lee, K. B.; Beaver, M. G.; Caram, H. S.; Sircar, S. Reversible chemisorption of carbon dioxide: Simultaneous production of fuel-cell grade H_2 and compressed CO_2 from synthesis gas. ***Adsorption*** (2007), 13, 385-397.
36. van Selow, E. R.; Cobden, P. D.; van den Brink, R. W.; Hufton, J. R.; Wright, A. Performance of sorption-enhanced water-gas shift as a pre-combustion CO_2 capture technology. ***Energy Procedia*** (2009), 1, 689-696.
37. Comas, J.; Laborde, M.; Amadeo, N. Thermodynamic analysis of hydrogen production from ethanol using CaO as a CO_2 sorbent. ***J. of Power Sources*** (2004), 138, 61-67.

Notation

$a_{p,cat}$ – Area to volume ratio of the catalyst extrudate in m^{-1};

$a_{p,sorb}$ – Area to volume ratio of the sorbent extrudate in m^{-1};

A_{col} – Cross sectional area of the reactor column in m^2;

B_i – Biot adimensional number;

$B_{p,cat}$ – Catalyst particle permeability in m^2;

C_i – Concentration of component "*i*" in the gas phase in mol/m^3;

$C_{CO2,\ feed}$ – Feed carbon dioxide concentration in the sorption experiments in mol/m^3;

$C_{cat,i}$ – Concentration of component "*i*" in the gas phase inside the catalyst in mol/m^3;

$\hat{C}_{ps,cat}$ – Calorific capacity of the catalyst extrudate in J/(kgcat.K);

$\hat{C}_{ps,sorb}$ – Calorific capacity of the sorbent extrudate in J/(kgcat.K);

$\hat{C}_{pw}$ – Calorific capacity of the column wall in J/(kgcat.K);

$\overline{C}_{sorb,i}$ – Average concentration of component "*i*" in the pore network of the sorbent extrudate in mol/m^3;

C_T – Total concentration in the gas phase in mol/m^3;

$\overline{C}_{T,cat}$ – Average total concentration in the gas phase inside the catalyst extrudate in mol/m^3;

$\overline{C}_{T,sorb}$ – Average total concentration in the gas phase inside the sorbent extrudate in mol/m^3;

$\hat{C}_{pg}$ – Calorific capacity of the gas phase at constant pressure in J/(mol.K);

$\hat{C}_{vg}$ – Calorific capacity of the gas phase at constant volume in J/(mol.K);

D_{ax} – Axial dispersion in the column in m^2/s;

D_{ij} – Binary diffusivity of the catalyst extrudate in m^2/s;

$D_{k,cat}$ – Knudsen diffusivity of the catalyst extrudate in m^2/s;

D_m – Molecular diffusivity in m^2/s;

$d_{microsphere,cat}$ – Average diameter of the microspheres of the catalyst extrudate in m;

$D_{p,cat}$ – Pore diffusivity in the catalyst particle in m^2/s;

$D_{p,sorb}$ – Pore diffusivity in the sorbent particle in m^2/s;

E_j – Energy of activation of reaction "*j*" in the catalyst in J/mol: SMR (j=1), WGS (j=2) and global SMR (j=3);

E_{sorb} – Heat of chemical reaction of CO_2 in the sorbent extrudate in J;

F_i – Effluent molar flowrate of component "*i*" in mmol/min;

$F_{i,feed}$ – Feed molar flowrate of component "*i*" in mmol/min;

F_{feed} – Feed total molar flowrate in mmol/min;

Gain – Amount of hydrogen produced per mol of methane fed during the feed step in mol_{H2}/mol_{CH4};

$h_{f,cat}$ – Film heat transfer coefficient of the catalyst extrudate in $W/(m^2_{cat}.K)$;

$h_{f,sorb}$ – Film heat transfer coefficient of the sorbent extrudate in $W/(m^2_{cat}.K)$;

h_w – Wall internal heat transfer coefficient in $W/(m^2_{col}.K)$;

h_{ext} – External heat transfer coefficient in $W/(m^2_{col}.K)$;

k_{0j} – Arrhenius pre-exponential factor of the reaction rate constant of reaction "*j*" in the catalyst extrudate: SMR (j=1), WGS (j=2) and global SMR (j=3);

$k_{0eq,CO2}$ – Arrhenius pre-exponential factor of the CO_2 sorption constants ($K_{eq,CO2}$) of site 1 or site 2 inside the sorbent extrudate in bar^{-1};

$K_{eq,CO2}$ – CO_2 sorption constant in site 1 or site 2 inside the sorbent extrudate in bar^{-1} (Bi-Langmuir);

K_i – Adsorption constant of component "*i*" in the solid phase of the catalyst extrudate in bar^{-1};

k_{0i} – Pre-exponential factor of the adsorption constant of component "*i*" in bar^{-1};

$k_{CO2,sorb}$ – Carbon dioxide sorption rate in the sorbent extrudates in s^{-1};

$k_{f,cat}$ – Film mass transfer coefficient of the catalyst extrudate in m/s;

$k_{f,sorb}$ – Film mass transfer coefficient of the sorbent extrudate in m/s;

k_g – Thermal conductivity of the gas mixture in W/(m.K);

k_{gi} – Thermal conductivity of the component "i" in the gas mixture in W/(m.K);

$K_{Global\ SMR}$ – Equilibrium constant for the Global SMR reaction in bar^2;

$k_{Global\ SMR}$ – Reaction rate constant for the Global SMR reaction in $mol.bar^{0.5}/(kg_{cat}.s)$;

K_{SMR} – Equilibrium constant for the SMR reaction in bar^2;

k_{SMR} – Reaction rate constant for the SMR reaction in $mol.bar^{0.5}/(kg_{cat}.s)$;

K_{WGS} – Equilibrium constant for the WGS reaction;

k_{WGS} – Reaction rate constant for the WGS reaction in $mol/(kg_{cat}.bar.s)$;

L_c – Column length in m;

L_{layer} – Layer length in m;

$L_{p,cat}$ – Length of the catalyst particle in m;

m_{cat} – Mass of catalyst kg;

M_i – Molecular weight of component "i" in g/mol;

m_{sorb} – Mass of sorbent kg;

P_i – Partial pressure of component "*i*" in bar;

$p_{i,sorb}$ – Partial pressure of component "*i*" inside the sorbent extrudate in bar;

P_{out} – Pressure at the outlet end of the column in bar;

Productivity – Amount of hydrogen produced per column volume and time in $mol_{H2}/(m^3.h)$;

$p_{T,cat}$ – Total pressure inside the catalyst extrudate in bar;

P_T – Total pressure inside the column in bar;

Purity – Average purity of the hydrogen produced during the feed step;

$\overline{q_i}$ – Average adsorbed concentration of component "*i*" in the sorbent in mol/kg;

$q_{eq,i}$ – Equilibrium sorption capacity of component "*i*" in the sorbent in mol/kg;

q_{max} – Maximum CO_2 sorption capacity for sites 1 (exothermic physical adsorption) and 2 (endothermic chemical reaction) in mol/kg;

Q – Volumetric effluent flowrate m^3/s;

Q_{total} – Volumetric flowrate in m^3/s;

R_c – Column radius in m;

R_{cat} – Radius of the catalyst extrudate in m;

r_{cat} – Radial position in the catalyst particle in m;

R_j – Reaction rate for SMR (j=1), WGS (j=2) and global SMR (j=3) reactions in mol/(kg_{cat}.s);

$\overline{R_j}$ – Average reaction rate in the radial direction for SMR (j=1), WGS (j=2) and global SMR (j=3) reactions in mol/(kg_{cat}.s);

$\overline{R_p}$ – Average extrudate radius in a mixture of extrudates of different radii in m;

$r_{pore,cat}$ – Average pore radius of the catalyst extrudate in nm;

$r_{pore,sorb}$ – Average pore radius of the sorbent extrudate in nm;

R_g – Ideal gas constant in J/(mol.K);

R_{sorb} – Radius of the sorbent extrudate in m;

S/C – Steam to carbon ratio;

S_{CO2} – Carbon dioxide selectivity;

% SERP – SERP enhancement factor;

T – Column fluid phase temperature in K;

t – Time in s;

T_{cat} – Catalyst particle temperature in K;

t_{cycle} – Duration of a reaction/regeneration cycle in s;

T_{feed} – Feed temperature in K;

$t_{reaction}$ – Duration of the reaction step in s;

$t_{regeneration}$ – Total duration of the regeneration step (depressurization + purge + pressurization) in s;

T_{sorb} – Sorbent particle temperature in K;

$\overline{t_{st}}$ – Stoichiometric time in s;

T_w – Wall temperature in K;

T_∞ or T_{oven} – Temperature of the surroundings (oven) in K;

u – Superficial gas velocity in m/s;

u_{feed} – Feed gas velocity in m/s;

u_i - Interstitial gas velocity in m/s

U – Global heat transfer coefficient in W/(m^2_{col}.K);

V_{cat} – Volume of catalyst extrudates inside the column in m^3;

v_{cat} – Catalyst intraparticle gas velocity in m/s;

V_{solid} – Total volume of solids inside the column in m^3;

$V_{sorbent}$ – Volume of sorbent extrudates inside the column in m^3;

w_{thick} – Thickness of the reactor wall in m;

x_{cat} – Catalyst weight fraction in a mixture of solids;

X_{CH4} – Methane conversion in %;

x_{sorb} – Sorbent weight fraction in a mixture of solids;

y_i – Molar fraction of component "i" in the fluid phase;

$y_{i,feed}$ – Feed molar fraction of component "i";

Y_{H2} – Hydrogen yield in g^{-1};

z – Axial coordinate of the column in m;

z_{cat} – Axial coordinate of the catalyst extrudate in m;

Greek letters

α – Catalyst/(total solids) ratio inside the reactor;

β - Ratio of physical to chemical sorption of CO_2 in the hydrotalcite sorbent;

ΔH_i – Heat of adsorption of component "*i*" in the catalyst in J/mol;

ΔH_j – Heat of reaction "*j*" in J/mol: SMR (j=1), WGS (j=2) and global SMR (j=3);

ΔH_{sorb} – Heat of physical adsorption of CO_2 in the sorbent extrudate in J;

ε_c – Column porosity;

ε_i – Lennard-Jones characteristic energy;

$\varepsilon_{p,cat}$ – Catalyst extrudate porosity;

$\varepsilon_{p,sorb}$ – Porosity of the sorbent extrudate;

λ_{ax} – Fluid phase thermal conductivity in W/m.K;

λ_{cat} – Thermal conductivity of the catalyst in W/m.K;

λ_w – Thermal conductivity of the r in W/m.K;

η_j – Effectiveness factor of reaction "*j*";

σ_i – Lennard-Jones characteristic length in Å;

ρ_{cat} – Density of the catalyst extrudate in kg/m^3;

ρ_{gas} – Density of the gas phase in kg/m^3;

$\rho_{solid,cat}$ – Solid density of the catalyst extrudate in kg/m^3;

$\rho_{solid,sorb}$ – Solid density of the sorbent extrudate in kg/m^3;

ρ_{sorb} – Density of the sorbent extrudate in kg/m^3;

ρ_w – Density of the column wall in kg/m^3;

τ_p – Tortuosity of the pore network of the catalyst extrudate;

$\upsilon_{j,i}$ – Stoichiometric coefficient of component "*i*" in reaction "*j*";

μ_{gas} – Gas viscosity in Pa.s;

Appendix A – Calculation of transport parameters

In Chapters 2, 3 and 4, several different mathematical models were developed. In order to solve each one, various transport parameters are required. This Appendix reports the correlations used to calculate the different transport parameters.

To estimate the axial dispersion parameters inside the column (D_{ax}, λ_{ax}) the correlations proposed by Wakao and Funazkri [1-3] were used. These correlations are valid in the range $3 < Re < 10000$.

$$\frac{\varepsilon_c D_{ax,i}}{D_{m,i}} = 20 + 0.5 Sc_i Re \qquad (A.1)$$

$$\frac{\lambda_{ax}}{k_g} = 7 + 0.5 PrRe \qquad (A.2)$$

where $D_{m,i}$ is the molecular diffusivity of component "i" in the gas mixture in m^2/s. The dimensionless groups Schmidt (Sc_i), Reynolds (Re) and Prandtl (Pr) were calculated as follows:

$$Sc_i = \frac{\mu_{gas}}{\rho_{gas} D_{m,i}} \tag{A.3}$$

$$Re = \frac{2\rho_{gas} \upsilon R_{cat}}{\mu_{gas}} \tag{A.4}$$

$$Pr = \frac{\mu_{gas} \hat{C}_{pg}}{k_g} \tag{A.5}$$

The molecular diffusivity of the gas mixture relating to component "i" was calculated as shown in equations A.6-A.10 [4]

$$D_{m,i} = \frac{1 - y_i}{\sum_{\substack{j=1 \\ j \neq i}}^{n} \frac{y_j}{D_{ij}}} \tag{A.6}$$

The binary diffusivity was calculated using the Chapman-Enskog equation [5].

$$D_{ij} = \frac{1.8809 \times 10^{-7} \sqrt{T^3 \left(\frac{1}{M_i} + \frac{1}{M_j} \right)}}{P_T \sigma_{ij}^2 \Omega_{ij}} \tag{A.7}$$

$$\Omega_{ij} = 1.06036 \left(\frac{\varepsilon_{ij}}{kT} \right)^{0.15610} + 0.19300 \, e^{-0.47635 \frac{kT}{\varepsilon_{ij}}} + 1.03587 e^{-1.52996 \frac{kT}{\varepsilon_{ij}}} + 1.76474 e^{-3.89411 \frac{kT}{\varepsilon_{ij}}} \tag{A.8}$$

$$\sigma_{ij} = \frac{\sigma_i + \sigma_j}{2} \tag{A.9}$$

$$\varepsilon_{ij} = \sqrt{\varepsilon_i \varepsilon_j} \tag{A.10}$$

where σ_i and ε_i are the characteristic Lennard-Jones length and energy.

The thermal conductivity of the gas mixture was calculated using the empirical relation proposed by Wassiljewa [5].

$$k_g = \sum_{i=1}^{n} \frac{y_i k_{gi}}{\sum_{j=1}^{n} y_j A_{ij}} \tag{A.11}$$

where Aij is a parameter calculated using the correlation from Mason and Saxena [5].

$$A_{ij} = \left[8\left(1+\frac{M_i}{M_j}\right)\right]^{-0.5}\left[1+\left(\frac{k_i}{k_j}\right)^{0.5}\left(\frac{M_j}{M_i}\right)^{0.25}\right]^2 \tag{A.12}$$

The pure component thermal conductivity was calculated using the equation proposed by Eucken as shown below [5]:

$$k_i = \left(\hat{C}_{pg,i} + \frac{5}{4}\frac{R}{M_i \times 10^{-3}}\right)\mu_i \tag{A.13}$$

The viscosity of the gas mixture was calculated according to the following equations [5]:

$$\mu_i = 2.669\times 10^{-6}\frac{(M_i T)}{\sigma_i^2 \Omega_\mu} \tag{A.14}$$

$$\Omega_\mu = 1.16145\left(\frac{\varepsilon_i}{kT}\right)^{0.14874} + 0.52487\ e^{-0.7732\frac{kT}{\varepsilon_i}} + 2.16178e^{-2.43787\frac{kT}{\varepsilon_i}} \tag{A.15}$$

To obtain the viscosity of the gas mixture the method of Wilke [5] was used.

$$\mu_{gas} = \sum_{i=1}^{n} \frac{y_i \mu_i}{\sum_{j=1}^{n} y_j \Phi_{ij}} \tag{A.16}$$

$$\Phi_{ij} = \left[8\left(1+\frac{M_i}{M_j}\right)\right]^{-1/2}\left(1+\sqrt{\frac{\mu_i}{\mu_j}}\left(\frac{M_j}{M_i}\right)^{1/4}\right)^2 \tag{A.17}$$

Considering ideal gas, the density of the gas mixture was calculated according to the following equation:

$$\rho_{gas} = \frac{P_T}{R_{gas}T}\left(\sum_{i=1}^{n} y_i M_i\right) \times 100 \quad \text{(A.18)}$$

where y_i is the molar fraction of component "i".

The pore diffusivity was calculated using the Bosanquet equation [3, 6]:

$$\frac{1}{D_{p,i}} = \tau_p\left(\frac{1}{D_{m,i}} + \frac{1}{D_{k,i}}\right) \quad \text{(A.19)}$$

The Knudsen diffusivity was calculated by:

$$D_{k,i} = 9.7 \times 10^{-9} r_p \sqrt{\frac{T}{M_i}} \quad \text{(A.20)}$$

where r_p is the pore radius in Å. This equation is only valid when the mean free path is larger than the pore radius [2].

The molar heat capacity at constant pressure of component "i" was calculated using equation A.21 [5].

$$\frac{C_{p,i}}{R} = A_0 + A_1 T + A_2 T^2 + A_3 T^3 + A_4 T^4 \quad \text{(A.21)}$$

Then, the molar heat capacity of the gas mixture was calculated as:

$$C_{pg} = \sum_{i=1}^{n} y_i C_{p,i} \quad \text{(A.22)}$$

The molar heat capacities at constant pressure and at constant volume in ideal gas are related using the following equation:

$$R = C_p - C_v \quad \text{(A.23)}$$

The global heat transfer coefficient was calculated according to [3, 7]:

$$\frac{1}{U} = \frac{1}{h_w} + \frac{w_{thick} R_{col}}{\lambda_w R_{ln}} + \frac{R_{col}}{(R_{col} + w_{thick}) h_{ex}} \quad \text{(A.24)}$$

$$R_{ln} = \frac{w_{thick}}{\ln\left(\frac{R_{col} + w_{thick}}{R_{col}}\right)} \quad \text{(A.25)}$$

where h_{ex} is the external heat transfer coefficient in W/m^2.K.

A.1. References

1. Wakao, N.; Funazkri, T. Effect of Fluid Dispersion Coefficients on Particle-to-Fluid Mass Transfer Coefficients in Packed Beds. *Chem. Eng. Sci.* (1978), 33, 1375-1384.

2. Yang, R. T. Gas separation by adsorption processes. First ed, Imperial College Press, London, 1987.

3. da Silva, F. A. Cyclic Adsorption Processes: Application to Propane/Propylene Separation. PhD thesis, University of Porto, Porto, 2003.

4. Bird, R. B.; Stewart, W. E.; Lightfoot, E. N. Transport Phenomena. Second ed, John Wiley & Sons, Inc, New York, 2002.

5. Poling, B. E.; Prausnitz, J. M.; O'Connell, J. P. The properties of gases and liquids. Fifth ed, McGraw-Hill International Editions, Boston, 2001.

6. Satterfield, C. N. Mass Transfer in Heterogeneous Catalysis. PhD thesis, M.I.T., Michigan, 1971.

7. Incropera, F. P.; Witt, D. P. D. Fundamentals of Heat and Mass Transfer. Fourth ed, John Wiley and Sons, New York, 1996.

Appendix B – SMR-SERP preliminary experiments

B.1. Introduction

Two preliminary experiments were made as steam methane reforming sorption-enhanced reaction process (SMR-SERP) proof-of-concept. These experiments were performed using the catalyst from Degussa catalyst and the cesium promoted hydrotalcite sorbent (MG30-Cs) in two different packing configurations: random and layered. An experiment using just catalyst was also performed to check the improvement of SMR-SERP over traditional SMR.

B.2. Experimental

The equipment used for the SMR-SERP proof-of-concept experiments is shown in Figure B.1. This equipment has the same

configuration as the one used for the steam methane reforming (SMR) experiments in Chapter 3.

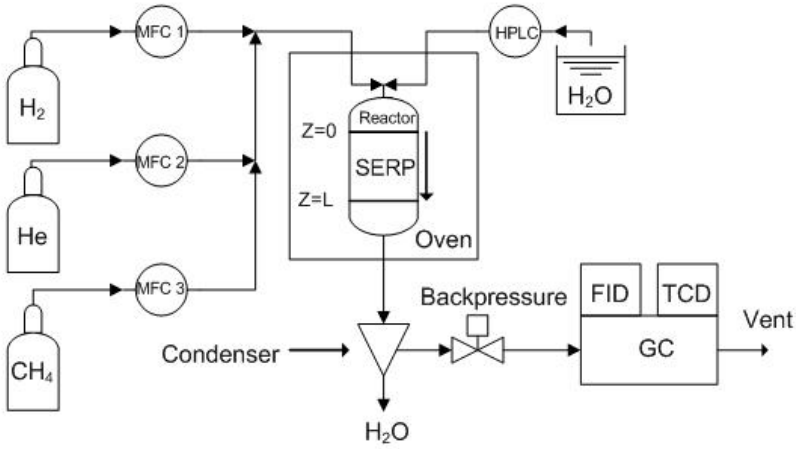

Figure B.1. Experimental set-up employed for the SMR-SERP proof-of-concept.

The Degussa catalyst and MG30-Cs sorbent were employed in the SMR-SERP proof-of-concept experiments. Two different catalyst/sorbent packing configurations were used: random mixing (Run 1) and layered (Run 2). In the random mixing, the catalyst and sorbent were physically mixed and then inserted into the reactor column. In the layered configuration a total of four alternating layers of catalyst and sorbent were used. A sorbent/catalyst ratio of 3 was used on both experiments. The same catalyst and sorbent samples were used for both runs.

The main purpose of these experiments was to test the SMR-SERP proof-of-concept. In order to provide a basis for comparison, SMR experiments were also performed using the same mass of catalyst (no sorbent). In the case of the SMR experiments the feed temperature was 823 K in order to observe the advantage of SERP over traditional SMR operated at higher temperature. The experimental conditions employed in the SMR-SERP experiments as well as the reactor solid composition of each experiment are reported in Table B.1.

Table B.1. Reactor column solid composition and operating conditions employed for the SMR experiment (catalyst only) and for the SMR-SERP proof-of-concept experiments with Degussa catalyst and MG30-Cs sorbent extrudates: layered and random mixing configurations.

Random mixing configuration (Run 1)				
m_{cat} **[kg] x 10^3**	18.195			
m_{sorb} **[kg] x 10^3**	53.901			
L_c **[m] x 10^3**	166			
ε_c	0.44			
Layered configuration (Run 2)				
Layer	**1**	**2**	**3**	**4**
m_{cat} **[kg] x 10^3**	9.146	0	9.060	0
m_{sorb} **[kg] x 10^3**	0	28.545	0	27.479
L_{layer} **[m] x 10^3**	24	64	23	55
ε_c	0.45	0.43	0.45	0.37
Catalyst only (Run 3)				
m_{cat} **[kg] x 10^3**	20.530			
L_c **[m] x 10^3**	50			
ε_c	0.42			
Operating Conditions				
	Reaction/sorption		**Regeneration**	
$y_{feed, CH4}$	0.21		0.00	
$y_{feed, H2O}$	0.79		0.75	
$y_{feed, He}$	0.00		0.25	
Q_{feed} **[SLPM]**[a]	1.38		1.45	
F_{feed} **[mmol/min]**	61.5		64.9	
S/C	3.7		0.0	
T_{oven} **[K]**	790[b]		790	
P_{out} **[bar]**	2.0		1.01	

a – Standard conditions are: 273 K and 1.01 bar.
b – In the case of catalyst only, T_{oven} = 823 K.

In order to measure the temperature inside the reactor column, thermocouples were placed at two different axial positions from feed inlet: 52 mm and 92 mm. In Run 3 the thermocouples could not be used due to the small length of the catalyst bed.

The reactor column was heated overnight in He flow at 1.1 K. Prior to each experiment, the catalyst was reduced during 1 h in a stream of pure H_2 (0.5 SLPM). After the reaction step of each run, the sorbent was regenerated using a stream of 25 % He in steam at 1.01 bar. In order to accommodate temperature variations in the reactor due to the exothermic nature of the sorption of steam in both the catalyst and the sorbent, the flow of steam was started prior to the methane flow.

B.3. Results and discussion

Three different experimental runs were performed to make a proof-of-concept of SMR-SERP. In the first one, the Degussa catalyst was randomly mixed with MG30-Cs hydrotalcite. The second run was performed employing a layered configuration with 2 layers of catalyst and two layers of sorbent. In the third run only catalyst was used in order to determine the advantage of SMR-SERP when compared to steam methane reforming. Figure B.2 shows the molar fraction and temperature histories during the reaction step in all the runs. The SMR thermodynamic equilibrium compositions using the same feed conditions were also calculated and are shown in Figure B.2(a and c) in order to provide a basis to evaluate the SMR-SERP.

Comparing the temperature peaks in Figure B.2(b and d), it is possible to see that the temperature profiles of the different solid configurations are quite different. In the case of the random configuration, the temperature decreases with time due to the endothermic SMR reactions. However, in the layered configuration a temperature peak can be observed. This temperature peak was

measured in the first sorbent layer and is due to the exothermic CO_2 sorption in the hydrotalcite material.

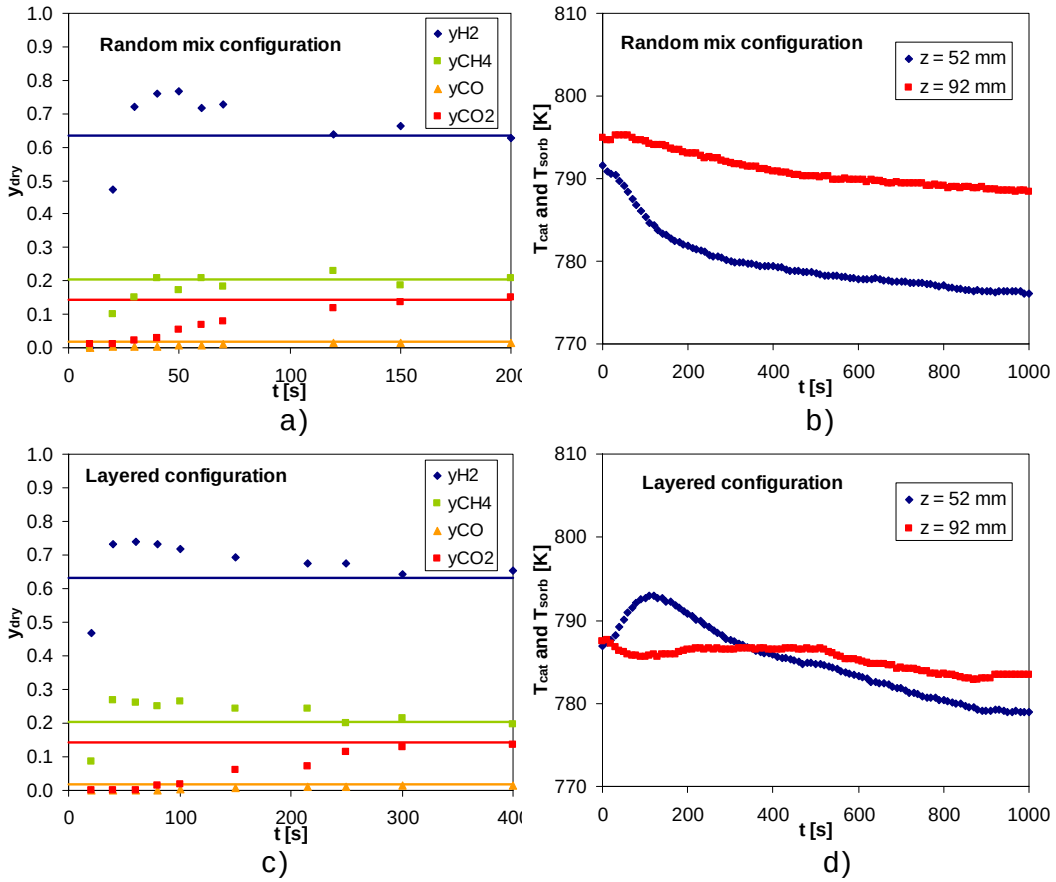

Figure B.2. Dry-basis molar fractions and temperature histories of the SMR-SERP experiments employing random mix (a-b) and layered (c-d) configurations of Degussa catalyst and MG30-Cs sorbent. Experimental conditions of the reaction step: 790 K, 2.0 bar, S/C = 3.7 and 61.5 mmol/min. Solid points are experimental results, lines are SMR thermodynamic equilibrium compositions for the same feed conditions.

When the random mixing of catalyst and sorbent were used, a H_2 dry-basis molar fraction of 0.77 was measured 50 s after the start of the reaction. This value is 21 % higher than the hydrogen composition in thermodynamic equilibrium (0.63). In the case of the layered configuration, the maximum hydrogen composition was 0.74. However,

with the layered configuration the CO_2 breakthrough took 70 s longer to detect and, as a result, the hydrogen molar fraction remained above equilibrium for a longer period of time. When the random mix configuration is used, the catalyst near the effluent end will produce CO_2 that will rapidly saturate the sorbent in its vicinity and thus the breakthrough of CO_2 is faster. Therefore the second sorbent layer acts as a guard bed that delays the CO_2 breakthrough.

Steam methane reforming experiments were also made at 823 K, employing a similar catalyst mass (Run 3 in Table B.1). One advantage of SERP concept is that it is possible to reach methane conversions and hydrogen purities higher than thermodynamic equilibrium due to the presence of the sorbent [1-3]. Thus, objective of Run 3 was to compare the traditional SMR with the SMR-SERP concept operating at lower temperatures. The effluent dry basis molar fractions are reported in Figure B.3.

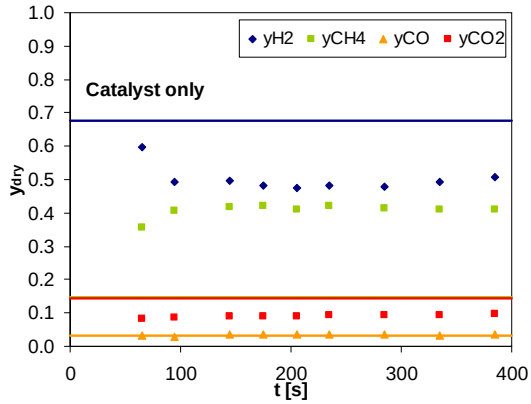

Figure B.3. Dry-basis molar fractions of the SMR experiments employing Degussa catalyst. Experimental conditions: 823 K, 2.0 bar, S/C = 3.7 and 61.5 mmol/min. Solid points are experimental results, lines are SMR thermodynamic equilibrium compositions for the same feed conditions.

Due to the mass and heat transfer resistances in the catalyst extrudates, the hydrogen content in the effluent was about 25 % lower than thermodynamic equilibrium. When comparing the SMR at 823 K (Figure B.3) with SMR-SERP operating at 790 K (Figure B.2), the SMR-SERP produced an effluent stream with 50 % more hydrogen and no carbon oxides.

The methane conversion was calculated for each run in order to provide a better assessment of the advantage of SMR-SERP over traditional SMR. In Figure B.4 it can be observed that the methane conversion was higher when the SMR-SERP layered configuration was used. With the random SMR-SERP configuration the methane conversion was about the same as the one obtained in the SMR experiment.

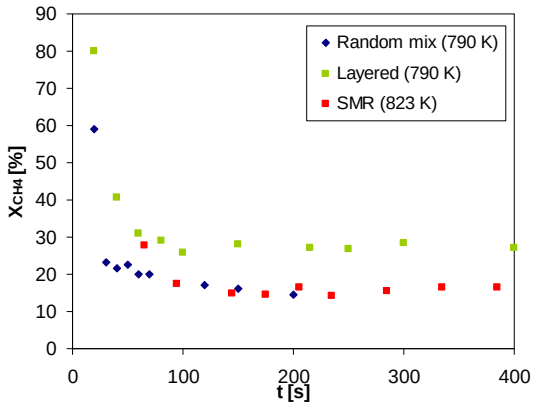

Figure B.4. Methane conversion obtained in the SMR-SERP and SMR experiments. Experimental conditions: 2.0 bar, S/C = 3.7 and 61.5 mmol/min. In the SMR-SERP experiments, random or layered mixing of Degussa catalyst was used. In the SMR experiments only Degussa catalyst was used.

The advantage of SERP is that, in Runs 1 and 2, it was possible to obtain an hydrogen content in the effluent stream 20 % higher than thermodynamic equilibrium. In the SMR experiment, the hydrogen

content was 25 % lower than equilibrium despite the higher temperature employed.

B.4. Conclusions

With the objective of providing proof of concept of steam methane reforming sorption enhanced reaction process (SMR-SERP), experiments were performed employing Degussa catalyst and MG30-Cs hydrotalcite with a sorbent/catalyst ratio of 3. Two different catalyst sorbent configurations were used: random mixing and layered. In the layered configuration, a total of four layers were used (2 of catalyst and 2 of sorbent). Additionally, a steam methane reforming (SMR) experiment was also performed in order to compare with the SMR-SERP experimental results.

In the SMR-SERP experiments an effluent H_2 molar fraction of 0.77 was obtained. This value is 21 % higher than thermodynamic equilibrium at the same operating conditions.

The two sorbent/catalyst configurations provided different results. The highest H_2 concentration in the effluent was obtained using the random packing. However, with the layered packing the hydrogen concentration remained above equilibrium during a longer period of time. This difference was due to the final sorbent layer that acted as a guard bed, preventing the early breakthrough of CO_2. With the layered configuration the CO_2 took 70 s longer to breakthrough.

Experiments were also made using just catalyst but using a feed temperature 30 K higher. Despite the higher temperature that favors the SMR reactions, the hydrogen molar fraction in the effluent was 50 %

lower than the one obtained in SMR-SERP experiments with layered configuration.

These results show the presence of a CO_2 sorbent effectively increases the hydrogen concentration and the methane conversion of the steam methane reforming, even when lower temperatures are employed thus providing proof-of-concept of the SERP concept.

B.5. References

1. Ding, Y.; Alpay, E. Adsorption-enhanced steam-methane reforming. *Chem. Eng. Sci.* (2000), 55, 3929-3940.

2. Mayorga, S. G.; Hufton, J. R.; Sircar, S.; Gaffney, T. R. Sorption Enhanced Reaction Process for the production of hydrogen. Phase I Final Report, Proceedings of U.S. DOE Hydrogen program Review, Washington DC, 1997.

3. Yong, Z.; Mata, V.; Rodrigues, A. E. Adsorption of carbon dioxide at high temperature - a review. *Sep. Purif. Technol.* (2002), 26, 195-205.